HAL
open science

Étude numérique de l'allumage diphasique de foyers annulaires multi-brûleurs

Théa Lancien

To cite this version:

Théa Lancien. Étude numérique de l'allumage diphasique de foyers annulaires multi-brûleurs. Autre. Université Paris Saclay (COmUE), 2018. Français. NNT : 2018SACLC072 . tel-01998191

HAL Id: tel-01998191

https://theses.hal.science/tel-01998191

Submitted on 29 Jan 2019

HAL is a multi-disciplinary open access archive for the deposit and dissemination of scientific research documents, whether they are published or not. The documents may come from teaching and research institutions in France or abroad, or from public or private research centers.

L'archive ouverte pluridisciplinaire **HAL**, est destinée au dépôt et à la diffusion de documents scientifiques de niveau recherche, publiés ou non, émanant des établissements d'enseignement et de recherche français ou étrangers, des laboratoires publics ou privés.

université PARIS-SACLAY

NNT: 2018SACLCO72

CentraleSupélec

Etude numérique de l'allumage diphasique de foyers annulaires multi-brûleurs

Thèse de doctorat de l'Université Paris-Saclay
préparée à CentraleSupélec

École doctorale n°579 Sciences mécaniques et énergétiques, matériaux et géosciences
Spécialité de doctorat: Combustion

Thèse présentée et soutenue à Gif-sur-Yvette, le 04/10/2018, par

Théa Lancien

Composition du Jury :

Bénédicte Cuenot CFD/Combustion Project Leader, CERFACS	Rapporteur
Luc Vervisch Professeur, INSA de Rouen (CORIA – UMR 6614)	Rapporteur
Christine Rousselle Professeure, Université d'Orléans (PRISME)	Présidente du jury
Christian Tenaud Directeur de Recherche, CNRS (LIMSI - UPR 3251)	Examinateur
Michel Cazalens Expert Combustion, SafranTech E&P	Examinateur
Sébastien Candel Professeur, CentraleSupélec (EM2C – UPR 288)	Examinateur
Olivier Gicquel Professeur, CentraleSupélec (EM2C – UPR 288)	Directeur de thèse
Ronan Vicquelin Maître de Conférences, CentraleSupélec (EM2C – UPR 288)	Co-Directeur de thèse

Thèse de doctorat

Remerciements

Je tiens en premier lieu à remercier tous les membres de mon jury, pour avoir accepté d'en faire partie et de se déplacer pour assister à ma soutenance. Merci à Bénédicte Cuenot et Luc Vervisch d'avoir endossé les rôles de rapporteur et rapporteuse de ma thèse, pour leurs remarques pertinentes et leurs idées sur les perspectives possibles de mon travail. Je remercie également Christine Rousselle d'avoir accepté la présidence de mon jury, ainsi que Christian Tenaud et Michel Cazalens d'y avoir été examinateurs. Je remercie enfin tout particulièrement Sébastien Candel qui, en plus d'être examinateur de ma thèse, m'a apporté une aide précieuse lors de la rédaction d'articles en tant que membre de l'équipe expérimentale sur MICCA-Spray.
Je vous remercie tous pour la qualité des échanges que nous avons pu avoir lors de la séance de questions et après.

Je voudrais ensuite remercier les deux personnes qui ont constitué l'encadrement de ma thèse. Olivier, même si tu étais moins disponible, merci d'avoir pris le temps quand tu en avais, pour ton recul et tes précieux conseils sur les présentations. Ronan, cette thèse et les trois (presque quatre) années passées au laboratoire n'auraient pas été les mêmes sans toi. Tu as toujours su garder du temps, voire en libérer si nécessaire, pour analyser des résultats, tenter de résoudre des problèmes ou mettre au point des stratégies de post-traitement. Merci pour ta disponibilité et ton écoute qui, je pense, est appréciée de tous tes doctorants.

Je tiens ensuite à remercier chaleureusement l'équipe administrative, Nathalie, Brigitte et Noï, pour leur aide, leur soutien et leur amitié. Merci de votre efficacité pour toutes les tâches administratives et de contribuer à la vie du laboratoire.
Je remercie également tous les permanents que j'ai eu l'occasion de croiser, Matthieu Boileau, qui a quitté le laboratoire au début de ma thèse, mais qui a eu le temps de m'initier à AVBP, Thomas Schmitt, qui a pris la relève et qui a résolu mes problèmes de parmetis sur chaque nouvelle machine, Aymeric Vié, pour ses éclairages sur le diphasique en version maths et Benedetta Franzelli, pour l'organisation de déjeuners animés et son implication dans la vie des doctorants au laboratoire.
Je remercie toute l'équipe expérimentale qui a travaillé sur MICCA-Spray,

Kévin Prieur, Guillaume Vignat, Daniel Durox, Thierry Schuller et Sébastien Candel, pour la qualité des données et des échanges. Je remercie particulièrement Kevin pour sa disponibilité, d'avoir accepté, toujours de bonne grâce, de vérifier plusieurs fois ses mesures, et pour son amitié.

L'expérience de vie qu'est le doctorat est nécessairement marquée par l'atmosphère du laboratoire. J'ai rencontré à l'EM2C des personnes extraordinaires. Je pense particulièrement à Abigail et Lorella, qui m'ont accompagnée et soutenue, et qui resteront des amies proches, mais aussi à Cédric et Pedro, partenaires de café matinal de la première heure et appuis fidèles. Merci à tous mes co-bureaux, de Chatenay ou de Saclay, Nicolas, Quentin, Chris, Valentin, et surtout Amanda, Davy, Léo, Giampaolo, Nicola et Livia (Oui, Livia compte comme co-bureau), d'avoir contribué à une atmosphère à la fois studieuse et joyeuse. Merci enfin à Arthur pour tous les échanges d'expériences sur les lombricomposteurs, je compte sur toi pour continuer à répandre la bonne parole. Pour finir, je remercie tous les doctorants et post-doctorants que j'ai croisés au cours de ma thèse, citer tout le monde serait trop long et trop risqué.

J'ai une pensée affectueuse pour tous les copains de Centrale, qui m'ont apporté et continuent de m'apporter soutien et amitié, qui ont largement contribué à me permettre d'oublier ma thèse le week-end. Un grand merci à Coline, Anaelle, Juliette et Babas d'être venus jusqu'à Saclay pour ma soutenance, merci aux autres d'être venus fêter ça le soir ! J'embrasse enfin Pauline, venue elle aussi jusqu'à Saclay, au point de devoir courir prendre son train après la soutenance. Promis, je serai à ta prestation de serment.

Il me reste à embrasser ceux qui ont largement participé à ma réussite, ma famille. Merci à mes parents pour leur soutien sans faille, quels que soient mes choix. Je remercie ma soeur Diane (en particulier pour les coupes de champagne que j'ai oubliées à la dernière minute) et mon frère Victor, que je retrouve tous les deux avec bonheur lors de mes retours dans le sud. Merci à Marie-Paule, Camille et Elsa de s'être libérées pour ma soutenance, votre présence m'a fait chaud au coeur, et à Eve, Irène et Léo pour leurs pensées positives.

Enfin, merci à Pierre, qui a tenu bon à mes côtés tout au long de mon doctorat, qui m'a aidée à mettre beaucoup de choses en perspectives. Merci pour ton soutien, ta présence, et les verres de Gin-tonic les soirs des journées compliquées.

Abstract

Ignition is one of the critical issues that arise in the design and dimensioning of aeronautic combustors, in particular when new technologies are envisioned to reduce the amount of pollutants generated by the combustion of fossil fuels. It is therefore important to achieve a detailed understanding of this complex process in realistic conditions in order to enable informed design choices leading to reliable, stable and safe operation of the engines. Some aspects of the ignition process have been largely studied, experimentally and numerically, in particular focusing on the initiation of a first flame kernel through energy deposition as well as on the propagation of this flame kernel towards the fuel injector, leading to flame stabilisation. Starting from fundamental considerations and studies on laminar gaseous flows, degrees of complexity have gradually been added to the set-ups to include turbulence and spray injection, in an effort to tend towards burners that reproduce realistic conditions. Most of the studies have however focused on single burner configurations, while the presence of multiple burners in most industrial chambers creates an additional level of complexity since the flame has to propagate from burner to burner and ignite them one by one. The success of this propagation phase is primordial for the establishment of a complete ignited state that yields the nominal power. This phase, called *light-round*, has been the focus of several experimental and numerical studies in the last decade, leading to the identification of some of the mechanisms driving the flame behaviour. A recent joint experimental and numerical analysis of the light-round in an annular combustion chamber with premixed propane and air injection not only showed the ability of the simulation to capture the processes involved, but also enabled to better understand the phenomena driving the propagation of the flame, in particular in terms of absolute velocity.
With the aim of getting closer to industrial gas turbines, newly available data was published on the light-round with liquid n-heptane injection, highlighting common features with the gaseous case as well as specific characteristics. In the present work, large eddy simulations (LES) of the light-round with two phase injection are carried out for three operating conditions with the AVBP solver, jointly developed by CERFACS and IFP Energy Nouvelles, and compared to experimental data. The liquid phase is described with a mono-disperse Eulerian approach. The numerical set-up, in particular concerning the liquid phase, is first carefully assessed through the simulation of a simpler configuration com-

posed of a single burner. The light-round simulation results are then compared in terms of flame structure and global duration to the corresponding experimental images of the flame front recorded by a high-speed intensified CCD camera and to the corresponding experimental delays. A detailed analysis of the three numerical light-round sequences allows to identify some key aspects of the flame propagation in the two-phase mixture. Calculations indicate that the volumetric expansion due to the chemical reaction at the flame induces a strong azimuthal flow in the fresh stream at a distance of several sectors ahead of the flame, which modifies conditions in this region. This creates heterogeneities in the liquid repartition and wakes on the downstream side of the swirling jets formed by the injectors, with notable effects on the motion of the leading point and on the absolute flame velocity. Finally, heat losses at the walls are accounted for during the light-round in order to assess the simulation's ability to retrieve the marked slowdown of the flame propagation observed experimentally when the quartz walls are at ambient temperature.

Résumé

La phase d'allumage est une composante critique à prendre en compte lors de la conception et du dimensionnement d'une chambre de combustion aéronautique, en particulier lorsque de nouvelles technologies ou architectures sont envisagées dans l'objectif de réduire les émissions de polluants causées par la combustion de carburants d'origine fossile. Il est donc primordial d'atteindre une compréhension détaillée du processus complexe qu'est l'allumage dans des conditions réalistes afin d'être en mesure de choisir les meilleures géométries qui assurent un fonctionnement fiable, stable et sûr des moteurs tout au long de leur cycle de vie. Certains aspects du processus d'allumage ont été largement étudiés dans la littérature, expérimentalement et numériquement. Un certain nombre d'études se sont concentrées sur l'initiation d'un noyau de flamme par un dépôt d'énergie, ainsi que sur la propagation de ce noyau de flamme vers l'injecteur jusqu'à ce qu'une flamme se stabilise. A partir de considérations fondamentales et d'études de flammes gazeuses laminaires, des niveaux de complexités ont petit à petit été ajoutés afin d'arriver à l'étude de flammes turbulentes se propageant dans des nuages de gouttes, dans l'objectif de tendre vers des configurations qui reproduisent davantage les conditions industrielles. La majorité des études ont cependant été réalisées sur des géométries comprenant un unique brûleur. La présence de plusieurs injecteurs ajoute un degré de complexité puisqu'un ou plusieurs fronts de flamme se propagent de brûleur à brûleur en les allumant un par un. La réussite de cette phase de propagation est primordiale pour l'établissement d'un état allumé complet et qui permet d'obtenir une puissance et un fonctionnement nominaux. Cette phase, appelée *light-round*, pour *allumage circulaire* en anglais, a fait l'objet d'un nombre croissant d'études expérimentales et numériques au cours de la dernière décennie, permettant l'identification de certains mécanismes qui pilotent la propagation de la flamme. Une récente étude expérimentale et numérique du *light-round* dans une chambre de combustion annulaire avec injection prémélangée de propane et d'air a non seulement montré la capacité de l'outil numérique à reproduire fidèlement la propagation de la flamme, mais a aussi conduit à une meilleure compréhension des phénomènes qui influent sur la propagation de flamme, en particulier sur sa vitesse absolue dans la chambre.
Dans l'objectif de se rapprocher du fonctionnement des chambres de combustion industrielles, de nouvelles données expérimentales ont été publiées sur

l'allumage circulaire avec injection de n-heptane liquide. Des caractéristiques similaires à celles des allumages gazeux ont été identifiées, mais aussi des aspects spécifiques à la nature diphasique de l'écoulement. Le travail présenté ici décrit la mise en place et la réalisation de simulations aux grandes échelles (ou LES pour *large eddy simulation* en anglais) réalisées, pour trois points de fonctionnement différents, avec le solveur AVBP, co-développé par le CERFACS et l'IFP Energies Nouvelles, et comparées avec les données expérimentales. La phase liquide est décrite par une approche Eulérienne mono-disperse. La configuration numérique, en particulier en ce qui concerne la phase liquide, est tout d'abord évaluée et validée par la simulation d'une configuration simplifiée, composée d'un unique injecteur. Les résultats de la simulation de l'allumage circulaire sont ensuite comparés en termes de structure de flamme et de délai d'allumage aux images expérimentales correspondantes, enregistrées par une caméra rapide, et aux temps d'allumages expérimentaux. Une analyse détaillée des trois séquences d'allumage numériques permet d'identifier certains aspects clés de la propagation de la flamme dans le mélange froid diphasique. Il apparaît que l'expansion volumétrique des gaz brûlés générée par la réaction chimique dans la flamme est responsable d'un important écoulement azimutal dans les gaz frais, plusieurs injecteurs en amont de la flamme, modifiant les conditions dans cette région. Des hétérogénéités sont créées dans le mélange gazeux et la répartition de liquide, ainsi qu'un sillage en aval des jets tourbillonnants formés par chaque injecteur, avec des effets notables sur le comportement de la pointe avant des fronts de flamme et sur la vitesse absolue de propagation. Enfin, les pertes thermiques aux parois sont prises en compte au cours de l'allumage, dans l'objectif d'évaluer la capacité de la simulation à retrouver la forte chute de la vitesse de propagation observée expérimentalement lorsque les parois en quartz sont à température ambiante.

Contents

Abstract **v**

Résumé **vii**

Introduction **1**

1 Equations and models for the large eddy simulation of reactive two-phase flows **23**
1.1 Introduction 24
1.2 Conservation equations for compressible gaseous flows 26
1.3 Equations and models for the liquid phase 34
1.4 Turbulent combustion modelling 54
1.5 Validation of the evaporation model with tabulated chemistry . 67
1.6 Conclusion 74

2 Simulation of the steady-state regime of the single burner configuration SICCA-Spray **77**
2.1 Introduction 78
2.2 Experimental configuration 80
2.3 Numerical set-up and geometry 83
2.4 Simulation of the unconfined configuration 88
2.5 Selection of the injected droplet diameter 96
2.6 Simulation of the confined configuration 104
2.7 Influence of the injected diameter 124
2.8 Conclusion 126

3 Large eddy simulation of light-round in MICCA-Spray and comparison with experiments **127**
3.1 Introduction 128
3.2 MICCA-Spray: experimental configuration 130
3.3 Numerical configuration and initial solution 133
3.4 Light-round simulation and results 142
3.5 Conclusion 157

4 Detailed analysis of light-round in MICCA-Spray with liquid n-heptane and air injection 159
4.1 Introduction 160
4.2 Volumetric expansion of the burnt gases 161
4.3 Flame fronts dynamics: global point of view 173
4.4 Behaviour of the leading points of the flame fronts 191
4.5 Flame-spray interactions 202
4.6 Conclusion 206

5 Impact of the walls temperature on the light-round in MICCA-Spray 209
5.1 Impact of the walls temperature in the experimental results . . 210
5.2 Numerical set-up of the light-round with cold walls 211
5.3 Light-round simulation and results 216
5.4 Analysis of the flow field modifications 225
5.5 Addition of radiative effects 232
5.6 Conclusion 232

Conclusion and perspectives 235

References 252

List of Tables

1.1 Summary of the initial conditions for the two equilibrium computation cases 68
1.2 Equilibrium values predicted by AVBP for Case 1, where $\Delta T^{init} =$ 0 K, for the MS_ref simulation (first column), the MS_mod simulation (second column) and the TTC simulation (last column). The error compared to the reference simulation is added in parentheses when it is greater than 0.01 %. 69
1.3 Equilibrium values predicted by AVBP for Case 2, where $\Delta T^{init} =$ 50 K, for the MS_ref simulation (first column), the MS_mod simulation (second column) and the TTC simulation (last column). The error compared to the reference simulation is added in parentheses when it is greater than 0.01 %. 70

2.1 Mesh characteristics for the SICCA-Spray 84
2.2 Summary of cell sizes for the SICCA-Spray grids. 86
2.3 NSCBC conditions applied on the boundary for the unconfined and confined versions of SICCA-Spray, with and without combustion. 86
2.4 Values of the evaluations of the injected diameter for each quadrature level. 98
2.5 Values of the evaluations weights corresponding to each evaluation of the injected diameter, calculated with the Clenshaw-Curtis quadrature rule, for each quadrature level. 99

3.1 Summary of the considered operating points with liquid n-heptane injection. 133
3.2 Mesh characteristics for the bi-sector and MICCA-Spray 136
3.3 Summary of cell sizes for the bi-sector and annular grids. 136

List of Figures

1 Illustration of the triple interaction in turbulent two-phase combustion: interactions are present between the flame, the turbulent flow and the spray of liquid droplets. 3

2 Group combustion diagram: spray combustion regimes against the total number of droplets N and the non dimensional separation distance S. The regimes are separated by iso-lines of critical values of the group number G. Extracted from Chiu et al. (1982) and Chigier (1983). 6

3 Three-phase nature of the ignition process illustrated on a cannular combustion chamber, extracted from Lefebvre and Ballal (2010). 9

4 Images of light intensity emitted by the flame fronts in the left (top) and right (bottom) halves of the MICCA chamber during a light-round sequence with premixed propane-air injection at $\Phi = 0.76$, in false colours for better visualisation, extracted from Bourgouin et al. (2013). 11

5 Light emission during the ignition sequence of n-heptane (top) and propane (bottom) fuels. Yellow corresponds to high light intensity while dark red represents low light emission. Each sequence features equivalent injection conditions : $U_b = 31.5$ m.s^{-1}, $\Phi = 0.90$ and $\mathcal{P} = 80$ kW, extracted from Prieur et al. (2017). . 12

6 Light-round delay τ_l when: the bulk velocity U_b (left), the equivalence ratio Φ (center or the power $\mathcal{P}$ (right) is kept constant for multiple fuels : propane (gaseous), n-heptane (liquid spray) and dodecane (liquid spray). Linear fits in dashed lines give the general trend for the different fuels, extracted from Prieur et al. (2017). 13

7 Side visualization by 5 kHz OH* chemiluminescence of a successful burner-to-burner flame propagation with a *sawtooth* behaviour. A succession of three burners is sketched. Images were extracted from Machover and Mastorakos (2017). 14

8 Two successive instants (t=14 and 19.2 ms) of the ignition sequence: surface crossing the middle of the chamber coloured by axial velocity (light blue: -20 m.s^{-1} to yellow: 20 m.s^{-1}), iso-surface of velocity coloured by temperature (turquoise blue: 273 K to red: 2400 K), and iso-surface of progress rate (shiny light blue) representing the flame front. The two high-speed hot jets used for ignition appear as red zones in the pictures (marked I1 and I2). The images were extracted from Boileau et al. (2008). 16

9 Flame fronts merging delays in MICCA for premixed propane-air injection at $\Phi = 0.74$ versus the bulk velocity U_{bulk}. Circles, diamonds, triangles and squares correspond to the experimental measurements, the two stars to the delays predicted by the numerical simulation. The dashed line shows the delays predicted by the model developed by Philip. This graph was extracted from Philip (2016). 17

1.1 Time evolution of a physical quantity in a turbulent flow computed with DNS, LES and RANS, extracted from Poinsot and Veynante (2012). 29

1.2 Turbulent energy spectrum as a function of the wave number.The computed and modelled ranges are shown for each computational technique. In LES, the cut-off value is noted k_c. Extracted from Poinsot and Veynante (2012). 30

1.3 Decomposition of the particle velocity $\mathbf{u}_p$ into a mesoscopic part $\check{\mathbf{u}}_l$ and an uncorrelated part $\mathbf{u}''_p$. 38

1.4 Definition of the heat fluxes at the surface of a single isolated droplet. In red is plotted the evolution of the temperature, uniform inside the droplet and evolving towards its far-field value T_∞ in the gaseous phase, adapted from Boileau (2007). 45

1.5 Illustration of the thickening procedure applied to a flame front (in red) too thin for the grid, yielding a thickened flame front (in blue). 55

1.6 Temporal evolution of the liquid mass density (top left), the droplet diameter (top right), gaseous and the liquid temperatures (bottom left) and the n-heptane mass fraction (bottom right) for cases MS_ref (blue), MS_mod (red) and TTC (green), for Case 1 where $\Delta T^{init} = 0$ K. 71

1.7 Left: temporal evolution of the liquid mass density. Right: relative error on the volume fraction α_l for cases MS_mod (blue), MS_mod with constant viscosity (red) and TTC (green), compared to case MS_ref, for Case 1 where $\Delta T^{init} = 0$ K. 72

1.8 Temporal evolution of the liquid mass density (top left), the droplet diameter (top right), gaseous and the liquid temperatures (bottom left) and the n-heptane mass fraction (bottom right) for cases MS_ref (bue), MS_mod (red) and TTC (green), for Case 2 where $\Delta T^{init} = 50$ K. 73
1.9 Top: Laminar flame speed depending on the equivalence ratio for 1D gaseous flames for the kinetic scheme C7H16-AIR-2S_DP (from Paulhiac (2015)) in green dots and USC2 (from Smallbone et al. (2009)) in red dots, compared to reference data (blue dashed lines) extracted from Davis and Law (1998). Bottom: Adiabatic flame temperature depending on the equivalence ratio. 74
1.10 Temporal evolution of the liquid mass density (left), the droplet diameter (right), for cases MS_ref (blue), TTC (red) and TTC_USC2 (green), for Case 1 where $\Delta T^{init} = 0$ K at the top and Case 2 where $\Delta T^{init} = 50$ K at the bottom. 75

2.1 Experimental burner SICCA-Spray. Left: photograph of the burner in the unconfined configuration, a sketch of the swirler appears in the top left-hand corner and a vertical tomography of the spray is shown in the top right-hand corner. Right: photograph of the burner with a confinement quartz with a diameter of 70 mm and a length of 150 mm. 81
2.2 Distribution of droplet diameter in the spray at $x = 2.5$ mm from the exhaust plane and $r = 4.5$ mm. The two vertical lines indicate the mean diameter D_{10} and the Sauter diameter D_{32}. . 82
2.3 Evolution of the internal (in blue) and external (in red) temperatures of the walls in SICCA-Spray, with combustion, plotted against the height. 83
2.4 Visualisation of the numerical domain (without the surrounding atmosphere) and the mesh around the swirler exhaust for the unconfined configuration. The atmosphere is visible on the mesh slice. 84
2.5 Visualisation of the numerical domain (without the surrounding atmosphere) and the mesh around the swirler exhaust for the confined configuration. 85
2.6 Tomography of the spray created by the liquid atomizer flush with the exit plane, without any confinement. Left: vertical tomography with a laser sheet going through the injector centerline, right: horizontal tomography at $x = 2$ mm. 87
2.7 Imposed velocity profiles on the fuel injection patch against the radius, fitted from experimental data. 88
2.8 Instantaneous (left) and average (right) fields of the axial velocity for the air flow simulation. 89

2.9 Mean (left) and RMS (right) velocity profiles for the gas phase at $x = 2.5$ mm from the exhaust plane: axial (top), tangential (middle) and radial component (bottom). −: Numerical results from the gaseous simulation; • : Experimental data. The radial position of the swirler exit hole is represented by the black dashed lines. 90

2.10 Mean axial (top) and radial (bottom) mean (left and rms (right) velocity fields, compared to the experiment (in symbols), for different mesh refinements. 92

2.11 Mean velocity profiles for the gas phase at $x = 2.5$ mm (left) and $x = 7.5$ mm (right) from the exhaust plane: Axial velocity (top) and azimutal velocity (bottom). Black curves represent the results from purely gaseous cases and the red curves the gaseous fields from two-phase flow cases. −: Numerical results; • : Experimental data. 93

2.12 Mean axial velocity for the liquid phase at $x = 2.5$ mm. −: Numerical results; ▲: Experimental arithmetic average; •: Experimental mass-weighted average. 94

2.13 Mean axial (left) and tangential (right) velocity fields for the liquid phase at $x = 7.5$ mm. −: Numerical results; • •: Mass-averaged experimental field; • •: Arithmetic average experimental velocity, Experimental profiles: - -: $d_l = 2 - 3\ \mu m$; - - : $d_l = 10 - 12\ \mu m$; - -: $d_l = 20 - 23\ \mu m$; - -: $d_l = 23 - 36\ \mu m$; - -: $d_l = 26 - 30\ \mu m$. - -: $d_l = 30 - 34\ \mu m$; 95

2.14 Response surface for the axial velocity at $x = 7.5$ mm and some of the numerical fields used for the expansion. 100

2.15 PCE approximation for the axial velocity at $r = 0$ mm (top left), $r = 3$ mm (top right), $r = 7$ mm (bottom left) and $r = 10$ mm (bottom right). −: PCE expansions; • : Numerical values from mono-disperse simulations. 101

2.16 Normalised L^2-norm of the different error criteria at $x = 7.5$ mm. Black curve: error on liquid axial velocity, blue curve: error on the liquid equivalent diameter and red curve: error on the two-phase laminar flame speed. 102

2.17 Comparison of the normalised L^2-norm of the different error criteria at $x = 7.5$ mm. Black curves: quadrature level 3, polynomial order 5, blue curves: quadrature level 4, polynomial order 5 and red curves: quadrature level 4, polynomial order 8. 104

2.18 Mean velocity profiles for the gas phase at $x = 5$ mm (left) and $x = 20$ mm (right) from the exhaust plane: Axial velocity (top), radial velocity (center) and azimuthal velocity (bottom). −: Numerical results; • : Experimental data. 105

2.19 RMS velocity profiles for the gas phase at $x = 5$ mm (left) and $x = 20$ mm (right) from the exhaust plane: Axial velocity (top), radial velocity (center) and azimuthal velocity (bottom). −: Numerical results; • : Experimental data. 106

2.20 Tangential cuts at $z = 0$ mm of the average (left) and instantaneous (right) axial gaseous velocity fields in the two-phase simulation of the confined configuration. The same color scale in used, from $u = -20$ m.s^{-1} in blue to $u = 20$ m.s^{-1} in red. White iso-lines of $u = 0$ m.s^{-1} are added. 107

2.21 Tangential cuts at $z = 0$ mm on an instantaneous solution of the confined mono-burner chamber, coloured by the liquid mass fraction $\alpha_l \rho_l$ (top), the gaseous equivalence ratio Φ_g (bottom left) and the total equivalence ratio $\Phi_{tot} = \Phi_g + \Phi_l$ (bottom right). 108

2.22 Comparison of the flame shape between the adiabatic walls case (left), the experiment (center) and the isothermal walls case (right). 110

2.23 Temporal evolution of the local pressure at a probe located at $x = 10$ mm, $y = 17.5$ mm and $z = 0$ mm. The red dashed line marks the instant of the flame lifting. 111

2.24 Left: Visualisation of the pressure field on a $z = 0$ plane. The flame position is highlighted by an iso-line of the heat release rate $hr = 1 \times 10^8$ J.s^{-1}.m^{-3}. Right: top view of an iso-surface of the heat release rate $hr = 1 \times 10^8$ J.s^{-1}.m^{-3}. 112

2.25 Left: Visualisation of the pressure field on a $z = 0$ plane for the case with relaxed walls. The flame position is highlighted by an iso-line of the heat release rate $hr = 1 \times 10^8$ J.s^{-1}.m^{-3}. Right: top view of an iso-surface of the heat release rate $hr = 1 \times 10^8$ J.s^{-1}.m^{-3}. 113

2.26 Comparison of the flame shape between the experiment (left), the iso-thermal relaxed walls simulation (center) and the iso-thermal walls non-relaxed case (right). 113

2.27 Visualisation of the precessing vortex core in an instantaneous solution with relaxed walls, highlighted by an iso-surface of the pressure at P = 99800 Pa. 114

2.28 Tangential cuts at $z = 0$ mm of the average (left) and instantaneous (right) axial gaseous velocity fields in the simulation with iso-thermal boundary conditions on the chamber walls. The same color scale in used, from $u = -20$ m.s^{-1} in blue to $u = 20$ m.s^{-1} in red. Black iso-lines of the heat release rate $HR = 1 \times 10^8$ W.m^{-3} are added. 114

2.29 Mean axial velocity profiles for the gas phase at different heights. −: adiabatic walls simulation; −: isothermal non-relaxed walls; −: isothermal relaxed walls; • : Experimental data. 115

2.30 Tangential cuts at $z = 0$ mm of the average (left) and instantaneous (middle) the axial gaseous temperature and of the instantaneous CO_2 mass fraction (right) in the simulation with iso-thermal boundary conditions on the chamber walls. The same color scale in used for the temperature, from $T_g = 260$ K in blue to $T_g = 1700$ K in red. Black iso-lines of the heat release rate $HR = 1 \times 10^8$ W.m^{-3} are added. 116

2.31 Average normal energy flux on the chamber internal wall. . . . 117

2.32 Non-dimensional Takeno's index multiplied by the local heat release rate. Top: TI on instantaneous fields, bottom: TI on average fields; left: adiabatic simulation, right: iso-thermal simulation. Red stands for positive values (premixed regime), blue for negative values (diffusion regime) and grey for zero (no combustion). 118

2.33 Scatter plots of temperature (left and middle) and heat release rate normalised by the global maximum (right) against mixture fraction for heights x = 0 mm, x = 2.5 mm, x = 5 mm, x = 10 mm and x = 20 mm. The temperature plot is displayed without any colouring (left), coloured by the local progress variable C (right). On each plot, the two red lines represent the global injected mixture fraction ($Z_{inj} = 0.056$) and the stoichiometric mixture fraction ($Z_{st} = 0.062$). 120

2.34 Top: true-color experimental images from three ignition sequences in SICCA-Spray. Bottom: close-up images at $t = 5$ ms and $t = 21$ ms. The images are extracted from Prieur et al. (2018). 122

2.35 Instantaneous fields of TI $\times$ HRR at six instants between $t = 69$ ms (top left) and $t = 74$ ms (bottom right), $t = 0$ ms corresponding to the insertion of the burnt gases sphere. Two iso-lines of the progress variable $c = 0.1$ (in white) and $c = 0.9$ in black are added. These instants are chosen to show the lifting of the flame in the simulation. 123

2.36 Average flame shapes for several values of the injected diameter, for $d_{inj} = D_{10} = 8$ μm (left), $d_{inj} = D_{32} = 20$ μm (center right), and $d_{inj} = D_{opt} = 15.3$ μm (right), compared to the experimental averaged Abel transform (center left). The white lines are iso-lines of the gaseous axial velocity at $u = 0$ m.s^{-1}. . 124

2.37 Mean axial velocity profiles for the gas phase at different heights for different values of the injected diameter.$D_{inj} = D_{opt}$; $-$: iso-thermal relaxed walls, $D_{inj} = D_{opt}$; $-$: iso-thermal relaxed walls, $D_{inj} = D_{32}$; $-$: iso-thermal relaxed walls, $D_{inj} = D_{10}$; $\bullet$: Experimental data (provided by K. Prieur and D. Durox). 125

3.1 Direct view of the MICCA-Spray combustion chamber. The sketch at the bottom right represents a cut of the swirler unit showing the gaseous (G arrows) and liquid (L arrow) injection. 131
3.2 Schematic top view of the MICCA-Spray backplane showing the swirlers positions, photo-multipliers (PM), spark plug and swirl direction. 132
3.3 Temporal evolution of the external quartz wall temperature between two injectors and at $x = 40$ mm with premixed propane-air injection. Left: evolution after the triggering of the ignition, $t = 0$ s corresponds to the ignition of the chamber. Right: temperature evolution after extinction of the chamber at $t = 0$ s. The temperatures were measured by applying a thermocouple against the wall. 133
3.4 Visualisation of the geometry and mesh of a bi-sector. The mesh is shown through a cylindrical slice at the middle of the chamber. 135
3.5 Visualisation of the instantaneous axial velocity u on a slice at $r = 175$ mm for case $\Phi = 0.89$, at instants $t = 0.3$ s (left) and $t = 0.4$ s (right). 137
3.6 Visualisation of the instantaneous n-heptane mass fraction $Y_{C_7H_{16}}$ on a slice at $r = 175$ mm for case $\Phi = 0.89$, at instants $t = 0.3$ s (left) and $t = 0.4$ s (right). 138
3.7 Visualisation of the instantaneous liquid density $\alpha_l \rho_l$ on a slice at $r = 175$ mm for case $\Phi = 0.89$, at instants $t = 0.3$ s (left) and $t = 0.4$ s (right). 139
3.8 Transient evolution of the mean gaseous equivalence ratio in the bi-sector chamber Φ_{gas}^{mean} for all three cases, each represented by a different color. The dots stand for the numerical data, which is approximated by an exponential curve in full lines. The left and right series of vertical lines respectively mark 95% and 99% of the estimated final values. 139
3.9 Visualisation of the instantaneous liquid density $\alpha_l \rho_l$ on a slice at $r = 175$ mm for cases $\Phi = 0.8$ (left), $\Phi = 0.89$ (middle) and $\Phi = 1.0$ (right), on a solution at 95% of the estimated final value. 140
3.10 Visualisation of the local gaseous equivalence ratio Φ_{gas} on a slice at $r = 175$ mm for cases $\Phi = 0.8$ (left), $\Phi = 0.89$ (middle) and $\Phi = 1.0$ (right), on a solution at 95% of the estimated final value. 140
3.11 Visualisation of the instantaneous liquid density $\alpha_l \rho_l$ on a slice at $r = 175$ mm for case $\Phi = 0.89$ on a solution at 95% of the estimated final value, with a simplified evaporation model (right) and the more complex one (left). 141
3.12 Fields extracted from a solution averaged over $\Delta t = 0.12$ s for case $\Phi = 0.89$. Left: iso-surface of the axial velocity $u = 5$ m.s^{-1}. Right: Slice at $r = 175$ mm coloured by the axial velocity u. . . 142

3.13 Axial cuts extracted from a solution averaged over $\Delta t = 0.12$ s for case $\Phi = 0.89$ coloured by the tangential gaseous velocity u_θ. 143

3.14 Left: Evolution of the autocorrelation for the axial gaseous velocity fluctuations on the axi-periodic patch at $x = 7.5$ ms (in black) and the corresponding exponential approximation (in red). Right: autocorrelation times for the three component of the velocity against the height on the chamber, for case $\Phi = 0.89$. 144

3.15 Light-round durations as a function of the global injected equivalence ratio. Diamond symbols stand for experimental results. The durations predicted by the simulations are represented by red circles. The green square indicates the light-round simulated before fixing the evaporation model. 145

3.16 Comparison between experimental and numerical flame configurations at three instants during the light-round sequence for case $\Phi = 0.8$, $t = 5$ ms (top), $t = 15$ ms (middle) and $t = 20$ ms (bottom). 146

3.17 Comparison between experimental and numerical flame configurations at three instants during the light-round sequence for case $\Phi = 0.8$, $t = 30$ ms (top), $t = 40$ ms (middle) and $t = 50$ ms (bottom). 147

3.18 Comparison between experimental and numerical flame configurations at three instants during the light-round sequence for case $\Phi = 0.89$, $t = 4$ ms (top), $t = 10$ ms (middle) and $t = 15$ ms (bottom). 148

3.19 Comparison between experimental and numerical flame configurations at three instants during the light-round sequence for case $\Phi = 0.89$, $t = 25$ ms (top), $t = 34$ ms (middle) and $t = 44$ ms (bottom). 149

3.20 Comparison between experimental and numerical flame configurations at three instants during the light-round sequence for case $\Phi = 1.0$, $t = 5$ ms (top), $t = 15$ ms (middle) and $t = 20$ ms (bottom). 150

3.21 Comparison between experimental and numerical flame configurations at three instants during the light-round sequence for case $\Phi = 1.0$, $t = 30$ ms (top), $t = 40$ ms (middle) and $t = 50$ ms (bottom). 151

3.22 Comparison between the integrated heat release rate in the chamber and the total light intensity obtained from the experimental images. Top left: $\Phi = 0.8$, top right: $\Phi = 0.89$, bottom: $\Phi = 1.0$. 152

3.23 Comparison between the integrated heat release rate in the chamber and the total light intensity obtained from the experimental images. •: Experimental data from one sequence, –: numerical data. Top left: $\Phi = 0.8$, top right: $\Phi = 0.89$, bottom: $\Phi = 1.0$. The black and blue solid lines mark the merging instant of the experimental and numerical sequences, respectively. The blue dashed lines highlight the beginning and the end of the numerical phases, identified by Roman numbers. 153

3.24 Evolution of the integrated heat release rate in each sector of the H+ side of the chamber (right) and the H- side (left) for cases $\Phi = 0.8$ (top), $\Phi = 0.89$ (middle) and $\Phi = 1.0$ (bottom). The beginning and the end of the phases identified on the numerical images are marked through black vertical dashed lines. The phases are labelled by Roman numbers. 155

3.25 Comparison of sectors ignition times for cases $\Phi = 0.8$ (left), $\Phi = 0.89$ (center) and $\Phi = 1.0$ (right), –: Simulation, H+, –: Simulation, H-, ••: Experimental measurements on the H- side of the chamber, each color stands for a different sequence. . . . 156

4.1 Schematic description of the unfolded surface for a given radius r^{cut}. The cylindrical cut is divided at sector S_0 and unfolded as shown. 161

4.2 Visualization of the tangential gaseous velocity on a cylinder of radius $r^{cut} = 175$ mm, crossing the injectors' centerlines, unfolded on a plane surface for the case $\Phi = 0.89$ at different instants. The lateral sides of the unfolded cylinder correspond to the location of the first ignited injector. Tangential velocities are counted positive from left to right and range from $u_\theta = -20$ m.S^{-1} in blue to $u_\theta = 20$ m.S^{-1} in red. Two iso-lines of the progress variable $\widetilde{c} = 0.1$ and $\widetilde{c} = 0.9$ (in black) highlight the position of the flame fronts. 162

4.3 Visualization of the axial gaseous velocity on a cylinder of radius $r^{cut} = 175$ mm, crossing the injectors' centerlines, unfolded on a plane surface for the case $\Phi = 1.0$ at different instants. The lateral sides of the unfolded cylinder correspond to the location of the first ignited injector. The velocity varies between $u_x = -30$ m.s^{-1} in blue and $u_x = +30$ m.s^{-1} in red. Two iso-lines of the progress variable $\widetilde{c} = 0.1$ and $\widetilde{c} = 0.9$ (in black) highlight the position of the flame fronts. 164

4.4 Schematic description of the radial cuts, for fixed azimuthal positions θ^{cut}. Two cuts are displayed for $\theta^{cut} = 78.25°$ on the H+ and H- sides as well as the definition of the angles. A lateral and a top view of the chamber are presented 166

4.5 Temporal evolution of the mean tangential gaseous velocity (u_θ for H+ in blue and $-u_\theta$ for H- in red) on the left and the mean axial gaseous velocity on the right (full lines), averaged over cuts for several values of θ^{cut}. The dashed lines represent the averaged heat release rate, associated to the right axis. Data from H+ cuts is presented in blue and data from H- in red. The vertical lines mark the instant of the flame crossing, based on the leading points position. The data presented here is extracted from case $\Phi = 0.8$. 167

4.6 Evolution of the mass flowrates (left) and mean velocities (right) at the chamber exit for the three cases. Left plots: -: burnt gases, -: total unburnt mixture, -: total mixture. The unburnt gases exiting the chamber are divided into: - -: unburnt gaseous mixture, - -: unburnt liquid. Right plots: -: burnt gases mean velocity, - : unburnt mixture mean velocity. 169

4.7 Evolution of the liquid mass flowrate at the chamber exit for each case, $\Phi = 0.80$ in blue, $\Phi = 0.89$ in red and $\Phi = 1.0$ in green. The black horizontal dashed line marks the total liquid mass flowrate injected in the chamber through the swirlers. . . 171

4.8 Evolution of the percentage of liquid mass flowrate at the chamber exit for each case, $\Phi = 0.80$ in blue, $\Phi = 0.89$ in red and $\Phi = 1.0$ in green. 172

4.9 Visualisation of TI $\times$ HRR during the flame propagation in case $\Phi = 0.89$ on a cylinder of radius $r^{cut} = 175$ mm, crossing the injectors' centerlines, unfolded on a plane surface. Data is presented for $t = 10$ ms (top), $t = 20$ ms (middle) and $t = 30$ ms (bottom). Positive values (from yellow to red) indicate premixed combustion areas while negative values (in shades of blue) non-premixed reaction areas. Two iso-lines of the progress variable $\widetilde{c} = 0.1$ and $\widetilde{c} = 0.9$ (in black) highlight the position of the flame fronts. 174

4.10 Visualisation of TI $\times$ HRR during the flame propagation in case $\Phi = 1.0$ on a cylinder of radius $r^{cut} = 175$ mm, crossing the injectors' centerlines, unfolded on a plane surface. Data is presented for $t = 15$ ms (top), $t = 25$ ms (middle) and $t = 40$ ms (bottom). Positive values (from yellow to red) indicate premixed combustion areas while negative values (in shades of blue) non-premixed reaction areas. Two iso-lines of the progress variable $\widetilde{c} = 0.1$ and $\widetilde{c} = 0.9$ (in black) highlight the position of the flame fronts. 175

4.11 Left: zoom on one injector during the light-round of case $\Phi = 0.89$ at $t = 30$ ms, the zoom area is identified by the black dashed line rectangle in Fig. 4.9. Centre: instantaneous solution of the stabilised flame in SICCA-Spray with adiabatic boundary conditions. Right: zoom on the propagating flame during the light-round of case $\Phi = 0.89$ at $t = 30$ ms, the zoom area is identified by the blue dashed line rectangle in Fig. 4.9. All images are coloured by TI×HRR with the colour scale displayed in Fig. 4.9. 175

4.12 Visualisation of the liquid density $\alpha_l \rho_l$ during the flame propagation in case $\Phi = 0.89$ on a cylinder of radius $r^{cut} = 175$ mm, crossing the injectors' centerlines, unfolded on a plane surface. Data is presented for $t = 0$ ms (top), $t = 20$ ms (middle) and $t = 30$ ms (bottom). Two iso-lines of the progress variable $\widetilde{c} = 0.1$ and $\widetilde{c} = 0.9$ (in black) highlight the position of the flame fronts. 176

4.13 Visualisation of the liquid density $\alpha_l \rho_l$ during the flame propagation in case $\Phi = 1.0$ on a cylinder of radius $r^{cut} = 175$ mm, crossing the injectors' centerlines, unfolded on a plane surface. Data is presented for $t = 0$ ms (top), $t = 15$ ms (middle) and $t = 40$ ms (bottom). Two iso-lines of the progress variable $\widetilde{c} = 0.1$ and $\widetilde{c} = 0.9$ (in black) highlight the position of the flame fronts. . . 177

4.14 Temporal evolution of the resolved flame surface A_{res} in full black lines, the total flame surface A_{tot} in dashed blue lines and the subgrid scale flame surface A_{sgs} in red dots. Results for the three cases are displayed: top left for case $\Phi = 0.8$, top right for case $\Phi = 0.89$ and bottom for case $\Phi = 1.0$. For each case, vertical dashed lines mark the beginning and the end of phases I to IV. 178

4.15 Evolution of normalised quantities for the three cases. Full lines: normalised integrated heat release rate, dashed lines: normalised total flame surface. Each quantity has been normalised by its maximum for the sake of comparison. 179

4.16 Average total and resolved flame flame surfaces over phase III, A_{tot}^{III} in blue and A_{res}^{III} in green, as displayed on Fig. 4.14, against the global equivalence ratio Φ, associated to the left axis. Light-round delay τ^{lr} in red against the global equivalence ratio Φ, associated to the right axis. 180

4.17 Evolution of the wrinkling factor $\{\Xi_\Delta\}_{res}$ for cases $\Phi = 0.8$ in blue, $\Phi = 0.89$ in red and $\Phi = 1.0$ in green during the light-round sequence. 181

4.18 Evolution of the resolved wrinkling $\Xi_{res} = A_{res}/A_0$ for cases $\Phi = 0.8$ in blue, $\Phi = 0.89$ in red and $\Phi = 1.0$ in green during the light-round sequence. 183

4.19 Evolution of the equivalence ratio averaged on the resolved flame front $\{\Phi\}_{res}$ for cases $\Phi = 0.8$ in blue, $\Phi = 0.89$ in red and $\Phi = 1.0$ in green during the light-round sequence. 184
4.20 Global light-round velocity as defined in Eq. 4.17 against the global injected equivalence ratio. 185
4.21 Consumption speeds in the large-eddy simulations of the light-round for the three cases, $\Phi = 0.8$ in blue, $\Phi = 0.89$ in red and $\Phi = 1.0$ in green. S_c^{TF} is plotted in dashed lines, S_c^{1D} in full lines, and the laminar flame speed S_l^0 of the global injected equivalence ratio for each case is added as horizontal dot-dashed lines. 187
4.22 Absolute flame speed averaged on the resolved LES flame surface for the three cases $\Phi = 0.8$ in blue, $\Phi = 0.89$ in red and $\Phi = 1.0$ in green. The beginning and the end of phases I to III are added for each case as vertical dashed lines. The horizontal lines mark the value of the global light-round velocity V^{lr} for each case. . . 189
4.23 Absolute turbulent flame speed S_a^T for the three cases $\Phi = 0.8$ in blue, $\Phi = 0.89$ in red and $\Phi = 1.0$ in green. The beginning and the end of phases I to III are added for each case as vertical dashed lines. 190
4.24 Instantaneous snapshot of the propagating flame for a case with preheated walls at $\Phi = 0.89$. The camera is positioned behind sector S_4. The flame front propagates from right to left. Extracted from Prieur et al. (2018). 192
4.25 Leading points trajectories projected on the chamber backplane for different value of the progress variable $\widetilde{c}$, for case $\Phi = 0.8$. The LP is defined on three different iso-surfaces, $\widetilde{c} = 0.1$ (blue), $\widetilde{c} = 0.5$ (red) and $\widetilde{c} = 0.9$ (green). 193
4.26 Leading points trajectories projected on the chamber backplane for the three cases: the blue, red and green lines respectively stand for $\Phi = 0.8$, $\Phi = 0.89$ and $\Phi = 1.0$ with the LP defined on the $\widetilde{c} = 0.9$ iso-surfaces. 194
4.27 Leading points height against their azimuthal position for H+ (blue lines) and H- (red lines) and all three cases: $\Phi = 0.8$ at the top, $\Phi = 0.89$ in the middle and $\Phi = 1.0$ at the bottom. 195
4.28 Comparison of sectors ignition times for cases $\Phi = 0.8$ (left), $\Phi = 0.89$ (center) and $\Phi = 1.0$ (right), in the simulation for H+: $-$: from sector-integrated heat release, $--$: from the leading point position, for H-: $-$: from sector-integrated heat release, $--$: from the leading point position, $\bullet\bullet$: Experimental measurements on the H- side of the chamber, each color stands for a different sequence. The origin of times is set for all sequences at the instant of ignition of sector S_1 (or S_{-1}). 196

4.29 Comparison of the azimuthal speed v_θ^{lp} of the leading point (in red) and the flow azimuthal velocity at the same point (in black) plotted with respect to the leading point angular position for H+ (right) and H- (left). Results are given for the three cases $\phi = 0.8$ (top), $\phi = 0.89$ (middle) and $\phi = 1.0$ (bottom). 198

4.30 Flame velocities for all three cases, top left: $\Phi = 0.8$, top right: $\Phi = 0.89$ and bottom: $\Phi = 1.0$. Several velocities are plotted: the light-round velocity V^{lr} in cyan dashed lines, the flame absolute turbulent velocity S_a^T in blue lines and the H+ and H- leading points absolute velocities in green and red lines, respectively. The phases are indicated through vertical black dashed lines. 200

4.31 Zoom on the flame front in the leading point area on an unfolded cylindrical cut at $r^{cut} = r^{lp}$, coloured by the tangential velocity, for case $\Phi = 0.80$ and at $t = 25.0$ ms. The flame is evidenced by white iso-lines of the progress variable $c = 0.1$ and $c = 0.9$. The LP is highlighted by the black circle. The tangential velocity is counted positive from right to left. The flame propagates from right to left. 201

4.32 Time evolution of the gaseous equivalence ratio, computed on the carbon atoms, at the leading point in H+ (blue lines) and H- (red lines) and for $\Phi = 0.8$ (top), $\Phi = 0.89$ (middle) and $\Phi = 1.0$ (bottom). The horizontal black dashed lines mark the global equivalence ratio injected for each case. 202

4.33 Visualisations of the unfolded cylindrical cut taken at $r^{cut} = 175$ mm unfolded on a plane surface for case $\Phi = 0.8$ at instant $t = 17$ ms. The cut is coloured by the tangential gaseous velocity (top), the liquid mass density (middle) and the liquid droplet diameter (bottom). Tangential velocities are counted positive from left to right. Two iso-lines of the progress variable $\widetilde{c} = 0.1$ and $\widetilde{c} = 0.9$ (in black) highlight the position of the flame fronts. The insert on the right represents the impact of the flame progress (red iso-surface) on the liquid spray, evidenced by a blue iso-surface at $\alpha_l \rho_l = 0.01$ kg.m^{-3}. 203

4.34 Visualisation of the effect of the flame fronts on the liquid sprays, evidenced by blue iso-surfaces of the liquid mass density $\alpha_l \rho_l = 0.01$ kg.m^{-3}. The flame fronts are represented by iso-surfaces of the progress variable $\widetilde{c} = 0.9$. Snapshots are taken for H- (left) and H+ (right) at $t = 25$ ms from case $\Phi = 0.8$. 204

4.35 Temporal evolution of the liquid mass density $\alpha_l \rho_l$ (black solid lines, right axis) and the gaseous equivalence ratio Φ_g (blue dashed lines, left axis) for the three cases $\Phi = 0.8$ (top), $\Phi = 0.89$ (middle) and $\Phi = 1.0$ (bottom) at point [$x = 2.5$ mm, $r = 0.175$ m, $\theta = 9\pi/16$]. The crossing of the flame can be evidenced by the decrease of the liquid density to zero. 205

5.1 Experimental values of the light-round durations as a function of the global injected equivalence ratio for n-heptane and air injection. The red diamond symbols stand for the experimental measurements carried out with pre-heated walls and the blue circles stand for measurements with walls at ambient temperature. 211

5.2 Axial slice of the computational domain, with the plenum coloured in pink, the chamber in red and the outer atmosphere in blue. The axial co-flow is represented by black arrows. 212

5.3 Visualisation of the field of y^+ at the wall on the internal chamber wall at instants $t = 15$ ms (top) and $t = 35$ ms (bottom). The flame fronts position is highlighted by two iso-lines of the progress variable at $c = 0.1$ and $c = 0.9$. 214

5.4 Visualisation of the instantaneous liquid density $\alpha_l \rho_l$ (left) and the gaseous equivalence ratio Φ_g on a slice at $r = 175$ mm for case $\Phi = 0.89$ on a solution at 95% of the estimated final value, with a simplified evaporation model. 217

5.5 Visualisation of the flame kernel on the initial solution for the light-round with iso-thermal walls at $T_{wall} = 300$ K. The flame kernel is represented by an iso-surface of the progress variable at $c = 0.9$ and the surrounding injectors are highlighted by iso-surfaces of the axial gaseous velocity $u = 25$ m.s^{-1}. The initial sphere's size had to be increase to compensate the losses at the bottom of the chamber. 218

5.6 Light-round durations as a function of the global injected equivalence ratio for n-heptane and air injection. Red diamond symbols stand for experimental results with pre-heated walls and blue circles with ambient temperature walls. The durations predicted by the simulations with adiabatic chamber walls are represented by green triangles for the LES with the *complex* evaporation model and a green square for the LES with the *simplified* evaporation model. The purple cross indicates the light-round duration predicted by the simulation with iso-thermal walls at $T_{wall} = 300$ K and with the *simplified* evaporation model. 219

5.7 Comparison between the adiabatic and iso-thermal walls numerical sequences at three instants during the light-round sequence for case $\Phi = 0.89$, $t = 5$ ms (top), $t = 15$ ms (middle) and $t = 20$ ms (bottom). 220

5.8 Comparison between the adiabatic and iso-thermal walls numerical sequences at three instants during the light-round sequence for case $\Phi = 0.89$, $t = 30$ ms (top), $t = 40$ ms (middle) and $t = 47$ ms (bottom). 221

5.9 Comparison between the adiabatic and iso-thermal walls numerical sequences at three instants during the light-round sequence for case $\Phi = 0.89$, $t = 48$ ms (top), $t = 49$ ms (middle) and $t = 50$ ms (bottom). 222

5.10 Comparison between experimental and numerical with light-round sequences with walls at ambient temperature. Three instants are displayed, $t = 5$ ms (top), $t = 15$ ms (middle) and $t = 20$ ms (bottom). 223

5.11 Comparison between experimental and numerical with light-round sequences with walls at ambient temperature. Three instants are displayed, $t = 30$ ms (top), $t = 40$ ms (middle) and $t = 50$ ms (bottom). 224

5.12 External chamber wall unfolded on a plane surface, coloured by the normal wall flux. Three instants are displayed, $t = 25$ ms (top), $t = 35$ ms (middle) and $t = 45$ ms (bottom). 225

5.13 Internal chamber wall unfolded on a plane surface, coloured by the normal wall flux. Three instants are displayed, $t = 25$ ms (top), $t = 35$ ms (middle) and $t = 45$ ms (bottom). 226

5.14 Zoom on the left flame front area on the external wall (left) and the internal wall (right) at $t = 35$ ms and coloured by the normal flux at the wall. The zoom areas are identified by the dashed rectangles on Figs. 5.12 and 5.13. 227

5.15 Axial cut of the flow field in the chamber at $X = 10$ mm, coloured by the gaseous temperature T_g, at four instants of the simulation, $t = 10$ ms (top left), $t = 25$ ms (top right), $t = 35$ ms (bottom left) and $t = 50$ ms (bottom right). 228

5.16 Axial cut of the flow field in the chamber at $X = 100$ mm, coloured by the gaseous temperature T_g, at four instants of the simulation, $t = 10$ ms (top left), $t = 25$ ms (top right), $t = 35$ ms (bottom left) and $t = 50$ ms (bottom right). 229

5.17 Transient evolution of the heat flux integrated over the different surfaces. The integrated flux on the internal chamber wall is plotted in blue, on the external wall in green and on the chamber bottom in red. The sum of the three contributions is plotted in cyan. 230

5.18 Visualization of the tangential gaseous velocity on a cylinder of radius $r^{cut} = 175$ mm, crossing the injectors' centerlines, unfolded on a plane surface for the case with iso-thermal walls (top) and with adiabatic walls (bottom): $t_{isoT} = 35.0$ ms and $t_{adiab} = 32.0$ ms. The instants were chosen to present similar flame fronts positions in the chamber. Tangential velocities are counted positive from left to right and range from $u_\theta = -20$ m.s^{-1} in blue to $u_\theta = 20$ m.s^{-1} in red. Two iso-lines of the progress variable $\widetilde{c} = 0.1$ and $\widetilde{c} = 0.9$ (in black) highlight the position of the flame fronts. 231

5.19 Visualization of the tangential gaseous velocity on a cylinder of radius $r^{cut} = 175$ mm, crossing the injectors' centerlines, unfolded on a plane surface for the case with iso-thermal walls (top) and with adiabatic walls (bottom): $t_{isoT} = 45$ ms and $t_{adiab} = 40$ ms. The instants were chosen to present similar flame fronts positions in the chamber. Tangential velocities are counted positive from left to right and range from $u_\theta = -20$ m.S^{-1} in blue to $u_\theta = 20$ m.S^{-1} in red. Two iso-lines of the progress variable $\widetilde{c} = 0.1$ and $\widetilde{c} = 0.9$ (in black) highlight the position of the flame fronts. 232

Introduction

General context

It is no longer possible to refute the considerable scientific evidence of climate change and to deny its anthropic origin. The large increase of pollutant gases releases into the atmosphere in the last few decades as well as deforestation and extractivist practices have led to stronger greenhouse effect and therefore a global increase of temperatures, but also to perturbations of the equilibrium between the forests, the oceans and the atmosphere that have ensured up to now conditions for life on Earth.
A large part of the pollutant gases are produced through the combustion of fossil fuels such as petroleum products or natural gas, that have been the means of carbon storage in the ground by processes lasting tens of millions of years and that are released into the atmosphere within a few decades. In the recent years, alternative methods of production have developed in order to generate low-carbon and renewable energy, that now rightfully compete with the combustion of fossil fuels. In this context, the domain of aeronautical transportation is particular, due to the capital importance of safety and reliability that are expected from the aircrafts, and specifically from their propulsion systems. To comply with obvious weight restrictions, aeronautical propulsion requires from its energy source a very high ratio of available power versus mass that only the combustion of liquid fuel is able to provide today. In the recent years, biofuels, produced either from biomass conversion or from hydrogenated vegetable oil, have emerged as a potential substitute to fossil kerosene with a more sustainable chain of production. While these bio-fuels constitute a potential way to reduce the carbon impact of aeronautical engines, their development still requires some research and validation before they can be fully trusted to replace fossil kerosene and power an aircraft carrying passengers. The use of such fuels does not solve other problems associated with the combustion of hydrocarbons, for instance the production of pollutant species such as nitrogen oxides or soot particles. In consequence, in the short to mean term, it is necessary to improve our knowledge of the combustion processes in the combustion chambers, and in particular during the critical phases of their operation in order to design engines that emit less pollutants while maintaining a high degree of safety.
From an industrial point of view, the knowledge and understanding of transient

phenomena such as ignition, flame propagation or combustion instabilities are particularly important to acquire because they have an impact on the safety limits and operating range of the combustors. Focusing on aeronautical engines, manufacturers need in particular to ensure that their aircrafts or helicopters are able to ignite and re-ignite in a short timespan (in case of in-flight accidental extinction) and in a reliable manner, for the most extreme conditions, at high altitudes where the ambient air is cold and rarefied.
The present thesis aims at providing additional knowledge on the light-round, defined as the specific phase of the ignition of an annular combustion chamber composed of multiple burners, during which flame fronts propagate and ignite each burner consecutively until a steady-state is reached. In an effort to get as close as possible to industrial configurations, the liquid fuel injection is accounted for by using liquid n-heptane, which generates specific challenges linked to the two-phase nature of the flow. The light-round is studied through the laboratory-scale combustion chamber MICCA-Spray, an annular combustor composed of 16 identical swirl injectors, designed at EM2C, that is fed with either gaseous or liquid fuel and air.
MICCA-Spray has been studied with premixed gaseous propane and air injection experimentally by Bourgouin et al. (2013) and numerically by Philip et al. (2015a); Philip et al. (2015b). More recently, Prieur et al. (2017) published results on the light-round using two-phase injection. In this work, operating points studied experimentally by Prieur et al. (2017) are simulated using large eddy simulation (LES) and the solver AVBP (Schönfeld and Rudgyard (1999); CERFACS (2011)) in order to identify the key mechanisms that drive the ignition delays and the flame behaviour.

Challenges of two-phase turbulent combustion

The prediction of two-phase combustion in turbulent flows is a challenging task, in particular due to the threefold interactions between the flame, the turbulent flow and the spray of liquid droplets, as is illustrated on Fig. 1.
These three aspects must first be captured individually, which already poses a number of difficulties, and then their interactions must be assessed and quantified. A brief description of the main phenomena at stake and of the existing numerical tools is given in the following.
First of all, **combustion** involves, depending on the complexity of the fuel, the reaction hundreds of species in a great number of chemical reactions with a large range of chemical timescales. While detailed kinetic schemes are available for most hydrocarbon fuels (Simmie (2003)), in realistic configurations, it is not possible to account for all the species and reactions while keeping reasonable computational costs. To deal with this problem, combustion can be handled through a tabulated chemistry approach, which will be detailed in chapter 1, or through the use of simpler kinetic scheme, such as skeletal or reduced schemes

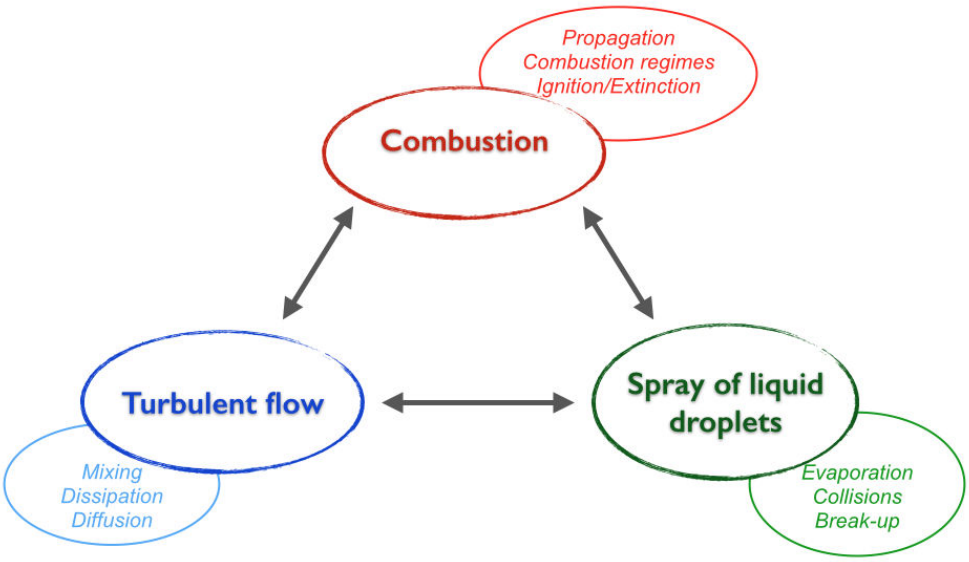

Figure 1: *Illustration of the triple interaction in turbulent two-phase combustion: interactions are present between the flame, the turbulent flow and the spray of liquid droplets.*

(tens of species and usually less than a hundred reactions), as can be found in Sung et al. (2001), Lu and Law (2008), Pepiot-Desjardins and Pitsch (2008) and Felden et al. (2018), or global chemical schemes (usually 1 to 2 reactions and less than 10 species), as detailed by Westbrook and Dryer (1981), Jones and Lindstedt (1988) and more recently by Franzelli et al. (2010). Usually, the choice of chemical kinetic scheme is done depending on the configuration to be studied and the mechanisms that one wants to capture. In particular, the smallest a kinetic scheme is, the more it was designed to reproduce specific characteristics of laminar flames, such as laminar flame speed, auto-ignition, extinction, pollutant emissions, ... Its selection is then a trade-off between computational cost and the quantities to be predicted.

Secondly, **turbulence** is one of the most complex phenomena encountered in fluid mechanics, and appears in flows for high enough Reynolds numbers. The presence of turbulence in a flow is often looked for in industrial applications because it enhances the transport and the mixing of fluids (Reynolds (1883)), but makes simulations more challenging since the structure of turbulence cannot today be described using a simple analytic theory, the relevant quantities of the flow being rather calculated by computational tools (Pope (2000)).

A turbulent flow can be characterised by dimensionless numbers that compare different physical effects. The Reynolds number Re (Eq. 1) characterises the laminar or turbulent aspect of a flow through the ratio of inertia forces over viscous forces. When the Reynolds number is low, the viscous forces are predominant and the flow is smooth and regular: it is *laminar*. On the other hand,

for high enough Reynolds numbers, the inertia forces are preponderant and the flow is *turbulent*, meaning that it has a chaotic and stochastic behaviour. In Eqs. 1, ρ is the density, u the velocity, L a characteristic dimension and μ the dynamic viscosity of the fluid.

$$\mathrm{Re} = \frac{\text{inertial forces}}{\text{viscous forces}} = \frac{\rho u L}{\mu} \tag{1}$$

Turbulent combustion is the two-way interaction that occurs when a flame evolves in a turbulent flow. Turbulence is affected by the strong accelerations generated through the flame fronts and by the large temperature changes that modify the gaseous kinematic viscosity. The presence of the flame can either increase or decrease the levels of turbulence of a flow, depending on the case (Damkoehler (1947)). Conversely, turbulence has a strong impact on the flame structure, it can enhance combustion by wrinkling of the flame surface or lead to local extinction by quenching.

To this already challenging problem is added that of the **spray of liquid droplets**. In itself, the numerical description of the liquid phase is a complicated task because its properties vary strongly during its atomisation process, from a liquid sheet when first injected to primary atomisation, with threads and packets of liquid, to secondary atomisation, where a spray of smaller droplets is formed.

During the two atomisation phases, turbulence plays a key role in the behaviour of the liquid phase by promoting events like collisions, break-up, coalescence. At the end of the atomisation, the obtained spray of droplets can be dense, therefore dominated by interactions between particles, or diluted, dominated by interactions between the particles and their surrounding flow. For the numerical simulation of applications where the atomisation process is not the main focus of the study, the spray is often considered as already fully atomised and no break-up nor coalescence are accounted for.

The impact of **turbulence on the particles** can be estimated through the use of the *Stokes number*, St, defined in Eq. 2 as the ratio of a particle relaxation time τ_p over the gaseous flow field characteristic time τ_k (Crowe et al. (1988)). The particle relaxation time is defined in Eq. 3 as a function of the particle diameter d_p, the liquid density ρ_l and the gaseous dynamic viscosity μ. Several possibilities exist for the choice of the flow field characteristic time, but it is usually taken as the time associated to the Kolmogorov scale l_k, expressed in Eq. 3, with u'_k the fluctuating velocity at the Kolmogorov scale.

$$\mathrm{St} = \frac{\text{particle relaxation time}}{\text{convective time}} = \frac{\tau_p}{\tau_k} \tag{2}$$

$$\text{with} \quad \tau_p = \frac{\rho_l d_p^2}{18\mu}, \ \tau_k = \frac{l_k}{u_k} \tag{3}$$

For small Stokes numbers (St $<<$ 1), the particle relaxation time is small compared to the eddy characteristic times, drag is predominant and the droplets are entrained by the flow. Their trajectories therefore tend to follow that of the carrier phase. Conversely, for St $>>$ 1, the droplets are much less sensitive to the flow fluctuations and have ballistic behaviour, meaning that they have their own motion, with little to no influence by the surrounding flow. When St $\sim$ 1, the two effects are of the same order of magnitude, a strong two-way interaction takes place, leading to preferential concentration of the droplets, which tend to concentrate in particular regions (Squires and Eaton (1991)).
Finally, **the spray and the flame** can come in contact and interact, creating some complex flame structures specific to two-phase combustion. To be able to react, the liquid fuel must first evaporate, which is obviously enhanced by the presence of a flame and the associated increase of temperature. Depending on the evaporation time scale, combustion can occur in a gaseous mixture, where the liquid droplets have fully evaporated before reaching the flame, or some droplets can survive to reach the flame front. In the first case, the flame is piloted by the repartition of gaseous fuel mass fraction while in the second some complex two-phase combustion mechanisms appear.
Spray flames have been classified into different categories by Chiu and coworkers (Suzuki and Chiu (1971); Chiu and Liu (1977); H. H. Chiu (1981); Chiu et al. (1982)) through the experimental characterisation of propagating flames in a mixture of hot oxidizer and fuel droplets. Four different combustion regimes were identified and reported in a diagram presented in Fig. 2. The authors found that droplets tend not to burnt individually, but rather in group, forming hybrid regions where droplets, gaseous fuel and flame cohabit. These structures were classified according to the group combustion dimensionless number G, defined as the ratio between the droplet evaporation rate and the gaseous species diffusion speed (see Fig. 2). G represents the degree of interaction between the phases and is proportional to $\frac{N^{2/3}}{S}$, where N is the total number of droplets and S is the separation number, defined as the ratio between the mean droplet spacing d and the radius of a diffusion flame surrounding a droplet vaporising in a quiescent oxidiser and having the mean properties of the spray. An expression for S is given on Fig. 2, extracted from Chigier (1983), as a function of d, the droplet radius r_p, and the gaseous Reynolds and Prandtl numbers (defined in Eqs. 1 and 4). The Prandtl (Pr) compares the viscous diffusion rate to the thermal diffusion rate. It is defined in (Eq. 4) as a function of the fluid dynamic viscosity μ , its heat capacity at constant pressure C_p and its thermal conductivity k. The Prandtl number is analogous to the Schmidt number (Sc) for molecular diffusive transfer, defined in Eq. 5, with D the fluid mass diffusivity. Both numbers play key roles in the liquid spray evaporation laws.

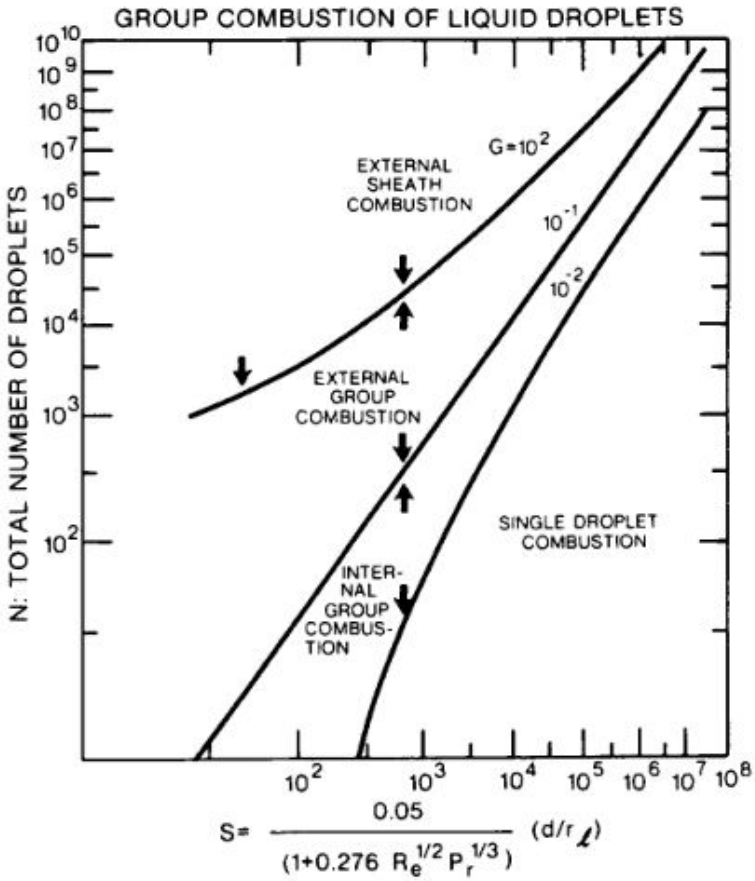

Figure 2: *Group combustion diagram: spray combustion regimes against the total number of droplets N and the non dimensional separation distance S. The regimes are separated by iso-lines of critical values of the group number G. Extracted from Chiu et al. (1982) and Chigier (1983).*

$$\mathrm{Pr} = \frac{\text{viscous diffusion rate}}{\text{thermal diffusion rate}} = \frac{\mu C_p}{k} \tag{4}$$

$$\mathrm{Sc} = \frac{\text{viscous diffusion rate}}{\text{molecular diffusion rate}} = \frac{\mu}{\rho D} \tag{5}$$

Iso-lines of the critical G numbers identified in the studies by Chiu *et al.* are reported in Fig. 2 to separate the different spray combustion regimes.
When G >> 1, the spray is very dense and the droplets are so close that heat cannot diffuse inside the cloud. In consequence, *external sheath combustion* is observed, where only the droplets located in an external layer of the spray evaporate and a flame stabilises around it. On the other hand, when G << 1, the droplets are far enough from each other to allow the burnt gases to fully penetrate the spray. *Single droplet combustion* then occurs, where a flame is

present around each individual droplet. Smooth transitions between these two extreme regimes are observed. *External group combustion* occurs for $G > 1$, the flame still remains around the cloud of droplets but the temperature rises inside the spray, enhancing the evaporation of all the droplets. Finally, $G < 1$, in *internal group combustion*, a main diffusion flame is also present around the core of droplets, which rise in temperature and evaporate, but an external ring is additionally formed by individual burning droplets.
A detailed description of the classification by Chiu *et al.* is proposed by Reveillon and Vervisch (2005) as well as an extension to include effects of the global injected equivalence ratio and of turbulence on the spray flame structure. Another extension was also proposed by Urzay (2011) to include effects due to the stoichiometry characteristics and the diffusion flame radius, suggesting that the group combustion number is not the only indicator of the combustion regime, but that different regimes can be found for identical values of G.
Due in particular to the threefold interaction between the spray, turbulence and combustion, it is challenging to try and find a global description of the mechanisms and the regimes involved in such configurations. The literature on spray combustion is very wide and the reader is referred to review articles such as Chigier (1983) or Reveillon and Vervisch (2005) for further details on combustion in droplet sprays.
While recent years progress in terms of numerical models and computational power have made it possible to carry out simulations of more and more complex configurations, the capture of combustion structures such as the ones described above requires the gaseous phase to be resolved with a precision that can only be achieved with direct numerical simulation (DNS), as was done for instance by Reveillon and Vervisch (2005), Nakamura et al. (2005), Reveillon and Demoulin (2007) or Wang et al. (2018), in which the computational grid is fine enough to capture all the scales of turbulence, down to the smallest ones. As is further detailed in the introduction of Chapter 1 (Sec. 1.1), the prohibitive computational cost of DNS methods limit their use to simple academic cases, with low levels of turbulence. An alternative largely used in the industry is the RANS approach (for Reynolds-Averaged Navier-Stokes), in which only the mean fields are resolved. The computational cost is greatly reduced but strong levels of modelling are introduced and no transient data is captured. Large eddy simulation, or LES, appears as a good intermediate approach between DNS and RANS, enabling the capture of the transient structures at the largest scales of the flow while the effect of the smallest structures whose description cannot be afforded is modelled. The principle of LES and a description of the equations and models required are given in chapter 1.
In LES, the cut-off frequencies are larger than the characteristic sizes of any of the two-phase combustion modes previously described. It is therefore not possible to represent them other than by modelling. In the present work and considering that the injected liquid fuel, n-heptane, is very volatile, the assumption is made that these kinds of combustion regimes, where droplets survive

long enough to enter the flame front, if they appear, are anecdotal and do not influence the overall flame propagation.

Ignition in realistic burners

As was previously mentioned, ignition in single of multi-burner combustors is a critical and dimensioning part of their operation. The initiation of the ignition sequence in any combustion system can be the result of *autoignition* mechanisms or be triggered by an external device, in which case one often talks about *forced ignition*. In the general case, autoignition occurs when fuel and oxidizer reach high enough temperatures so that some chemical reaction is able to take place. The delay between the introduction of the reactants and the creation of a viable flame kernel is called *ignition delay* and depends on the characteristics of the fuel and oxidizer, but also largely on the local pressure and temperature conditions. Autoignition has been widely studied and some of the literature on the subject is summarised in reviews articles such as the ones by Aggarwal (1998), Mastorakos (2009) or Aggarwal (2014).
In the case of forced ignition, the initial solution is too cold to allow chemical reaction to proceed, and an external device has to be used in order to kick-start the reaction by a deposition of energy in the unburnt mixture. The advantage of this method is that, provided that the device is well adapted, the triggering of the ignition once the fuel is injected can be completely controlled, both in terms of delay and of position of the initial flame kernel. Most industrial systems are equipped with forced ignition devices, which include spark generation through electric discharges (also called spark plugs), laser ignition or torch igniter, with a large predominance of the first in aeronautical engines.
In realistic gas turbines, a successful ignition sequence, from the generation of a spark to the stabilisation of a steady-state flame around each injector, can be decomposed into several phases that may be studied separately or successively. Lefebvre and Ballal (2010) identified three phases for the ignition of a combustor composed of several burners, that are described hereafter and illustrated on Fig. 3:

1) **Kernel generation:** the ignition triggering device deposits certain amounts of energy in the cold flow which locally increases the temperature until a flame kernel is created that is able to propagate.
2) **Kernel propagation:** the kernel, having met with favourable conditions for its expansion, propagates towards the first fuel injector until a flame stabilises in its vicinity.
3) **Flame propagation from burner to burner:** in the case of multiple injector combustion chamber, as is found in most industrial gas turbines, the flame propagates on each side of the initial injector in order to ignite the rest of the chamber until a flame has stabilised around each injector.

In order to achieve successful ignition of a given chamber, each of these phases

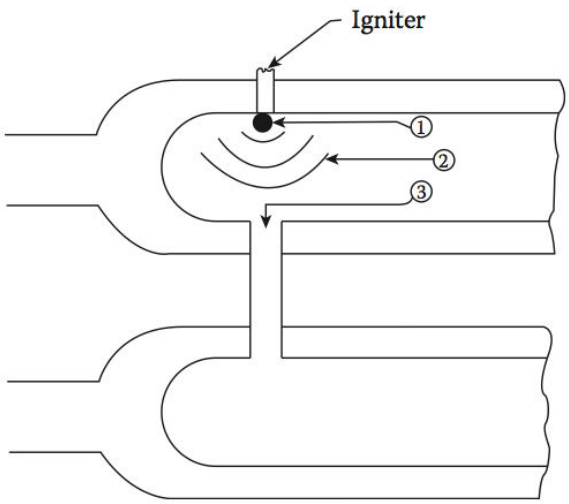

Figure 3: *Three-phase nature of the ignition process illustrated on a cannular combustion chamber, extracted from Lefebvre and Ballal (2010).*

must be successful and the final phase must lead to a stable flame around each injector.

For a flame kernel to be created and the first phase to succeed, the igniting device must be able to provide enough energy to the flow so as to heat it up faster than the energy is diffused by thermal diffusion (Lefebvre and Ballal (2010)). Ballal and Lefebvre (Ballal and Lefebvre (1977)) showed that the minimum energy, referred to as MIE, required to ignite an homogeneous gaseous mixture corresponds to the energy needed to heat a sphere of the unburnt mixture up to its adiabatic flame temperature, the sphere having a diameter corresponding to the *quenching distance*, the minimum size at which a flame kernel is able to survive and propagate. When considering heterogeneities of mixture fraction, in non-premixed gaseous cases or non-premixed sprays, other factors tend to have an impact on the MIE (Ballal and Lefebvre (1979); Aggarwal (1998)), which then has a probabilistic behaviour. The MIE is therefore generally defined as the amount of energy which yields a 50% chance of ignition (Aggarwal (1998)). Models for the determination of the MIE depending on the initial mixture characteristics were proposed by Peters and Mellor (1980) and Ballal and Lefebvre (1981b), with a focus on the impact of the spray. In the recent years, experimental studies have measured ignition probabilities in realistic burners with gaseous premixed (Shy et al. (2010); Cardin et al. (2013)) and non-premixed (Ahmed et al. (2007)) injection and more recently in the presence of liquid fuel (Marchione et al. (2009); Letty et al. (2012); Wandel (2014)). The existing studies up to 2009 have been reviewed by Mastorakos (2009). Numerically, the study of the initiation of the flame kernel is made difficult by the complex non-equilibrium physics that are involved in the process.

The recent advances in computing performance have however allowed the use of LES to determine the failure or success of phase I (often associated to phase II studies) in gaseous partially premixed or non-premixed configurations (Lacaze et al. (2009); Subramanian et al. (2010); Esclapez et al. (2015)) to obtain probability maps for the ignition. In the last few years, an increasing number of studies have focused on the kernel creation in two-phase flows, using LES (Jones and Tyliszczak (2010); Eyssartier et al. (2013); Collin-Bastiani et al. (2018)) or DNS (Neophytou et al. (2010)) in an effort to study configurations as close as possible to industrial ones.

Once a flame kernel has been created, it starts to propagate, thus marking the beginning of the second phase, whose success or failure depends on the ability of the flame to survive, expand further and finally stabilise around the fuel injector. Birch et al. (1981) and Smith et al. (1988) studied the ignition probability of a natural gas jets and showed that two ignition probabilities have to be considered, the probability to create a kernel previously detailed, and the probability to ignite the burner, which largely depends on the flow field conditions and configuration. Unlike in phase I, the flame propagation mechanisms in the fresh mixture have to be additionally considered in phase II. Flame propagation in laminar flows, including ignition and extinction mechanisms, has been studied numerically for counterflow configurations with gaseous injection by Richardson and Mastorakos (2007) and later with spray flames by Greenberg et al. (2012) and Greenberg et al. (2013), highlighting the role played by the local strain rate on the flame structures. Most of the previously mentioned experimental and numerical studies on phase I in turbulent flows also consider phase II. Many experimental and numerical studies have focused on the turbulent flame propagation in spark-ignition engines (Granet et al. (2012); Mounaïm-Rousselle et al. (2013)). Additionally, Peterson et al. (2011) and Peterson et al. (2014) conducted experimental investigations on the failure of phase II in spray-guided spark-ignited direct-injection engine, with liquid fuel injection. The authors identified three main mechanisms responsible for the ignition failures that occurred after a flame kernel had been created: locally lean conditions created by non-uniformities in the fuel repartition, excessive air dilution with nitrogen and the presence of convection velocities that entrain the kernel away from the fuel spray.

As is also the case for phase I, the global tendency in the literature is to study the second phase on systems that are more and more realistic. To do so, liquid spray injections of kerosene or diesel surrogates are considered, as was done by Collin-Bastiani et al. (2018) who compared LES and experimental sequences of spark ignition and flame propagation in a two-phase swirled burner.

Most industrial systems being composed of several fuel injectors, it is then natural to focus on the third and last phase identified by Lefebvre and Ballal (2010), during which the flame propagates from burner to burner until complete ignition is achieved. In case of annular configurations, as are typically found in gas turbines, this last phase is called *light-round*. It plays a crucial role in

the chamber ignition process since its success or failure determines whether a complete and stable ignition is reached, thus enabling the chamber to yield its nominal power. The identification of the phenomena at stake during the light-round in successful ignition sequences in realistic combustors constitutes a first step towards understanding and predicting the whole ignition process. In the recent years, the light-round phase has been the focus of several experimental studies that have allowed to identified two propagation modes. Additionally, advances in computing performances have allowed simulations of such a complex transient process to be carried out.

Propagation mechanisms during the light-round in realistic configurations

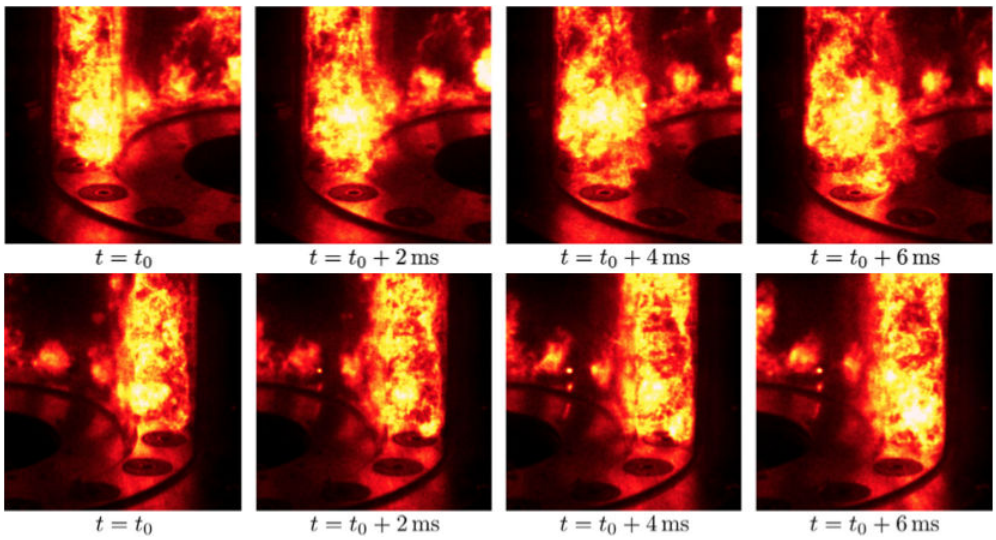

Figure 4: *Images of light intensity emitted by the flame fronts in the left (top) and right (bottom) halves of the MICCA chamber during a light-round sequence with premixed propane-air injection at* $\Phi = 0.76$*, in false colours for better visualisation, extracted from Bourgouin et al. (2013).*

The MICCA chamber was designed at EM2C Laboratory to study ignition and combustion instabilities. It is composed of sixteen swirl injectors distributed in an circular pattern and two transparent quartz walls that delimit the annular chamber. In their study of MICCA, fed with premixed gaseous propane-air, Bourgouin et al. (2013) observed the mechanisms of the flame propagation from one ignited burner to the neighbouring un-ignited one by frontal and side image recording with a high-speed camera. For the whole range of operating conditions that were considered, in which the equivalence ratio and the bulk velocity were varied with a fixed geometry, the same propagation pattern from burner to burner was always observed, in which a flame tip could be identified

that propagated azimuthally towards the next injector, remaining around the same height, in the bottom quarter of the chamber. Figure 4 displays images of the flame fronts that propagate in the left half of the chamber (top images) and in the right half (bottom images), in false colors for better visualisation, extracted from Bourgouin et al. (2013) from a case at an equivalence ratio $\Phi = 0.76$. The propagation mechanism can be observed on Fig. 4, as well as the influence of the local clockwise swirling motion generated by the injectors, that was found to impact the local flame tips radial and axial positions, which are for the considered injectors close to the inner quartz wall in the left half-chamber and close to the outer wall in the right one. The authors also showed that the global flame front propagation velocity was affected to some extent by this motion, leading to small asymmetries towards the end of the light-round.

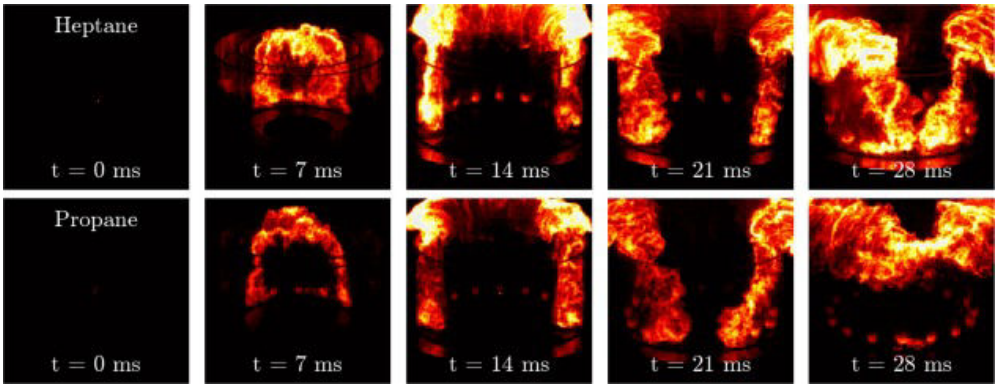

Figure 5: *Light emission during the ignition sequence of n-heptane (top) and propane (bottom) fuels. Yellow corresponds to high light intensity while dark red represents low light emission. Each sequence features equivalent injection conditions :* $U_b = 31.5\ m.s^{-1}$, $\Phi = 0.90$ *and* $\mathcal{P} = 80\ kW$, *extracted from Prieur et al. (2017).*

These results were recently extended by Prieur et al. (2017) to include two-phase injection, through the modification of the injection system on MICCA, now called MICCA-Spray, to allow spray injection. Similar diagnostics were used to analyse the flame propagation patterns and the influence of the injection on the light-round delay. The comparison of the flame behaviour between premixed propane-air and liquid n-heptane and air, both with the new injection system, displayed in Fig. 5, showed similar flame structures and propagation mechanisms, though the propagation speeds are different.
Additionally, the authors conducted a systematic study of the light-round delay, defined as the time difference between the first development of a flame kernel and the merging of the fronts on the other side of the chamber, identified from the high speed camera images, for a wide set of operating conditions and for three different fuels: gaseous propane, liquid n-heptane and liquid dodecane. The measured light-round delays are displayed on Fig. 6, each graph corresponding to one constant parameter between the bulk velocity U_b (left), the

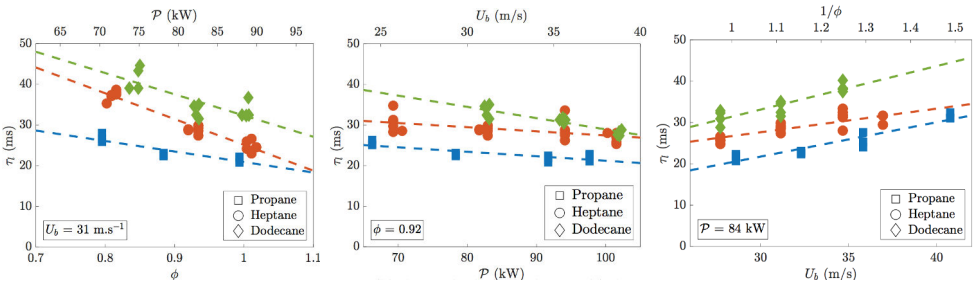

Figure 6: *Light-round delay τ_l when: the bulk velocity U_b (left), the equivalence ratio Φ (center or the power $\mathcal{P}$ (right) is kept constant for multiple fuels : propane (gaseous), n-heptane (liquid spray) and dodecane (liquid spray). Linear fits in dashed lines give the general trend for the different fuels, extracted from Prieur et al. (2017).*

equivalence ratio Φ (middle) and the global power $\mathcal{P}$ (right). Each coloured symbol stands for a different fuel (blue squares for propane, orange circles for n-heptane and green diamonds for dodecane) and estimated trends obtained from linear fits are added as dashed lines. For equivalent operating conditions, the premixed gaseous injection systematically yields the shortest light-round delay, and with two-phase injection, the fastest propagation is obtained for n-heptane, a trend that the authors attribute to its higher volatility compared to dodecane.

The light-round in a realistic combustor has also been studied experimentally by another group, at Cambridge university, on an annular combustion chamber composed of 12 to 18 identical burners, with or without swirling units, and with a bluff-body that stabilises the flames. The chamber diameter $D_{chamber} = 212$ mm makes it twice smaller than MICCA with approximately the same number of injectors. It has been studied with methane and air premixed injection by Bach et al. (2013), for equivalence ratios ranging from $\Phi = 0.64$ to $\Phi = 0.75$, and by Machover and Mastorakos (2017) in very lean conditions, with $\Phi = 0.3$ to $\Phi = 0.4$ and with non-premixed injection by Machover and Mastorakos (2016), for Φ varying between 0.6 and 0.9, with and without swirl. In all these studies, the authors found that the flame propagation from burner to burner, with a swirled injection, adopted a *sawtooth* pattern, evidenced on Fig. 7, which displays side visualisations of OH* chemiluminescence during the light-round, focused on three injectors. On the top left image, at $t = t_0$, a flame has stabilised around the left injector, and begins to propagate towards the next one in the top right image ($t = t_0 + 5$ ms), where flame elements are seen to travel both axially towards the exit of the chamber and tangentially towards the injector in the middle, until it is captured by this injector's central recirculation zone at $t = t_0 + 7$ ms and $t = t_0 + 10$ ms (middle images). The flame then travels back towards the bottom of the chamber and fully ignites the injector ($t = t_0 + 12$ ms, bottom left image). On the images at $t = t_0 + 10$ ms and $t = t_0 + 12$ ms, a flame element is already propagating

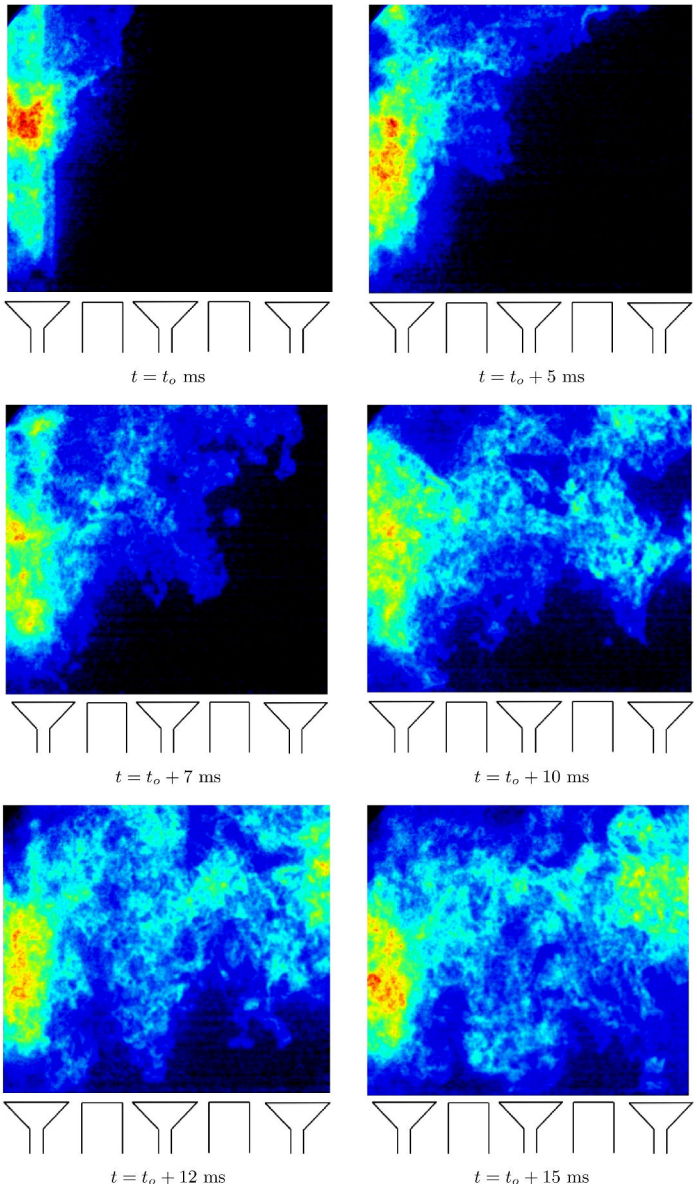

Figure 7: *Side visualization by 5 kHz OH* chemiluminescence of a successful burner-to-burner flame propagation with a sawtooth behaviour. A succession of three burners is sketched. Images were extracted from Machover and Mastorakos (2017).*

towards the third injector and being captured by its recirculation zone, leading to its ignition on the bottom right image, at $t = t_0 + 15$ ms. Machover and Mastorakos (2017) obtained the flame absolute propagation speed from measurements of the area covered by the flame on images taken from the top of the chamber and compared them for different values of the inter-injector spacing and the bulk velocity. It was found that the absolute propagation speed

increases with the bulk velocity, which is consistent with the conclusions of Prieur et al. (2017) (see the plot on the right in Fig. 6).
These two propagation modes, the azimuthal and the sawtooth propagation, present separately in MICCA and the Cambridge burner, were both observed on the KIAI burner, with gaseous premixed methane/air injection by Barré et al. (2014) and more recently with liquid fuel and air injection for four different fuels by Marrero Santiago et al. (2017). The KIAI burner is a linear array of swirler units which can be composed of 2 to 5 injectors. The authors of both papers showed that the inter-injector distance, varied with the number of injectors, had a direct influence on the propagation mode. Additionally, in the case of spray injection (Marrero Santiago et al. (2017)), the linear configuration of the chamber allowed to observe the droplet spray through Mie diffusion by introducing a laser sheet from the side of the chamber, crossing the injectors centerlines. The interaction of the neighbouring sprays was shown to be modified by the distance between the injectors, thus changing the gaseous fuel repartition in the un-ignited steady-state. Along with front and top images, the Mie diffusion diagnostic during the ignition sequences led to the identification and the description of the mechanisms at stake in the propagation of the flame. In particular, the effect of the expansion of the burnt gases on the fresh mixture during the ignition sequence and its impact on the flame fronts propagation speed were evidenced.
The annular aspect of industrial-like combustion chambers limits the diagnostics that can be installed. In particular, optical diagnostics involving laser sheets are difficult and often hindered by the curvature of the quartz walls. This can be circumvented by making use of a linear multi-burner array, as was done by Barré et al. (2014) and Marrero Santiago et al. (2017), but some phenomena specific to the light-round, for instance the merging phase or distance interaction of the flame fronts through a symmetric thrust effect in the fresh gases, are then lost. The simulation tool appears then as a powerful way to gain access to quantities that are impossible or very difficult to measure in annumar systems.
The first large eddy simulation of the ignition of a full annular combustion chamber was performed by Boileau et al. (2008), on a helicopter chamber composed of 18 swirlers and fed with liquid JP10, a kerosene surrogate, and air. Two hot jets at opposite positions in the chamber were used to trigger the ignition, creating four separate fronts that each propagated in a quarter of the chamber. Detailed analysis of the ignition sequence showed that, due to the thermal expansion of the burnt gases, a flow was generated in the fresh gases and a thrusting effect was exerted on the flame fronts. The flow generated by each swirler also had a notable effect on the radial and azimuthal positions of the flame fronts leading point. Images of the flame propagation in the chamber are presented in Fig. 8. The initial arch-like propagation of the flame is apparent on the top image as well as the creation of four distinct fronts. Though no comparison with experimental data was available, the mechanisms identified

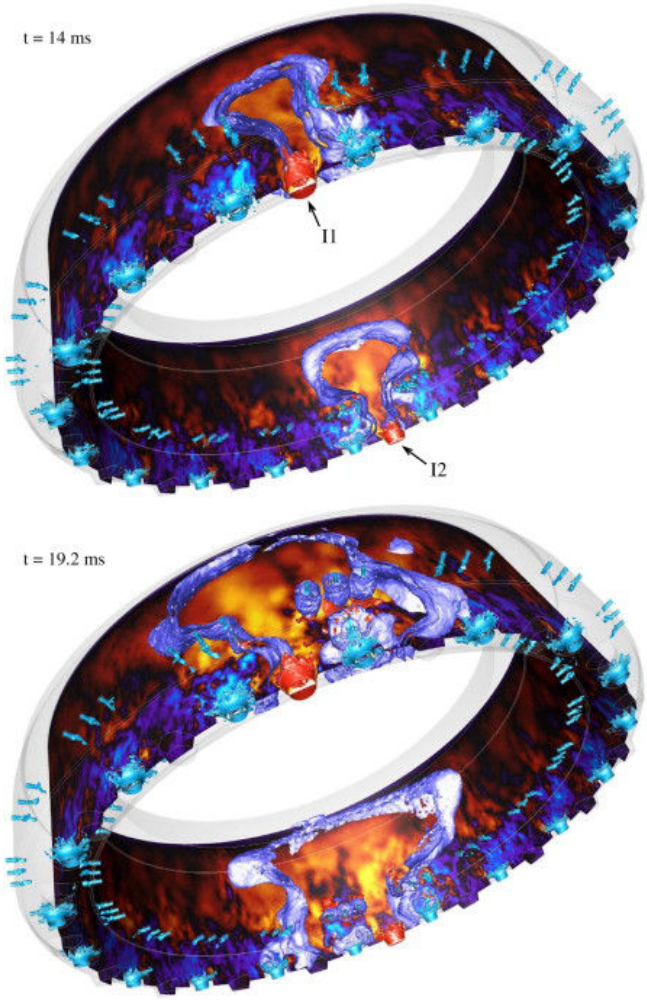

Figure 8: *Two successive instants (t=14 and 19.2 ms) of the ignition sequence: surface crossing the middle of the chamber coloured by axial velocity (light blue: -20 $m.s^{-1}$ to yellow: 20 $m.s^{-1}$), iso-surface of velocity coloured by temperature (turquoise blue: 273 K to red: 2400 K), and iso-surface of progress rate (shiny light blue) representing the flame front. The two high-speed hot jets used for ignition appear as red zones in the pictures (marked I1 and I2). The images were extracted from Boileau et al. (2008).*

in the simulation as influencing the propagation were later retrieved in the experimental studies mentioned above.

Numerical simulations of the ignition sequences in the MICCA chamber (Philip et al. (2015a) and Philip et al. (2015b)) and in the KIAI linear array (Barré et al. (2014)) have been carried out with premixed gaseous injection. Comparisons showed excellent agreement in terms of propagation speed and light-round delay. The simulations were able to capture and reproduce the propagation mechanisms identified in the experiments.

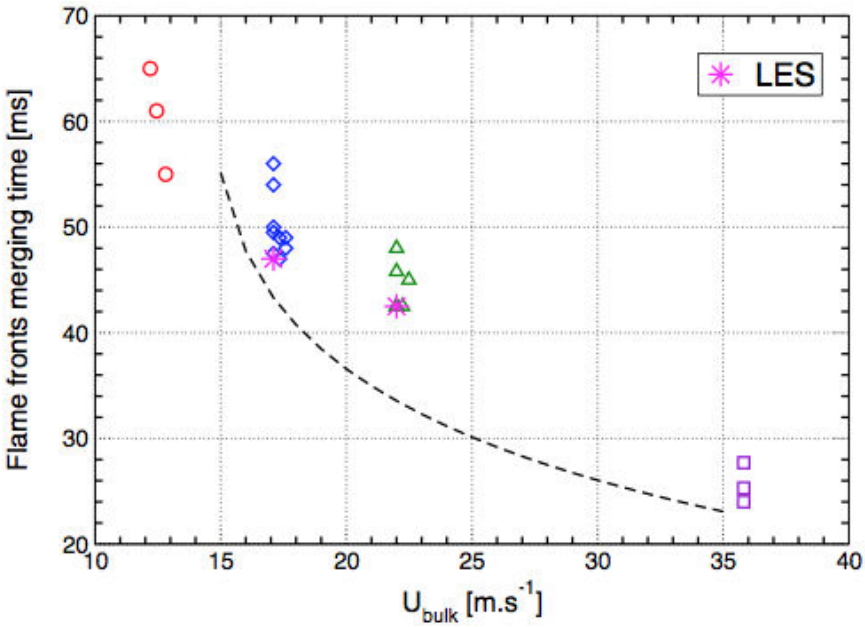

Figure 9: *Flame fronts merging delays in MICCA for premixed propane-air injection at* $\Phi = 0.74$ *versus the bulk velocity* U_{bulk}*. Circles, diamonds, triangles and squares correspond to the experimental measurements, the two stars to the delays predicted by the numerical simulation. The dashed line shows the delays predicted by the model developed by Philip. This graph was extracted from Philip (2016).*

From there, more detailed post-processing of the simulations of the light-round in the annular chamber carried out by Philip (2016), for an equivalence ratio of $\Phi = 0.74$ and two values of the bulk velocity, allowed to better quantify the role played by the burnt gases thermal expansion on the absolute displacement velocity of the flame and to identify preferential propagation zones for the leading flame elements around the swirlers. A model was proposed for the flame absolute turbulent speed to account for the effect of the bulk velocity. As is evidenced in Fig. 9, the model is in satisfactory agreement with both experimental and LES results, the global trends are correctly described and the analysis of the different terms of the model showed that the phenomena that control the light-round is retrieved.

In light of the results obtained with large eddy simulation by Philip and coworkers (Philip et al. (2015a); Philip et al. (2015b); Philip (2016)) and of the newly available experimental data on the light-round with liquid spray injection obtained by Prieur et al. (2017), it is now relevant to envision the simulation of the ignition in MICCA-Spray, accounting for the liquid n-heptane injection.
As will be further detailed in chapter 1, two main approaches are available for the large eddy simulation of two-phase reacting flows, both relying on mesoscopic models (Fox (2012)): the Eulerian-Eulerian approach, where moments

of the number density function (NDF) are transported (Sanjosé et al. (2011); Senoner et al. (2009)) and the Eulerian-Lagrangian model where a set of individual particles are followed (Chrigui et al. (2012); Jones et al. (2012); Luo et al. (2011)). In the Eulerian-Lagrangian framework, accounting for polydispersion is straightforward, while the Eulerian-Eulerian approach requires an additional set of transport equations for each moment and/or class of particle sizes, notably increasing the computational cost. On the other hand, envisioning the simulation of a transient ignition process with the Lagrangian methods requires the use of computational load balancing that is complex to handle on parallel machines (Garcia (2009); Ham et al. (2003)). This is expected to be difficult in a situation where the flame fronts traverse the annular chamber, requiring a dynamical treatment of computational load balancing between ignited and un-ignited injectors. As a compromise between cost and accuracy, and considering the computational tools and resources available, the present study focuses on the simulation of MICCA-Spray light-round sequence in a mono-disperse Eulerian-Eulerian framework.

Objectives of the thesis

The aim of this thesis is the characterisation and understanding of light-round in gas turbines by considering systems whose complexity is closer to that of industrial ones with the accounting for two-phase flows.
Large eddy simulation is used to predict the light-round sequence in MICCA-Spray, operated with liquid n-heptane and air. Attention is focused on successful ignition sequences in order to extract the relevant mechanisms.

Organisation of the manuscript

Chapter 1: The equations and models used for the simulation of reactive two-phase flows are presented. Particular emphasis is put on the description of the liquid phase equations and closure models. The three-dimensional Navier-Stokes equations for compressible flows are solved for the gaseous phase, while the dispersed phase is represented using an Eulerian mono-dispersed approach.

Chapter 2: Large-eddy simulations of the SICCA-Spray burner, which represents one sixteenth of the annular chamber MICCA-Spray, are carried out. The numerical set-up is presented and validated step by step using the available experimental data. The first comparisons with experimental data show the importance of the choice of the injected droplets diameter in this simplified framework. The impact of this key parameter upon the numerical results is assessed through the use of uncertainty quantification tools and optimal values are obtained by the definition of relevant evaluation criteria. Finally, the reactive case is studied, with adiabatic and isothermal boundary conditions at the chamber walls, highlighting the impact of the heat losses on the flame shape.

Chapter 3: Large eddy simulations of relight sequences of the MICCA-Spray combustor are presented, using the Thickened Flame model for LES (TFLES) turbulent combustion model. The pre-heated quartz walls are considered to be adiabatic in the simulation. Three operating points are considered, for three values of the equivalence ratio. The establishment of the cold flow is carefully assessed to ensure that a steady-state has been reached that can be compared to the experiment. Validations with experimental data are performed that include comparison of the direct visualisations of the flame, as well as quantitative comparisons of the different flame propagation durations, in the whole chamber (light-round duration) and between injectors (sector ignition delays).

Chapter 4: A detailed analysis the numerical simulation of the light-round for the three operating points presented in chapter 3 is carried out. Calculations indicate that the volumetric expansion due to the chemical reaction at the flame induces a strong azimuthal flow in the fresh stream at a distance of several sectors ahead of the flame, which modifies conditions in this region. Specific post-processing is applied in order to identify the key mechanisms that drive the flame fronts propagation and the light-round process, comparing the three simulated cases.

Chapter 5: An initial attempt is made to account for the heat losses at the walls during the light-round in order to retrieve the marked slowdown of the flame propagation observed experimentally when the quartz walls are at ambient temperature. The boundary conditions at the chamber walls are set to iso-thermal as was successfully done for the steady-state simulation of SICCA-Spray in chapter 2.

Achievements and Highlights

Publications in international peer reviewed journals:

- Large-eddy simulation of light-round in an annular combustor with liquid spray injection and comparison with experiments
  T. Lancien, K. Prieur, D. Durox, S. Candel and R. Vicquelin
  Journal of Engineering for Gas Turbines and Power, 140(2), **2017**
  Presented at the ASME Turbo Expo 2017, Charlotte, USA
- Leading point behavior during the ignition of an annular combustor with liquid n-heptane injectors
  T. Lancien, K. Prieur, D. Durox, S. Candel and R. Vicquelin
  Proceedings of the Combustion Institute **2018**, *Accepted*
  Presented at the International Symposium on Combustion 2018, Dublin, Ireland

Contributions to international and national conferences (abstract reviewed):

- Uncertainty quantification of injected droplet size in mono-dispersed Eulerian simulations
  T. Lancien, N. Dumont, K. Prieur, D. Durox, S. Candel, O. Gicquel, and R. Vicquelin
  Presented at the International Conference on Multiphase flows (ICMF), Firenze, Italy, May 2016
- Large-eddy simulation of light-round in an annular combustor equipped with n-heptane spray injectors
  T. Lancien, K. Prieur, D. Durox, S. Candel and R. Vicquelin
  Presented at the International Conference on Numerical Combustion (ICNC) 2017, Orlando, USA
- Light-round in an annular combustor with liquid n-heptane injectors: study of flame propagation under several operating conditions
  T. Lancien, K. Prieur, D. Durox, S. Candel and R. Vicquelin
  Presented at Colloque INCA, Safran Tech, Magny-Les-Hameaux, France, October 2017

Various highlights:

- Selection of the TIMBER project for the 14th PRACE Project Access Call, for a total allocation of 33 million hours.
- Selection of the results from MICCA-Spray light-round simulations for the scientific highlights of GENCI's 2017 annual report.

Acknowledgements

This thesis was financed by the French Agence Nationale de la Recherche (ANR) within the TIMBER project ANR14-CE23-0009-01.
This work was granted access to the HPC resources of TGCC, CINES and IDRIS, under allocations 2015-x20152b0164, 2016-020164 and 2017-A0022B10118 made by GENCI and PRACE allocation n14-2016153551.

Chapter 1

Equations and models for the large eddy simulation of reactive two-phase flows

This chapter presents the numerical models used for the simulations carried out throughout the manuscript, using the AVBP solver, developed by CERFACS and IFP Energies Nouvelles. The different sets of equations used for the large-eddy simulation (LES) of a reactive two-phase flow are successively presented, as well as their interaction terms. The three-dimensional Navier-Stokes equations for compressible flows are solved for the gaseous phase, while the dispersed phase is represented using an Eulerian mono-dispersed approach. Two turbulent combustion models have initially been envisioned and their implementation is detailed in this chapter. All the equations, models and approximations presented here are then used for the simulation of the steady-state flame in the single burner SICCA-Spray in chapter 2 and of light-round sequences in MICCA-Spray, in chapters 3 to 5.

Contents

1.1 Introduction **24**
1.2 Conservation equations for compressible gaseous flows **26**
1.2.1 Transport equations for the gaseous phase 26
1.2.2 Computational approaches for gaseous turbulent flows 28
1.2.3 Filtered equations for LES 29
1.2.4 Approximations and closure models 31
1.2.5 Thermodynamic properties for the gaseous phase in AVBP 33
1.3 Equations and models for the liquid phase **34**
1.3.1 Approaches for the description of the dispersed phase 34
1.3.2 The Lagrangian approach 34
1.3.3 Equations for the Eulerian description of the spray . 35
1.3.4 Exchange terms between the phases 40
1.3.5 Closure models for the liquid phase 41
1.3.6 Filtered equations for the liquid phase 50
1.3.7 Approximations and closure models for the LES of the dispersed phase 51
1.3.8 Thermodynamic properties for the liquid phase in AVBP 53
1.4 Turbulent combustion modelling **54**
1.4.1 The thickened flame model for LES (TFLES) 54
1.4.2 The filtered tabulated chemistry model for LES (F-TACLES) 59
1.4.3 Adaptation of the coupling with the liquid phase for tabulated chemistry 63
1.5 Validation of the evaporation model with tabulated chemistry **67**
1.5.1 Equilibrium state 68
1.5.2 0D evaporation 71
1.5.3 Selection of a detailed chemical scheme 73
1.6 Conclusion **74**

1.1 Introduction

The representation of fluid motion using numerical tools has naturally soared alongside the development of computational power and performance of the past few decades. The numerical simulation of a flow field implies that the equations of fluid mechanics, called the *Navier-Stokes equations*, must be solved on a

discrete mesh. Numerical simulation constitutes an interesting tool for the understanding of most practical fluid mechanics configurations for which no exact solution to the Navier-Stokes equations exists. In giving access to a greater number of physical quantities, simulation can prove to be an essential complement to experimental measurements in the study of complex systems. Indeed, it is easy to extract quantities such as pressure, temperature or density from a numerical instantaneous or average solution in a non intrusive manner, while the same measurements would be much more difficult to carry out in the experiment. Yet the simulation cannot stand alone and a crucial point is that of its thorough validation against experimental data before it can be fully trusted.

First of all, depending on the numerical tools and computational power available, and on the complexity of the system, a certain amount of modelling is often required. As will be further detailed in this chapter, the exact representation of a turbulent flow field by numerical simulation can be done by *Direct Numerical Simulation* (DNS), in which all the turbulent structures must be captured by the discrete mesh, leading to prohibitive computational costs for all but the simplest configurations. An alternative numerical tool to capture transient turbulent flow fields is *Large Eddy Simulation*, or LES, which solves the largest structures of the flow and models the effect of the smallest structures. This considerably lessens the computational cost but makes it necessary to use closure models for the unknown terms. Extensive validations of the predictions of the simulation are therefore essential to ensure that the modelling part captures the correct physics.

Secondly, a reactive three-dimensional turbulent flow is a deeply multi-physics problem and it is often not possible to account for all the phenomena in the simulation. A priori assumptions have to be made as to the preponderance of some physical phenomena over others. Here again, validations against experimental data are the only thing that can confirm these hypotheses or, on the contrary, highlight the necessity to account for additional physical effects. This is for instance illustrated in chapter 5 with the effect of heat losses at the walls.

The work presented in this manuscript is part of a joint numerical and experimental study of the annular multi-burner combustion chamber MICCA-Spray, described in chapter 3. The present chapter details the numerical tools that are later used for the simulation of the light-round sequence with liquid n-heptane and air injection with the solver *AVBP*, developed by CERFACS and IFP Energies Nouvelles (CERFACS (2011)). The set of equations used on the gaseous phase is first presented, along with the closure models that are required following the filtering procedure. Secondly, the description of the liquid phase is considered, with two main approaches available that are briefly presented. Special attention is given to the expressions of the exchange terms between the phases, before and after the filtering of the equations. Two turbulent combustion models are finally presented, the Thickened Flame Model for LES (TFLES, Colin et al. (2000)) and the Filtered Tabulated Chemistry

model for LES (FTACLES, Fiorina et al. (2010)), with a focus on their implementation in the context of a two-phase flow simulation, since both models were initially developed for purely gaseous premixed combustion.

1.2 Conservation equations for compressible gaseous flows

1.2.1 Transport equations for the gaseous phase

The transport equations that need to be solved to describe a compressible gaseous flow are presented in the following. This set of equations is composed of the Navier-Stokes equations (mass conservation, Eq. 1.1, and the three equations of momentum conservation, Eq. 1.2), the equations of conservation of species mass fractions (Eq. 1.3) and of energy (Eq. 1.4). In the presence of a liquid dispersed phase, additional source terms should be added in each equation that are not included here and will be presented in section 1.3.
The set of equations is as follows:

$$\frac{\partial \rho}{\partial t} + \frac{\partial \rho u_i}{\partial x_i} = 0 \tag{1.1}$$

$$\frac{\partial \rho u_j}{\partial t} + \frac{\partial}{\partial x_i}(\rho u_i u_j) = -\frac{\partial P}{\partial x_j} + \frac{\partial \tau_{ij}}{\partial x_i} + \rho g_i \tag{1.2}$$

$$\frac{\partial \rho Y_k}{\partial t} + \frac{\partial \rho Y_k u_i}{\partial x_i} = -\frac{\partial}{\partial x_i}(J_{k,i}) + \dot{\omega}_k \tag{1.3}$$

$$\frac{\partial \rho E}{\partial t} + \frac{\partial}{\partial x_i}(\rho E u_i) = -\frac{\partial}{\partial x_j}(u_i P) + \frac{\partial}{\partial x_i}(\tau_{ij} u_i) - \frac{\partial}{\partial x_i} q_i + \dot{\omega}_T + \dot{Q}_r \tag{1.4}$$

In these equations, ρ stands for the gaseous density, u_i for the i-component of the velocity, P for the pressure and E for an energy per unit mass (the sum of the sensible energy e_s and the kinetic energy $(1/2\ u_i^2)$). Y_k represents the mass fraction of the k-th species, with k varying from 1 to N, the number of species and g_i the i-component of the gravity vector $\mathbf{g}$.
In the momentum and energy transport equations, Eqs. 1.2 and 1.4, the ij-component of the viscous stress tensor τ_{ij} is defined as:

$$\tau_{ij} = \mu \left(\frac{\partial u_i}{\partial x_j} + \frac{\partial u_j}{\partial x_i} \right) - \frac{2}{3}\mu \frac{\partial u_k}{\partial x_k} \delta_{ij} \tag{1.5}$$

with μ the dynamic viscosity and δ_{ij} the Kronecker symbol ($\delta_{ij} = 1$ if $i = j$, 0 otherwise).
Additionally, the gas mixture verifies the equation of state for ideal gases:

$$P = \rho r T \tag{1.6}$$

with T the temperature and $r = \frac{\mathcal{R}}{W}$ the gas constant of the mixture, W the mean molar mass and $\mathcal{R} = 8.3143$ J.mol^{-1}.K^{-1} the universal gas constant.
Gravity effects on the gaseous mixture are neglected in all the simulations.
In the species mass fractions transport equation (Eq. 1.3), $\dot{\omega}_k$ corresponds to the species chemical source term and $J_{k,i}$ is the i-component of the diffusion flux of species k, written:

$$J_{k,i} = \rho V_{k,i} Y_k \tag{1.7}$$

To conserve the total mass of the mixture, $\dot{\omega}_k$ and $V_{k,i}$ must verify the two following relations:

$$\sum_{k=1}^{N} \dot{\omega}_k = 0 \tag{1.8}$$

$$\sum_{k=1}^{N} Y_k V_{k,i} = 0 \tag{1.9}$$

The species diffusion velocities $V_{k,i}$ is usually described using the Hirschfelder and Curtis approximation (Hirschfelder et al. (1954)) which proposes an approximation of the species diffusion velocity $V_{k,i}$ while introducing a correction velocity $\mathbf{V}^c$ so that Eq. 1.9 is verified:

$$V_{k,i} = -\frac{D_k}{Y_k}\frac{W_k}{W}\frac{\partial X_k}{\partial x_i} + V_i^c \tag{1.10}$$

$$V_i^c = \sum_{k=1}^{N} D_k \frac{W_k}{W}\frac{\partial X_k}{\partial x_i} \tag{1.11}$$

So that the diffusive species flux is written:

$$J_{k,i} = \rho Y_k V_{k,i} = -\rho \left(D_k \frac{W_k}{W}\frac{\partial X_k}{\partial x_i} - Y_k V_i^c \right) \tag{1.12}$$

where W and W_k are the molar mass of the mixture and of species k, respectively, X_k is the mole fraction, defined as $X_k = Y_k W / W_k$ and D_k is the diffusion coefficient of species k.
Species k mass fraction source term $\dot{\omega}_k$ is the sum of $\dot{\omega}_{k,j}$ with $j \in [1, M]$ the reaction rates for species k in each of the M reactions that compose the kinetic scheme. For each reaction, $\dot{\omega}_{k,j}$ is computed using an Arrhenius law.
The expression for the conductive heat flux q_i is given in Eq. 1.13. It is composed of two terms, one that accounts for the heat diffusion in the mixture, expressed following Fourier law and which depends on the gradient of the temperature T and on the thermal conductivity λ, and a second term that represents the heat flux caused by the species diffusion with different sensible enthalpies $h_{s,k}$. $V_{k,i}$ is the i-component of species k diffusion velocity, expressed in Eq. 1.10.

$$q_i = \underbrace{-\lambda \frac{\partial T}{\partial x_i}}_{\text{mixture heat diffusion}} + \underbrace{\rho \sum_{k=1}^{N} h_{s,k} Y_k V_{k,i}}_{\text{species enthalpy diffusion}} \tag{1.13}$$

Finally, two source terms are present in Eq. 1.4, the heat release rate from the chemical reaction $\dot{\omega}_T$ and a non-chemical source term $\dot{Q}_r$ that accounts for other possible heat sources, such as electric spark, laser or radiation for instance. The heat release rate is computed from the species reaction rates $\dot{\omega}_k$ and the species mass enthalpy of formation $\Delta h^0_{f,k}$, taken at $T = T_{ref} = 0$ K in AVBP:

$$\dot{\omega}_T = -\sum_{k=1}^{N} \dot{\omega}_k \Delta h^0_{f,k} \tag{1.14}$$

1.2.2 Computational approaches for gaseous turbulent flows

To compute numerically the evolution of a gaseous flow, the system of equations 1.1 to 1.3 needs to be solved on a grid that divides the physical space into small elements. The size of these elements is an important parameter since it determines the scale of the smaller structures that will be captured. In any flow, the amount of inertia forces is controlled by the Reynolds number, $Re = \frac{\rho u l}{\mu}$, also defined in Eq. 1, with l a characteristic dimension of the geometry and μ the dynamic viscosity. For high enough Reynolds numbers, the flow becomes turbulent, meaning that its behaviour is irregular and contains some randomness, so that it has to be looked at from a stochastic point of view. In particular, the aerodynamic structures have sizes that belong to a very large range of scales, from the system dimension l to the Kolmogorov scale l_K, which corresponds to the smallest size an eddy can have where inertia and diffusion forces are of the same order of magnitude (Kolmogorov (1941)).
In order to capture all the scales of the system, the grid used to solve the Navier-Stokes equations needs to be at least smaller than the Kolmogorov scale. In this case, all the scales of turbulence are explicitly captured and no model is necessary. This method is called Direct Numerical Simulation, or DNS. However, the constraint of the element size leads to grids composed of a very large number of points, which means that the simulation costs increase very rapidly with the complexity of the considered case. With the current available computing resources, DNS is only accessible for academic cases, meaning small geometries and small Reynolds numbers.
Numerical methods have been developed to try and bypass the computational cost issue that arises with DNS. The RANS method (for Reynolds Averaged Navier-Stokes), focuses on the resolution of the mean quantities of the flow, introducing models to account for the turbulence that is not computed. The

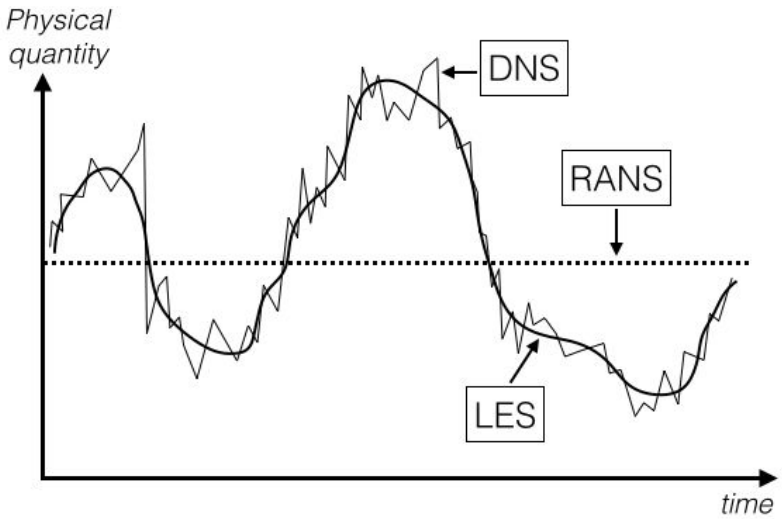

Figure 1.1: *Time evolution of a physical quantity in a turbulent flow computed with DNS, LES and RANS, extracted from Poinsot and Veynante (2012).*

balance equations are averaged before their resolution, so that a RANS simulation yields the average over time of all the quantities. RANS techniques are commonly used in the industry because they provide results for stationary flows for a moderate computational cost (the grid elements only need to be as large as the mean features of the flow). However, even though techniques like U-RANS (Unsteady Reynolds Averaged Navier-Stokes) allow to capture some of the transient phenomena, the fact that all the turbulent structures have to be modelled is not satisfactory if one wants to understand the local transient behaviour of the flow.
An intermediate technique between DNS and RANS that has been largely developed in the recent years is Large Eddy Simulation (LES). In LES, the turbulent large scales are explicitly calculated and the smaller scales are modelled using subgrid scale models. The equations are filtered using a method that is detailed in the next section.
The three different techniques that can be used in CFD are summarised in Fig. 1.1: the turbulent fluctuations of a physical quantity will be fully resolved by DNS while a RANS simulation would capture the mean value. The LES presents an intermediate method that would be able to retrieve the large-scale fluctuations.

1.2.3 Filtered equations for LES

The idea behind LES can be summarized in Fig. 1.2 in terms of turbulent energy spectrum: the largest turbulent structures, that have the lowest wave-numbers, are explicitly captured by the LES grid whereas the smallest ones, that have

a wave-number above the cut-off value k_c, and therefore belong to the subgrid scale, are modelled.

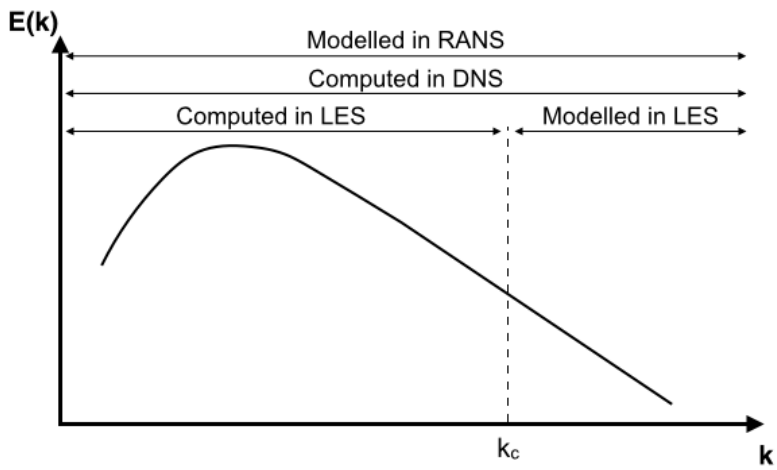

Figure 1.2: *Turbulent energy spectrum as a function of the wave number. The computed and modelled ranges are shown for each computational technique. In LES, the cut-off value is noted k_c. Extracted from Poinsot and Veynante (2012).*

To allow their resolution on the LES grid, Eqs. 1.1 to 1.3 need to be spatially filtered. This is done by performing the convolution product of the equations and a spatial filter of characteristic size Δ, noted G_Δ, usually a box or a Gaussian filter. The filtered value $\overline{\Phi}$ of a variable Φ is therefore written:

$$\overline{\Phi}(\mathbf{x}) = \int \Phi(\mathbf{x}')G_\Delta(\mathbf{x}-\mathbf{x}')d\mathbf{x}' \tag{1.15}$$

The variable Φ can then be decomposed into two parts, the filtered part $\overline{\Phi}$ and the subgrid scale part: $\Phi' = \Phi - \overline{\Phi}$.
When the density varies in the flow, it is convenient to weight the spatial average quantities by the density, in a procedure that is similar to the *Favre average* (Favre (1965)), noted $\widetilde{\Phi}$ and defined as:

$$\overline{\rho}\widetilde{\Phi} = \overline{\rho\Phi} = \int \rho(\mathbf{x}')\Phi(\mathbf{x}')G_\Delta(\mathbf{x}-\mathbf{x}')d\mathbf{x}' \tag{1.16}$$

After the spatial filtering operation, equations 1.1, 1.2, 1.4 and 1.3 become:

$$\frac{\partial \overline{\rho}}{\partial t} + \frac{\partial \overline{\rho}\widetilde{u}_i}{\partial x_i} = 0 \tag{1.17}$$

$$\frac{\partial \overline{\rho}\widetilde{u}_j}{\partial t} + \frac{\partial}{\partial x_i}\left(\overline{\rho}\widetilde{u}_i\widetilde{u}_j\right) = -\frac{\partial \overline{P}}{\partial x_j} + \frac{\partial \overline{\tau_{ij}}}{\partial x_i} + \frac{\partial \tau^t_{ij}}{\partial x_i} \tag{1.18}$$

$$\frac{\partial \overline{\rho}\widetilde{Y}_k}{\partial t} + \frac{\partial}{\partial x_i}\left(\overline{\rho}\widetilde{Y}_k\widetilde{u}_i\right) = -\frac{\partial}{\partial x_i}\left(\overline{J_{k,i}}\right) + \overline{\dot{\omega}_k} - \frac{\partial}{\partial x_i}\left(J^t_{k,i}\right) \tag{1.19}$$

$$\frac{\partial \overline{\rho}\widetilde{E}}{\partial t} + \frac{\partial}{\partial x_i}\left(\overline{\rho}\widetilde{E}\widetilde{u}_i\right) = -\frac{\partial \overline{Pu_i}}{\partial x_i} + \frac{\partial \overline{\tau_{ij}u_i}}{\partial x_j} - \frac{\partial \overline{q_i}}{\partial x_i} + \overline{\dot{\omega}_T} + \overline{\dot{Q}_r} - \frac{\partial q^t_i}{\partial x_i} \tag{1.20}$$

with τ^t_{ij} the subgrid-scale (SGS) Reynolds stresses, q^t_i the SGS energy fluxes and $J^t_{k,i}$ the SGS species fluxes:

$$\tau^t_{ij} = -\overline{\rho}\left(\widetilde{u_iu_j} - \widetilde{u}_i\widetilde{u}_j\right) \tag{1.21}$$

$$q^t_i = \overline{\rho}\left(\widetilde{Eu_i} - \widetilde{E}\widetilde{u}_i\right) \tag{1.22}$$

$$J^t_{k,i} = \overline{\rho}\left(\widetilde{Y_ku_i} - \widetilde{Y}_k\widetilde{u}_i\right) \tag{1.23}$$

These three unresolved quantities are not known and require closure models that will be presented in the next section. Additionally, the filtered laminar diffusion fluxes for species $\overline{J_{k,i}}$ and energy $\overline{q_i}$ and the pressure velocity term $\overline{Pu_i}$ need to be modelled.

1.2.4 Approximations and closure models

In the set of equations 1.17 to 1.19, several terms are not known and their models or approximations are presented in what follows.

Pressure velocity term: this term is usually approximated by $\overline{Pu_i} \approx \overline{P}\widetilde{u}_i$ (Poinsot and Veynante (2012)).

Viscous tensor: the laminar filtered stress tensor $\overline{\tau_{ij}}$ is approximated as:

$$\overline{\tau_{ij}} = \overline{\mu\left(\frac{\partial u_i}{\partial x_j} + \frac{\partial u_j}{\partial x_i}\right) - \frac{2}{3}\mu\frac{\partial u_k}{\partial x_k}\delta_{ij}} \tag{1.24}$$

$$\approx \overline{\mu}\left(\frac{\partial \widetilde{u}_i}{\partial x_j} + \frac{\partial \widetilde{u}_j}{\partial x_i}\right) - \frac{2}{3}\overline{\mu}\frac{\partial \widetilde{u}_k}{\partial x_k}\delta_{ij} \tag{1.25}$$

The diffusive species flux vector is expressed as:

$$\overline{J_{k,i}} = \overline{\rho Y_k V_{k,i}} \approx -\overline{\rho}\left[\overline{D_k}\frac{W_k}{W}\frac{\partial \widetilde{X}_k}{\partial x_i} - \widetilde{Y}_k\widetilde{V}^c_i\right] \tag{1.26}$$

Similarly, **the filtered heat flux** becomes:

$$\overline{q_i} = \overline{-\lambda \frac{\partial T}{\partial x_i} + \sum_{k=1}^{N} J_{k,i}\ h_{s,k}} \tag{1.27}$$

$$\approx -\overline{\lambda} \frac{\partial \widetilde{T}}{\partial x_i} + \sum_{k=1}^{N} \overline{J_{k,i}}\ \widetilde{h}_{s,k} \tag{1.28}$$

Finally, **the three subgrid-scale terms** that appear during the filtering procedure of the equations are by construction unknown. Several closure models have been developed for these terms, the ones used in AVBP are presented here.

$$\tau_{ij}^t = -\overline{\rho}\left(\widetilde{u_i u_j} - \widetilde{u}_i \widetilde{u}_j\right) \approx \overline{\rho}\nu_t \left(\frac{\partial \widetilde{u}_i}{\partial x_j} + \frac{\partial \widetilde{u}_j}{\partial x_i}\right) - \frac{2}{3}\overline{\rho}\nu_t \frac{\partial \widetilde{u}_k}{\partial x_k}\delta_{ij} \tag{1.29}$$

$$J_{k,i}t = \overline{\rho}\left(\widetilde{u_i Y_k} - \widetilde{u}_i \widetilde{Y}_k\right) \approx -\overline{\rho}\left(D_k^t \frac{W_k}{W}\frac{\partial \widetilde{X}_k}{\partial x_i} - \widetilde{Y}_k \widetilde{V}_i^{c,t}\right) \tag{1.30}$$

with ν_t the subgrid-scale turbulent viscosity, $D_k^t = \frac{\nu_t}{\mathrm{Sc}_k^t}$, Sc_k^t the turbulent Schmidt number, fixed at 0.6 in AVBP and $V_i^{c,t} = \sum_{k=1}^{N} D_k^t \frac{W_k}{W}\frac{\partial \widetilde{X}_k}{\partial x_i}$.

$$q_i^t = \overline{\rho}\left(\widetilde{u_i E} - \widetilde{u}_i \widetilde{E}\right) \approx -\lambda^t \frac{\partial \widetilde{T}}{\partial x_i} + \sum_{k=1}^{N} J_{k,i}^t \widetilde{h_{s,k}} \tag{1.31}$$

with $\lambda^t = \frac{\mu^t \overline{C_p}}{\mathrm{Pr}^t}$, $\mu^t = \overline{\rho}\nu^t$ and $\mathrm{Pr}^t = 0.6$ is fixed.
Several turbulence models for **the turbulent viscosity** ν^t are available in AVBP. In the simulations that were carried out in the present study, the WALE model (Nicoud and Ducros (1999)), for *wall adapting linear eddy*, is used, which propose to write ν_t as:

$$\nu_t = (C_w \Delta)^2 \frac{\left(s_{ij}^d s_{ij}^d\right)^{3/2}}{\left(\widetilde{S}_{il}\widetilde{S}_{ij}\right)^{5/2} + \left(s_{ij}^d s_{ij}^d\right)^{5/4}} \tag{1.32}$$

$$\text{with } \widetilde{S}_{ij} = \frac{1}{2}\left(\frac{\partial \widetilde{u}_i}{\partial x_j} + \frac{\partial \widetilde{u}_j}{\partial x_i}\right) - \frac{1}{3}\frac{\partial \widetilde{u}_k}{\partial x_j}\delta_{ij} \tag{1.33}$$

$$\text{and } s_{ij}^d = \frac{1}{2}\left(\widetilde{g}_{ij}^2 + \widetilde{g}_{ij}^2\right) - \frac{1}{3}\widetilde{g}_{kk}^2 \delta_{ij} \tag{1.34}$$

$$\widetilde{g}_{ij}^2 = \frac{\partial \widetilde{u}_i}{\partial x_k} \times \frac{\partial \widetilde{u}_k}{\partial x_j} \tag{1.35}$$

C_w is a model constant, fixed to $C_w = 0.57$ in the version of the solver that was used, and Δ is the filter characteristic size, here the cube-root of the cell's volume: $\Delta = \sqrt[3]{V}$.

1.2.5 Thermodynamic properties for the gaseous phase in AVBP

The standard reference state used in AVBP is $P_{ref} = 1$ atm and $T_{ref} = 0$ K. For each species, values of the molar sensible enthalpy $h^m_{s,k}$ and molar entropy s^m_k are tabulated against the temperature T, between 0 K and 5000 K, every 100 K, using the JANAF tables (Stull et al. (1971)). The sensible enthalpy, the entropy and the sensible energy, in mass units, for each value of T_i, with $i \in [1, 51]$ are therefore retrieved as follows:

$$h_{s,k}(T_i) = \int_{T_0=0K}^{T_i} C_{p,k} dT = \frac{h^m_{s,k}(T_i) - h^m_{s,k}(T_0)}{W_k} \tag{1.36}$$

$$s_k(T_i) = \frac{s^m_k(T_i)}{W_k} \tag{1.37}$$

$$e_{s,k}(T_i) = \int_{T_0=0K}^{T_i} C_{v,k} dT = h_{s,k}(T_i) - r_k T_i \tag{1.38}$$

where $r_k = \frac{\mathcal{R}}{W_k}$ is the gas constant of the species and $C_{p,k}$ and $C_{v,k}$ respectively stand for the heat capacities at constant pressure and at constant volume. The values of $h_{s,k}(T)$, $s_k(T)$ and $e_{s,k}(T)$ of the k-th species at a temperature $T \in [T_i, T_{i+1}[$ is linearly interpolated:

$$h_{s,k}(T) = h_{s,k}(T_i) + (T - T_i)\frac{h_{s,k}(T_{i+1}) - h_{s,k}(T_i)}{T_{i+1} - T_i} \tag{1.39}$$

$$s_k(T) = s_k(T_i) + (T - T_i)\frac{s_k(T_{i+1}) - s_k(T_i)}{T_{i+1} - T_i} \tag{1.40}$$

$$e_{s,k}(T) = e_{s,k}(T_i) + (T - T_i)\frac{e_{s,k}(T_{i+1}) - e_{s,k}(T_i)}{T_{i+1} - T_i} \tag{1.41}$$

The heat capacities are then assumed to be constant between T_i and T_{i+1} and are reconstructed as:

$$C_{p,k}(T) = \frac{h_{s,k}(T_{i+1}) - h_{s,k}(T_i)}{T_{i+1} - T_i} \text{ for } T \in [T_i, T_{i+1}[\tag{1.42}$$

$$C_{v,k}(T) = \frac{e_{s,k}(T_{i+1}) - e_{s,k}(T_i)}{T_{i+1} - T_i} \text{ for } T \in [T_i, T_{i+1}[\tag{1.43}$$

The sensible energy and enthalpy of the gaseous mixture are finally expressed as:

$$\rho e_s = \sum_{k=1}^{N} \rho_k e_{s,k} = \rho \sum_{k=1}^{N} Y_k e_{s,k} \tag{1.44}$$

$$\rho h_s = \sum_{k=1}^{N} \rho_k h_{s,k} = \rho \sum_{k=1}^{N} Y_k h_{s,k} \tag{1.45}$$

1.3 Equations and models for the liquid phase

1.3.1 Approaches for the description of the dispersed phase

Contrarily to the gaseous fields which are most often described from an Eulerian point of view and using continuous mechanics, two main approaches exist for the numerical representation of a dilute spray, both relying on a mesoscopic point-particle approximation (Fox (2012)): the Lagrangian approach and the Eulerian approach. In the Lagrangian approach, the spray is seen as an ensemble of discrete particles with their respective diameter and velocity, that are individually tracked using point mechanics. On the other hand, in the Eulerian approach, the liquid phase is seen as a continuous phase described by local quantities averaged over the particles. These two approaches are further described in the next sections.

1.3.2 The Lagrangian approach

In the lagrangian approach, each particle (which can be a physical particle or a numerical particle representing a cluster of physical ones) is individually tracked in the computational domain and is considered isolated, perfectly spherical and rigid. The gas phase is described by the Navier-Stokes equations given in section 1.2.1, the system of equations solved for a particle k is:

$$\frac{d\mathbf{x}_{p,i}^k}{dt} = \mathbf{v}_{p,i}^k \tag{1.46}$$

$$\frac{d}{dt}\left(m_p^k\ \mathbf{v}_{p,i}^k\right) = \mathbf{F}_{p,i}^k \tag{1.47}$$

$$\frac{dm_p^k}{dt} = \dot{m}_p^k \tag{1.48}$$

$$\frac{d}{dt}\left(m_p^k\ h_p^k\right) = \dot{Q}_p^k \tag{1.49}$$

where $\mathbf{x}_p^k$ is the particle position, $\mathbf{v}_p^k$ its velocity, m_p^k its mass, h_p^k its enthalpy, T_p^k its temperature, $\mathbf{F}_p^k$ the external forces applied on the particle, $\dot{m}_p^k$ its evaporation rate and $\dot{Q}_p^k$ the heat transfer rate received from the gaseous phase.
One of the advantages of the Lagrangian method is that it requires no modelling efforts to account for effects such as polydispersion or trajectory crossings. It is therefore often used in RANS simulations as well as in LES (examples of simulations in the Lagrangian framework can be found in Luo et al. (2011), Chrigui et al. (2012), Jones et al. (2012) Shum-Kivan et al. (2016) or Giusti and Mastorakos (2017)). However, efficient algorithms are necessary for the precise localisation of the particles on the Eulerian grid to ensure mass conservation. The interpolation of the droplets' properties on the mesh is also

an issue to compute the coupling terms between the two phases, which makes the use high-order schemes necessary to limit the resulting numerical diffusion, therefore increasing the computational cost. The statistical convergence required by the LES and the size of the domain imposes to track up to several millions of particles simultaneously. When performing massively parallel LES, the most efficient decomposition is the division of the computational domain into as many sub-domains as the number of processors. Besides the fact that exchanging Lagrangian particles between two processors is a delicate task (Garcia et al. (2005)), the optimised decomposition of the Eulerian grid for the gaseous flow might not be adequate for the Lagrangian solver. Indeed, the Lagrangian particles are generally not spatially distributed in the same way as the Eulerian cells. Moreover, in the case of the ignition of an annular combustor, the propagation of the flame inside the chamber evaporates the droplets it encounters, thus changing the particle distribution with time. Even with an initially optimised load repartition on the processors, an unbalance is generated as time progresses that needs to be handled dynamically. This is for instance done by Ham et al. (2003) who define a threshold value for the unbalance of the load repartition beyond which a new partition is calculated.

1.3.3 Equations for the Eulerian description of the spray

The Eulerian approach does not account for the history of each particle, but deals with the local average properties of the spray, which is considered as a continuous fluid. The main advantage of the Eulerian approach is that the equations are solved on the same grid as that of the gaseous phase, so that no interpolation is needed to compute the coupling terms and the presence of the liquid phase does not impact the efficiency of the mesh partitioning.
Two main types of operator can be used for the local average: *volumic* or *statistic*, which lead to two formalisms with their respective hypothesis, transported variables and closure models.
The description of the formalism derived from volumic (or ensemble) averaging, also called the two-fluid model, can be found in details in Février et al. (2005) and Kaufmann (2004). This method relies on the hypothesis that the Navier-Stokes equations can be applied on both phases, and that at a given time, a given location in the flow will be occupied by either one of the pure phases or an interface between the phases.
In AVBP, the set of equations that are solved for the liquid phases have been obtained with the statistical average. The procedure that leads to these equations is briefly summarised in what follows. This approach is also called the *mesoscopic* approach, and more detailed descriptions of their implementation can be found in CERFACS (2011) and Boileau (2007).
The mesoscopic approach is based on the kinetic theory of gases formulated by Chapman and Cowling (1970) and uses a set of mesoscopic variables to describe the particles' properties and reduce the degrees of freedom. The liquid

particles are seen as point particles with properties such as velocity, mass, temperature,... upon which forces and exchange terms apply.
The mesoscopic approach requires a number of hypotheses on the two-phase mixture that are presented hereafter as **H1**, **H2**, **H3**, **H4** and **H5**. Additionally, a mono-dispersed spray assumption is made through hypotheses **H7** and **H8**, motivated by the geometries studied in the present work and the computational resources available:

H1 - The atomization process is complete, meaning that no secondary break-up occurs and the particles are perfectly spherical droplets.
H2 - The density ratio between gas and liquid allows to assume that the only force exerted by the carrier phase on the droplets is drag.
H3 - The temperature, and therefore the sensible enthalpy, is assumed to be homogeneous inside each droplet.
H4 - A dilute spray assumption is made ($\alpha_l < 0.01$), so the liquid volume fraction is negligible before the gaseous one: $\alpha_g = 1 - \alpha_l \approx 1$. This leads to the next two hypotheses.
H5 - The interactions between droplets are negligible.
H6 - The liquid phase has little influence over the carrier phase, which allows the use of a probability density function conditioned by one realization.
H7 - The spray is mono-disperse and mono-kinetic: at one point in time and space, the droplets all have the same diameter and velocity.
H8 - Similarly, at one point in time and space, the droplets have the same temperature.
H9 - Random uncorrelated motion is neglected.

Detailed demonstrations for the derivation of the conservation equations can be found in Kaufmann (2004) and Boileau (2007), only the main steps are presented here. Statistical averages are used to deduce the mesoscopic quantities from the droplets physical states. In the following, variables with the index $\cdot_p$ refer to particles properties while those denoted $\cdot_l$ refer to mesoscopic quantities.
The main steps for the derivation of the equations are:

- A particle Probability Density Function (PDF) is defined for the dispersed phase, conditioned by one realisation of the carrier phase.
- A Boltzmann-type transport equation is written for this PDF, using its properties as detailed in Chapman and Cowling (1970).
- The PDF is used to define a local statistical average for the spray's properties, written $\langle \cdot \rangle_l$.
- A general transport equation of quantity Ψ, called *Enskog equation*, is obtained by multiplying the previous equation by Ψ and by filtering it

with the average operator $\langle\cdot\rangle_l$.

- The Enskog equation is successfully applied to a set of variables to obtain the transport equations and the set of Eulerian conservation equations for the mean behaviour, or mesoscopic behaviour, of the liquid phase.
- Closure models are defined for the unclosed terms.

Statistical averages at a given point x and instant t

The statistical average of quantity Ψ, noted $\{\Psi\}_l$, is defined as its mean value over all the possible realisations on the dispersed phase:

$$\{\Psi\}_l = \frac{1}{\breve{n}_l}\int \Psi(\mathbf{c}_p,\zeta_p,\mu_p) f_p(\mathbf{c}_p,\zeta_p,\mu_p,\mathbf{x},t|\mathcal{H}_p)\ d\mathbf{c}_p d\zeta_p d\mu_p \tag{1.50}$$

with $\mathbf{c}_p$, ζ_p, μ_p the velocity, temperature and mass of each particle, f_p the probability density function for the particle density, conditioned by one carrier phase realisation $\mathcal{H}_p$, and $\breve{n}_l$ the mean droplet number density:

$$\breve{n}_l = \int f_p(\mathbf{c}_p,\zeta_p,\mu_p,\mathbf{x},t|\mathcal{H}_p)\ d\mathbf{c}_p d\zeta_p d\mu_p \tag{1.51}$$

Similarly to compressible gaseous flows where Favre averages are commonly used, it is often more convenient to use a mass-weighted average when the droplet mass varies:

$$\breve{\Psi} = \langle\Psi\rangle_l = \frac{1}{\rho_l\breve{\alpha}_l}\int \mu_p\Psi(\mathbf{c}_p,\zeta_p,\mu_p) f_p(\mathbf{c}_p,\zeta_p,\mu_p,\mathbf{x},t|\mathcal{H}_p)\ d\mathbf{c}_p d\zeta_p d\mu_p \tag{1.52}$$

with ρ_l the liquid density and $\breve{\alpha}_l$ is the liquid volume fraction, that is to say the fraction of volume occupied by the liquid phase per unit of volume, defined by:

$$\rho_l\breve{\alpha}_l = \breve{n}_l\,\{m_p\}_l = \int \mu_p f_p(\mathbf{c}_p,\zeta_p,\mu_p,\mathbf{x},t|\mathcal{H}_p)\ d\mathbf{c}_p d\zeta_p d\mu_p \tag{1.53}$$

As was done in Boileau (2007), two notations are introduced in Eq. 1.52 to improve clarity. In the general case, the first one $\breve{\cdot}$ will be preferred, but the second one, $\langle\cdot\rangle_l$ may sometimes lead to expressions that are easier to read.
The two averages are linked by the following relation:

$$\rho_l\breve{\alpha}_l\,\langle\Psi\rangle_l = \breve{n}_l\,\{m_p\Psi\}_l \ \text{ with } m_p = \rho_l\frac{\pi}{6}d_p^3 \tag{1.54}$$

In the case of a monodispersed spray, all the particles at a given point $(\mathbf{x},t)$ have the same diameter d_p, and therefore the same mass m_p, leading to $\{m_p\}_l = m_p$. The two average operators are then equivalent:

$$\breve{\Psi} = \{\Psi\}_l \tag{1.55}$$

$$\breve{\alpha}_l = \frac{\pi}{6}\breve{n}_l d_l^3 \tag{1.56}$$

Transported quantities for the liquid phase

The procedure previously described leads to transport equations for the following mesoscopic variables:
- $\breve{n}_l$ the number of particles per volume unit
- $\rho_l\breve{\alpha}_l$ the density of liquid in the two-phase mixture
- $\rho_l\breve{\alpha}_l\breve{\mathbf{u}}_l$, with $\breve{\mathbf{u}}_l$ the liquid mesoscopic velocity vector
- $\rho_l\breve{\alpha}_l\delta\breve{\theta}_l$, with $\delta\breve{\theta}_l$ the uncorrelated energy (defined in the next paragraph)
- $\rho_l\breve{\alpha}_l\breve{h}_{s,l}$, with $\breve{h}_{s,l}$ the mesoscopic sensible enthalpy: $\breve{h}_{s,l} = C_{p,l}\left(\breve{T}_l - T_{l,ref}\right)$, with $C_{p,l}$ the liquid heat capacity, assumed constant every 10 K.

For further use, a vector of the transported conservative mesoscopic variables is defined: $\mathbf{w}_l = (\breve{n}_l, \rho_l\breve{\alpha}_l,\ \rho_l\breve{\alpha}_l\breve{u}_l,\ \rho_l\breve{\alpha}_l\breve{v}_l,\ \rho_l\breve{\alpha}_l\breve{w}_l,\ \rho_l\breve{\alpha}_l\delta\breve{\theta}_l,\ \rho_l\breve{\alpha}_l\breve{h}_{s,l})^T$.

Uncorrelated quantities

The mesoscopic quantities defined though the statistical average represent the mean behaviour of an ensemble of droplets. However, as is described in Février et al. (2005), the actual behaviour of each individual particle is not identical to that of the ensemble. In particular, the velocity $\mathbf{u}_p$ of a particle can be decomposed into two contributions, the mesoscopic velocity $\breve{\mathbf{u}}_l$ and a residual part, called the *uncorrelated velocity* $\mathbf{u}_p''$ (see Fig. 1.3):

$$\mathbf{u}_p = \breve{\mathbf{u}}_l + \mathbf{u}_p'' \text{ with } \left\langle \mathbf{u}_p'' \right\rangle_l = 0 \tag{1.57}$$

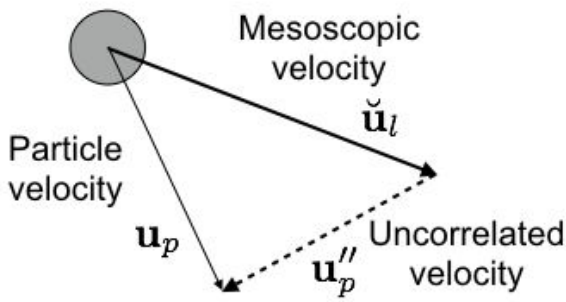

Figure 1.3: *Decomposition of the particle velocity $\mathbf{u}_p$ into a mesoscopic part $\breve{\mathbf{u}}_l$ and an uncorrelated part $\mathbf{u}_p''$.*

The uncorrelated energy $\delta\breve{\theta}_l$, is defined as:

$$\delta\breve{\theta}_l = \frac{1}{2}\left\langle u_{p,i}'' u_{p,i}'' \right\rangle_l \tag{1.58}$$

When it is accounted for, the variable $\rho_l \breve{\alpha}_l \delta\breve{\theta}_l$ is transported. In all the simulations presented in this work, all random uncorrelated motion is neglected (hypothesis **H9**). The transport equation is still presented in the following for information.

Transport equations

The final set of Eulerian equations for the dispersed phase that is solved in AVBP and accounting for hypotheses **H1** to **H8**, is:

$$\frac{\partial}{\partial t}\breve{n}_l + \frac{\partial}{\partial x_j}\breve{n}_l\breve{u}_{l,j} = 0 \tag{1.59}$$

$$\frac{\partial}{\partial t}\rho_l\breve{\alpha}_l + \frac{\partial}{\partial x_j}\rho_l\breve{\alpha}_l\breve{u}_{l,j} = -\Gamma \tag{1.60}$$

$$\frac{\partial}{\partial t}\rho_l\breve{\alpha}_l\breve{u}_{l,i} + \frac{\partial}{\partial x_j}\rho_l\breve{\alpha}_l\breve{u}_{l,i}\breve{u}_{l,j} = \mathbb{T}\left(u''_{p,i}\right) - \Gamma\breve{u}_{l,i} + F_{d,i} \tag{1.61}$$

$$\frac{\partial}{\partial t}\rho_l\breve{\alpha}_l\delta\breve{\theta}_l + \frac{\partial}{\partial x_j}\rho_l\breve{\alpha}_l\breve{u}_{l,j}\delta\breve{\theta}_l = \mathbb{T}\left(\frac{1}{2}u''_{p,i}u''_{p,i}\right) + \mathbb{U}_\theta - \Gamma\delta\breve{\theta}_l + W_\theta \tag{1.62}$$

$$\frac{\partial}{\partial t}\rho_l\breve{\alpha}_l\breve{h}_{s,l} + \frac{\partial}{\partial x_j}\rho_l\breve{\alpha}_l\breve{u}_{l,j}\breve{h}_{s,l} = +\Lambda_l + \Phi_l \tag{1.63}$$

In equations 1.61 and 1.62, the operator $\mathbb{T}$ is the uncorrelated flux operator defined as $\mathbb{T}(\Psi) = -\frac{\partial}{\partial x_j}\rho_l\alpha_l\langle u''_{p,j}\Psi\rangle_l$, $\mathbb{U}_\theta$ represents for the effects of the uncorrelated velocities tensor on the uncorrelated energy and W_θ the uncorrelated energy variation due to drag. Further details on the uncorrelated quantities can be found in Boileau (2007) and Sierra (2012). Since no uncorrelated motion was accounted for here, all the terms dealing with uncorrelated quantities are set to zero and the corresponding equation is removed in the following.
Γ is the mass exchange rate due to evaporation, using hypothesis **H7** which gives $\langle m_p\rangle = m_p$:

$$\Gamma = -\rho_l\breve{\alpha}_l\left\langle\frac{1}{m_p}\frac{dm_p}{dt}\right\rangle_l = \breve{n}_l\left\{\frac{dm_p}{dt}\right\}_l \tag{1.64}$$

Φ_l and Λ_l are respectively the variations of sensible enthalpy due to conductive heat transfer in the liquid phase and to mass transfer with the gaseous phase and their expressions are given in Eqs. 1.65 and 1.66. To simplify these expressions, hypothesis **H8** allows to write $\breve{h}_{s,l} = h_{s,p}$:

$$\Phi_l = \rho_l\breve{\alpha}_l\left\langle\frac{dh_{s,p}}{dt}\right\rangle_l \tag{1.65}$$

$$\Lambda_l = \rho_l\breve{\alpha}_l\left\langle\frac{h_{s,p}}{m_p}\frac{dm_p}{dt}\right\rangle_l = \rho_l\breve{\alpha}_l\frac{\breve{h}_{s,l}}{m_p}\left\langle\frac{dm_p}{dt}\right\rangle_l = \breve{n}_l\breve{h}_{s,l}\left\langle\frac{dm_p}{dt}\right\rangle_l = \Gamma\breve{h}_{s,l} \tag{1.66}$$

1.3.4 Exchange terms between the phases

Equations 1.59 to 1.63 can be written in a more compact form with the vectorial equation:

$$\frac{\partial \mathbf{w}_l}{\partial t} + \nabla \cdot \mathbf{F}_l = \mathbf{s}_l \tag{1.67}$$

where $\mathbf{F}_l$ is the flux tensor and $\mathbf{s}_l$ the source terms vector. $\mathbf{w}_l$ is the vector of liquid conservative mesoscopic variables:

$$\mathbf{w}_l = \begin{pmatrix} \breve{n}_l \\ \rho_l \breve{\alpha}_l \\ \rho_l \breve{\alpha}_l \breve{u}_{l,i} \\ \rho_l \breve{\alpha}_l \breve{v}_{l,i} \\ \rho_l \breve{\alpha}_l \breve{w}_{l,i} \\ \rho_l \breve{\alpha}_l \breve{h}_{s,l} \end{pmatrix} \tag{1.68}$$

Since no uncorrelated motion is accounted for, the only source terms present in the equations are that of exchanges with the gaseous phase:

$$\mathbf{s}_l = \mathbf{s}_{g-l} = \begin{pmatrix} 0 \\ -\Gamma \\ -\Gamma \breve{u}_l + F_{d,x} \\ -\Gamma \breve{v}_l + F_{d,y} \\ -\Gamma \breve{w}_l + F_{d,z} \\ \Lambda_l + \Phi_l \end{pmatrix} \tag{1.69}$$

The source terms to be added to the gaseous phase equations presented in Sec. 1.2.1 can now be retrieved. Writing the system of equations 1.1 to 1.4 in its vectorial form gives:

$$\frac{\partial \mathbf{w}}{\partial t} + \nabla \cdot \mathbf{F} = \mathbf{s} \tag{1.70}$$

with $\mathbf{w}$ the vector of gaseous conservative variables $\mathbf{w} = (\rho,\ \rho u,\ \rho v,\ \rho w,\ \rho Y_k,\ \rho E)^T$, $k \in [1, N]$, $\mathbf{F}$ the flux tensor and $\mathbf{s}$ the source terms vector. The source terms vector is composed of the chemical source terms (already present in the equations 1.1-1.4) and the source terms due to exchanges with the liquid phase:

$$\mathbf{s} = \mathbf{s}_c + \mathbf{s}_{l-g} = \begin{pmatrix} 0 \\ 0 \\ 0 \\ 0 \\ \dot{\omega}_k \\ \dot{\omega}_T \end{pmatrix} + \begin{pmatrix} \Gamma \\ \Gamma \breve{u}_l - F_{d,x} \\ \Gamma \breve{v}_l - F_{d,y} \\ \Gamma \breve{w}_l - F_{d,z} \\ \Gamma \delta_{k,F} \\ \Lambda_g + \Phi_g + \frac{1}{2}\Gamma \breve{u}_{l,i}\breve{u}_{l,i} - \breve{u}_{l,i} F_{d,i} \end{pmatrix} \tag{1.71}$$

The total heat exchanges at the interface between the spray and the liquid can also be written $\Pi_g = \Lambda_g + \Phi_g$ and $\Pi_l = \Lambda_l + \Phi_l$ and the global balance of energy at the interface gives:

$$\Pi_g + \Pi_l = \Lambda_g + \Phi_g + \Lambda_l + \Phi_l = 0 \tag{1.72}$$

1.3.5 Closure models for the liquid phase

1.3.5.1 Drag

The exchange term $\mathbf{F}_d$ that appears in Eqs. 1.71 and 1.69 in linked to the drag force exerted by the gaseous phase on an individual droplet:

$$\mathbf{F}_d = \rho_l \breve{\alpha}_l \left\langle \frac{\mathbf{F}_p}{m_p} \right\rangle_l \tag{1.73}$$

Kaufmann (2004) showed that for dense droplets ($\rho_l \gg \rho_{gas}$) and small diameters ($d \leq 50\mu$m), the other forces acting on the droplets (Basset force, Lift, Magnus effect,...) are negligible before the drag (hypothesis **H2** in Sec. 1.3.3). In AVBP, the drag force exerted on one particle $\mathbf{F}_p$ is classically expressed with the Stokes model (Stokes (1851)). A Reynolds number is first defined for the particle and its relative velocity:

$$Re_p = \frac{d_p|\mathbf{u} - \mathbf{u}_p|}{\nu} \tag{1.74}$$

where ν is the laminar viscosity of the gas surrounding the droplet.
When $Re_p \ll 1$, the viscous term is dominant before the inertial force around the droplet, and the drag force can be written (Stokes (1851)):

$$\mathbf{F}_p = C_D \frac{\pi d_p^2}{8} \rho |\mathbf{u} - \mathbf{u}_p| \ (\mathbf{u} - \mathbf{u}_p) \tag{1.75}$$

with $C_D = \frac{24}{Re_p}$ is the drag coefficient. When the particle Reynolds number is not small before unity, this simplified expression for C_D in no longer valid and the obtention of an analytical solution of difficult (Kaufmann (2004)). However, up to the particle critical Reynolds number $Re_{d,crit} = 3.7 \times 10^5$, the Schiller-Naumann empirical correlation can be used to account for greater Reynolds numbers (Schiller and Naumann (1935)):

$$C_D = \frac{24}{Re_p}(1 + 0.15 Re_p^{0.687}) \tag{1.76}$$

A relaxation time for the particle τ_p can be defined:

$$\tau_p = \frac{\tau_p'}{1 + 0.15 Re_p^{0.687}} \text{ with } \tau_p' = \frac{\rho_l d_p^2}{18 \mu_l} \tag{1.77}$$

so that the drag force exerted on one particle is written:

$$\mathbf{F}_p = m_p \frac{1}{\tau_p}(\mathbf{u} - \mathbf{u}_p) \tag{1.78}$$

Using Eqs. 1.73 and 1.78, the drag term $\mathbf{F}_d$ can finally be expressed as:

$$F_{d,i} = \rho_l \breve{\alpha}_l \frac{u_i - \breve{u}_{l,i}}{\tau_p}, \ i = 1, 3 \tag{1.79}$$

1.3.5.2 Mass transfer

The evaporation rate Γ that appears in the exchange terms between the phases is expressed:

$$\Gamma = -\breve{n}_l \{\dot{m}_p\}_l \text{ with } \dot{m}_p = \frac{dm_p}{dt} \tag{1.80}$$

In LES simulations, where the detailed flow fields in and around the droplets are not solved, the mass evolution of an individual droplet $\dot{m}_p$ requires a closure model. Assuming that a given droplet is isolated from its neighbours (hypothesis **H5**), Sirignano (1999) divides the available droplet-vaporization models into six types, sorted by increasing complexity:
(i) Constant droplet temperature models, which yield the *d2-law*, the temperature inside the droplet is uniform and constant, and the square of the droplet diameter varies linearly with time.
(ii) Uniform droplet temperature, but varying with time, models, which means that the droplet thermal conductivity is assumed to be infinite.
(iii) Spherically symmetric transient droplet heating models, where a finite thermal conductivity is considered but without any flow inside the droplet.
(iv) Vortex model of droplet heating, where the droplet internal flow field is modelled with a vortex.
(v) The Navier-Stokes equations are solved in the droplet and the surrounding gas.

The main difference between the models resides in the treatment of the heating of the liquid phase which usually controls the rate of evaporation of the droplets. In most LES simulations and in the present work, a uniform droplet temperature model (type (ii)) is used for its good trade-off between physical accuracy and reasonable computational cost. This model is actually a limit of type (iii) models, when the droplet heating time is small before its lifetime (Sirignano (1999)).
The two main hypothesis of a uniform temperature model are an infinite thermal conductivity in the liquid phase, so that the temperature in the droplet is uniform at each instant, and a thermodynamic equilibrium at the interface between the gas and the liquid, so that the Clausius Clapeyron relation can be applied.
Kuo (1986) provides a detailed description of how to obtain the expression of the individual droplet's evaporation rate $\dot{m}_p$ by integrating the conservation equation of the fuel mass fraction Y_F between the interface of the droplet ($r = \zeta$) and the infinity ($r \to \infty$):

$$\dot{m}_p = -\pi \; d_p \; \mathrm{Sh} \; [\rho D_F] \; \ln(1 + \mathrm{B_M}) \tag{1.81}$$

The *Sherwood number* Sh represents the ratio of mass transfer through convection and through diffusion. Equation 1.81 introduces a modified Sherwood

number,

$$\mathrm{Sh}^* = \mathrm{Sh}\frac{\mathrm{B_M}}{\ln\left(1+\mathrm{B_M}\right)}, \tag{1.82}$$

which is identical to the original Sherwood number in the case of a non-evaporating droplet. In the case of heat transfer between a flow and a single spherical particle, and when the relative velocity between the gas and the liquid is not zero, as is the case in a three dimensional turbulent configuration, the Sherwood number can be approximated by the *Ranz-Marshall correlation* (Ranz and Marshall (1952)):

$$\mathrm{Sh}^* \approx 2 + 0.55\mathrm{Re}_p^{1/2}\mathrm{Sc}_F^{1/3} \tag{1.83}$$

The expression $[\rho D_F]$ is composed of the gaseous density and the fuel species diffusion coefficient D_F. The product is obtained in the simulation through the fuel species Schmidt number Sc_F and the gas viscosity μ:

$$[\rho D_F] = \frac{\mu}{\mathrm{Sc}_F} \tag{1.84}$$

Finally, $\mathrm{B_M}$ is the *Spalding mass number* and depends on the fuel mass fraction difference between the interface ζ and the infinity:

$$\mathrm{B_M} = \frac{Y_{F,\zeta} - Y_{F,\infty}}{1 - Y_{F,\zeta}} \tag{1.85}$$

The value for $Y_{F,\infty}$ is easily retrieved from the local eulerian gaseous variables, but $Y_{F,\zeta}$ needs to be expressed as a function of known or retrievable quantities, for instance the fuel molar fraction at the surface $X_{F,\zeta}$ and the molar weights:

$$Y_{F,\zeta} = \frac{X_{F,\zeta}W_F}{X_{F,\zeta}W_F + \left(1 - X_{F,\zeta}\right)\overline{W}_{nF,\zeta}} \tag{1.86}$$

where W_F is the fuel species molar weight and $\overline{W}_{nF,\zeta}$ is the molar weight of a fictive mixture composed of all the species other than the fuel at the surface. Assuming that no other phenomenon changes the local species composition, evaporation modifies the mixing factor between the fuel vapour and this *pseudo-mixture*, which does not change composition between the interface and the infinity. In consequence, $\overline{W}_{nF,\zeta} = \overline{W}_{nF,\infty}$ and they can be expressed with quantities at the far-field and the gas mixture molar weight $\overline{W}$:

$$\overline{W}_{nF,\zeta} = \overline{W}_{nF,\infty} = \frac{1 - Y_{F,\infty}}{1 - Y_{F,\infty}\frac{\overline{W}}{W_F}}\overline{W} \tag{1.87}$$

The fuel molar fraction $X_{F,\zeta}$ can be retrieved from the partial pressure of the fuel species at the interface $P_{F,\zeta}$ and the gaseous pressure through Dalton's law for ideal mixtures of perfect gases:

$$X_{F,\zeta} = \frac{P_{F,\zeta}}{P} \tag{1.88}$$

where $P_{F,\zeta}$ is the fuel species partial pressure at the droplet surface. The droplet having been supposed at thermodynamic equilibrium, $P_{F,\zeta}$ is actually equal to the saturated vapour pressure P_{sat} at temperature T_ζ and can be retrieved using the Clausius-Clapeyron law in its integrated form for a gaseous-liquid phase change:

$$P_{sat}\left(T\right) = P_{cc}\ \exp\left[\frac{W_F L_v(T_{ref})}{\mathcal{R}}\left(\frac{1}{T_{cc}} - \frac{1}{T}\right)\right] \tag{1.89}$$

T_{cc} and P_{cc} are respectively the reference pressure and temperature corresponding to an arbitrary point of the saturation curve, $\mathcal{R}$ is the universal gas constant and L_v the mass latent heat of vaporisation.
In AVBP, tables of $P_{sat}(T)$ are computed for values of the temperature every 10 K using Eq. 1.89 and stored before the simulation. The temperature at the surface of the droplet T_ζ is supposed equal to T_p (hypothesis **H3**) and $P_{F,\zeta}(T_p)$ is interpolated in the P_{sat} table.
The spray being monodispersed (hypothesis **H8**), Eqs. 1.80 and 1.81 give the evaporation rate Γ:

$$\Gamma^* = \pi\ \breve{n}_l\ \mathrm{Sh}\ [\rho D_F]\ \ln(1 + \mathrm{B_M}) \tag{1.90}$$

1.3.5.3 Heat transfer

Single isolated droplet

Similarly to the mass transfer rate, the heat exchange rates can be retrieved from that of a single isolated droplet. The methodology presented in the following section uses the classical Spalding model (Spalding (1953)), along with some later improvements.
The heat flux transmitted to the liquid droplet at the surface ϕ_p^t is redistributed into two contributions, a flux due to mass transfer by evaporation ϕ_p^{ev} and a flux due to conductive transfer ϕ_p^c. The same decomposition can be done for the heat flux entering the gas phase $\phi_g^t = \phi_g^{ev} + \phi_g^c$. These fluxes are represented in Fig. 1.4.
The definition of the fluxes at the interface gives the global balance:

$$\phi_p^t + \phi_g^t = 0 \tag{1.91}$$

$$\phi_p^c + \phi_p^{ev} + \phi_g^c + \phi_g^{ev} = 0 \tag{1.92}$$

ϕ_g^{ev} represents flux of sensible enthalpy of the fuel species $h_{s,F}$ transported from the liquid to the gas by the mass flux of fuel $-\dot{m}_p$ ($\dot{m}_p < 0$), defined in Eq. 1.81, and can therefore be expressed as:

$$\phi_g^{ev} = -\dot{m}_p h_{s,F}(T_\zeta) \tag{1.93}$$

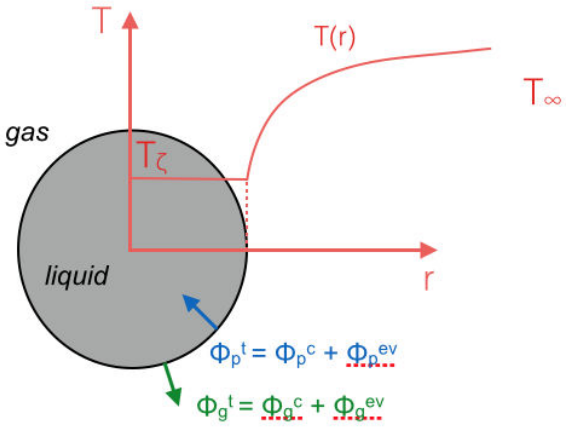

Figure 1.4: *Definition of the heat fluxes at the surface of a single isolated droplet. In red is plotted the evolution of the temperature, uniform inside the droplet and evolving towards its far-field value T_∞ in the gaseous phase, adapted from Boileau (2007).*

Similarly, the enthalpy variation in the liquid due to evaporation ϕ_l^{ev} is the product of the liquid mass variation and the liquid sensible enthalpy at the surface:

$$\phi_p^{ev} = \dot{m}_p h_{s,l}(T_\zeta) \tag{1.94}$$

The gaseous conductive flux around a droplet without any phase change is proportional to the temperature gradient at the surface:

$$\phi_g^c = \left(-4\pi r^2 \lambda_g \frac{dT}{dr}\right)\bigg|_\zeta \tag{1.95}$$

where the gaseous thermal conductivity λ is obtained from the Prandtl number Pr and the heat capacity of the *film mixture*, detailed in Sec. 1.3.5.4:

$$\lambda_g = \frac{\mu C_p^{film}}{\mathrm{Pr}} \tag{1.96}$$

The temperature evolution in the gaseous phase around the droplet can be derived from the mass conservation (Eq. 1.97) and the transport equation for the energy (Eq.1.98), written for the gaseous flow around an isolated droplet ($u_\infty = 0$) in spherical coordinates, supposing a quasi-steady ($\partial t = 0$) and and spherical ($\partial\theta = \partial\varphi = 0$) problem:

$$\text{mass conservation:} \qquad \rho u_r (4\pi r^2) = cte = \dot{m}_F \tag{1.97}$$

$$\text{energy conservation:} \qquad \rho u_r r^2 \frac{dh_{s,g}(r)}{dr} = \frac{d}{dr}\left(\frac{\lambda_g}{C_p} r^2 \frac{dh_{s,g}(r)}{dr}\right) \tag{1.98}$$

where $h_{s,g}(r)$ is the local gaseous sensible enthalpy and $\dot{m}_F$ the fuel species mass fraction source term in the gaseous phase ($\dot{m}_F = -\dot{m}_p$).
The insertion of Eq. 1.97 into Eq. 1.98 and an integration using the limit condition at $r = r_\zeta$ gives:

$$\dot{m}_F h_{s,g}(r) = 4\pi \frac{\lambda_g}{C_p(r)} r^2 \frac{dh_{s,g}(r)}{dr} + c_1 \tag{1.99}$$

$$\text{with} \quad c_1 = \dot{m}_F h_{s,g}(r_\zeta) \underbrace{-4\pi \frac{\lambda_g}{C_p(r_\zeta)} r_\zeta^2 \frac{dh_{s,g}(r)}{dr}\bigg|_\zeta}_{\phi_g^c} \tag{1.100}$$

Assuming that at the surface, temperature variations are small, the heat capacity can locally be considered constant so that $\frac{dh_{s,g}(r)}{dr}\Big|_\zeta = C_p(r_\zeta)\frac{dT}{dr}\Big|_\zeta$ and the expression for ϕ_g^c appears in the integration constant.
Equation 1.99 can be re-written:

$$\dot{m}_F \left[h_{s,g}(r) - h_{s,g}(r_\zeta) - \frac{\phi_g^c}{\dot{m}_F} \right] = 4\pi \frac{\lambda_g}{C_p(r)} r^2 \frac{dh_{s,g}(r)}{dr} \tag{1.101}$$

$$\frac{dr}{r^2} = \frac{4\pi\lambda_g}{C_p(r)\dot{m}_F} \frac{dh_{s,g}(r)}{h_{s,g}(r) - h_{s,g}(r_\zeta) - \frac{\phi_g^c}{\dot{m}_F}} \tag{1.102}$$

The integration of this expression, using the limit condition at the far-field ($r \to \infty$) and assuming as before that in the gaseous phase around the droplet, temperature variations are small enough that $C_p(r) = C_p(r_\zeta)$, gives:

$$-\frac{1}{r} + c_2 = \frac{4\pi\lambda_g}{C_p(r_\zeta)\dot{m}_F} \ln \left[h_{s,g}(r) - h_{s,g}(r_\zeta) - \frac{\phi_g^c}{\dot{m}_F} \right] \tag{1.103}$$

$$\text{with} \quad c_2 = \frac{4\pi\lambda_g}{C_p(r_\zeta)\dot{m}_F} \ln \left[h_{s,g}(r_\infty) - h_{s,g}(r_\zeta) - \frac{\phi_g^c}{\dot{m}_F} \right] \tag{1.104}$$

This last expression, evaluated at the droplet surface $r = r_\zeta$ gives:

$$\dot{m}_F = \frac{4\pi\lambda_g r_\zeta}{C_p(r_\zeta)} \ln\left(\mathrm{B_T} + 1\right) \tag{1.105}$$

where $\mathrm{B_T}$ is the Spalding number for heat transfer:

$$\mathrm{B_T} = \frac{(T_\infty - T_\zeta)\dot{m}_F C_p(r_\zeta)}{-\phi_g^c} \tag{1.106}$$

Since $\dot{m}_F = -\dot{m}_p$, two expressions have been found for the evaporation rate, in Eqs 1.81 and 1.105, which can be used to retrieve a new expression for B_T that depends on the mass Spalding number $\mathrm{B_M}$ and the fuel species Lewis number Le_F:

$$\mathrm{B_T} = (1 + \mathrm{B_M})^{1/\mathrm{Le}_F} - 1 \text{ with } \mathrm{Le}_F = \frac{\mathrm{Sc}_F}{\mathrm{Pr}} = \frac{\mu}{[\rho D_F]} \cdot \frac{\lambda_g}{\mu C_p} \tag{1.107}$$

The combination of Equations 1.105 and 1.106 finally lead to an expression for the gaseous conductive flux around the droplet ϕ_g^c:

$$\phi_g^c = \pi d_l \ \mathrm{Nu}^* \ \lambda_g (T_\zeta - T_\infty) \frac{\ln(\mathrm{B_T}+1)}{\mathrm{B_T}} \tag{1.108}$$

$$\text{with } \mathrm{Nu}^* = 2 + 0.55 \ \mathrm{Re}_p^{1/2} \ \mathrm{Pr}^{1/3} \tag{1.109}$$

Similarly to the Sherwood number for mass transfer, a modified Nusselt number $\mathrm{Nu}^* = \mathrm{Nu}\frac{\mathrm{B_T}}{\ln(\mathrm{B_T}+1)}$ is introduced and expressed from the original Nusselt number that represents the ratio of convective heat transfer over conductive heat transfer. As was done on the Sherwood number in Eq. 1.83, Nu^* can be approximated, in the case of a flow around a single isolated spherical droplet, by the *Ranz-Marshall correlation* (Ranz and Marshall (1952)) given in Eq. 1.109. In the original Spalding model (Spalding (1953)), all the equations presented above were derived for an individual isolated and immobile droplet. The use of the Ranz-Marshall correlations for the Sherwood and Nusselt numbers allows to account for relative velocities between the gas and the droplets. In these expressions, when the relative velocity tends to zero, $\mathrm{Re}_p \to 0$ so that Nu^* and $\mathrm{Sh}^* \to 2$, which is the value used by Spalding (1953).
Abramzon and Sirignano (1989) proposed another amelioration of Spalding's model by replacing the Sherwood and Nusselt approximations by new expressions to account for the creation of a boundary layer around the droplet that influences the transfers:

$$\mathrm{Sh}^* = 2 + \frac{\mathrm{Sh}^*_{RM} - 2}{F(\mathrm{B_M})} \tag{1.110}$$

$$\mathrm{Nu}^* = 2 + \frac{\mathrm{Nu}^*_{RM} - 2}{F(\mathrm{B_T})} \tag{1.111}$$

where Sh^*_{RM} and Nu^*_{RM} are the values obtained from the Ranz-Marchall correlations and F is the generic function:

$$F(\mathrm{B}) = (1+\mathrm{B})^{0.7} \ \frac{\ln(1+\mathrm{B})}{\mathrm{B}} \tag{1.112}$$

To summarize, the exchange terms for a single isolated droplet are written:

$$\phi_g^{ev} = -\dot{m}_p h_{s,F}(T_\zeta) \tag{1.113}$$

$$\phi_l^{ev} = \dot{m}_p h_{s,p}(T_\zeta) \tag{1.114}$$

$$\phi_g^c = \pi d_l \ \mathrm{Nu}^* \ \lambda_g (T_\zeta - T_\infty) \frac{\ln(\mathrm{B_T}+1)}{\mathrm{B_T}} \tag{1.115}$$

$$\phi_l^c = -(\phi_g^c + \phi_l^{ev} + \phi_g^{ev}) \tag{1.116}$$

$$\text{with } \dot{m}_p = -\pi \ d_p \ \mathrm{Sh}^* \ [\rho D_F] \ \ln(1+\mathrm{B_M}) \tag{1.117}$$

Exchanges between the spray and the gas

The total mesoscopic heat exchanges between the spray and the gaseous phase, written Π_g and Π_l (see Sec. 1.3.4), are also divided into conductive contributions Φ_g and Φ_l and convective ones Λ_g and Λ_l, respectively from liquid to gas and gas to liquid. These exchanges correspond to the sum of all exchanges between individual droplets and the gas, and can be expressed using the average defined in Eq. 1.50:

$$\Lambda_g = \breve{n}_l\{\Phi_g^{ev}\}_l = \breve{n}_l\{-\dot{m}_p h_{s,F}(T_\zeta)\}_l \tag{1.118}$$

$$\Lambda_l = \breve{n}_l\{\Phi_l^{ev}\}_l = \breve{n}_l\{\dot{m}_p h_{s,p}(T_\zeta)\}_l \tag{1.119}$$

$$\Phi_g = \breve{n}_l\{\phi_g^c\}_c \tag{1.120}$$

$$\Phi_l = \breve{n}_l\{\phi_p^c\}_l \tag{1.121}$$

The global balance at the interface between the droplet and the gas in Eq. 1.92 is still valid for the interface between the spray and the gas, so the $\Pi_g + \Pi_l = 0$ (see Eq. 1.72).
The uniform temperature model gives $T_\zeta = T_p$. Additionally, hypothesis **H8** states that all particles located at position $\mathbf{x}$ and at instant t have the same temperature $\breve{T}_l$. Supposing that all these particles also have the same Nusselt number and using Eq. 1.80 for the expression of the mass transfer rate, the exchange terms can be written:

$$\Lambda_g = \Gamma h_{s,F}(\breve{T}_l) \tag{1.122}$$

$$\Lambda_l = -\Gamma \breve{h}_{s,l}(\breve{T}_l) \tag{1.123}$$

$$\Phi_g = \pi \breve{n}_l d_l \mathrm{Nu}^* \lambda \left(\breve{T}_l - T_\infty\right) \frac{\ln(\mathrm{B_T}+1)}{\mathrm{B_T}} \tag{1.124}$$

$$\Phi_l = -\left(\Lambda_g + \Lambda_l + \Phi_g\right) \tag{1.125}$$

$$\text{with } \Gamma = \pi\ \breve{n}_l\ \mathrm{Sh}^*\ [\rho D_F]\ \ln(1+\mathrm{B_M}) \tag{1.126}$$

1.3.5.4 Film properties

The diffusive transport coefficients $[\rho D_F]$ and λ used in Eqs. 1.124 and 1.126 were assumed to be independent of the radial coordinate r during the integrations of the expressions. This is not strictly true since they depend on the temperature, which varies from T_ζ at the surface to T_∞ at the far-field and on the local composition. These variations can be accounted for by using a reference, or *film*, mixture (of composition Y_k^{film}) at a reference temperature T^{film} to compute the coefficients. Hubbard et al. (1975) proposed the following expression, called the *1/3 law*, where the coefficient 1/3 was obtained to fit experimental data:

$$T^{film} = (1-\frac{1}{3})T_\zeta + \frac{1}{3}T_\infty \tag{1.127}$$

$$Y_k^{film} = (1-\frac{1}{3})Y_{k,\zeta} + \frac{1}{3}Y_{k,\infty} \tag{1.128}$$

The transport coefficients are then calculated using this reference state:

$$C_p^{film} = \sum_k Y_k^{film} C_{p,k} \tag{1.129}$$

$$[\rho D_F] = \frac{\mu^{film}}{\mathrm{Sc}_F} \tag{1.130}$$

$$\lambda = \frac{\mu^{film} C_p^{film}}{\mathrm{Pr}} \tag{1.131}$$

with C_p^{film} the heat capacity of the reference mixture.
Finally, the computation of the film dynamic viscosity μ^{film} depends on the chosen evaporation model and is detailed in the next section.
The properties of this reference state are also called *film properties*.

1.3.5.5 Simplified and Complex evaporation models in AVBP

Two variations of the evaporation models are available in AVBP, a *simplified* version and a *complex* version, the difference being in the determination of the Prandtl number Pr and the fuel species Schmidt number Sc_F used in the computation of the exchange terms, in particular through Eqs. 1.130 and 1.131 and the computation of the film mixture viscosity μ^{film}
In the simplified model, constant values for Pr and Sc_F are given by the chemical scheme data files that were calculated in reactive conditions on the burnt gases at stoichiometry. These values were initially used for the reduced chemical scheme, and there is no reason why these values should predict the correct evaporation laws. In addition, the film mixture viscosity is computed with a power law and only depends on the film temperature:

$$\mu^{film} = \mu(t^{film}) = \mu_{ref} \left(\frac{T^{film}}{T_{ref}} \right)^b \tag{1.132}$$

where μ_{ref} and T_{ref} are the reference viscosity and temperature and b is the power law coefficient. All three values are constants that are given in the data files of the chemical mechanism.
Sanjosé (2009) compared in her PhD thesis the evaporation law predicted by Spalding's law and these simplified coefficients with a detailed transient evaluation of the transport and thermodynamic coefficients from a complete kinetic theory by Hirschfelder et al. (1954) using the solver CANTERA and showed that the models used for the properties of the gaseous phase have a large impact on the evaporation process and that the existing model in particular overestimated the evaporation times. However, this last method requires many evaluations by CANTERA routines, which greatly increases the computational cost and makes it unsuited for LES simulations.
As a compromise, Sierra (2012) proposed a new model, called *complex* model in AVBP, in which the Prandtl and Schmidt numbers used in the evaporation

model, here called Pr^{evap} and Sc^{evap} are estimated *a priori* from an evaporation calculation using detailed properties for the gas. Their transient evolution during the evaporation process is not taken into account, contrary to what was done in the study by Sanjosé (2009), but Sierra (2012) showed that this method allows to obtain better results than the simplified model without other increase in the CPU cost than the *a priori* estimation.
In addition, a more complex expression for the μ^{film} was introduced by Sierra (2012), in particular to account for the composition of the film mixture. The film mixture viscosity is computed using Wilke's formula (Bird et al. (1960)):

$$\mu^{film} = \sum_{i=1}^{N} \frac{X_i^{film}\mu_i^{film}}{\sum_{j=1}^{N} X_i^{film}\Phi_{ij}} \tag{1.133}$$

$$\text{with} \quad \Phi_{ij} = \frac{1}{\sqrt{8}}\left(1+\frac{W_i}{W_j}\right)^{-1/2}\left[1+\left(\frac{\mu_i^{film}}{\mu_j^{film}}\right)^{1/2}\times\left(\frac{W_j}{W_i}\right)^{1/4}\right]^2 \tag{1.134}$$

with N the number of species in the mixture, X_i^{film} the molar fraction of the i-th species in the film mixture, W_i its molar mass. The viscosity of species i in the film mixture μ_i^{film} is taken at $T = T^{film}$ and computed using the power law defined in Eq. 1.132: $\mu_i^{film} = \mu_i(T^{film})$.

1.3.6 Filtered equations for the liquid phase

As was done for the gaseous phase equations, the equations for the liquid phase are filtered so that they can be accurately solved by the LES solver. The filtered value of a liquid mesoscopic quantity $\breve{f}_l$, noted $\overline{\breve{f}_l}$, is defined as in Eq. 1.15:

$$\overline{\breve{f}_l}(\mathbf{x}) = \int \breve{f}_l(\mathbf{x}')G_\Delta(\mathbf{x}-\mathbf{x}')d\mathbf{x}' \tag{1.135}$$

The Favre filtering for liquid mesoscopic quantities, noted $\widehat{f}_l$, is similar to that of gaseous quantities (Eq. 1.16), replacing the gaseous density ρ by the dispersed phase mesoscopic density $\breve{\alpha}_l\rho_l$, where ρ_l is constant and can be simplified, so that:

$$\overline{\breve{\alpha}_l}\widehat{f}_l = \overline{\breve{\alpha}_l\breve{f}_l} \tag{1.136}$$

Similarly, for the droplet density $\breve{n}_l$, and neglecting the subgrid scale variations of the droplet diameter (which amounts to assume that the spray is spatially monodispersed at the subgrid scale and $\overline{d_l} \approx d_l$), one obtains:

$$\overline{\breve{n}_l\breve{f}_l} = \overline{\frac{6\breve{\alpha}_l}{\pi d_l^3}\breve{f}_l} = \frac{6}{\pi d_l^3}\overline{\alpha_l}\widehat{f}_l = \overline{n_l}\widehat{f}_l \tag{1.137}$$

The filtering procedures being only applied to mesoscopic quantities, the diacritic $\breve{}$ is omitted in the following to increase clarity.
As was mentioned previously, the uncorrelated motion is neglected in all the simulations carried out in the present work, so the corresponding flux terms in the transport equations are removed, as well as the equation for the uncorrelated motion $\delta\breve{\theta}_l$. The conservation equations for the dispersed phase (Eqs. 1.59 to 1.63) are filtered, thus giving the following system:

$$\frac{\partial}{\partial t}\overline{n_l} + \frac{\partial}{\partial x_j}\overline{n}_l\widehat{u}_{l,j} = 0 \tag{1.138}$$

$$\frac{\partial}{\partial t}\rho_l\overline{\alpha_l} + \frac{\partial}{\partial x_j}\rho_l\overline{\alpha_l}\widehat{u}_{l,j} = -\overline{\Gamma} \tag{1.139}$$

$$\frac{\partial}{\partial t}\rho_l\overline{\alpha_l}\widehat{u}_{l,i} + \frac{\partial}{\partial x_j}\rho_l\overline{\alpha_l}\widehat{u}_{l,i}\widehat{u}_{l,j} = \frac{\partial}{\partial x_j}\left(\overline{\tau}^t_{l,ij}\right) - \overline{\Gamma\breve{u}_{l,i}} + \overline{F}_{d,i} \tag{1.140}$$

$$\frac{\partial}{\partial t}\rho_l\overline{\alpha}_l\widehat{h}_{s,l} + \frac{\partial}{\partial x_j}\rho_l\overline{\alpha_l}\widehat{u}_{l,j}\widehat{h}_{s,l} = \overline{\Lambda_l} + \overline{\Phi_l} - \frac{\partial\overline{q}^t_{h,j}}{\partial x_j} \tag{1.141}$$

$\overline{\tau}^t_l$ is the subgrid scale stress tensor for the dispersed phase:

$$\overline{\tau}^t_{l,ij} = -\rho_l\overline{\alpha}_l\left(\widehat{u_{l,i}u_{l,j}} - \widehat{u}_{l,i}\widehat{u}_{l,j}\right) \tag{1.142}$$

$\overline{q}^t_{h,j}$ is the subgrid scale liquid sensible enthalpy flux:

$$\overline{q}^t_{h,j} = \rho_l\overline{\alpha_l}\left(\widehat{u_{l,j}h_{s,l}} - \widehat{u}_{l,i}\widehat{h}_{s,l}\right) \tag{1.143}$$

These two tensors, as well as the terms $\overline{\Gamma}$, $\overline{\Gamma\breve{u}_{l,i}}$, $\overline{F}_{d,i}$, $\overline{\Lambda_l}$ and $\overline{\Phi_l}$, are not known are require approximations and closure models that are presented in the next section.

1.3.7 Approximations and closure models for the LES of the dispersed phase

1.3.7.1 Closure models for the subgrid scale tensors

In the version of the AVBP solver that was used for the simulations (V7.0.1), the sensible enthalpy flux at the subgrid scale is neglected:

$$\overline{q}^t_{h,j} = 0 \tag{1.144}$$

The subgrid scale stress tensor for the liquid phase, $\overline{\tau}^t_l$, is modelled by Moreau et al. (2010) by analogy to the gaseous Reynolds stress tensor (Eq. 1.21). The deviatoric part is modelled using the compressible Smagorinsky model (Smagorinsky (1963)) and the isotropic part with the Yoshizawa model (Yoshizawa (1986)):

$$\overline{\tau}^t_{l,ij} = -\rho_l \overline{\alpha}_l \left(\widehat{u_{l,i} u_{l,j}} - \widehat{u}_{l,i} \widehat{u}_{l,j} \right) \tag{1.145}$$

$$\textit{model: } \overline{\tau}^t_{l,ij} = 2\rho_l \overline{\alpha_l} \nu_{l,t} \left(\widehat{S}_{l,ij} - \frac{1}{3} \widehat{S}_{l,kk} \delta_{ij} \right) + 2\rho_l \overline{\alpha_l} \kappa_{l,t} \widehat{S}_{l,ij} \delta_{ij} \tag{1.146}$$

$$\text{with: } \widehat{S}_{l,ij} = \frac{1}{2} \left(\frac{\partial \widehat{u}_{l,i}}{\partial x_j} + \frac{\partial \widehat{u}_{l,j}}{\partial x_i} \right) - \frac{1}{3} \frac{\partial \widehat{u}_{l,k}}{\partial x_k} \delta_{ij} \tag{1.147}$$

$$\textit{Smagorinsky model: } \nu_{l,t} = C_{S,l} \Delta^2 \sqrt{2 \widehat{S}_{l,ij} \widehat{S}_{l,ij}} \tag{1.148}$$

$$\textit{Yoshizawa model: } \kappa_{l,t} = 2 C_{Y,l} \Delta^2 \widehat{S}_{l,ij} \tag{1.149}$$

The models constants are fixed to *a priori* values (Moreau et al. (2010)): $C_{S,l} = 0.02$ and $C_{Y,l} = 0.012$.
In the considered simulations, the liquid n-heptane, being very volatile, is expected to only be present at the bottom of the chamber where the smallest cell sizes are found (between $\Delta x = 0.12$ mm and $\Delta x = 0.5$ mm. The unresolved part of the liquid velocity can therefore be supposed negligible before the resolved one. In consequence, and to be consistent with envisaged comparisons with simulations in the Lagrangian framework, for which no LES model is implemented in AVBP, the sub-grid scale stress tensor for the liquid phase is not taken into account.

1.3.7.2 Exchange source terms

During the filtering procedure, some unclosed terms appeared in the exchange terms between the phases. Supposing that no exchange occurs at the sub-grig scale, the approximations used to obtain the filtered values of the exchange terms are presented hereafter.
The filtered evaporation rate $\overline{\Gamma}$ is approximated by:

$$\overline{\Gamma} = -\overline{\pi \breve{n}_l d_l \mathrm{Sh}^* [\rho D_F] \ln(1 + \mathrm{B_M})} \tag{1.150}$$

$$\approx \pi \overline{n_l} d_l \overline{\mathrm{Sh}^*} \frac{\overline{\mu}}{\mathrm{Sc}_F} \ln(1 + \overline{\mathrm{B}}_\mathrm{M}) \tag{1.151}$$

$$\text{with } \overline{\mathrm{Sh}^*} \approx 2 + \frac{\overline{\mathrm{Sh}} - 2}{F(\overline{\mathrm{B}_\mathrm{M}})}, \ \overline{\mathrm{Sh}} \approx 2 + 0.55 \overline{\mathrm{Re}}_p^{1/2} \overline{\mathrm{Sc}_F}^{1/3} \tag{1.152}$$

$$\text{and } \overline{\mathrm{B}}_\mathrm{M} \approx \frac{Y_{F,\zeta}(\widehat{T}_l) - \widetilde{Y}_F}{1 - Y_{F,\zeta}(\widehat{T}_l)} \tag{1.153}$$

The momentum exchanges due to evaporation $\overline{\Gamma u_{l,i}}$ are therefore expressed:

$$\overline{\Gamma u_{l,i}} \approx \overline{\Gamma} \widehat{u}_{l,i} \tag{1.154}$$

The momentum variation due to the drag force $\overline{F}_d$ is:

$$\overline{F}_{d,i} = \overline{\frac{\rho_l \overline{\alpha_l}}{\tau_p}\left(u_i - \breve{u}_{l,i}\right)} \approx \frac{\rho_l \overline{\alpha_l}}{\overline{\tau}_p}\left(\widetilde{u}_i - \widehat{u}_{l,i}\right) \tag{1.155}$$

The sensible liquid enthalpy variation by evaporation $\overline{\Lambda}_l$ is:

$$\overline{\Lambda}_l = -\overline{\Gamma h_{s,l}} \approx \overline{\Gamma}\widehat{h}_{s,l} \tag{1.156}$$

Finally, the sensible liquid enthalpy variation by conduction $\overline{\Phi}_l$ can be expressed:

$$\overline{\Phi}_l = -\overline{\Lambda}_l - \overline{\Phi}_g - \overline{\Lambda}_g \tag{1.157}$$

$$\text{with } \overline{\Lambda}_g = \overline{\Gamma h_{s,F}} \tag{1.158}$$

$$\approx \overline{\Gamma} h_{s,F}(\widehat{T}_l) \tag{1.159}$$

$$\text{and } \overline{\Phi}_g = \overline{\pi \breve{n}_l d_l \mathrm{Nu}^* \lambda(\breve{T}_l - T_\infty)\frac{\ln(\mathrm{B_T}+1)}{\mathrm{B_T}}} \tag{1.160}$$

$$\approx \pi \overline{n}_l d_l \overline{\mathrm{Nu}}^* \lambda(\widehat{T}_l - \widetilde{T})\frac{\ln(\overline{\mathrm{B}}_\mathrm{T}+1)}{\overline{\mathrm{B}}_\mathrm{T}} \tag{1.161}$$

$$\overline{\mathrm{Nu}}^* = \overline{2 + \frac{\mathrm{Nu}-2}{F(\mathrm{B_T})}} \approx 2 + \frac{\overline{\mathrm{Nu}}-2}{F(\overline{\mathrm{B}}_\mathrm{T})} \tag{1.162}$$

$$\overline{\mathrm{Nu}} = \overline{2 + 0.55\mathrm{Re}_p^{1/2}\mathrm{Pr}^{1/3}} \approx 2 + 0.55\overline{\mathrm{Re}}_p^{1/2}\overline{\mathrm{Pr}}^{1/3} \tag{1.163}$$

$$\overline{\mathrm{B}}_\mathrm{T} = \overline{(1+\mathrm{B_M})^{\frac{1}{\mathrm{Le}_F}}} \approx (1+\overline{\mathrm{B}}_\mathrm{M})^{\frac{1}{\overline{\mathrm{Le}}_F}} \tag{1.164}$$

1.3.8 Thermodynamic properties for the liquid phase in AVBP

As for the gaseous phase (see Sec. 1.2.5), the reference state for the liquid phase is $P_{ref} = 1$ atm and $T_{ref} = 0$ K. Some properties for the liquid phase are stored in the data files, such as the liquid density ρ_l, which is assumed constant and the critical temperature T_{crit}.
Additionally, the latent heat of vaporisation $L_v(T)$ of the liquid species and the saturated vapour pressure $P_{sat}(T)$ are stored from 0 K to the species critical temperature, every 10 K, calculated using Eq. 1.89 .
The pressure at the surface of the droplets is then retrieved by interpolation from the table of $P(T)$, in order to compute the mass transfer rate, as shown in Sec. 1.3.5.2.
The latent heat of vaporisation is mainly used in the evaporation models and to compute a table of the liquid sensible enthalpy $h_{s,l}(T)$. For each value of $T_i = i \times 10$ with $i \in [0, T_{crit}/10]$:

$$h_{s,l}(T_i) = h_s(T_i) - L_v(T_i) \tag{1.165}$$

with h_s the gaseous sensible enthalpy. The $h_{s,l}$ table is mainly used in AVBP to retrieve the local liquid temperature T_l from the transported value of the liquid sensible enthalpy $\widehat{h}_{s,l}(T_l)$.

1.4 Turbulent combustion modelling

The modelling of combustion is a difficult task because of the complexity of the phenomena at stake. Indeed, a combustion process involves a large range of chemical timescales and lengths that are not compatible with the cost reduction objectives of LES. This complexity is increased with that of the reactants, in particular when dealing with heavy or multi-component fuels as can be encountered in industrial applications.
The typical size of a LES grid cell ranges between 0.1 and a few mm, while the reactive thickness of a flame front is of the order of magnitude of the tenth of millimetre at atmospheric pressure, and can be even smaller when considering some intermediate species. It is therefore not possible to solve the flame front on the LES grid and some modelling has to be included.
Additionally, when combustion occurs in a turbulent flow, some coupling mechanisms take place that further complicate modelling. Indeed, the presence of a flame front generates flow accelerations that impact the turbulence. Conversely, the eddies that compose the turbulent field modify the flame front shape and structure, in particular by changing the flame wrinkling. The prediction of these interactions is essential for the accuracy of a reactive simulation.
Descriptions of the existing modelling approaches for the LES of premixed and non-premixed combustion can be found in Poinsot and Veynante (2012) and Fiorina et al. (2015). In the present study, the combustion is assumed to occur in the premixed regime, an hypothesis which is *a posteriori* verified. Two premixed combustion models were initially envisioned, the Thickened Flame model for LES (TFLES, presented in Sec. 1.4.1) and Filtered Tabulated Chemistry model for LES (FTACLES, presented in Sec. 1.4.2). Unfortunately, although it the compatibility between the two-phase equations and the FTACLES model had been implemented and validated in AVBP, it was not possible to carry out the reactive LES simulations on the studied configurations, and will be the focus of further studies. The modifications that were done in the code are still presented here for future use.

1.4.1 The thickened flame model for LES (TFLES)

The idea behind the thickened flame model (TF), which was first proposed by Butler and O'Rourke (1977), is that since the flame front is too thin to be resolved on a coarse grid, a thickening factor can be applied to the relevant quantities so as to obtain a thicker flame front that the grid is able to resolve. However, a critical aspect in the prospect of modelling propagating flames is that of their displacement speed. In particular, the thickening procedure must ensure that it does not modify the laminar flame speed.

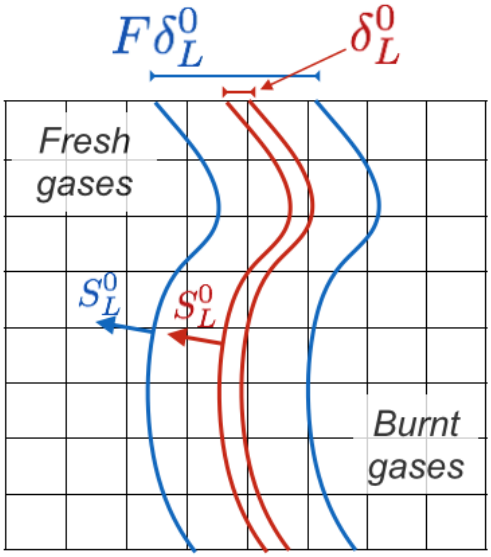

Figure 1.5: *Illustration of the thickening procedure applied to a flame front (in red) too thin for the grid, yielding a thickened flame front (in blue).*

1.4.1.1 Thickening model for a laminar flame

For a premixed laminar flame, Kuo (1986) states that the laminar flame speed S_L^0 and the laminar flame thickness δ_L^0 verify:

$$S_L^0 \propto \sqrt{D_{th}A} \qquad \text{and} \qquad \delta_L^0 \propto \frac{D_{th}}{S_L^0} = \sqrt{\frac{D_{th}}{A}} \tag{1.166}$$

where D_{th} is the thermal diffusivity and A the pre-exponential constant in the Arrhenius law for a single-step chemistry. It appears clearly that multiplying the diffusivity by a factor F while dividing the Arrhenius constant, and therefore the chemical source term, by the same factor increases the flame thickness while the laminar flame speed remains constant. The same procedure is applied on the species molecular diffusivities D_k and the corresponding source terms. The thickening procedure therefore modifies the following quantities:

$$D_{th} \longrightarrow FD_{th} \tag{1.167}$$
$$D_k \longrightarrow FD_k \tag{1.168}$$
$$\dot{\omega}_T \longrightarrow \dot{\omega}_T/F \tag{1.169}$$
$$\dot{\omega}_k \longrightarrow \dot{\omega}_k/F \tag{1.170}$$

As is illustrated in Fig. 1.5, the original laminar flame front, in red, of thickness δ_L^0, too small to be captured by the coarse grid, is thickened to $\delta_L^1 = F\delta_L^0$ by the thickening procedure, giving the blue front, which is now thick enough for the grid. The propagation speed, S_L^0, remains constant throughout the procedure.

The species mass fractions transport equation written in Eq. 1.3 becomes with the TF model:

$$\frac{\partial \rho Y_k}{\partial t} + \frac{\partial \rho Y_k u_i}{\partial x_i} = -\frac{\partial}{\partial x_i}(F J_{k,i}) + \frac{\dot{\omega}_k}{F} \tag{1.171}$$

$$\text{with } J_{k,i} = -\rho \left(D_k \frac{W_k}{W} \frac{\partial X_k}{\partial x_i} - Y_k V_i^c \right) \tag{1.172}$$

The same modification is applied to the energy equation.

1.4.1.2 Thickening model for LES

As was already mentioned, in a turbulent reactive flow, two-way interactions are present between the flame and the turbulent structures. In a TF simulation. the thickening of the reaction zone renders the flame front less sensitive to perturbations by the smaller vortices. The resulting flame is less wrinkled by turbulent motion, which reduces the flame surface and therefore the reactants consumption rate (Angelberger et al. (1998)), and obviously cannot be wrinkled at scales lower than the LES cut-off scale. To make up for this effect, Colin et al. (2000) proposed to introduce an efficiency function E in the transport equations to account for this loss of subgrid scale wrinkling. Equation 1.171 becomes:

$$\frac{\partial \overline{\rho} \widetilde{Y}_k}{\partial t} + \frac{\partial \overline{\rho} \widetilde{Y}_k \widetilde{u}_i}{\partial x_i} = -\frac{\partial}{\partial x_i}(E F \overline{J_{k,i}}) + \frac{E \overline{\dot{\omega}_k}}{F} \tag{1.173}$$

E corresponds to the ratio of the subgrid scale wrinkling of the non-thickened flame (of thickness δ_L^0) and that of the thickened flame (of thickness $\delta_L^1 = F\delta_L^0$). The total flame surface of a flame front A_{tot} can be decomposed into two contributions, the resolved surface A_{res} that is captured by the LES grid and the subgrid scale flame surface $A_{res} = A_{tot} - A_{res}$. The subgrid scale wrinkling of a flame front of thickness δ, noted $\Xi(\delta)$, is then defined as the ratio of the total flame surface and the resolved flame surface:

$$\Xi(\delta) = \frac{A_{tot}}{A_{res}} \tag{1.174}$$

In the flame thickened from δ_L^0 to δ_L^1, the predicted value for wrinkling of the flame front $\Xi(\delta_L^1)$ is therefore underestimated by the factor E:

$$E = \frac{\Xi(\delta_L^0)}{\Xi(\delta_L^1)} \tag{1.175}$$

The subgrid scale wrinkling is not known in the simulation and has to be modelled. Many expressions have been proposed and a detailed review can be found in Volpiani (2017).

The first expression for the subgrid scale wrinkling was proposed by Colin et al. (2000), assuming that the flame surface and the turbulence are at equilibrium at the subgrid scale level, as:

$$\Xi = 1 + \alpha \frac{\Delta_e}{S_L^0} \langle a_T \rangle_s \tag{1.176}$$

with $\langle a_T \rangle_s$ the subgrid scale strain rate, Δ_e the filter size and α a constant to be determined.
The subgrid scale strain rate $\langle a_T \rangle_s$ is found to depend on the filter size Δ_e, the subgrid scale turbulent velocity u'_{Δ_e} and the spectral efficiency function Γ, defined in Eq. 1.178 from fittings of DNS data:

$$\langle a_T \rangle_s = \Gamma \frac{u'_{\Delta_e}}{\Delta_e} \tag{1.177}$$

$$\Gamma\left(\frac{\Delta_e}{\delta_L^1}, \frac{u'_{\Delta_e}}{S_L^0}\right) = 0.75 \exp\left[-\frac{1.2}{\left(u'_{\Delta_e}/S_L^0\right)^{0.3}}\right]\left(\frac{\Delta_e}{\delta_L^1}\right)^{2/3} \tag{1.178}$$

The efficiency function E is then expressed:

$$E = \frac{\Xi(\delta_L^0)}{\Xi(\delta_L^1)} = \frac{1 + \alpha\Gamma\left(\frac{\Delta_e}{\delta_L^0}, \frac{u'_{\Delta_e}}{S_L^0}\right)\frac{u'_{\Delta_e}}{S_L^0}}{1 + \alpha\Gamma\left(\frac{\Delta_e}{\delta_L^1}, \frac{u'_{\Delta_e}}{S_L^0}\right)\frac{u'_{\Delta_e}}{S_L^0}} \tag{1.179}$$

As is shown in Colin et al. (2000), the function E varies between $E_{min} = 1$ (no correction required) and $E_{max} = \left(\frac{\delta_L^1}{\delta_L^0}\right)^{2/3} = F^{2/3}$. The filter size Δ_e is an input of the model and in typically chosen at $\Delta_e \simeq 10\Delta_x$ with $\Delta_x = \sqrt[3]{V_{cell}}$ the characteristic mesh size. For details on the determination of α and u'_{Δ_e}, the reader is invited to refer to Colin et al. (2000).

In the present work, the efficiency function is rather computed following Charlette et al. (2002), where the subgrid scale wrinkling is written:

$$\Xi\left(\frac{\Delta_e}{\delta_L^0}\right) = \left(1 + \min\left[\frac{\Delta}{\delta_L^0}, \Gamma\frac{u'_{\Delta}}{S_L^0}\right]\right)^{\beta} \tag{1.180}$$

with $\beta = 0.5$ a constant of the model, u'_{Δ} the subgrid scale turbulent velocity and $\Gamma\left(\frac{\Delta_e}{\delta_L^0}, \frac{u'_{\Delta_e}}{S_L^0}, Re_{\Delta_e}\right)$ the spectral efficiency function estimated in Charlette et al. (2002).
As is shown in Charlette et al. (2002), if the ratio $\Delta/\delta_L^1 = \Delta/F\delta_L^0 = 1$, as is the case in most applications, then the function $\Gamma\left(\frac{\Delta_e}{F\delta_L^0}\right)) = 0$ and $\Xi\left(\frac{\Delta_e}{F\delta_L^0}\right) = 1$. The authors therefore recommend the following expression for E:

$$E = \Xi\left(\frac{\Delta_e}{\delta_L^0}\right) = \left(1 + \min\left[\frac{\Delta_e}{\delta_L^0}, \Gamma\frac{u'_{\Delta_e}}{S_L^0}\right]\right)^{\beta} \tag{1.181}$$

1.4.1.3 Dynamic thickening

The thickened flame model was developed by Colin et al. (2000) for perfectly premixed cases. However, in the case of partially premixed configurations, when mixing between the reactants occur outside of the reaction zone, the species and thermal diffusion fluxes are overestimated by a factor F.
In order to extend the TF model to partially premixed and non-premixed configurations, the Dynamically Thickened Flame (DTF) model was proposed by Legier et al. (2000). A flame sensor S is introduced to detect the reaction zones and the TF model in only applied where the sensor is activated:

$$S = \tanh\left(\beta' \frac{\Omega}{\Omega_0}\right) \text{ with } \beta' = 50 \tag{1.182}$$

$$\Omega = Y_F^{\nu'_F} Y_O^{\nu'_O} \exp\left(-\Gamma_T \frac{E_a}{\mathcal{R}T}\right) \tag{1.183}$$

$$F = 1 + (F_{max} - 1)S \tag{1.184}$$

Γ_T is the parameter used to activate the thickening function before the reaction and a typical value is $\Gamma_T = 0.5$. Ω_0 is the maximum value of Ω in a laminar non-thickened 1D flame. ν'_F and ν'_O are the stoichiometric coefficients of the fuel and the oxidizer, respectively.
The simulated domain can be divided into three regions, the fresh gases, the burnt gases and the reaction zone. In the fresh and burnt gases, no combustion occurs, so the flame sensor is not activated and $S = 0$. In consequence, no thickening is applied, $F = 1$ and $E = 1$. In the reaction zone, the sensor is activated: $S = 1$. The thickening is applied so that $F = F_{max}$ and $E > 1$. The hyperbolic tangent in the expression of the sensor leads to a smooth transition between the reactive region and the fresh or burnt gases, so that F and E vary continuously.

In cases where flame fronts can encounter large panels of mesh sizes, a unique value for the filter size Δ_e may not be adapted if one wants to ensure reasonable levels of thickening. For instance, during the simulation of the light-round in MICCA-Spray, presented in chapter 3, a flame front propagates on the whole height of the chamber while the mesh grid is very fine at the bottom and around the liquid injection ($\Delta_x = 0.15$ mm to $\Delta_x = 0.5$ mm) and is progressively coarsened towards the top, up to $\Delta_x = 1$ mm. The local mesh size is accounted for through the variation of the maximum value of the thickening factor F_{max} depending on the local Δ_x and the user-specified number of points n that should be in the thickened flame front:

$$F_{max} = n \frac{\delta_L^0}{\Delta_x} \tag{1.185}$$

Typically, $n = 5$ is enough to capture the flame front and the gradients present within. This value was used on the reactive simulations of SICCA-Spray, but

stronger gradients appeared during the flame propagation in MICCA-Spray which made it necessary to use $n = 7$.

1.4.1.4 Dynamic thickening of a two-phase flame

In the case of a two-phase turbulent reactive flow, the liquid is not necessarily fully prevaporized before encountering a flame front, whether the residence time is not sufficient or a saturated state is reached. In order to preserve the local two-phase flame structure and dynamics, Boileau (2007) proposed a modified version of the dynamic thickened flame model, called TP-TFLES, in which the Damköhler number for evaporation, defined as the ratio between the evaporation characteristic time and the chemical one $Da_e = \tau_e/\tau_c$, is kept constant. If the chemical source terms are divided by the thickening factor F, the same must be done to the evaporation source terms.
As is explained in Boileau (2007), the sources term due to the drag force should also be divided by F, but this effect is supposed to be of second order and was not included in the equations. Moreover, the impact of the modification of the flame wrinkling and surface on the evaporation of the droplets is not clear and probably not linear. In the absence of more information, Boileau (2007) chose not to include any impact of the subgrid scale wrinkling on the evaporation and the efficiency function E is identical to that of the gaseous model.
To summarize, the TP-TFLES model modifies the exchange terms between the phases as follows:

$$\overline{\mathbf{s}}_{g-l}^{TP-TFLES} = \begin{pmatrix} 0 \\ -\overline{\Gamma}/F \\ -\overline{\Gamma}\widehat{u}_l/F + \overline{F}_{d,x} \\ -\overline{\Gamma}\widehat{v}_/F + \overline{F}_{d,y} \\ -\overline{\Gamma}\widehat{w}_l/F + \overline{F}_{d,z} \\ -\overline{\Lambda}_l/F + \overline{\Phi}_l/F \end{pmatrix} \tag{1.186}$$

$$\mathbf{s}_{l-g}^{TP-TFLES} = \begin{pmatrix} \overline{\Gamma}/F \\ \overline{\Gamma}\widehat{u}_l/F - \overline{F}_{d,x} \\ \overline{\Gamma}\widehat{v}_l/F - \overline{F}_{d,y} \\ \overline{\Gamma}\widehat{w}_l/F - \overline{F}_{d,z} \\ \overline{\Gamma}\delta_{k,F}/F \\ \overline{\Lambda}_g/F + \overline{\Phi}_g/F + \frac{1}{2}\widehat{u}_{l,i}\widehat{u}_{l,i}\overline{\Gamma}/F - \widehat{u}_{l,i}\overline{F}_{d,i} \end{pmatrix} \tag{1.187}$$

1.4.2 The filtered tabulated chemistry model for LES (F-TACLES)

Another approach for the numerical simulation of turbulent combustion is that proposed by the model FTACLES (Filtered Tabulated Chemistry for LES), developed by Fiorina et al. (2010) for premixed flames and Auzillon et al. (2012)

for stratified flames. The chemistry and transport properties are described with a tabulated chemistry approach, detailed in section 1.4.2.1, based on filtered flamelets, and interactions between combustion and turbulence are accounted for through additional terms in the table (see sections 1.4.2.2 and 1.4.2.3).

1.4.2.1 Principles of tabulated chemistry

The idea of tabulating laminar premixed flamelets in order to predict turbulent flames was first applied to premixed combustion by Bradley et al. (1988) and Abd Al-Masseeh et al. (1991) and to non-premixed combustion by Bradley et al. (1998).
Maas and Pope (1992a) and Maas and Pope (1992b), through the mathematical analysis of the chemical characteristic times, obtained in the phase space a low-dimensional manifold for a chosen set of conditions, called the ILDM method, for Intrinsic Low Dimensional Manifold. In short, the eigenvalues of a given complex chemical scheme are determined and the largest time scales are used to determine a reduced set of variables from which all the other quantities can be deduced through the construction of a look-up manifold. The authors showed that this method worked well for high temperature areas.
The model was later extended, in particular to lower temperature regions, by Gicquel et al. (2000), Fiorina et al. (2003), van Oijen et al. (2001) and Goey et al. (2003) in two similar approaches respectively called FPI (Flame prolongation of ILDM) and FGM (Flamelet Generated Manifold). In these models, a three-dimensional laminar or turbulent flame front is considered as composed of one-dimensional laminar premixed flames, so the look-up tables are generated from these one-dimensional flames, computed using detailed chemical mechanisms. A limited set of coordinates, such as the progress variable, the mixture fraction, the enthalpy,..., written $(\psi_1, ..., \psi_n)$ with n the dimension of the look-up table, is then used as coordinates for the tabulated values.
In LES simulations, instead of solving a transport equation for each of the N species present in the considered mixture and chemical mechanism (Eq. 1.3), n transport equations are solved for each of the look-up table coordinate and the other variables are then simply retrieved from the database. In the case of perfectly premixed combustion with adiabatic walls, the one-dimensional evolution of the variables perpendicularly to the three-dimensional flame front is assumed to be that of a unique laminar one-dimensional flamelet. In consequence, all the variables can be uniquely related to a progress variable c.
The definition of the progress variable may vary depending on the considered reactions and chemical scheme. The main constraint for the choice of its expression is that it must be monotonic through the laminar one-dimensional flame front, so that any function $\varphi^{tab}(c)$ is injective. In the present study, the progress variable is defined in Eq. 1.188 as proposed by Fiorina et al. (2003) and is normalised so that it varies between 0 in the unburnt gases and 1 in the burnt gases:

$$c = \frac{Y_{CO_2} + Y_{CO}}{Y^{eq}_{CO_2} + Y^{eq}_{CO}} \tag{1.188}$$

If the local mixing is not homogeneous, for instance in a two-phase mixture where the local evaporation of the droplets creates heterogeneities of the fuel mass fraction, it is necessary to additionally transport the mixture fraction z defined, for a n-heptane/air premixed flamelet at the equivalence ratio Φ, as:

$$z = \frac{1}{1 + s\frac{Y^{fuel}_{C_7H_{16}}}{\Phi \times Y^{air}_{O2}}} \quad \text{with} \quad \Phi = s\frac{Y^u_{C_7H_{16}}}{Y^u_{O_2}} \tag{1.189}$$

where s is the reaction stoichiometric coefficient ($s = 3.52$ for the reaction of n-heptane with air), Y^u_k is the kth-species mass fraction in the unburnt mixture, $Y^{fuel}_{C_7H_{16}}$ is the n-heptane mass fraction in the fuel mixture ($Y^{fuel}_{C_7H_{16}} = 1$ in the present study) and Y^{air}_{O2} is the oxygen mass fraction in air ($Y^{air}_{O2} = 0.233$).
At this point, the three-dimensional flame front is represented by the FGM/FPI model by a collection of one-dimensional premixed flamelets stored in a look-up table. At any point in the flame front, the knowledge of the values of c and z, which are transported, allows to retrieve the corresponding values of the tabulated quantities. The reaction rate of all species in all the reactions that compose the chosen chemical mechanism are predicted with no additional cost. In the context of LES simulation however, the issue raised with TFLES in introduction of section 1.4 remains valid: the LES grid is too coarse to be able to capture the flame front thickness and some modelling has to be introduced.

1.4.2.2 F-TACLES model

The F-TACLES model, for Filtered Tabulated Chemistry for LES, was developed by Vicquelin et al. (2009) and Fiorina et al. (2010) to apply the FGM/FPI methodology to LES simulation of turbulent and compressible reacting flows. The compressible aspect of the flow and the boundary conditions are treated with the TTC method (for Tabulated Thermo-chemistry for Compressible flows, developed by Vicquelin et al. (2011)). In the F-TACLES model (Fiorina et al. (2010)), the look-up table is generated using filtered 1D laminar flames with a filter of size Δ. Similarly to the thickening factor F for the TFLES model, a pertinent selection of the value of Δ allows to resolve the flame front on the LES grid (between 5 and 7 points in the flame front).
A new dimension Δ is therefore added to the look-up table, and the coordinate c is replaced by its filtered value $\widetilde{c}$.
Similarly to what was done to obtain the LES equations, the transport equation for the filtered progress variable writes:

$$\frac{\partial \overline{\rho}\widetilde{c}}{\partial t} + \frac{\partial}{\partial x_i}\left(\overline{\rho}\widetilde{u}_i\widetilde{c}\right) = \frac{\partial}{\partial x_i}\left(\overline{\rho D \frac{\partial c}{\partial x_i}}\right) - \frac{\partial}{\partial x_i}\left(\overline{\rho}\left(\widetilde{u_i c} - \widetilde{u}_i\widetilde{c}\right)\right) + \overline{\dot{\omega}_c} \tag{1.190}$$

The filtered reaction rate $\overline{\dot{\omega}_c} = \overline{\dot{\omega}_c}(\widetilde{c}, \Delta)$ is obtained from the tabulated reaction rate in the look-up table.
The diffusion flux term $\frac{\partial}{\partial x_i}\left(\overline{\rho D \frac{\partial c}{\partial x_i}}\right)$ is often approximated as:

$$\frac{\partial}{\partial x_i}\left(\overline{\rho D \frac{\partial c}{\partial x_i}}\right) \approx \frac{\partial}{\partial x_i}\left(\overline{\rho} D \frac{\partial \widetilde{c}}{\partial x_i}\right) \tag{1.191}$$

However, Fiorina et al. (2010) show that this approximation is only valid when the filter size Δ remains smaller than the flame thickness δ_L^0. When $\Delta > \delta_L^0$, large differences appear that impact in particular the prediction of the flame propagation speed. To make up for this problem, Fiorina et al. (2010) propose to use a correction factor $\alpha_c[\widetilde{c}, \Delta]$ such that:

$$\frac{\partial}{\partial x_i}\left(\overline{\rho D \frac{\partial c}{\partial x_i}}\right) \approx \frac{\partial}{\partial x_i}\left(\alpha_c[\widetilde{c}, \Delta] \overline{\rho} D \frac{\partial \widetilde{c}}{\partial x_i}\right) \tag{1.192}$$

where $\alpha_c[\widetilde{c}, \Delta]$ is stored in the look-up table and retrieved for the simulation.
The unclosed subgrid scale convection term $-\frac{\partial}{\partial x_i}\left(\overline{\rho}\left(\widetilde{u_i c} - \widetilde{u}_i \widetilde{c}\right)\right)$ can be expressed as:

$$\frac{\partial}{\partial x_i}\left(\overline{\rho}\left(\widetilde{u_i c} - \widetilde{u}_i \widetilde{c}\right)\right) = -\rho_0 S_L^0 \frac{\partial}{\partial x_i}(\overline{c} - \widetilde{c}) = \Omega_c[\widetilde{c}, \Delta] \tag{1.193}$$

The term is in practice treated as a source term and stored as such in the look-up table. Since it only depends on $\widetilde{c}$ and Δ, it can even be included in the tabulated value of the chemical source term $\overline{\dot{\omega}_c}$.
The same procedure is performed to the energy equation, leading to the tabulation of a correction factor $\alpha_E[\widetilde{c}, \Delta]$ and a convection source term $\Omega_E[\widetilde{c}, \Delta]$.
The F-TACLES model was later extended to stratified flames by Auzillon et al. (2012) and to non-adiabatic flames by Mercier et al. (2014). The modified expressions of the α and Ω coefficients can be found in the corresponding articles.

1.4.2.3 Interaction with turbulence

Similarly to the TFLES model, the thicker flame front is less susceptible to wrinkling by the turbulence. This loss of wrinkling leads to a loss of flame surface and therefore of the reactants consumption rate. Not accounting for the sugbrid scale wrinkling would lead to large errors in the turbulent flame front velocity (Poinsot and Veynante (2012)).
The transport equation for the filtered progress variable is hence modified as:

$$\begin{aligned}\frac{\partial \overline{\rho}\widetilde{c}}{\partial t} + \frac{\partial}{\partial x_i}\left(\overline{\rho}\widetilde{u}_i\widetilde{c}\right) = \frac{\partial}{\partial x_i}\left(\Xi\left(\frac{\Delta_e}{\delta_L^0}\right) \alpha_c[\widetilde{c}, z, \Delta]\overline{\rho} D \frac{\partial \widetilde{c}}{\partial x_i}\right) \\ + \Xi\left(\frac{\Delta_e}{\delta_L^0}\right) \overline{\dot{\Omega}_c}[\widetilde{c}, z, \Delta] + \Xi\left(\frac{\Delta_e}{\delta_L^0}\right) \overline{\dot{\omega}_c}[\widetilde{c}, z, \Delta]\end{aligned} \tag{1.194}$$

The subgrid scale flame wrinkling $\Xi\left(\frac{\Delta_e}{\delta_L^0}\right)$ is estimated using the model of Charlette et al. (2002) already described in section 1.4.1.2 and Eq. 1.180.

1.4.3 Adaptation of the coupling with the liquid phase for tabulated chemistry

In the solver AVBP, all the thermodynamic quantities are defined with a reference temperature $T^a_{ref} = 0$ K. In the multi-species environment (TFLES combustion model), the computation of the exchange terms is straightforward since both phases have the same reference temperature. However, when using the F-TACLES model, and more generally the TTC framework, the 1D flamelets used for the generation of the look-up table have been computed with a 1D solver (such as CHEMKIN, Cantera, FlameMaster,...) that uses a reference temperature $T^b_{ref} = 298$ K. A conversion is therefore necessary when computing the exchange terms between the phases since they no longer have the same reference temperature.
Additionally, sensible quantities are considered in the energy equations for the liquid phase and gaseous phase in a multi-species simulation. In the TTC formalism, the total energy is transported for the gaseous phase and stored in the table, meaning that the exchange terms cannot be computed in the same manner in tabulated chemistry as in multi-species transport.
In the following, the upperscript ^{a} denotes quantities evaluated with a reference temperature $T^a_{ref} = 0$ K and ^{b} at $T^b_{ref} = 298$ K. The absence of upperscript means that the quantity in question does not depend on the reference temperature.

1.4.3.1 Summary of the exchange rates in the multi-species formulation in AVBP

The evaporation rate Γ and the energy transfer rates Φ and Λ, already detailed in sections 1.3.4, 1.3.5 and 1.3.7.2 for their filtered version, in a LES simulation where the gaseous species mass fractions are transported and where both gaseous and liquid phases are at the reference temperature $T^a_{ref} = 0$ K are written:

$$\Gamma^a = \pi\ \breve{n}_l\ \mathrm{Sh}^*\ [\rho D_F]\ \ln(1+\mathrm{B_M}) \tag{1.195}$$

$$\Lambda^a_g = \Gamma h^a_{s,F}(\breve{T}_l) \tag{1.196}$$

$$\Lambda^a_l = -\Gamma \breve{h}^a_{s,l}(\breve{T}_l) \tag{1.197}$$

$$\Phi^a_g = \pi \breve{n}_l d_l \mathrm{Nu}^* \lambda \left(\breve{T}_l - T_\infty\right) \frac{\ln(\mathrm{B_T}+1)}{\mathrm{B_T}} \tag{1.198}$$

$$\Phi^a_l = -\left(\Lambda^a_g + \Lambda^a_l + \Phi^a_g\right) \tag{1.199}$$

In the expressions of the evaporation rate (Eq. 1.195) and the energy transfer towards the gas by conduction (Eq. 1.198), no variable depends on the reference temperature, so that $\Gamma^a = \Gamma$ and $\Phi^a_g = \Phi_g$.
In a multi-species AVBP simulation, the sensible enthalpy of the gaseous fuel species $h^a_{s,F}(\breve{T}_l)$ used in Eq. 1.196 is retrieved from an interpolation in the

gaseous enthalpy table for the corresponding species, stored every 100 K (see Sec. 1.2.5). In TTC, the gaseous fuel sensible enthalpy at the liquid temperature cannot be easily retrieved. It is therefore convenient to replace $h^a_{s,F}(\breve{T}_l)$ by the equivalent expression using the species latent heat L_v:

$$h^a_{s,F}(\breve{T}_l) = \breve{h}^a_{s,l}(\breve{T}_l) + L_v(\breve{T}_l) \tag{1.200}$$

The advantage of the expression in Eq. 1.200 is that no stored gaseous thermodynamic data is used, making it compatible to both multi-species and tabulated chemistry frameworks. This expression was implemented in AVBP and used for the validation cases presented in Sec. 1.5.
The energy transfer towards the liquid by conduction can therefore be expressed as:

$$\Phi^a_l = -\left(\Phi_g + \Lambda^a_l + \Lambda^a_g\right) \tag{1.201}$$

$$= -\Phi_g - \Gamma\left[h^a_{s,F}(\breve{T}_l) - \breve{h}^a_{s,l}(\breve{T}_l)\right] \tag{1.202}$$

$$= -\Phi_g - \Gamma\left[\breve{h}^a_{s,l}(\breve{T}_l) + L_v(\breve{T}_l) - \breve{h}^a_{s,l}(\breve{T}_l)\right] \tag{1.203}$$

$$= -\Phi_g - \Gamma L_v(\breve{T}_l) \tag{1.204}$$

The latent heat does not depend on the reference temperature, so $\Phi^a_l = \Phi_l$ and the exchange source terms for the multi-species simulation are re-written in the more flexible form, which make it transparent for both TTC and multi-species formalisms:

$$\Gamma = \pi\ \breve{n}_l\ \mathrm{Sh}^*\ [\rho D_F]\ \ln(1 + \mathrm{B_M}) \tag{1.205}$$

$$\Lambda^a_g = \Gamma\left(h^a_{s,l}(\breve{T}_l) + L_v(\breve{T}_l)\right) \tag{1.206}$$

$$\Lambda^a_l = -\Gamma\breve{h}^a_{s,l}(\breve{T}_l) \tag{1.207}$$

$$\Phi_g = \pi\breve{n}_l d_l \mathrm{Nu}^*\lambda\left(\breve{T}_l - T_\infty\right)\frac{\ln(B_T + 1)}{\mathrm{B_T}} \tag{1.208}$$

$$\Phi_l = -\Phi_g - \Gamma L_v(\breve{T}_l) \tag{1.209}$$

1.4.3.2 Energy exchange terms by convection in the TTC framework

As mentioned previously, two difficulties arise when envisioning the use of tabulated chemistry in a two-phase flow simulation. First, the generated flamelets, and so all the stored thermodynamic variables, have a reference temperature $T^b_{ref} = 298$ K, which is different from that of the transported liquid phase $T^a_{ref} = 0$ K. This has to be taken into account during the computation of the exchange terms. Finally, the energy used in TTC for the gaseous phase is the *total* energy while the liquid transport equations are not modified between multi-species and TTC frameworks, meaning that the liquid *sensible* enthalpy is available, which means that the sources terms calculations have to be modified accordingly.

The modifications between the models are:

$$T^a_{ref} \longrightarrow T^b_{ref} \tag{1.210}$$

$$h^a_{s,F} \longrightarrow h^b_F \tag{1.211}$$

$$\Lambda^a_g = \Gamma h^a_{s,F}(\breve{T}_l) \longrightarrow \Lambda^b_{t,g} = \Gamma h^b_F(\breve{T}_l) \tag{1.212}$$

where h^b_F is the total enthalpy of the gaseous fuel species with a reference temperature $T^b_{ref} = 298$ K.

Similarly to the sensible gaseous fuel species enthalpy, the total enthalpy $h^b_F(\breve{T}_l)$ is not easily retrieved in the TTC framework since the liquid temperature is not necessarily equal to the gaseous temperature and $h^b_F(\breve{T}_l)$ cannot simply be read from the table. An alternative method to compute its value has to be found.

The difference between the total and sensible gaseous enthalpies is the standard enthalpy of formation $\Delta h^{0,b}_f$, as shown in Eq. 1.213, which is a constant that can be stored in the look-up table.

$$h^b_F(\breve{T}_l) = h^b_{s,F}(\breve{T}_l) + \Delta h^{0,b}_f \tag{1.213}$$

Moreover, the use of the definition of the sensible enthalpy allows to easily change the reference temperature:

$$\begin{aligned} h^b_{s,F}(\breve{T}_l) &= \int_{T^b_{ref}}^{\breve{T}_l} C_p(T)dT \\ &= \int_{T^b_{ref}}^{T^a_{ref}} C_p(T)dT + \int_{T^a_{ref}}^{\breve{T}_l} C_p(T)dT \\ &= h^b_{s,F}(T^a_{ref}) + h^a_{s,F}(\breve{T}_l) \end{aligned} \tag{1.214}$$

$h^b_{s,F}(T^a_{ref})$ is also a constant that only depends on T^a_{ref} and T^b_{ref} and can be stored in the look-up table.

Combining Eqns. 1.200, 1.213 and 1.214, the total enthalpy of the gaseous fuel species at $T^b_{ref} = 298$ K can finally be expressed as:

$$h^b_F(\breve{T}_l) = \breve{h}^a_{s,l}(\breve{T}_l) + L_v(\breve{T}_l) + h^b_{s,F}(T^a_{ref}) + \Delta h^{0,b}_f \tag{1.215}$$

For a two-phase simulation using the TTC framework for the gaseous phase, the exchange source terms are finally computed as such:

$$\Gamma = \pi\ \breve{n}_l\ \mathrm{Sh}^*\ [\rho D_F]\ \ln(1 + \mathrm{B_M}) \tag{1.216}$$

$$\Lambda^b_{t,g} = \Gamma \left(\breve{h}^a_{s,l}(\breve{T}_l) + L_v(\breve{T}_l) + h^b_{s,F}(T^a_{ref}) + \Delta h^{0,b}_f \right) \tag{1.217}$$

$$\Lambda^a_l = -\Gamma \breve{h}^a_{s,l}(\breve{T}_l) \tag{1.218}$$

$$\Phi_g = \pi \breve{n}_l d_l \mathrm{Nu}^* \lambda \left(\breve{T}_l - T_\infty \right) \frac{\ln(\mathrm{B_T} + 1)}{\mathrm{B_T}} \tag{1.219}$$

$$\Phi_l = -\Phi_g - \Gamma L_v(\breve{T}_l) \tag{1.220}$$

So that the total heat flux towards the gas Pi_g^b and towards the liquid Π_l^a are written:

$$\Pi_g^b = \Lambda_{t,g}^b + \Phi_g \tag{1.221}$$

$$= \Gamma \left(\breve{h}_{s,l}^a(\breve{T}_l) + L_v(\breve{T}_l) + h_{s,F}^b(T_{ref}^a) + \Delta h_f^{0,b} \right) + \Phi_g \tag{1.222}$$

$$\Pi_l^a = \Lambda_l^a + \Phi_l = -\Pi_g^b + \Gamma \left(h_{s,F}^b(T_{ref}^a) + \Delta h_f^{0,b} \right) \tag{1.223}$$

1.4.3.3 Computation of the film properties

In section 1.3.5.4 the film properties used to compute the transport coefficients $[\rho D_F]$ and λ were introduced. In the TTC framework, the species mass fraction are neither transported nor all stored in the look-up table, so the mass fractions in the film mixture cannot be computed through Eq. 1.128 directly.
Similarly to the gaseous enthalpies, an alternative expression is looked for in order to compute the film properties, and in particular C_p^{film}, which can be used in both multi-species and TTC frameworks.
As was already done in Eq. 1.86 of section 1.3.5.2, the film mixture can be seen as a mixture of the fuel species, of heat capacity $C_{p,fuel}$, and of a *pseudo-mixture* of all the other species, whose heat capacity is noted $C_{p,nF}$, with respective mass fractions Y_{fuel}^{film} and $\left(1 - Y_{fuel}^{film}\right)$, so that the film heat capacity is:

$$C_p^{film} = Y_{fuel}^{film} \times C_{p,fuel} + \left(1 - Y_{fuel}^{film}\right) \times C_{p,nF} \tag{1.224}$$

Since the evaporation process only impacts the composition through a source term for the mass fraction of fuel, the pseudo-mixture composed of all the species excepting the fuel is identical at the surface, in the film mixture, and at the infinity, so that at the far-field, $C_{p,nF}$ is the same as in the film mixture:

$$\begin{aligned} C_{p,\infty} &= \sum_{k=1}^{N} Y_k \times C_{p,k} \\ &= Y_{fuel} \times C_{p,fuel} + (1 - Y_{fuel}) \times C_{p,nF} \end{aligned} \tag{1.225}$$

with Y_{fuel} the fuel species gaseous mass fraction computed on the Eulerian grid. Combining Eqs. 1.224 and 1.225, the film heat capacity can be written as:

$$C_p^{film} = Y_{fuel} C_{p,fuel} + \frac{1 - Y_{fuel}^{film}}{1 - Y_{fuel}} \left(C_{p,\infty} - Y_{fuel} C_{p,fuel} \right) \tag{1.226}$$

In a multi-species simulation, the fuel mass fraction at the far-field Y_{fuel} is transported and therefore directly available. With tabulated chemistry, a progress variable is transported, so the only solution to obtain the fuel mass fraction is to store it in the look-up table and to retrieve it during the simulation:

$Y_{fuel} = Y_{fuel}^{tab}(\widetilde{c}, z, \Delta)$. The same expression can here be used for both multi-species and TTC simulations to compute the film heat capacity C_p^{film}.
While the new expression that was found for C_p^{film} in Eq. 1.226 that is strictly equivalent to the previous one in Eq. 1.129, it was not possible to do the same for the film viscosity μ^{film}. In the multi-species environment, μ^{film} depends on the film temperature and composition T^{film} and Y_k^{film} (the latter only in the *complex* model), as recommended in Bird et al. (1960) and detailed in sect 1.3.5.4. Since the gaseous mass fractions of all the species are not available in tabulated chemistry, nor is it possible to consider storing them in the look-up table, the choice was made to use the viscosity stored in the table $\mu^{film} = \mu^{tab}(\widetilde{c}, z, \Delta)$ in the TTC framework. Two sources of error are introduced at this point that would require a correction: the viscosity is no longer taken at the film conditions but at that of the surrounding gas, therefore at the far-field, and the temperature is that of the table and no longer that of the film.
In future works, a power law as in Eq. 1.132 could be used to account for temperature difference between the table and the liquid, as is done by Saghafian et al. (2015). The laminar viscosity could also be tabulated against the mixture fraction so that its value at the film composition could be retrieved.

Most of the modifications that have been done to the AVBP code to allow tabulated chemistry in a two-phase simulation should not impact the results of evaporation simulations. This is demonstrated in the next section where a series of test cases are carried out to compare the different models.

1.5 Validation of the evaporation model with tabulated chemistry

To validate the implementation of the coupling between the phases, several test cases have been carried out. This is done step by step to validate the different changes made to the evaporation law and previously detailed. The computation of the equilibrium state is first assessed in section 1.5.1 before validating the evaporation law on 0D cases in sections 1.5.2. All the simulations presented here were carried out using the Abramzon-Sirignano evaporation law (Abramzon and Sirignano (1989), see Sec. 1.3.5) and the *complex* model (see Sec. 1.3.5.5).
In order to validate the evaporation routine in TTC, the generation of the look-up table was first done using as much as possible data from the AVBP databases. In consequence, transport and thermodynamic data was computed and tabulated based on the AVBP mixture C7H16-AIR-2S_DP (Paulhiac (2015)), even though no chemistry is accounted for here. In particular, quantities such as enthalpy, entropy, and therefore heat capacities, are computed and tabulated following the AVBP thermodynamic description (see sections 1.2.5 for details).
A one-dimensional table with a coordinate z is created from the computation

of the mixing of air and n-heptane, with z varying from 0 (pure air) to 1 (pure n-heptane), with the solver AGATH.
AGATH is an in-house code that computes thermodynamics, transport and kinetics properties. It also solves several 0D and 1D sets of equations found in reactive flows: homogeneous reactors, detonations, premixed and non-premixed flamelets.

1.5.1 Equilibrium state

Initial values	Case 1: $\Delta T^{init} = 0$K	Case 2: $\Delta T^{init} = 50$K
T_g [K]	298 K	350 K
T_l [K]	298 K	300 K
d_l [μm]	15 μm	15 μm
n_l [m^{-3}]	5.656×10^{10} m^{-3}	5.656×10^{10} m^{-3}
$\alpha_l \rho_l$ [kg.m^{-3}]	6.8765×10^{-2} kg.m^{-3}	6.8765 kg.m^{-3}
$Y_{C_7H_{16}}$ [-]	0	0
Y_{O_2} [-]	0.233	0.233
Y_{N_2} [-]	0.767	0.767
$\rho_{tot} = \rho_g + \rho_l \alpha_l$	1.2486 kg.m^{-3}	1.07333 kg.m^{-3}
$\rho_{F,tot} = \rho_g Y_{C_7H_{16}} + \rho_l \alpha_l$	6.8765×10^{-2} kg.m^{-3}	6.8765×10^{-2} kg.m^{-3}

Table 1.1: *Summary of the initial conditions for the two equilibrium computation cases*

First of all, the ability of the code to predict the correct equilibrium state, possibly saturated or not, of a two-phase mixture is investigated. Three numerical set-ups are considered:

- A reference multi-species simulation is first performed, identified hereafter as *MS_ref*, with the pre-existing and validated version of the solver AVBP.
- A second multi-species simulation, identified as *MS_mod*, is carried out using the modified version of the code where all the adaptations for tabulated chemistry detailed previously have been implemented.
- A TTC simulation is finally carried out, using the table previously described.

The numerical set-up is identical for the three cases, the numerical scheme is TTGC, the domain is a square box composed of 10 elements in each direction with $\Delta x = 4.6 \times 10^{-6}$ mm and no-slip adiabatic wall boundary conditions on all the boundaries. The code actually simulates the transient evaporation of the liquid, but attention is here first focused on the final state, which only depends on the thermodynamic data and not on the evaporation law, in order to validate the changes made in sections 1.4.3.1 and 1.4.3.2.
In the complex evaporation model, the Prandtl and Schmidt numbers are respectively $\mathrm{Pr}^{evap} = 0.735$ and $\mathrm{Sc}_F^{evap} = 0.69$, computed using detailed properties

in AGATH for pure n-heptane at $T = 298$ K.
Two initial solutions are considered, first no temperature difference between the gas and the liquid is present ($T_g^{init} = T_l^{init} = 298$ K) and then a temperature difference of $\Delta T^{init} = 50$ K is introduced ($T_g^{init} = 350$ K and $T_l^{init} = 300$ K) to change the final equilibrium state. The initial data for the two cases is summarized in table 1.1. Both the gaseous and liquid phase are initially at rest $u = u_l = 0$ m.s^{-1}. The values of the total density $\rho_{tot} = \rho_g + \rho_l \alpha_l$ and the fuel density $\rho_{F,tot} = \rho_g Y_{C_7H_{16}} + \rho_l \alpha_l$ are also monitored to check mass conservation.

Results for Case 1: $\Delta T^{init} = 0$ K:

Equilibrium values	MS_ref	MS_mod	TTC
T_g [K]	275.31 K	275.31 K	275.31 K
T_l [K]	275.31 K	275.31 K	275.31 K
d_l [μm]	6.288 μm	6.288 μm	6.290 μm (0.045 %)
n_l [m^{-3}]	5.656×10^{10} m^{-3}	5.656×10^{10} m^{-3}	5.656×10^{10} m^{-3}
α_l [-]	7.361×10^{-6}	7.361×10^{-6}	7.371×10^{-6} (0.136 %)
$Y_{C_7H_{16}}$ [-]	0.051224	0.051224	0.051219 (0.010 %)
ρ_{tot}	1.2486 kg.m^{-3}	1.2486 kg.m^{-3}	1.2486 kg.m^{-3}
$\rho_{F,tot}$	0.068765 kg.m^{-3}	0.068765 kg.m^{-3}	0.068765 kg.m^{-3}

Table 1.2: *Equilibrium values predicted by AVBP for Case 1, where $\Delta T^{init} = 0$ K, for the MS_ref simulation (first column), the MS_mod simulation (second column) and the TTC simulation (last column). The error compared to the reference simulation is added in parentheses when it is greater than* 0.01 *%.*

Equilibrium values obtained in the simulation of case with $T_g^{init} = T_l^{init} = 298$ K are presented in Table 1.2 for the MS_ref simulation (first column), the MS_mod simulation (second column) and the TTC simulation (last column). The error compared to the reference simulation is added in parenthesis when it is greater than 0.01 %.
As was expected, no difference is observed between the two MS simulations, confirming that the new formulations that were introduced are strictly equivalent to the old ones. Both gaseous and liquid phases are at strictly identical states. In these cases, the evaporation is not complete and a saturated state is reached.
The table used for the TTC case is one-dimensional with the coordinate z varying from $z = 0$ in pure air and $z = 1$ in pure n-heptane, generated at a temperature $T^{tab} = 298$ K. Table 1.2 shows that the equilibrium temperatures are identical between the reference and the TTC case. A slight difference appears on the liquid volume fraction α_l, and therefore on the diameter d_l and the fuel mass fraction $Y_{C_7H_{16}}$, which come from the viscosity μ used in the exchange source terms that is tabulated at $T = T^{tab} = 298$ K in TTC and

computed at $T = T^{film}$ in the reference case. This effect is further evidenced in section 1.5.2 where the evaporation law is validated.
In all cases, the total density and that of the fuel species ρ_{tot} and $\rho_{F,tot}$ are identical to their initial values given in Tab. 1.1, which validates that the mass is conserved.

Results for Case 2: $\Delta T^{init} = 50$ K:

Equilibrium values	MS_ref	MS_mod	TTC
T_g [K]	315.71 K	315.71 K	315.71 K
T_l [K]	287.07 K	287.35 K	287.41 K (0.119 %)
d_l [μm]	1.00952 μm	1.00981 μm	1.009 μm
n_l [m^{-3}]	5.656×10^{10} m^{-3}	5.656×10^{10} m^{-3}	5.656×10^{10} m^{-3}
α_l [-]	3.047×10^{-8}	3.049×10^{-8}	3.047×10^{-8} (0.020 %)
$Y_{C_7H_{16}}$ [-]	0.06405	0.06405	0.06405
ρ_{tot}	1.073331 kg.m^{-3}	1.073331 kg.m^{-3}	1.073330 kg.m^{-3}
$\rho_{F,tot}$	0.068765 kg.m^{-3}	0.068765 kg.m^{-3}	0.068765 kg.m^{-3}

Table 1.3: *Equilibrium values predicted by AVBP for Case 2, where $\Delta T^{init} = 50$ K, for the MS_ref simulation (first column), the MS_mod simulation (second column) and the TTC simulation (last column). The error compared to the reference simulation is added in parentheses when it is greater than* 0.01 *%.*

In this second configuration, the initial gaseous temperature is increased so that the liquid is fully evaporated. To avoid numerical issues with the eulerian equations of the liquid, minimal values have been imposed on the liquid droplet diameter and number of particles at $d_l^{min} = 1.0$ μm and $n_l^{min} = 2.4 \times 10^8$ m^{-3}. In the absence of liquid velocity, the number of droplets is constant (see Eq. 1.138) and the minimum value is applied to d_l: the evaporation is stopped if the computed mass source term would lead to a diameter lower than its minimum value. The look-up table used for this simulation is generated using $T^{tab} = 350$ K.
For this case also, the two multi-species simulations MS_ref ans MS_mod yield the same equilibrium state, although slight differences can be seen on the liquid temperature (0.098% error), the droplet diameter (0.038% error) and the liquid volume fraction (0.06% error), which is a numerical effect of the clipping on the diameter, which does not necessarily exactly stop evaporation at the same diameter.
The TTC simulation gives results with a very small errors on some quantities compared to the reference case, that remain acceptable. In particular, accurate results are obtained even though the equilibrium gaseous temperature $T^{eq} = 315.17$ K is very different from the tabulated temperature $T^{tab} = 350$ K, at which μ is tabulated.

Finally, in these cases also, the total and fuel mass are conserved.

1.5.2 0D evaporation

In addition to the ability to predict the equilibrium state of a two-phase mixture, it is important to check that the evaporation law is well retrieved, meaning that the transient evolution of the different quantities should be correct. In a three-dimensional turbulent simulation with combustion, the flame may encounter droplets that have not reached an equilibrium with the surrounding gas yet, so the transient states should be captured. While, in the previous section, attention was focused on the final value, transient data is here observed for the same two cases. The obtention of accurate evaporation laws will validate the modifications introduced in Sec. 1.4.3.3.

Results for Case 1: $\Delta T^{init} = 0$ K:

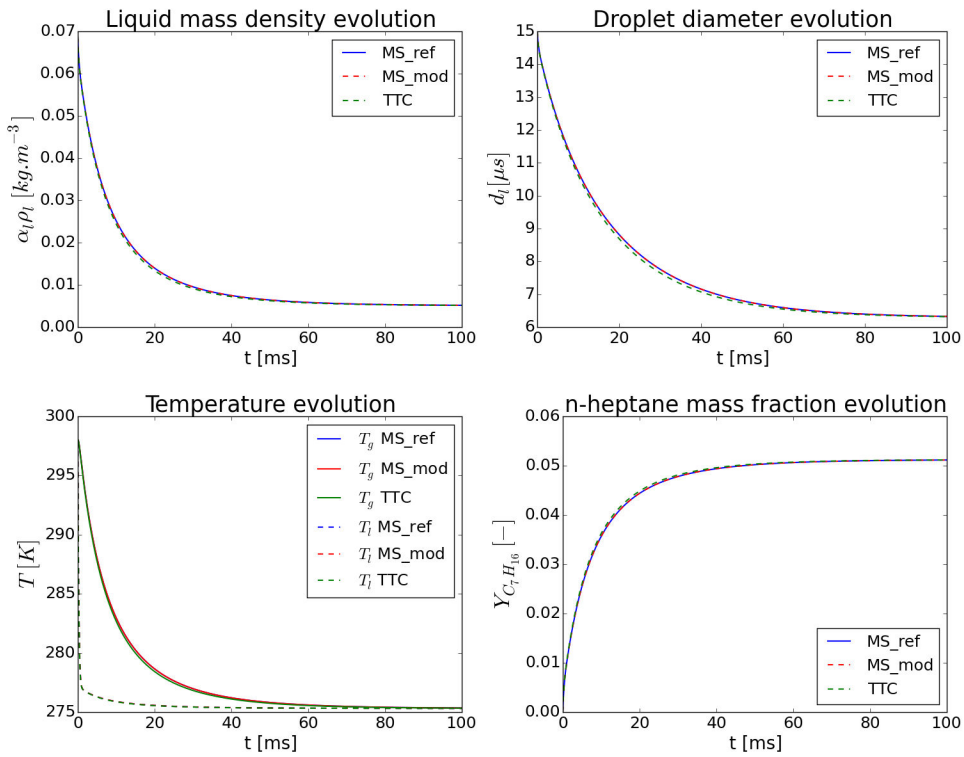

Figure 1.6: *Temporal evolution of the liquid mass density (top left), the droplet diameter (top right), gaseous and the liquid temperatures (bottom left) and the n-heptane mass fraction (bottom right) for cases MS_ref (blue), MS_mod (red) and TTC (green), for Case 1 where $\Delta T^{init} = 0$ K.*

Temporal evolutions are displayed in Fig. 1.6 for the liquid mass density (top left), the droplet diameter (top right), gaseous and the liquid temperatures

(bottom left) and the n-heptane mass fraction (bottom right), for all three considered numerical set-ups. As was observed on the equilibrium values, the two multi-species cases exhibit identical evaporation laws. This further validates the implementation of the modified coupling formulation between the phases previously detailed, which should not and do not change the code results.
Furthermore, the small discrepancy already observed on the TTC case due to the tabulation of the viscosity is also evident on the evaporation law. Since μ appears in the expression of the energy transfer (Eqs. 1.124 and 1.126), its variation have an influence in the gaseous temperature evolution (bottom left in Fig.1.6) and on the mass exchange rate, therefore the remaining liquid mass density $\alpha_l \rho_l$ and droplet diameter d_l (top plots in Fig.1.6).

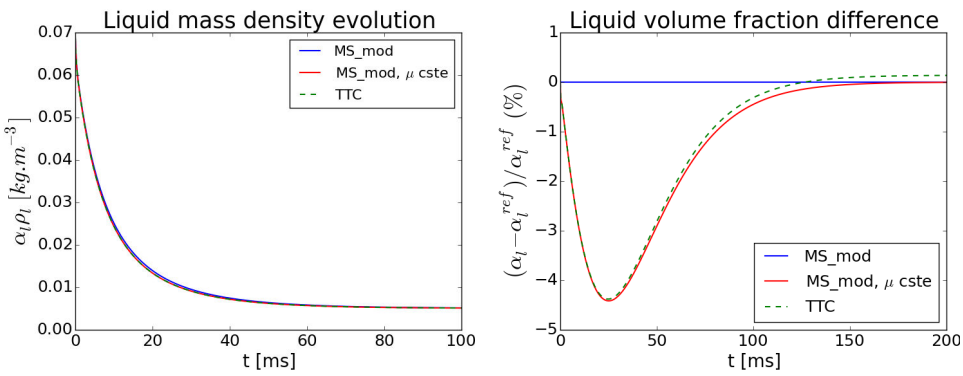

Figure 1.7: *Left: temporal evolution of the liquid mass density. Right: relative error on the volume fraction α_l for cases MS_ mod (blue), MS_ mod with constant viscosity (red) and TTC (green), compared to case MS_ ref, for Case 1 where $\Delta T^{init} = 0$ K.*

The origin of the observed differences is evidenced by a third multi-species simulation, in which the viscosity μ is artificially fixed at the value used in the TTC case. The results are plotted in Fig. 1.7. On the left is plotted the liquid volume fraction α_l evolution and on the right the evolution of its relative error for each case compared to the reference MS_ref. While initially, no difference was present on case MS_mod, the modification of the value of the viscosity leads to the multi-species case behaving like the TTC case. This confirms that the value of μ^{tab} is indeed responsible for the minor discrepancies observed in Fig. 1.6. The relative error does not exceed 5 %, which remains acceptable.

Results for Case 2: $\Delta T^{init} = 50$ K:

Similarly, Fig. 1.8 presents the evaporation law for Case 2, where $\Delta T^{init} = 50$ K. As expected, the two multi-species simulations give the same results, while the TTC simulation slightly overestimates the evaporation speed, leading to the droplet diameter decreasing faster than in the reference case. The discrepancy being small, the choice was made not to include any correction on the tabulated viscosity to account for differences between T^{tab} and T^{film}.

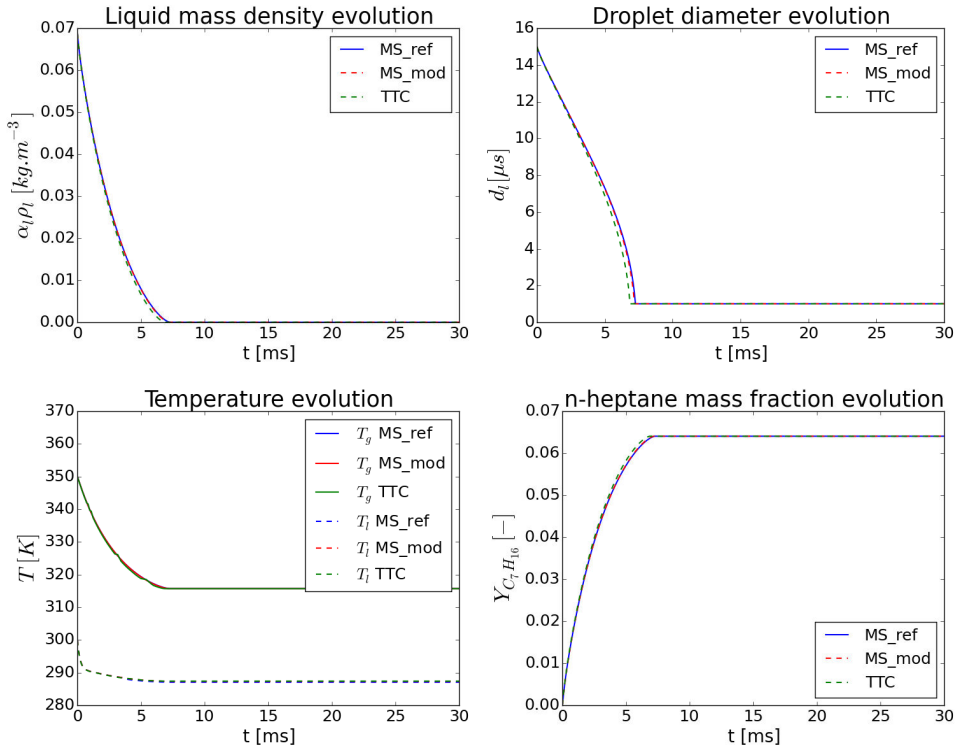

Figure 1.8: *Temporal evolution of the liquid mass density (top left), the droplet diameter (top right), gaseous and the liquid temperatures (bottom left) and the n-heptane mass fraction (bottom right) for cases MS_ref (bue), MS_mod (red) and TTC (green), for Case 2 where* $\Delta T^{init} = 50$ *K.*

1.5.3 Selection of a detailed chemical scheme

A considerable advantage of tabulated chemistry is that it allows the use of detailed chemical schemes with no additional computational cost. The previous validation cases were carried out using thermodynamic data extracted from a two-step mechanism containing 6 species in order to allow comparison and to highlight possible discrepancies between the multi-species and tabulated chemistry simulations.

The detailed mechanism that was chosen for the FTACLES simulations is the one proposed by Smallbone et al. (2009), and is composed of 65 species and 315 reactions, hereafter denoted USC2, and the corresponding evaporation cases TTC_USC2. Simulation of one-dimensional gaseous laminar flames have been carried out with the solver AGATH for this kinetic scheme as well as the two-step mechanism used for the TFLES simulations C7H16-AIR-2S_DP2, obtained by Paulhiac (2015).

The two mechanisms are compared in terms of laminar flame speed S_l^0 and adiabatic flame temperature T_{ad} with reference data extracted from Davis and

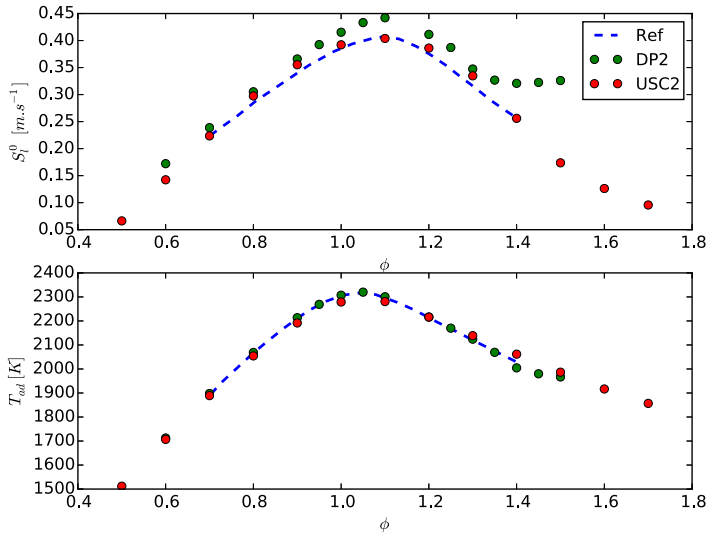

Figure 1.9: *Top: Laminar flame speed depending on the equivalence ratio for 1D gaseous flames for the kinetic scheme C7H16-AIR-2S_DP (from Paulhiac (2015)) in green dots and USC2 (from Smallbone et al. (2009)) in red dots, compared to reference data (blue dashed lines) extracted from Davis and Law (1998). Bottom: Adiabatic flame temperature depending on the equivalence ratio.*

Law (1998), for a range of equivalence ratios in Fig. 1.9. Both mechanisms exhibit good results on the adiabatic flame temperature, but the more detailed scheme USC2 is able to retrieve the correct laminar flame speed around the stoichiometry, where the two-step mechanism overestimates it. For very rich flames, only the USC2 scheme is able to capture the decrease in laminar flame speed.

The same evaporation test cases have been carried out to validate the ability of the chemical scheme to predict the evaporation of the droplets. Results are presented on Fig. 1.10, for $\Delta T^{init} = 0$ K at the top and $\Delta T^{init} = 50$ K at the bottom. Some slight differences are present on both cases that are due to the differences in the computation of the thermodynamic and transport coefficients. Overall, the two kinetic schemes predict evaporation behaviours that are in good agreement.

1.6 Conclusion

The objective of this chapter was to present the equations and models that are used in the following chapters. The equations of the large-eddy simulation of the gaseous phase as solved in the AVBP solver are first presented, along with the closure models selected for the present work's simulations. The dispersed

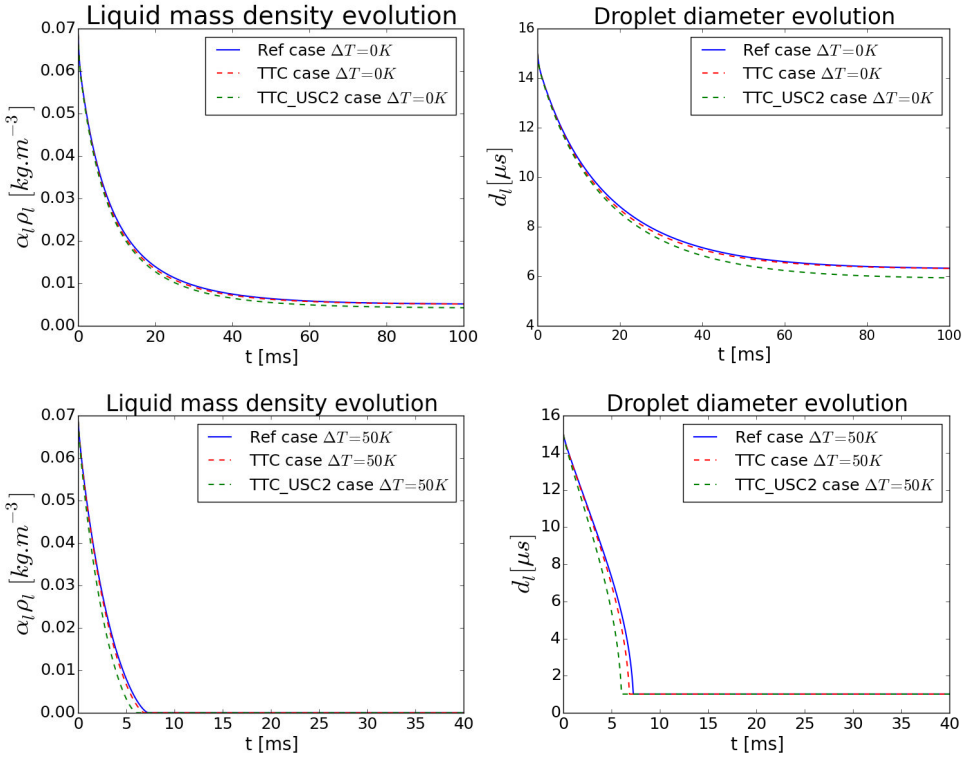

Figure 1.10: *Temporal evolution of the liquid mass density (left), the droplet diameter (right), for cases MS_ ref (blue), TTC (red) and TTC_ USC2 (green), for Case 1 where* $\Delta T^{init} = 0$ *K at the top and Case 2 where* $\Delta T^{init} = 50$ *K at the bottom.*

phase can be treated with two main approaches, the Lagrangian approach which is briefly presented and the Eulerian approach, used in this work and therefore detailed in this chapter. Closure models are required to obtain expressions for the exchange terms between the phases that are afterwards filtered using a filtering procedure that is similar to the one used on the gaseous equations.
In order to capture the flame evolution in the turbulent flow on the LES grid, a turbulent combustion models is necessary. The TFLES model proposes to artificially thicken the flame front so that it can cover enough mesh points. The F-TACLES model uses a different approach to describe the chemical mechanisms on the coarse LES grid. Based on tabulated chemistry for partially premixed flames, a set of one-dimensional flamelets are generated, filtered and tabulated in a look-up table that contains all the data necessary for the reactive simulations.
While the use of the multi-species environment with an evaporating dispersed phase was already available, some modifications to the AVBP code had to be made for the practical implementation of tabulated chemistry models (such as F-TACLES) for two-phase flows. These alterations have been detailed in

this chapter, as well as the relevant test cases that allowed to validate their implementation and the choice of kinetic scheme.

Chapter 2

Simulation of the steady-state regime of the single burner configuration SICCA-Spray

The present chapter deals with large-eddy simulations of the laboratory-scale two-phase burner SICCA-Spray, which represents one sixteenth of the annular chamber MICCA-Spray and is composed of one of the latter's injection units and a cylindrical transparent quartz chamber. The dispersed liquid spray is described with a mono-disperse Eulerian approach and the first comparisons with experimental data show the importance of the choice of the injected droplets diameter in this simplified framework. The impact of this key parameter upon the numerical results is carefully assessed through the use of uncertainty quantification tools and optimal values are obtained by the definition of relevant evaluation criteria. Finally, the reactive case is studied, with adiabatic and isothermal boundary conditions at the chamber walls, highlighting the impact of the heat losses on the flame shape in steady operating conditions. For all the studied configurations, comparisons with the available experimental data show a good agreement, thus validating the numerical set-up for simulations of the light-round sequence in MICCA-Spray, presented in chapter 3.

Contents

2.1 Introduction **78**
2.2 Experimental configuration **80**
2.2.1 Experimental set-ups: SICCA-Spray and MICCA-Spray 80
2.2.2 Imaging and instrumentation 81
2.3 Numerical set-up and geometry **83**
2.3.1 Computational domain and mesh 84
2.3.2 Numerical set-up and modelling 85
2.3.3 Boundary conditions 86
2.3.4 Numerical description of the liquid fuel injection . . 87
2.4 Simulation of the unconfined configuration **88**
2.4.1 Air flow simulation 89
2.4.2 Mesh convergence 91
2.4.3 Two-phase flow simulation 91
2.5 Selection of the injected droplet diameter **96**
2.5.1 Surface response generation 96
2.5.2 Selection of the polynomial order 99
2.5.3 Optimization of the injected diameter 100
2.5.4 Convergence 103
2.6 Simulation of the confined configuration **104**
2.6.1 Non-reactive flow 105
2.6.2 Reactive flow 109
2.6.3 Impact of the heat losses 116
2.6.4 Flame analysis 118
2.6.5 Flame lifting process 121
2.7 Influence of the injected diameter **124**
2.8 Conclusion **126**

2.1 Introduction

In the previous chapter, equations and models for the numerical simulation of two-phase reactive flows were presented. Before considering the study of the light-round in MICCA-Spray, it is interesting to assess and validate the different models available on a smaller configuration. Experimentally, the injector units used in MICCA-Spray have first been characterised on a single burner configuration called SICCA-Spray, fed with air and liquid n-heptane, which can be operated with and without the confinement provided by a cylindrical quartz wall. When installed, the wall creates a confinement that was chosen to be

similar to that seen by a flame in MICCA-Spray's annular chamber. From an experimental perspective, beyond the relative simplicity of SICCA-Spray, compared with MICCA-Spray, the study of the mono-burner presents the advantage to facilitate most optical diagnostics. In particular, measurement techniques based on laser sheets illuminating the spray or solid particles disseminated in the air tank can be used thanks to the central position of the spray, contrary to the complete annular chamber. The information obtained from such diagnostics on the aerodynamic behaviour of the gaseous and liquid phases can be used to validate the simulations and provide information regarding the accuracy of the numerical models.

The aim of the present chapter is to describe the process and the validation steps that led to the selection of a first numerical set-up for the simulation of the light-round in the annular chamber MICCA-Spray. Such validation process includes steps that range from the air flow simulation to simulations of the steady-state flame.

Envisioning such large scale simulations with liquid spray injection gives rise to several modelling issues. First of all, one is first faced with the problem of describing the spray atomization process. This cannot be included in such calculations and the dispersed liquid phase injected in the simulations needs to be modelled. This issue is considered in the present chapter. In addition, a compromise has to be found for the description of the polydisperse droplet mist to be consistent with the available computational resources. As motivated in the previous chapter, the choice was made to make use of an Eulerian-Eulerian approach for all the simulations carried out in the present thesis. While accounting for polydispersity in the Eulerian-Lagrangian framework is straightforward, the Eulerian-Eulerian approach requires additional transport equations for moments and/or classes of particle sizes (Massot (2007), Vié et al. (2013)), which strongly impact the computational cost. In order to find the best compromise between cost and accuracy, under constraints of limited computational resources, a specific method is proposed in section 2.5 to investigate the possible use of a monodisperse Eulerian-Eulerian representation of a polydisperse spray. An optimum value of the monodisperse injected droplets diameter that best represents the evolution of the spray is deduced by computing a surface response on monodisperse Eulerian simulations thanks to an uncertainty quantification (UQ) methodology. This optimal diameter is then used in the simulation of SICCA-Spray with combustion for the prediction of the stabilised flame. Finally, the impact of the heat losses at the quartz and the bottom of the chamber is investigated.

2.2 Experimental configuration

2.2.1 Experimental set-ups: SICCA-Spray and MICCA-Spray

The two configurations of the experimental burner SICCA-Spray are displayed in Fig. 2.1. In the unconfined configuration (left picture), no chamber is present at the exit of the swirler and the swirling spray is directly released in the atmosphere. The direct optical access to the air and droplets flow allows measurements of the velocity fields as well as the characterisation of the droplet mist. However, it is not possible to stabilize a flame in this case, so diagnostics are only performed on cold flows. When the confinement is added (right picture), in the form of a cylindrical quartz chamber, the achieved local equivalence ratio in the combustion chamber allows to sustain a flame.
The air injected in the system flows from a plenum through a swirl injector ("G" arrows on the sketch in Fig. 2.1) before meeting the n-heptane liquid injector, a simplex atomizer located with a 6 mm recess from the convergent exhaust ("L" arrows). The two-phase flow exits the swirler system through a diameter $d = 8$ mm with a measured swirl number $S = 0.68$, defined in Eq. 2.1, where R_{ref} is a characteristic radius, chosen as the radius at the exit of the swirler, $R_{ref} = 4$ mm. Both air and liquid are injected at ambient temperature.

$$S = \frac{1}{R_{ref}} \frac{\int_r u_x u_\theta r^2 dr}{\int_r u_x^2 r dr} \tag{2.1}$$

The studied operating conditions, chosen to match that of the first simulated operating point on MICCA-Spray, detailed in chapter 3, correspond to air mass flow rate 1.84 g/s and liquid n-heptane mass flow rate 0.11 g/s. The overall injected equivalence ratio is $\Phi = 0.9$.
To improve the atomization process, the liquid is supplied at a pressure of 9 bar. A tomographic slice of the droplet spray, visualized by means of an argon-ion laser at 514.5 nm, is displayed in Fig. 2.1. The hollow cone shape of the flow appears clearly, with an inner recirculation zone where few droplets are present. The droplet diameter repartition measured at one point located inside the spray (at the radius $r = 4.5$ mm from the injector centreline) and 2.5 mm above the exhaust plane is presented in Fig. 2.2 in the form of the spray's number density function. The number density function, of NDF, corresponds to the number of droplets that have a certain diameter compared to the total number of droplets in the spray. This allows to observe the level of polydispersity in spray: a monodisperse spray would have a NDF with a shape close to the Dirac function while a strongly polydisperse spray would present a flatter NDF. In the present case, the number density function spans from $d_l = 0.5$ μm to $d_l = 35$ μm, which shows that the spray is polydisperse, though moderately since the droplets diameter range remains narrow.
The mean diameter $D_{10} = (\sum_N d)/N$ and the Sauter Mean Diameter $D_{32} = (\sum_N d^3)/(\sum_N d^2)$ are indicated for the considered point ($r = 4.5$ mm, $z = 2.5$

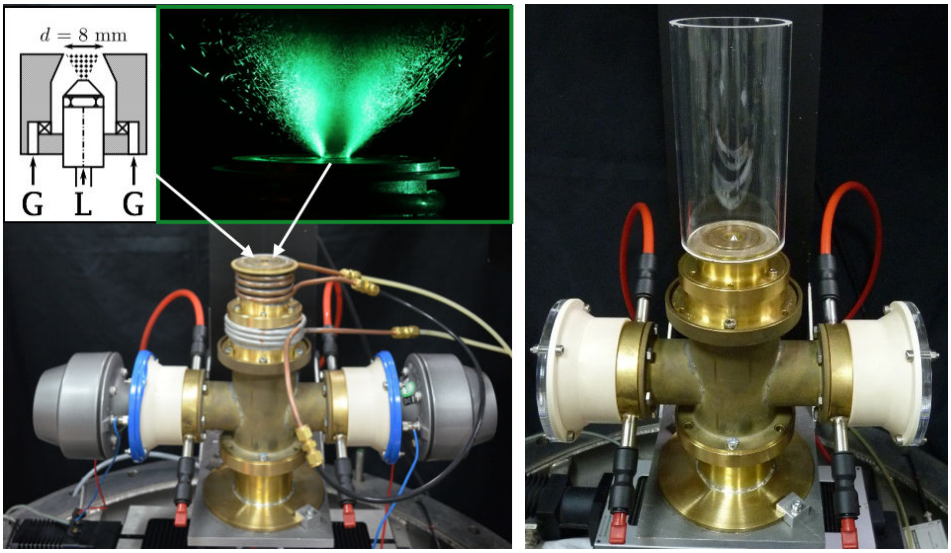

Figure 2.1: *Experimental burner SICCA-Spray. Left: photograph of the burner in the unconfined configuration, a sketch of the swirler appears in the top left-hand corner and a vertical tomography of the spray is shown in the top right-hand corner. Right: photograph of the burner with a confinement quartz with a diameter of 70 mm and a length of 150 mm.*

mm) in Fig. 2.2. With $D_{10} = 8.1\ \mu m$, the spray is mainly constituted of small droplets. In the perspective of combustion, the evaporation rate of the droplets constitutes an important property of the spray. This phenomenon for a polydisperse spray is determined by the spray repartitions in mass and surface (Lefebvre and Ballal (2010)). For reactive flow simulations, the mean droplet diameter (Riber et al. (2009); Sanjosé et al. (2011)) or the Sauter Mean Diameter (Cheneau B (2015)) can be considered as an equivalent mono-disperse spray simulation to represent a polydisperse spray.

2.2.2 Imaging and instrumentation

SICCA-Spray is equipped with a set of optical diagnostics that provide information on the aerodynamic flow and the reactive field. A brief summary of the methods that led to the experimental results used to validate the simulations is given here. The exhaustive list of all the available equipment present on SICCA-Spray can be found in Prieur (2017).
A Phase Doppler Anemometry system (PDA) is used to measure the velocity and diameter of particles present in the gaseous stream. When no liquid is injected, air velocities are measured by injecting small oil particles ($d_p < 2\ \mu$m) that behave as tracers of the flow. For a two-phase flow, the PDA measures the velocities and the diameter of each droplet crossing the measurement region and the gaseous fields are deduced by isolating the data from the smallest droplets.

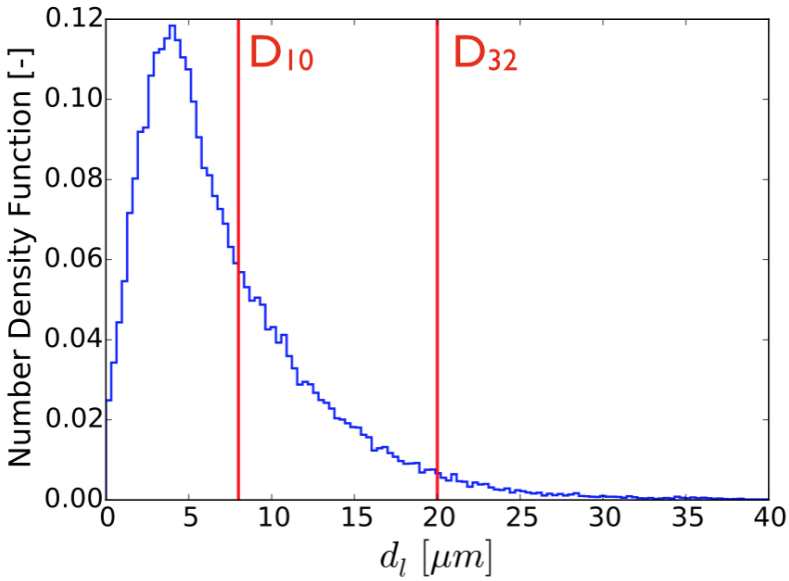

Figure 2.2: *Distribution of droplet diameter in the spray at $x = 2.5$ mm from the exhaust plane and $r = 4.5$ mm. The two vertical lines indicate the mean diameter D_{10} and the Sauter diameter D_{32}.*

Measurements were carried out at different distances from the injector exhaust plane on the unconfined configuration. With confinement, while velocity measurements are possible on the air with oil particles when the liquid injection is shut off, the presence of liquid droplets that do not evaporate completely before hitting the wall creates a film down the quartz walls that disrupts the laser beams and prevents measurements. As a consequence, in the confined configuration, velocities of the fully gaseous flow are the only data available for the cold flow.
The ignition sequence and the stabilised flame were observed by a high-speed camera equipped with a CH* filter for chemiluminescence. Gaseous velocities were measured in the confined configuration, with flame, through Particle Image Velocimetry (PIV) and the injection of solid particles in the air stream that do not burn and therefore give velocity information even in the flame front.
Finally, temperature measurements have been carried out by applying thermochromic paint on the inside of the walls and on the bottom of the chamber and exposing it to the flame for 5 min, an exposition time that is limited by the reaction of the paint to high temperatures. The external temperature of the walls is also measured by applying K-thermocouple on the quartz at several heights, after the chamber has reached thermal equilibrium. Temperature results are displayed in Fig. 2.3. Both profiles exhibit a maximum for the same height, at $x \approx 35$ mm, which corresponds to the height the flame impacts the wall in the experiment. It is worth mentioning that the thermochromic paint

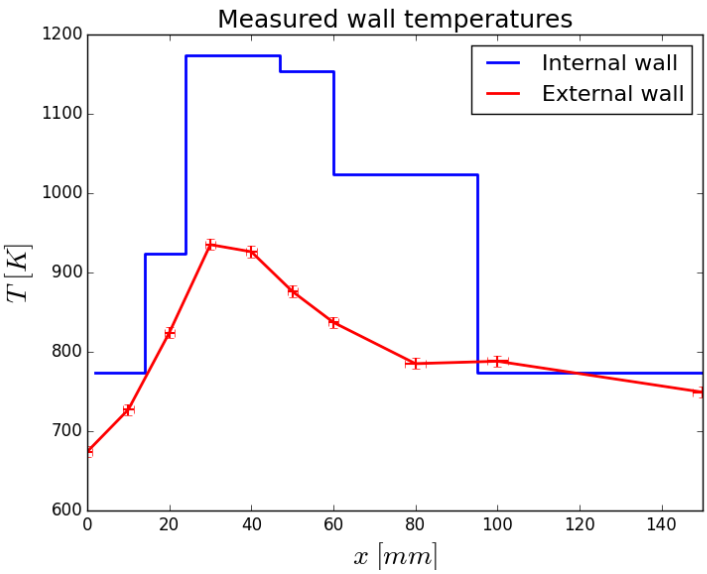

Figure 2.3: *Evolution of the internal (in blue) and external (in red) temperatures of the walls in SICCA-Spray, with combustion, plotted against the height.*

changes color when exposed to a certain local temperature. The paint that was used has a color scales that contains 14 irregular levels between 433 K and 1513 K. The color level taken by the paint can only increase, so that the color at the end of the exposition period corresponds to the maximum local temperature the quartz was exposed to and not to an average one. The color changes being quite sudden, the retained temperature is actually the minimum of the corresponding range. To summarize, if the color at a given point corresponds to the range $[T_i; T_{i+1}]$, that means that at at least one instant during the exposition period, this point was exposed to a temperature $T_{max} \in [T_i; T_{i+1}[$. Large uncertainties are associated to the measurement by thermochromic paint (blue curve), that are not reported on Fig. 2.3 for visibility reasons. Those associated to the thermocouple measurements, in red, are very small and are displayed on the red curve.

2.3 Numerical set-up and geometry

As already mentioned, the single burner configuration is used as a test case for the selection and the validation of the different models prior to the simulation of the full annular chamber. The numerical set-up presented in this section may therefore not be optimal for such a case as SICCA-Spray since the compromise between cost and accuracy is done with the simulation of full chamber in mind.

2.3.1 Computational domain and mesh

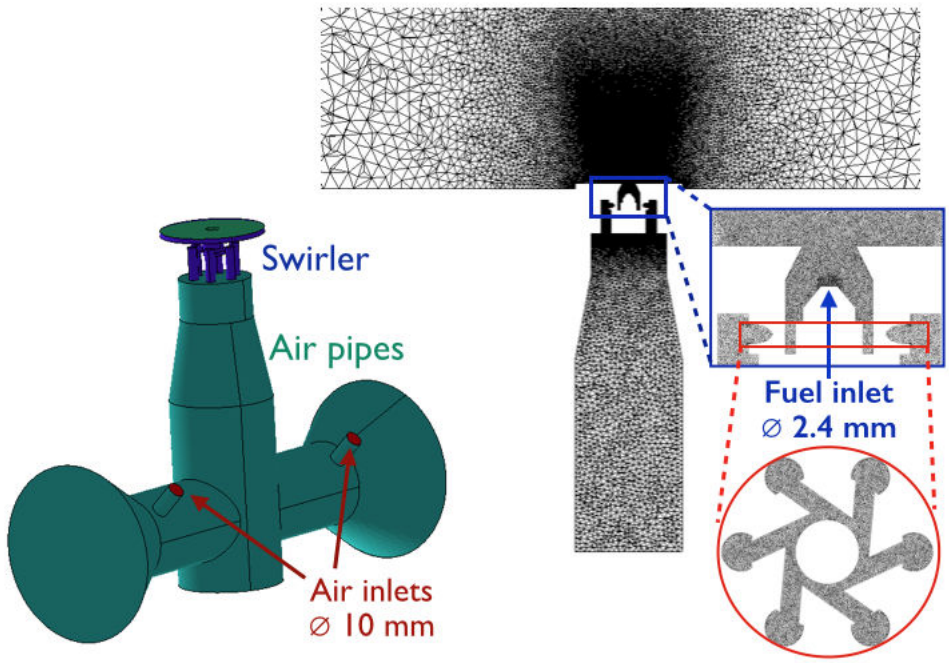

Figure 2.4: *Visualisation of the numerical domain (without the surrounding atmosphere) and the mesh around the swirler exhaust for the unconfined configuration. The atmosphere is visible on the mesh slice.*

Element and node counts	Unconfined	Confined
Number of nodes	3 Million	3.58 Million
Number of cells	17.5 Million	20.1 Million

Table 2.1: *Mesh characteristics for the SICCA-Spray*

Since SICCA-spray is operated experimentally in two configurations (unconfined and confined), two distinct computational domains have to be generated. These computational domains, respectively displayed in Figs. 2.4 and 2.5, are defined to be as close as possible to the experimental geometry. In both cases, the air plenum is included in its entirety and the air injection is done through two air guides with a 10 mm diameter. A large atmosphere is added (not shown in Fig. 2.5 but visible on the mesh slice in Fig. 2.4) around the exhaust plane. In the unconfined case, the swirling spray generated by the injection system is directly released into the atmosphere, which is placed around the exit platform. In the confined case, the atmosphere is added around the chamber exit. In both cases, an inlet is present in the atmosphere, with a relatively slow velocity of

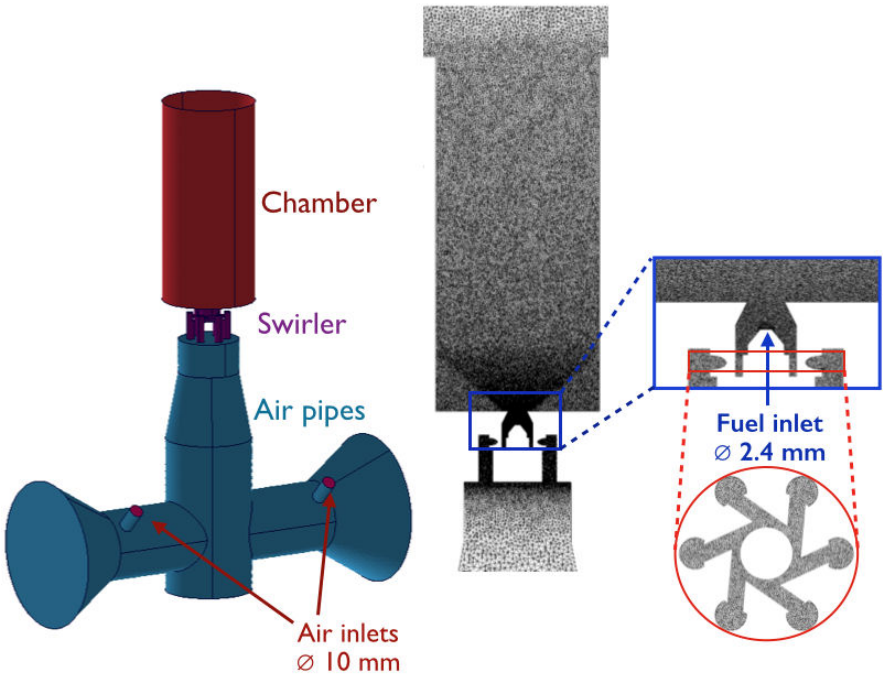

Figure 2.5: *Visualisation of the numerical domain (without the surrounding atmosphere) and the mesh around the swirler exhaust for the confined configuration.*

$u_n = 1$ m.s^{-1}, to mimic the air entrainment generated by the exhaust gases. The domain where the spray is observed experimentally is refined in order to capture its dynamics. The mesh is then progressively coarsened. In the chamber of the unconfined case, and in anticipation of a light-round sequence where a vertical flame front propagates in the chamber, the coarsening ratio between the bottom and the top of the chamber is limited to 2. The mesh and element sizes are summarized in Tabs. 2.1 and 2.2. The cell sizes are such that 10 nodes are present in the swirler tubes and 40 nodes in the swirler unit exit diameter.

2.3.2 Numerical set-up and modelling

The models and numerical tools used for the simulations presented hereafter were detailed in chapter 1. Both gaseous and liquid phases are described using the two-step Taylor-Galerkin weighted residual central distribution numerical scheme, TTGC (Colin and Rudgyard (2000)), third order in time and space. The subgrid scale turbulence of the gaseous phase is described using the Wall Adapting Local Eddy model (WALE) model (Nicoud and Ducros (1999)). As has been motivated in chapter 1, the liquid dispersed phase is represented using a mono-disperse Eulerian approach. The models used for the coupling between the liquid and the gaseous phase were presented in chapter 1.

Mesh region	Unconfined Δx	Confined Δx
Liquid injection	0.3 mm	0.13 mm
Swirler	0.3 mm	0.2 mm
Bottom of swirling spray	0.3 mm	0.2 mm
Top of swirling spray	0.7 mm	0.5 mm
Bottom of the chamber	-	0.5 mm
Top of the chamber	-	1 mm

Table 2.2: *Summary of cell sizes for the SICCA-Spray grids.*

As was explained in Sec. 1.3.5.5, two variations of the Abramzon and Sirignano (1989) evaporation model are available, the *simplified* model and the *complex* model. The simplified model was used for the simulations of the un-confined configuration of the mono-burner, as well as for the cold flow (pure air and with liquid) and the reactive simulations with the adiabatic walls of the confined configuration. After the first light-round simulation, which will be presented in chapter 3, the choice was made to switch to the complex evaporation model, which was used also for the simulations of SICCA-Spray with iso-thermal wall boundary conditions presented in Sec. 2.6.2.

2.3.3 Boundary conditions

Boundary condition	Physical parameters	Relax coefficients
Gaseous inlet	$\rho u_n = 14.1$ kg.s^{-1}.m^{-2} $T_g = 298$ K $Y_{O_2} = 0.233$; $Y_{N_2} = 0.767$	100000 s^{-1}
Liquid inlet	u_l, n_l from experimental profiles $T_l = 298$ K $d_l = 20$ μm or 15.3 μm	100000 s^{-1}
Atmosphere inlet	$u_x = 1$ m.s^{-1} $T_g = 298$ K $Y_{O_2} = 0.233$; $Y_{N_2} = 0.767$	100000 s^{-1}
Outlet	$P_{atm} = 101325$ Pa	800 s^{-1}
Walls	Wall law, adiabatic or isothermal	-

Table 2.3: *NSCBC conditions applied on the boundary for the unconfined and confined versions of SICCA-Spray, with and without combustion.*

The boundary conditions are standard Navier-Stokes characteristic boundary conditions (NSCBC, Poinsot and Lele (1992)) and are set according to the ex-

perimental parameters. A summary of the imposed conditions can be found in Tab. 2.3. On the gaseous inlets, ρu_n is fixed to impose the experimental mass flowrate. The injected gas and liquid temperatures are set to 298 K. In a first approximation, and in anticipation of the light-round simulations presented in chapter 3, all the walls are considered adiabatic. This gives satisfactory results for simulation without combustion (see sections 2.4 and 2.6), but, as shown in section 2.6.2, it fails to predict the correct steady flame shape in the confined configuration. The chamber walls conditions are replaced in Sec. 2.6.2 by isothermal conditions with the temperature profile measured in the experiment and displayed in Fig. 2.3.

2.3.4 Numerical description of the liquid fuel injection

Regarding the liquid spray, the choice of an Eulerian mono-disperse description makes it necessary to model the experimental poly-disperse distribution exiting the atomizer with a single value for the droplets diameter. The first simulations are carried out injecting the measured Sauter diameter from Fig. 2.2, $d_l^{inj} = D_{32} = 20\ \mu$m. A dedicated study, presented in Sec. 2.5 (also found in Lancien et al. (2016)), has then been carried out to select an optimal value for the injected diameter.

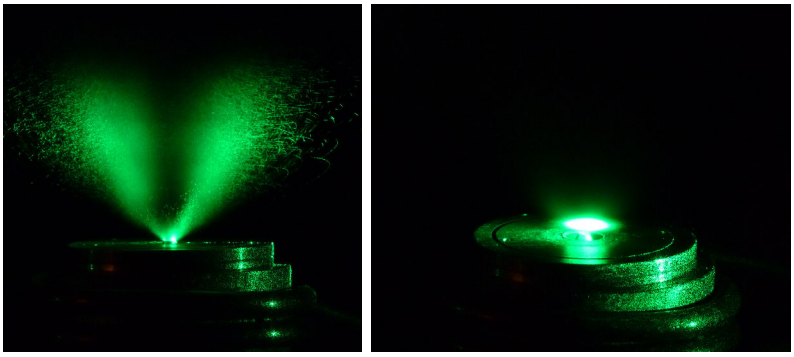

Figure 2.6: *Tomography of the spray created by the liquid atomizer flush with the exit plane, without any confinement. Left: vertical tomography with a laser sheet going through the injector centerline, right: horizontal tomography at $x = 2$ mm.*

The fuel injection device (see the insert on Fig. 2.1 for its position), was especially designed for MICCA-Spray in order to comply with global power limitations imposed by the burnt gases evacuation system. In consequence, the atomizer does not correspond to classical geometries for which models exist to represent the resulting swirling spray (see for instance the FIMUR model proposed by Sanjosé et al. (2011)) and no *a priori* profiles were available. Additionally, the 6 mm recess between the chamber bottom and the fuel injection makes it impossible to measure the liquid velocity profiles generated by the atomizer. It was however possible to adjust the axial position of the liquid

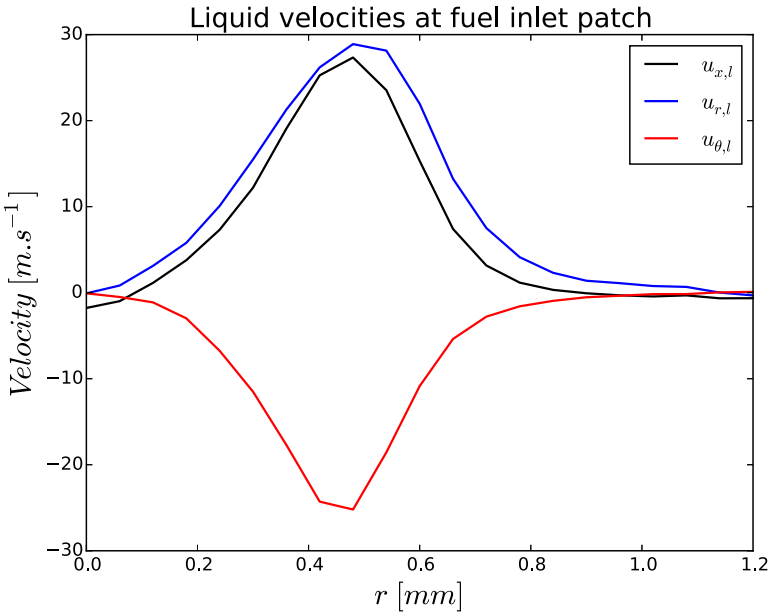

Figure 2.7: *Imposed velocity profiles on the fuel injection patch against the radius, fitted from experimental data.*

atomizer to make it flush with the chamber bottom plane, so that droplet velocity profiles could be measured as low as possible, which was at $x = 2$ mm. Vertical and horizontal tomographies of the spray generated in this case are displayed on Fig.2.6. The laser sheet, being reflected by the droplets, highlight the hollow cone structure of the spray. Very few droplets appear to be present in the central recirculation zone, which is quite intense and seems to go up to a few from the injection plane. The measured velocity profiles at $x = 2.5$ mm are then scaled to fit on the numerical injection patch of diameter $d_{inj,l} = 2.4$ mm. The axial, radial and tangential profiles imposed in the simulation are displayed on Fig. 2.7 against the radius, respectively in black, blue and red. The hollow cone structure is retrieved on the velocities, with the double peaks on the axial velocity and the clockwise rotating motion on the tangential component. In the center of the patch, slightly negative axial velocities are present due to the foot of the recirculation zone, which are clipped to zero in the simulation. The liquid flowrate is imposed through the droplet number density n_l, for which a double Gaussian profile is set.

2.4 Simulation of the unconfined configuration

The simulation is first carried out on the unconfined configuration by only injecting the air to establish the gaseous flow. Mean velocity fields are calculated and validated against experimental data. Fuel droplets are then injected in

the flow. It is worth noting that the gaseous solution used to initialize all the two-phase flow simulations with different values of the injected diameter is the same. Once the velocity fields are established, statistical mean fields are computed. Several consecutive average fields are compared to ensure statistical convergence of the velocity field. For both air and two-phase simulations of the un-confined configuration, the flow was found to be converged after 100 ms of physical time and the averages were computed over 50 ms.

2.4.1 Air flow simulation

Figure 2.8 presents an instantaneous (left) and average (right) field of the axial velocity for the simulation of the air flow, without any injection of liquid droplets. As could be expected, characteristics typical of a swirled flow are retrieved. Two high velocity peaks are present that mark the position of the swirled cone and an intense inner recirculation zone (IRZ) can be seen. This IRZ does not go very high above the injector, in particular compared to the IRZ in the cold flow of the confined configuration later presented in Sec. 2.6.1) but is very intense and goes upstream down to the fuel injector, where it is bound to interact with the fuel injection when it is activated. Since there is no confinement, the outer recirculation zone (ORZ) is quite weak, as can be seen on the average profile, where the negative velocity outside the jet is around 5 m.s^{-1}.

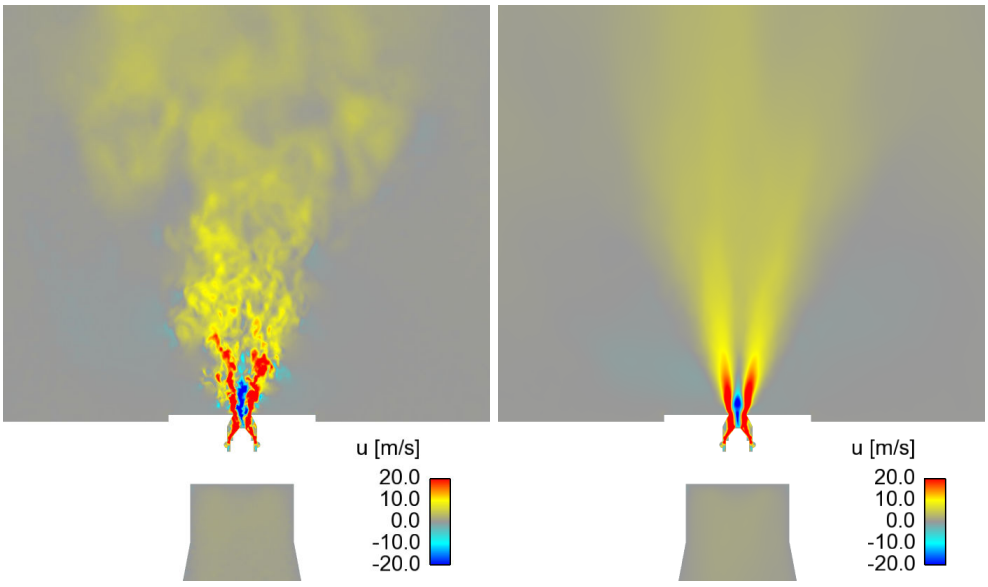

Figure 2.8: *Instantaneous (left) and average (right) fields of the axial velocity for the air flow simulation.*

Profiles of the axial, tangential and radial components of the mean and rms velocities of the gaseous flow at $x = 2.5$ mm are displayed in Fig. 2.9. The

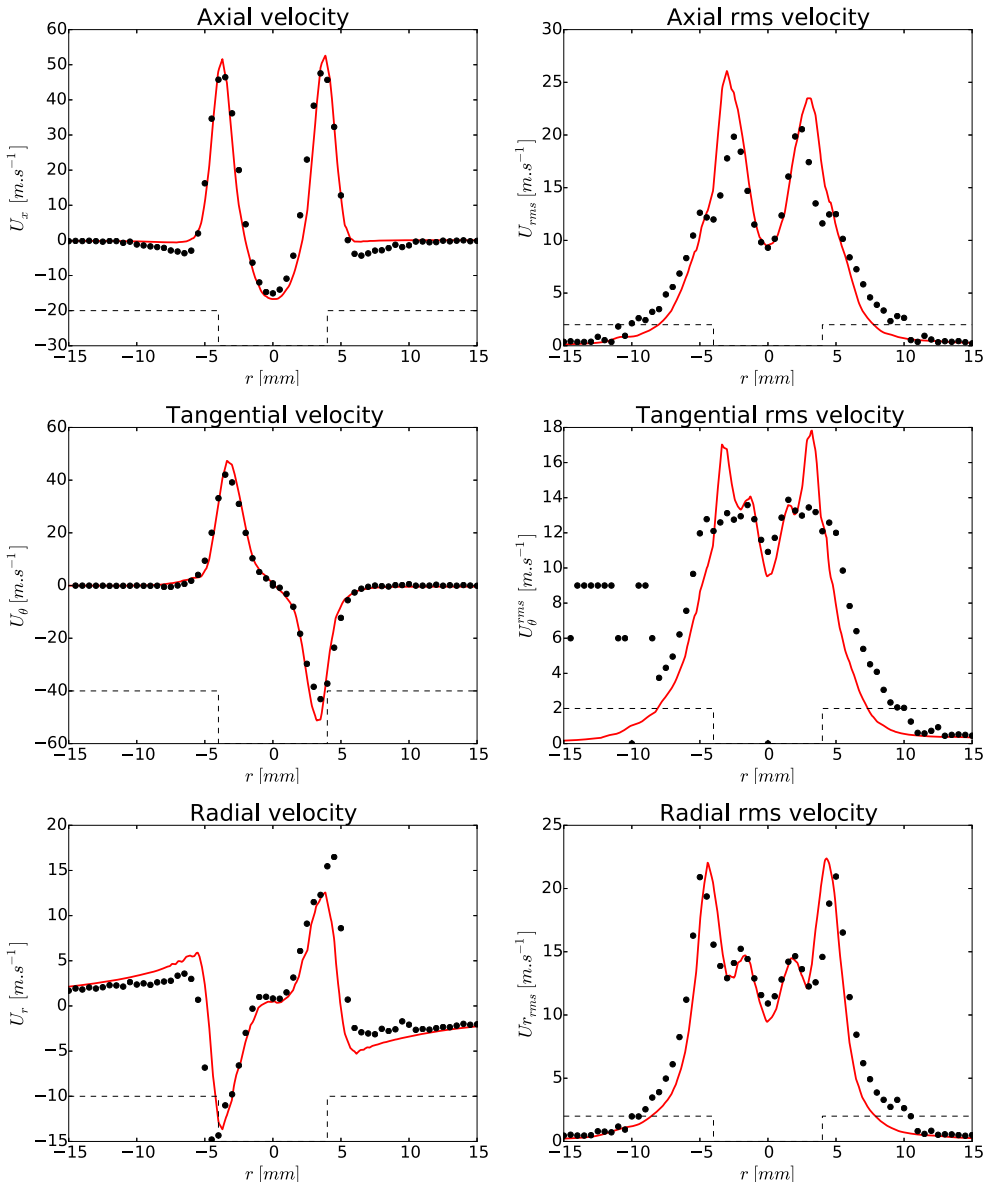

Figure 2.9: *Mean (left) and RMS (right) velocity profiles for the gas phase at $x = 2.5$ mm from the exhaust plane: axial (top), tangential (middle) and radial component (bottom). −: Numerical results from the gaseous simulation; • : Experimental data. The radial position of the swirler exit hole is represented by the black dashed lines.*

symbols represent the experimental data and the full lines show the numerical results.

The radial position of the swirler exit disk is represented as black dashed lines. Excellent agreement is achieved on the mean profiles. In particular, the simulation retrieves the width and intensity of the central recirculation zone (CRZ),

typical of a swirled flow. The radial position of the swirled cone is also very well captured. Finally, the intensities of the different components of the velocity are accurately predicted. In addition, the turbulence intensities are in agreement between simulation and experiment, which further validates the numerical set-up for the gaseous phase. In particular, the double peaks that appear on the radial and tangential rms velocities due to the presence of shear layers are retrieved.

2.4.2 Mesh convergence

In order to ensure that the different computed numerical fields are mesh-independent, it is necessary to focus on the convergence of the mesh. To do so, the gaseous flow was converged for three different refinements, hereafter designated as *Scale 1.5*, *Scale 1* and *Scale 0.75*. Scale 1 is the refinement used to obtain the previously presented results. The notion of *scale* corresponds to the multiplying factor applied to the requested cell sizes in the mesh generator. The number of cells and of nodes obtained for the different scaling factors are therefore not proportional. The mesh *scale 1.5* is therefore composed of 3.86 million cells and 687000 nodes while the mesh *scale 0.75* comprises 32.1 million cells and 5.59 million nodes, to be compared with the *scale 1* mesh, already presented in Sec. 2.3.1, composed of 17.5 million cells ans 3 million nodes.
The profiles for the radial and axial components of the mean velocity and the rms velocity are shown in Fig. 2.10. While some evolution is present between the scales 1.5 and 1 on both mean and rms profiles, similar results are achieved between scales 1 and 0.75. Two main conclusions can be drawn from these observations, (1) refining the scale 1 mesh does not lead to any improvement of the results and only increases the computational cost, (2) coarsening it decreases the results quality. The scale 1 mesh therefore appears to be the best compromise between computational cost and accuracy, and is therefore validated for further simulations.

2.4.3 Two-phase flow simulation

Once the numerical set-up has been validated for the gaseous flow, the liquid phase is added to the simulation. The results presented in this section come from the simulation in which $d_l^{inj} = 20$ μm. In the experiment, the liquid droplets velocities and diameter have been measured at each point and can be compared to the numerical results. In order to get an estimation of the gaseous velocities in the spray, the smallest droplets ($d_l = 2$ to 5 μm) are assumed to behave as tracers of the flow. The average velocity of these droplets at any point therefore corresponds to the local gaseous velocity.
The gaseous velocity profiles at $x = 2.5$ mm and $x = 7.5$ mm are displayed on Fig. 2.11. At each height, the profiles were averaged over the tangential coordinate. The black curves represent data from the purely gaseous simu-

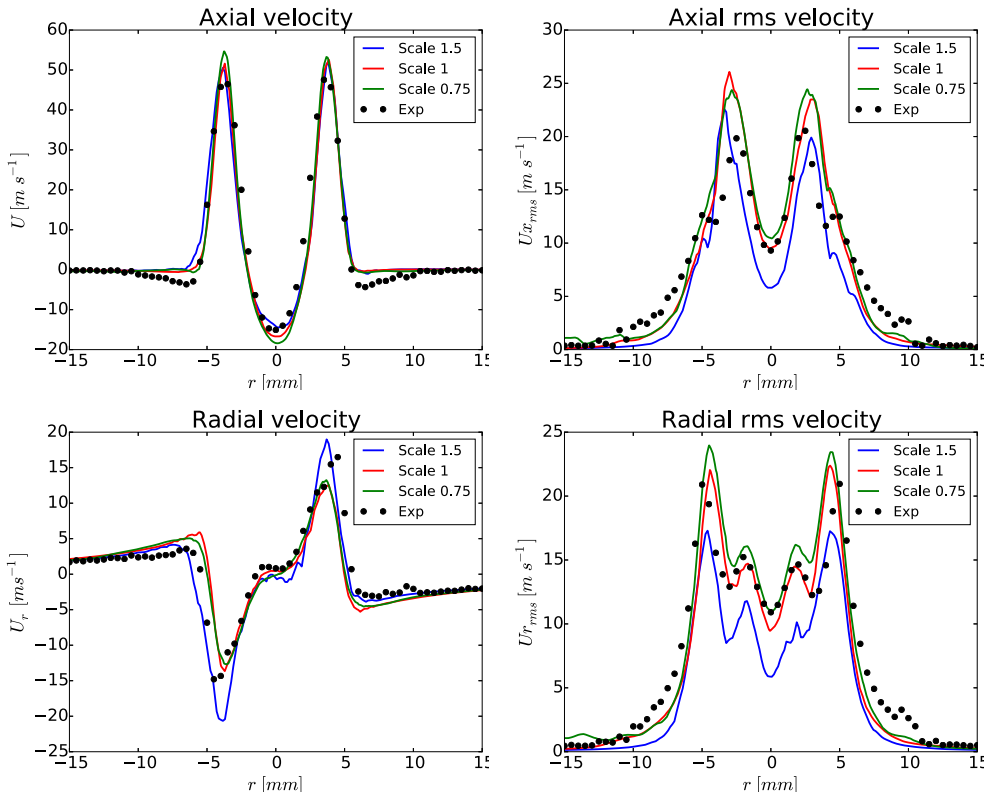

Figure 2.10: *Mean axial (top) and radial (bottom) mean (left and rms (right) velocity fields, compared to the experiment (in symbols), for different mesh refinements.*

lation and experiment (presented in the previous section and only measured experimentally at $x = 2.5$ mm) and the red curves gaseous profiles from the two-phase cases. The experimental gaseous flow at $x = 2.5$ mm (left graphs) is nearly identical with or without droplets, which indicates that the dispersed liquid phase has little influence on the gaseous phase. This effect is also seen in the simulation, which is able to retrieve the experimental data with a good accuracy at both heights.

Comparison between experimental and numerical liquid velocities is less straightforward than that of the gaseous velocities due to the differences of droplet diameter. Since the numerical simulation is monodisperse, the three components of the numerical liquid velocity vector are clearly defined. However, experimentally, a range of diameter is present for each point, and droplets behave differently depending on their size.

Figure 2.12 shows the profiles of the mean axial velocity of the liquid phase at an axial distance of $x = 2.5$ mm from the burner exhaust plane. Two different experimental averaged velocities are plotted. The triangles correspond to the arithmetic mean of the droplet's velocity, meaning that every droplet has the

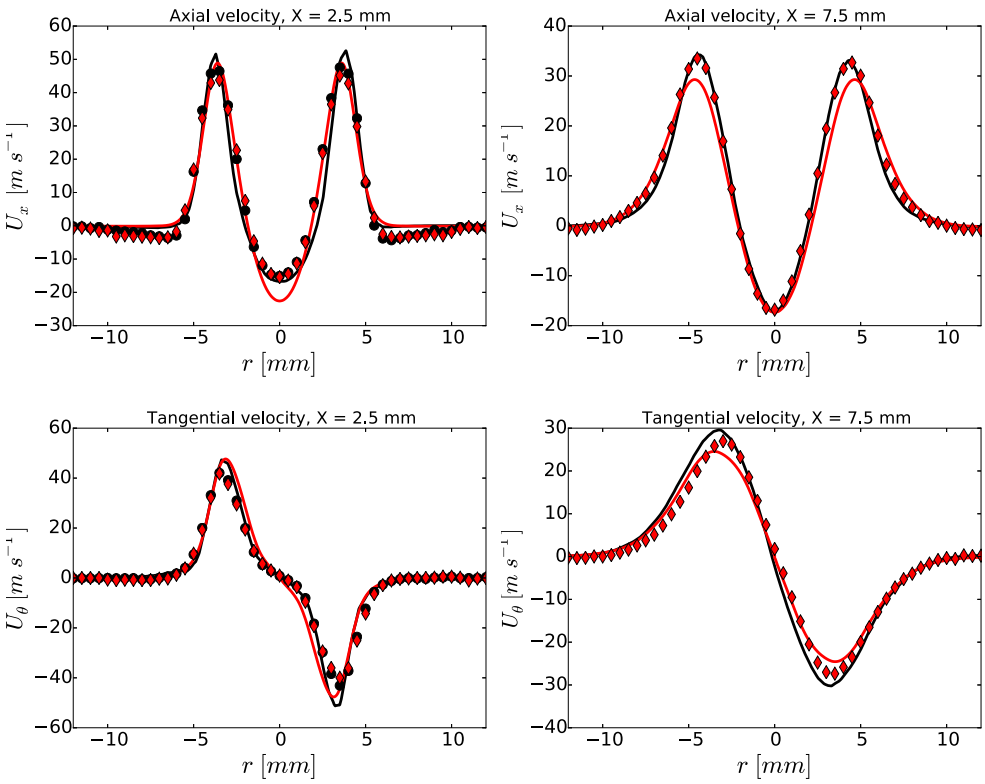

Figure 2.11: *Mean velocity profiles for the gas phase at $x = 2.5$ mm (left) and $x = 7.5$ mm (right) from the exhaust plane: Axial velocity (top) and azimutal velocity (bottom). Black curves represent the results from purely gaseous cases and the red curves the gaseous fields from two-phase flow cases. −: Numerical results; • : Experimental data.*

same weight in the average, whatever its mass is. The predicted numerical velocity profile does not agree with this type of measurement, which can be explained. On the one hand, as the experimental spray is mainly populated (in number) by small droplets (see Fig 2.2), the experimental mean velocity is therefore governed by small droplets dynamics which, having a smaller Stokes number (defined in the Eq. 2), tend to follow the air flow. On the other hand, the simulated disperse liquid phase corresponds to droplets whose diameter at the injection is equal to the spray's Sauter Mean Diameter $D_{32} = 20\ \mu m$. Because of this injected diameter that is larger than the majority of droplets, the simulated droplets will have a relatively more ballistic type of trajectory and their velocity relaxes to the gas velocity with a larger characteristic time, which explains the discrepancy between the results.

In light of these considerations, the numerical fields can be compared to the experimental velocities weighted by each particle's mass. Indeed, the final objective of this study is to represent a burning poly-disperse spray with a mono-disperse approach, which means describing accurately the spray mass distri-

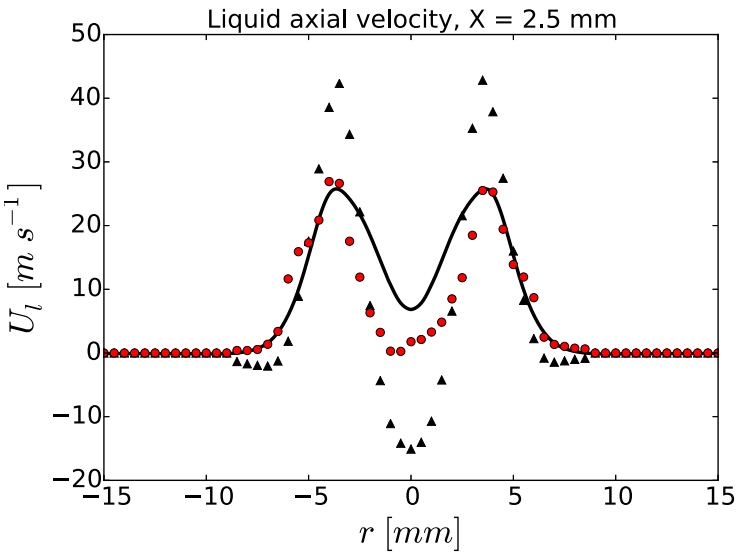

Figure 2.12: *Mean axial velocity for the liquid phase at $x = 2.5$ mm. −: Numerical results; ▲: Experimental arithmetic average; ●: Experimental mass-weighted average.*

bution and momentum. Weighting the droplets velocities by their mass seems therefore appropriate. This field is plotted in red symbols in Fig. 2.12. The numerical results are much closer to the experimental mass-averaged velocity than they were to the arithmetic average. As with the gaseous fields, the radial position of the spray is well recovered, as well as the magnitude of the peaks. The central recirculation zone that appears in the axial velocity profile is also satisfactorily captured.

Figure 2.13 shows the radial profiles for the mean liquid axial (left) and tangential (right) velocities, including size-conditioned statistics (without mass-weighting inside each class), at $x = 7.5$ mm in the flame experimental stabilization zone. The full lines represent the numerical results, while the experimental mass-averaged velocity and arithmetic average are respectively represented in black and red circles. The dotted lines show the experimental velocities for several classes of droplets. To ensure experimental convergence, only points where enough data (more than 100 droplets) have been collected are plotted. Comparing the different experimental fields, it appears that the different droplet classes behave quite similarly, with a spreading due to the different drag relaxation time: the smallest droplets, having smaller Stokes number, have had time since their exit from the atomizer to relax towards the gaseous flow field behaviour, while the bigger droplets are less sensitive to drag and therefore still have their own motion. Due to drag and the fact that even the bigger droplets are relatively small, the differences between the classes are lessening compared to the measurements at $x = 2.5$ mm. In consequence, the mass-

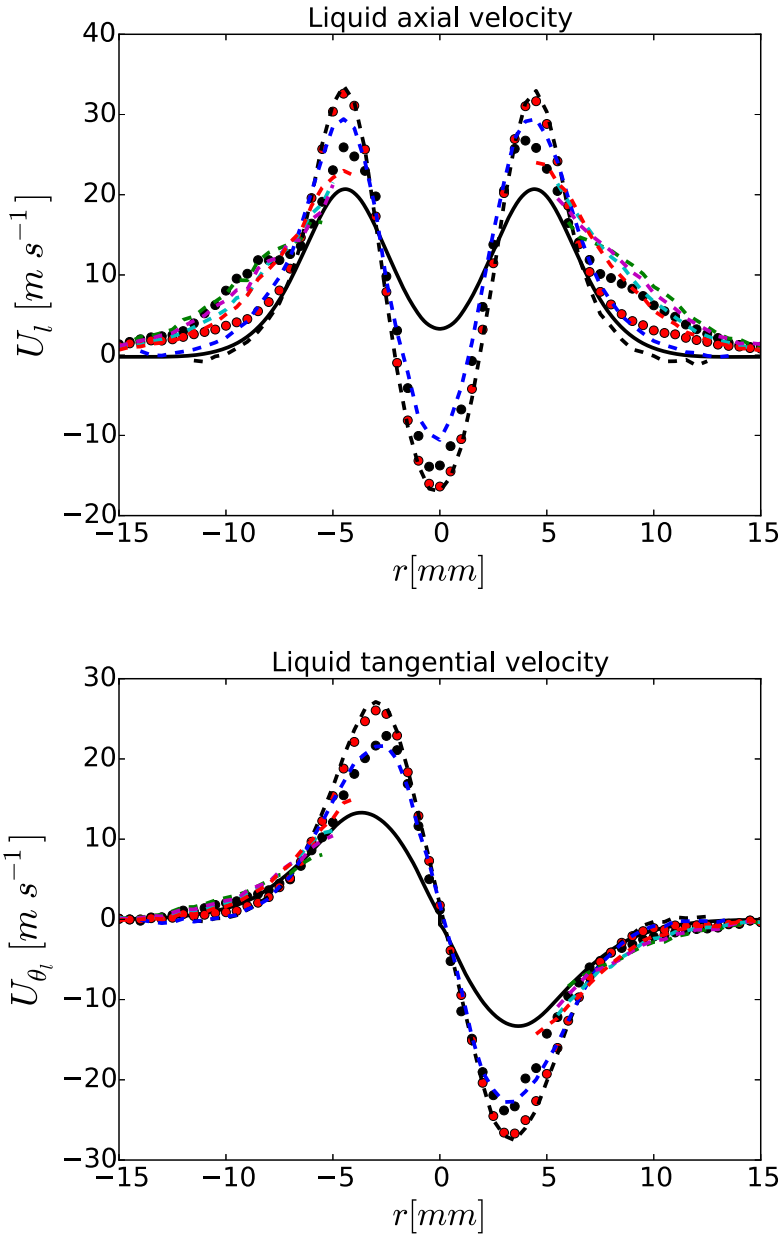

Figure 2.13: *Mean axial (left) and tangential (right) velocity fields for the liquid phase at $x = 7.5$ mm. —: Numerical results; • •: Mass-averaged experimental field; • •: Arithmetic average experimental velocity, Experimental profiles: - -: $d_l = 2-3$ μm; - -: $d_l = 10-12$ μm; - -: $d_l = 20-23$ μm; - -: $d_l = 23-36$ μm; - -: $d_l = 26-30$ μm. - -: $d_l = 30-34$ μm;*

averaged field is at this height quite close to the arithmetic average. Indeed,

since the measurement plane $x = 7.5$ mm is further away from the burner exhaust plane, the bigger droplets have had more time to relax towards a more uniform flow. Figure 2.11 showed that the gaseous velocity field was very well predicted. However, some discrepancies appear for the liquid phase fields. First of all, only very small droplets are present in the center recirculation zone in the experiment, whereas the numerical 20 μm droplets are not sensitive to the same entrainment effect in the center recirculation zone, which is therefore not retrieved by the simulation. Looking at the two high velocity peaks indicates that, though the simulation is very accurate in predicting the gaseous peaks as well as the radial position of the spray, it is not able to retrieve the correct magnitude of the average liquid velocity. The larger droplets that are numerically resolved are not sufficiently entrained by the air flow to be representative of the mass-weighted liquid velocity. The numerical profile is however closer to the experimental 20 μm-class velocity (in red), indicating that, while the injected droplets do not behave like the average of the spray, their dynamics match the corresponding experimental class.
Consequently, although the general behaviour of the two-phase flow is retrieved qualitatively, the single simulation of a mono-disperse spray with $d_l^{inj} = D_{32}$ is not able to accurately predict the magnitude of the mean velocity fields of a poly-disperse spray, which is not surprising. However, if one focuses on the corresponding experimental class of droplet, the simulation is in fair agreement with its evolution. In light of these observations, considering the mono-disperse description as a surrogate model of the poly-disperse spray, an optimal injected diameter should be determined in order to retrieve a spray dynamics representative of the experimental one.

2.5 Selection of the injected droplet diameter

In order to select an optimal value for the injected diameter, a separate study was conducted to observe the effects of its variations on the two-phase flow.

2.5.1 Surface response generation

An interesting approach in order to evaluate the impact of one or several parameters on a complex system is uncertainty quantification and the Polynomial Chaos Expansions, hereafter referred to as PCE (Xiu and Karniadakis (2002), Reagana et al. (2003)). PCE allows to estimate uncertain fields that depend on both deterministic and uncertain parameters. Any given uncertain field u can be written as $u(\mathbf{x}, \omega)$ where $\mathbf{x}$ represents the set of deterministic parameters and ω the uncertain ones. In the present study the injected diameter d_l^{inj} is considered as the unique uncertain parameter. Through PCE, one is able to

estimate the uncertain field u with the polynomial decomposition:

$$u(\mathbf{x}, d_l^{inj}) \approx \sum_{k=0}^{N} a_k(\mathbf{x}) P_k(d_l^{inj}) \tag{2.2}$$

For any value of the deterministic parameters $\mathbf{x}$, and knowing the value of the polynomial coefficients $a_k(\mathbf{x})$, $u(\mathbf{x}, d_l^{inj})$ is approximated by a linear combination of the chaos polynomials P_k, that only depend on the uncertain parameter, and therefore becomes a continuous function of d_l^{inj}, whose study is then straightforward.
The polynomials P_k are defined considering the probability density function (PDF) π associated to the uncertain parameter d_l^{inj}, varying in the interval I. A scalar product can be defined:

$$< f, g >= \int_I f(\omega) g(\omega) \pi(\omega) d\omega \tag{2.3}$$

and from that a basis of orthogonal polynomials P_k ($\forall\ i,\ j,\ < P_i, P_j > =\ \delta_{ij}$). In the present study, the distribution of the uncertain injected diameter distribution $\pi(d_l^{inj})$ is considered uniform between 0.5 μm and 35 μm (see Fig. 2.2). The polynomial basis is then made of Gauss-Legendre polynomials, initially defined on the interval $[-1, 1]$. A rescaling of the input of these polynomials allows to obtain $P_k(\omega)$.
The coefficients $a_k(x)$ from the Eqn. 2.2 can then be expressed as:

$$\forall\ k,\ \forall\ \mathbf{x},\ a_k(\mathbf{x}) =< u(\mathbf{x}, \cdot), P_k >= \int_I u(\mathbf{x}, \omega) P_k(\omega) \pi(\omega) d\omega \tag{2.4}$$

The coefficients $a_k(\mathbf{x})$ being defined by integrals, their computation can be carried out with a quadrature rule, meaning that their value can be approximated as a sum. Equation 2.5 gives a general formula for the approximation of the integral of a function f using a finite set of evaluations x_i and the corresponding weights w_i, that are defined by the *quadrature rule*:

$$\int f(x) \pi(x) dx = \sum_i w_i f(x_i) \tag{2.5}$$

For the present study, the Clenshaw-Curtis nested quadrature rule (Clenshaw and Curtis (1960)) was retained for its fast convergence and ability to limit the number of evaluations for each quadrature level, which is a great benefit given that each evaluation corresponds to one LES with a different injected diameter ($M = 2^l + 1$ evaluations of are required for the l-quadrature level). The *nested* aspect of this quadrature rule constitutes another great advantage because the increase of the quadrature level simply adds evaluations while reusing the evaluations from the lower levels. This allows to evaluate easily the convergence of the approximations, as will be shown later. Due to the computational cost of each simulation, the maximum quadrature level was limited to 4.

	Quadrature level			
	1	2	3	4
Injected droplet diameter d_l^{inj} $[\mu m]$	0.5	0.5	0.5	0.5
	-	-	-	0.83
	-	-	1.81	1.81
	-	-	-	3.41
	-	5.55	5.55	5.55
	-	-	-	8.17
	-	-	11.15	11.15
	-	-	-	14.38
	17.75	17.75	17.75	17.75
	-	-	-	21.12
	-	-	24.35	24.35
	-	-	-	27.33
	-	29.95	29.95	29.95
	-	-	-	32.09
	-	-	33.69	33.69
	-	-	-	34.67
	35.0	35.0	35.0	35.0

Table 2.4: *Values of the evaluations of the injected diameter for each quadrature level.*

The corresponding values for the evaluations of d_l^{inj} obtained according to the Clenshaw-Curtis quadrature rule are summarized in Table 2.4. For the highest quadrature level that was considered, 17 simulations were performed. Each simulation was started from the same converged air flow field, the two-phase flow was simulated for 15 ms before the fields were averaged over 30 additional milliseconds. Each simulation, without the convergence of the air flow, was run on 512 processors on the IDRIS cluster TURING and required 20000 CPU hours. The whole study therefore cost 340000 CPU hours.
Once all the simulations have been sufficiently converged and average fields have been extracted, the coefficients a_k associated to the uncertain field $u(\mathbf{x}, d_l^{inj})$ are computed from the quadrature rule given in Eq. 2.6. The obtained PCE (Eq. 2.2) is used to build a response surface of LES results in terms of d_l^{inj}.

$$a_k(\mathbf{x}) = \int_I u(\mathbf{x}, d_l^{inj}) P_k(d_l^{inj}) \pi(d_l^{inj}) d d_l^{inj} \tag{2.6}$$

$$\approx \sum_i w_i u(\mathbf{x}, d_{l,i}^{inj}) P_k(d_{l,i}^{inj}) \tag{2.7}$$

The weights w_i associated to the evaluations $x_i = d_{l,i}^{inj}$, obtained using the Clenshaw-Curtis quadrature rule for each quadrature level are given in Tab. 2.5. Each field can then be estimated by the polynomial approximation for any value of the injected diameter, even ones that were not simulated. In other words,

$x_i = d_{l,i}^{inj}$ $[\mu m]$	w_i for quadrature level:			
	1	2	3	4
0.5	0.16667	3.3333×10^{-2}	7.9365×10^{-3}	1.9608×10^{-3}
0.83	-	-	-	1.8684×10^{-2}
1.81	-	-	7.3109×10^{-2}	3.7741×10^{-2}
3.41	-	-	-	5.4453×10^{-2}
5.55	-	0.26667	0.13968	6.9478×10^{-2}
8.17	-	-	-	8.1586×10^{-2}
11.15	-	-	0.18085	9.0737×10^{-2}
14.38	-	-	-	9.6257×10^{-2}
17.75	0.66666	0.40000	0.19682	9.8205×10^{-2}
21.12	-	-	-	9.6257×10^{-2}
24.35	-	-	0.18085	9.0737×10^{-2}
27.33	-	-	-	8.1586×10^{-2}
29.95	-	0.26667	0.13968	6.9478×10^{-2}
32.09	-	-	-	5.4453×10^{-2}
33.69	-	-	7.3109×10^{-2}	3.7741×10^{-2}
34.67	-	-	-	1.8684×10^{-2}
35.0	0.16667	3.3333×10^{-2}	7.9365×10^{-3}	1.9608×10^{-3}

Table 2.5: *Values of the evaluations weights corresponding to each evaluation of the injected diameter, calculated with the Clenshaw-Curtis quadrature rule, for each quadrature level.*

at a given point in space and for a given physical field, the polynomial reconstruction yields an estimation of this field according to the injection diameter. This provides a way to determine an optimal diameter more efficiently than by carrying out a parametric study with a finite set of values.
An example of response surface is given in Fig. 2.14 for the liquid velocity at $x = 7.5$ mm. The radial profile of the axial liquid velocity, such as was plotted on Fig. 2.13, can now be obtained for any value of the injected diameter and becomes a 3D surface. As could be expected, when smaller droplets are injected, the central recirculation zone is more intense and the velocity profiles are closer to the gaseous one. On the other side of the plot, when the droplets are bigger, they have a more ballistic behaviour, leading to the disappearance of the central recirculation zone and less intense velocity peaks.

2.5.2 Selection of the polynomial order

In the approximation of the uncertain field u given in Eq. 2.2 and for a given quadrature level l, the order N of the polynomial approximation (which also corresponds to the maximum degree of the polynomials) has to be selected. Figure 2.15 shows the evolution of the predicted value for the mean axial liquid velocity at $x = 7.5$ mm, at four different distances from the injector central

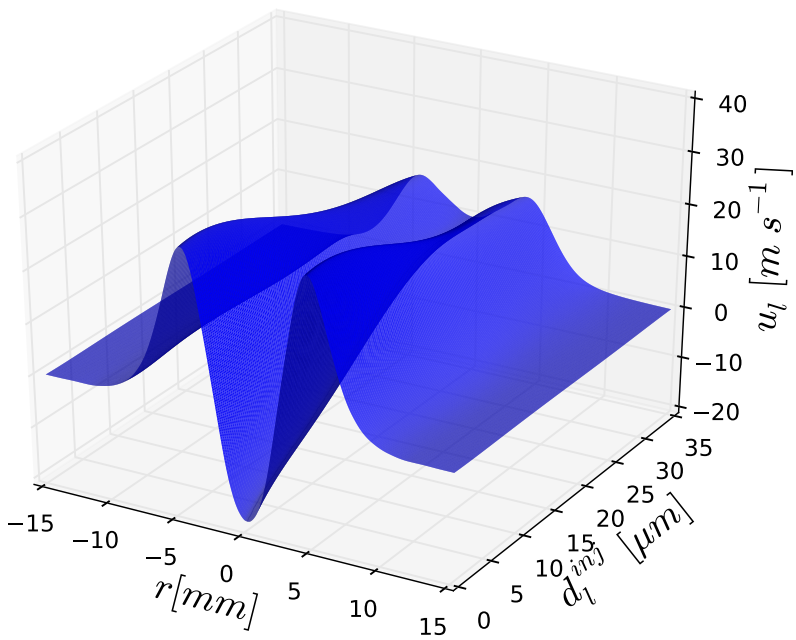

Figure 2.14: *Response surface for the axial velocity at $x = 7.5$ mm and some of the numerical fields used for the expansion.*

axis (r), and for different values of the polynomial order N, for the quadrature level 3. To evaluate the quality of the polynomial interpolations, the values extracted from the nine LES used for this quadrature level are reported as black dots. It appears that the lower orders (from 1 to 4) are not able to capture all the variations of the velocity according to the injected diameter, contrary to degrees 5 and 6. The curves of degree 6 (in magenta) exhibit some oscillations and tend to diverge at the extremity, a phenomenon which is known as the Runge effect (sciteRunge1901). This is even more marked as the polynomial degree is increased. For that reason, the choice was made to use the degree 5 interpolation (in cyan) for the result analysis.

2.5.3 Optimization of the injected diameter

Response surfaces can be built for any quantity of interest. In order to determine a better value for the injection diameter, it is necessary to define one or several relevant criteria. A first optimization criterion can be the minimization of the numerical error on the axial liquid velocity $u_{l,exp}^{poly}$, obtained with local mass-weighted average of the measured droplets velocity. The error corresponding to the criterion is computed by the Euclidian norm: $\epsilon_1(d_l^{inj})$, defined for a given height x as:

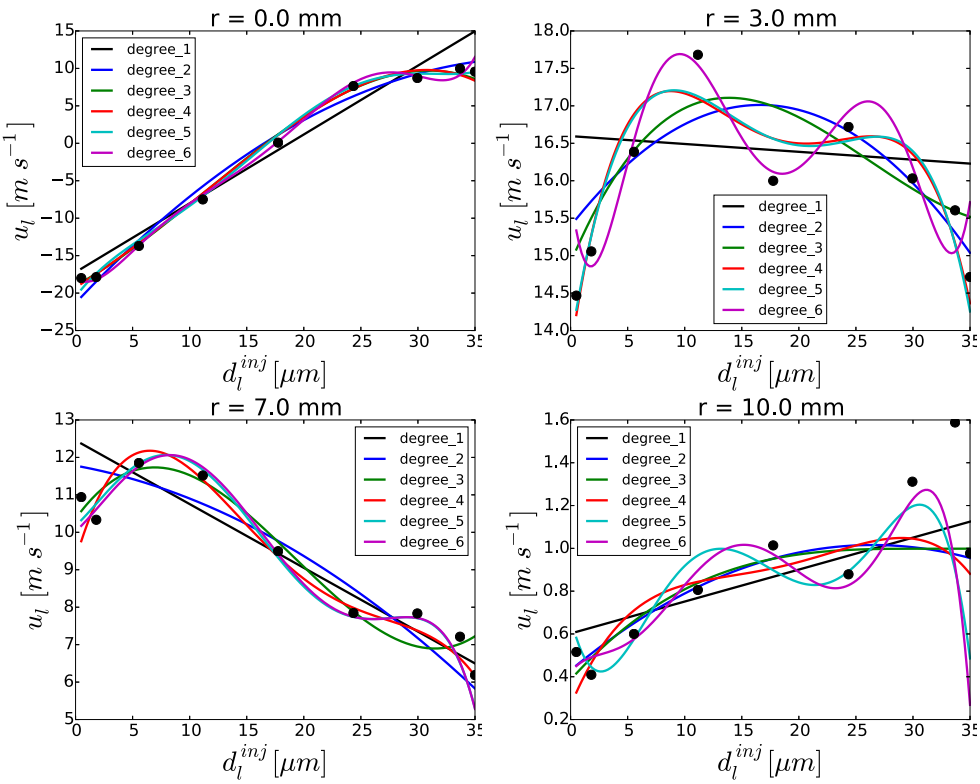

Figure 2.15: *PCE approximation for the axial velocity at $r = 0$ mm (top left), $r = 3$ mm (top right), $r = 7$ mm (bottom left) and $r = 10$ mm (bottom right). −: PCE expansions; • : Numerical values from mono-disperse simulations.*

$$\epsilon_1(d_l^{inj}) = ||u_l^{PCE}(d_l^{inj}) - u_{l,exp}^{poly}||_2$$
$$= \sqrt{\frac{1}{N_{exp}} \sum_{j=1}^{N_{exp}} \left[u_l^{PCE}(r_j, d_l^{inj}) - u_{l,exp}^{poly}(r_j)\right]^2} \tag{2.8}$$

where u_l^{PCE} is the PCE approximation of the axial liquid velocity in the mono-disperse simulations and $\{r_1, ..., r_j, ..., r_{N_{exp}}\}$ correspond to the N_{exp} experimental poly-disperse points of measure at the considered height. This criterion allows to quantify the ability of the simulation to retrieve the aerodynamic behaviour of the droplets. A geometrical domain has to be chosen for the computation of the norm, which can be the whole domain or a reduced region of interest. Since the final objective is to retrieve the flame shape, a possibility is to focus on the area of the flame stabilisation in the experiment. In the un-confined configuration, no flame can stabilize on the burner because the dilution by the atmosphere is too important, therefore the flame stabilization in the confined case was retained for the optimization. Obviously, in an ideal

case, since the targeted simulation is that of the flame with confinement, a more adequate optimisation would have been on the cold two-phase flow with confinement, but the presence of the quartz walls prevent velocity measurements due to some liquid streaming down the walls.
The flame in the confined configuration is lifted and stabilizes around a height of $x = 7.5$ mm. The choice was therefore made to focus on this height for the comparison and evaluation of the injected droplet diameter.

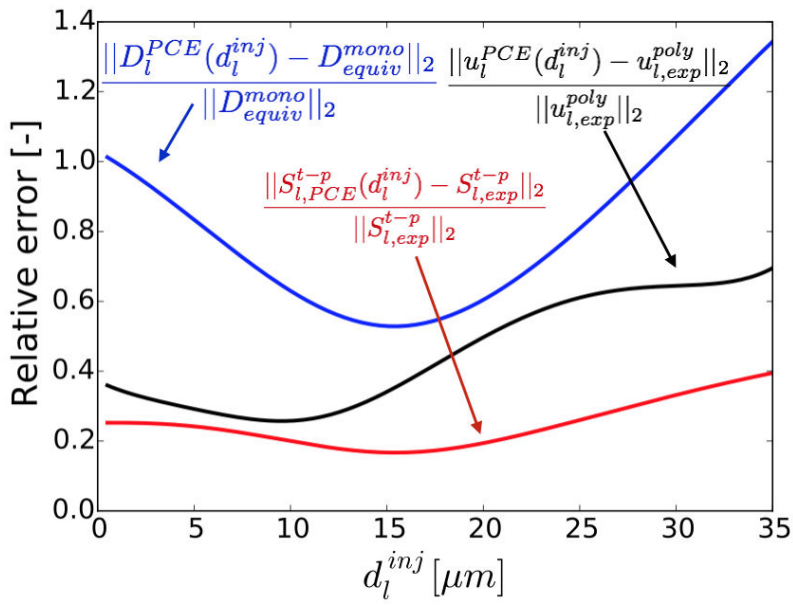

Figure 2.16: *Normalised L^2-norm of the different error criteria at $x = 7.5$ mm. Black curve: error on liquid axial velocity, blue curve: error on the liquid equivalent diameter and red curve: error on the two-phase laminar flame speed.*

The corresponding relative error associated to the axial liquid velocity is plotted in Fig. 2.16, as the black curve, against the injection diameter. An optimal value for the injected diameter, which minimizes the error, clearly appears at $d_l^{inj} = 9.7$ μm for this criterion. However, the relative error at this point is of 27%, further highlighting the difficulty to represent the aerodynamics of a polydisperse spray with a monodisperse approach.
The final objective being reactive simulations of flame propagation in a two-phase flow, a key quantity that the simulation should be able to retrieve is the laminar burning speed, to consider here in the presence of droplets. Ballal and Lefebvre (1981a) gave an expression for such a two-phase laminar flame speed S_l^{t-p}, whose validity has been investigated numerically by Neophytou

and Mastorakos (2009):

$$S_l^{t-p} = \alpha_g \left[\frac{C_3^3 \rho_l D_{32}^2}{8 C_1 \rho_g \ln(1+B)} + \frac{\alpha_g^2}{S_L^2} \right]^{-0.5} \tag{2.9}$$

with α_g the thermal conductivity, ρ_l and ρ_g the liquid and gaseous densities, B the Spalding number and S_L the gaseous laminar flame speed. This formula is valid for a polydisperse spray, with $C_1 = D_{20}/D_{32}$ and $C_3 = D_{30}/D_{32}$. In the case of a mono-disperse spray, the coefficients C_1 and C_3 are both equal to unity, so that an equivalent mono-disperse diameter that conserves the two-phase laminar burning speed can be written as:

$$D_{equiv}^{mono} = D_{32}^{poly} \times \sqrt{\frac{C_3^3}{C_1}} \tag{2.10}$$

A different criterion could therefore be the injected diameter that best retrieves this equivalent monodisperse diameter at $x = 7.5$ mm. The comparison between this predicted diameter and the equivalent one with respect to the flame speed as defined in Eqn. 2.10 is plotted in Fig. 2.16 as the blue curve, again using the relative error norm. The corresponding error on S_l^{t-p} is given in red. It appears that the optimal diameter varies strongly depending on the criterion used. In order to retrieve the liquid velocity fields, injecting small droplets, with a diameter around 9.5 μm, which is close to the spray's mean diameter D_{10}, seems optimal. However, to reproduce the flame speed, a better injection diameter would be around 15.3 μm. For this diameter, the relative error on the flame speed is of 16%, which remains noticeable. These results are consistent with the definition of the diameters given by Lefebvre (1989), who states that among a set of available representative diameters, the D_{10} represents the velocity fields while the D_{32} is more suited for combustion.

2.5.4 Convergence

As already mentioned, the previous results were extracted from the Polynomial Chaos Expansions with a Quadrature Level (QL) of 3 and a Polynomial Order (PO) of 5. The polynomial order selection was motivated in section 2.5.2, however, the question of its influence, as well as that of the quadrature level, on the conclusions regarding the injected diameter, remains to be addressed.
Figure 2.17 displays the relative error for the two previously described criteria, for the liquid axial velocity (top curves) and the two-phase laminar flame speed (bottom curves), for different degrees of convergence. The black curves represent the results obtained with a QL of 3 and a PO of 5 (also presented in Fig. 2.16), while the red curves correspond to the same PO and a QL of 4. The comparison of the two pairs of curves (one for each criterion) shows very similar trends and that increasing the quadrature level does not improve the results, suggesting that a QL of 3 is enough to obtained converged results.

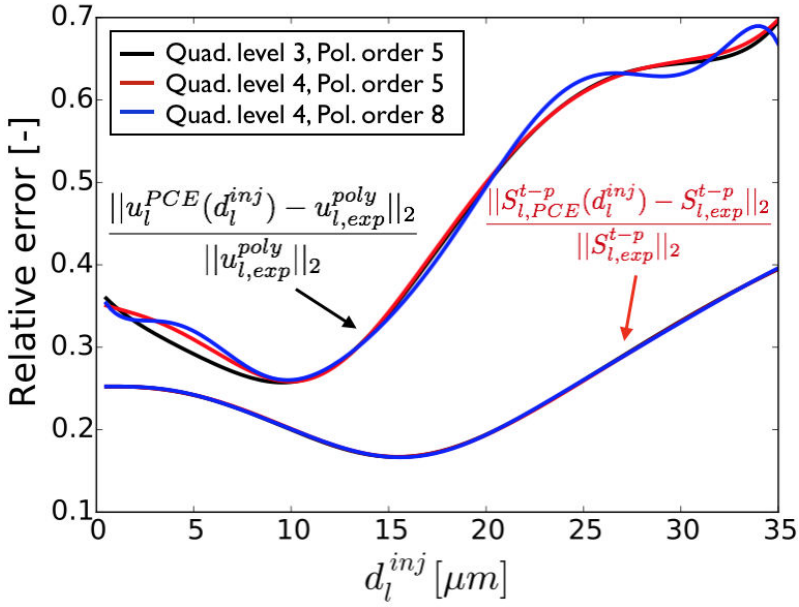

Figure 2.17: *Comparison of the normalised L^2-norm of the different error criteria at $x = 7.5$ mm. Black curves: quadrature level 3, polynomial order 5, blue curves: quadrature level 4, polynomial order 5 and red curves: quadrature level 4, polynomial order 8.*

Additionally, the blue curves correspond to a QL of 4 and an increased PO of 8. Similarly to what was observed in section 2.5.2, some oscillations appear towards the extreme values of the injected diameter on the velocity curve when the PO in increased too much, but overall, and particularly on the flame speed criterion, very little difference is observed between the red and blue curves, and the conclusions in terms of optimal diameter remain identical.
In conclusion, the selected optimal diameter, from the two-phase laminar flame speed S_l^{t-p}, $d_{l,opt}^{inj} = 15.3\ \mu m$, can be considered independent from both quadrature level and polynomial order. The quadrature level 3, for which 9 LES evaluations are required, was even sufficient to obtain converged results, though the simulation on the 8 additional points corresponding to QL 4 were necessary to reach this conclusion. Unless explicitly mentioned, all the following simulations are carried out with this value of the injected diameter.

2.6 Simulation of the confined configuration

The numerical set-up that was validated in the unconfined configuration is here applied to the confined case, with the selected injected diameter $d_l^{inj} = 15.3\ \mu$m. As could be seen on the picture of the burner on the right in Fig. 2.1, cylindrical quarts are added around the exit of the swirler, with a diameter of 75 mm and a length of 150 mm.

2.6.1 Non-reactive flow

2.6.1.1 Air flow simulation

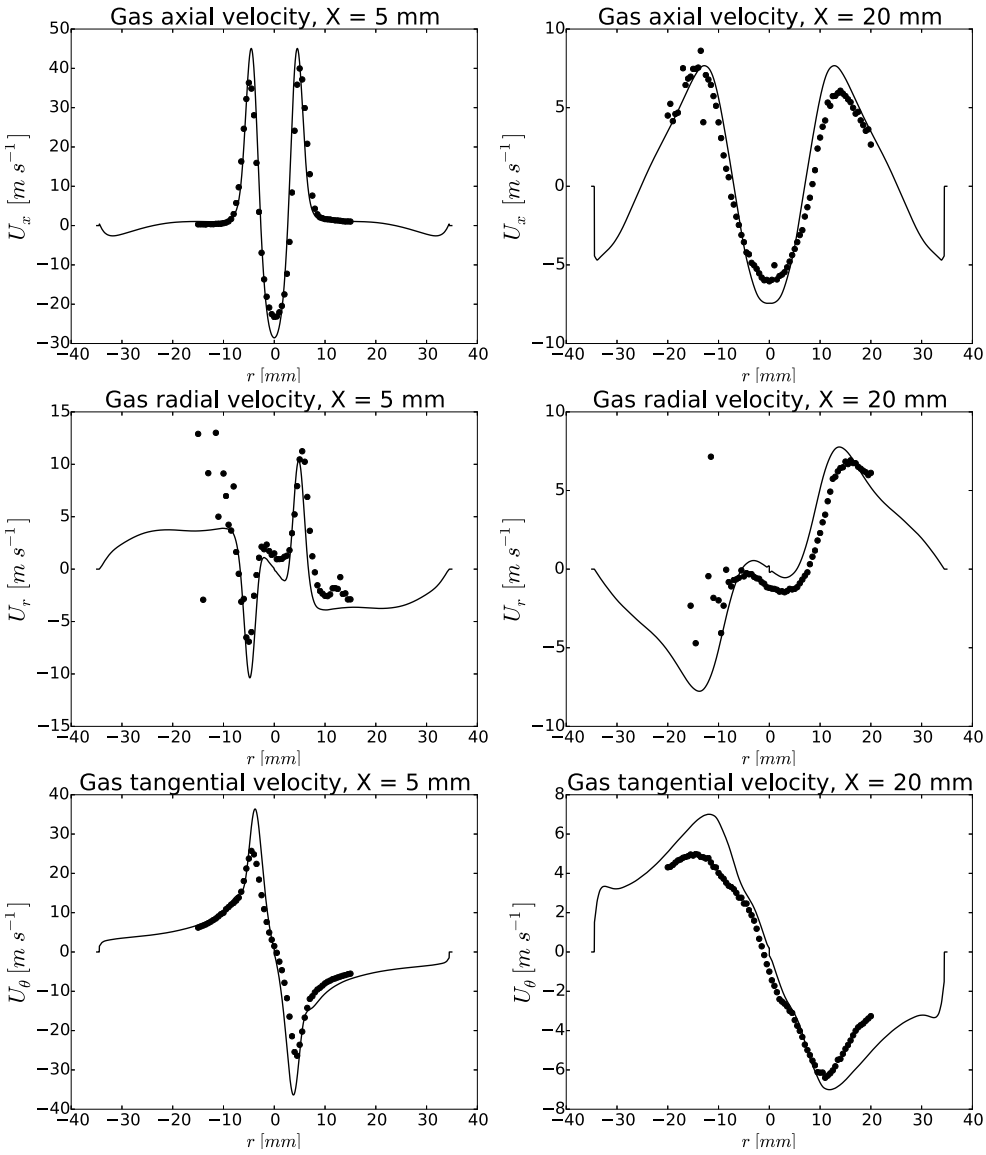

Figure 2.18: *Mean velocity profiles for the gas phase at $x = 5$ mm (left) and $x = 20$ mm (right) from the exhaust plane: Axial velocity (top), radial velocity (center) and azimuthal velocity (bottom). −: Numerical results; • : Experimental data.*

For the confined configuration, experimental data is available on the purely gaseous flow for the three components of the air velocity u_x, u_r and u_θ at six different heights, measured from the chamber backplane: 2.5 mm, 5 mm, 7.5 mm, 10 mm, 15 mm and 20 mm. Figures 2.18 and 2.19 present the profiles at

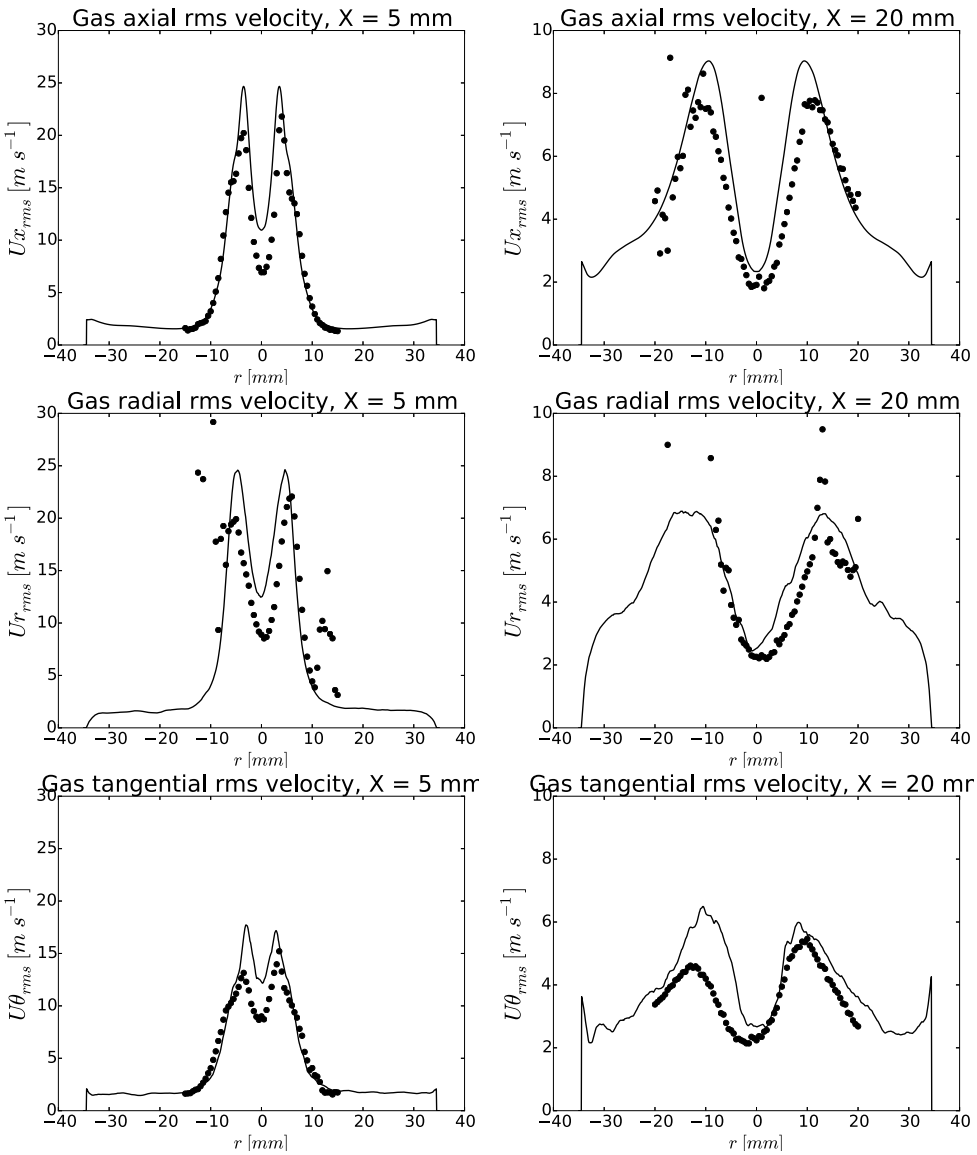

Figure 2.19: *RMS velocity profiles for the gas phase at $x = 5$ mm (left) and $x = 20$ mm (right) from the exhaust plane: Axial velocity (top), radial velocity (center) and azimuthal velocity (bottom). −: Numerical results; • : Experimental data.*

5 mm (left) and 20 mm (right) for the axial (top), radial (center) and tangential (bottom) mean velocities (Fig 2.18) and RMS velocities (Fig. 2.19). The different plots show that the simulation is able to retrieve the main features of the spray both near the swirler exit and further down the flow. The radial position of the swirled spray, evidenced by the positive axial velocity peaks, is well retrieved. The outer and central recirculation zones are also fairly well captured. Finally, the turbulence levels (Fig. 2.19) are well predicted.

2.6.1.2 Two-phase flow simulation

No experimental data is available for the liquid phase in the confined configuration of SICCA-Spray. However, the validations carried out on the unconfined case give some confidence to the results.

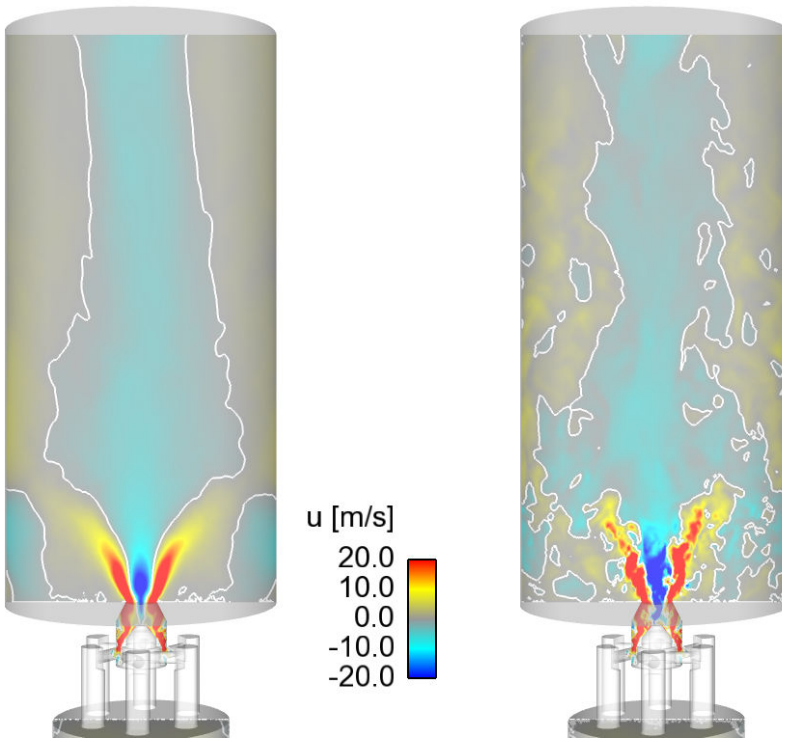

Figure 2.20: *Tangential cuts at $z = 0$ mm of the average (left) and instantaneous (right) axial gaseous velocity fields in the two-phase simulation of the confined configuration. The same color scale in used, from $u = -20$ $m.s^{-1}$ in blue to $u = 20$ $m.s^{-1}$ in red. White iso-lines of $u = 0$ $m.s^{-1}$ are added.*

On Fig. 2.20 are shown the average and an instantaneous fields of the axial gaseous velocity. The central recirculation zone that was already observed in the un-confined simulation is retried, with a similar high intensity at the bottom. It is however much longer due to the confinement and goes up to the chamber exit, on both average and instantaneous fields, meaning that some dilution with air coming from the atmosphere is taking place, thus modifying the global equivalence ratio in the chamber. An outer recirculation zone (ORZ) is now present, evidenced by the negative velocity regions at the bottom of the chamber. The ORZ is able to trap some of the droplets present in the hollow cone spray, which increases the local equivalence ratio.
Instantaneous fields of the liquid volume fraction α_l, the gaseous equivalence

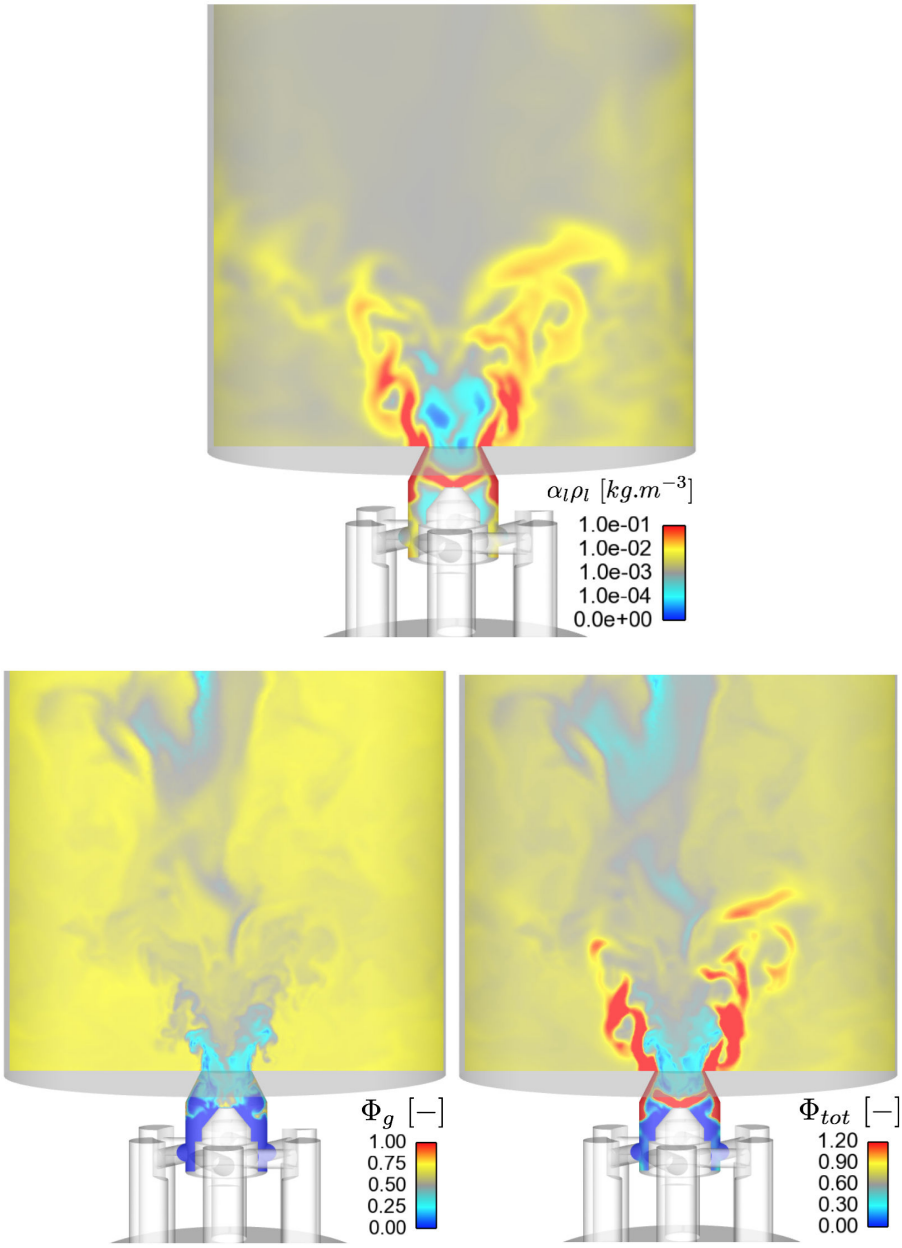

Figure 2.21: *Tangential cuts at $z = 0$ mm on an instantaneous solution of the confined mono-burner chamber, coloured by the liquid mass fraction $\alpha_l \rho_l$ (top), the gaseous equivalence ratio Φ_g (bottom left) and the total equivalence ratio $\Phi_{tot} = \Phi_g + \Phi_l$ (bottom right).*

ratio Φ_g and the local total (gaseous and liquid) equivalence ratio $\Phi_{tot} = \Phi_g + \Phi_l$ are presented in Fig. 2.21. Even without flame, the liquid droplets appear to be completely evaporated before reaching the top of the chamber. The liquid mass

is concentrated at the bottom of the chamber. This could be expected since n-heptane is a highly volatile species. Some of the droplets and fuel mass fraction is captured by the outer recirculation zone, allowing the local equivalence ratio to increase and reach the n-heptane flammability limits. However, the very intense central recirculation zone shown on Fig. 2.20 that brings air from the atmosphere towards the bottom of the chamber and dilutes the mixture limits the equivalence ratio: in the ORZ, $\Phi_g \approx \Phi_{tot} \approx 0.75$, which is lower that the injected global value $\Phi = 0.89$.

2.6.2 Reactive flow

A first simulation of the stabilised flame in the mono-burner has been carried out by assuming that the walls are adiabatic. The TFLES combustion model described in Section 1.4 is used for all the SICCA simulations presented hereafter. As shown in this section, these conditions do not lead to the correct prediction of the stabilisation of the flame. A second simulation was then carried out, using isothermal boundary conditions on the chamber walls. The results from both simulations (adiabatic and isothermal) are presented here and compared to the experimental flame in terms of shape and position within the burner. Experimental profiles of the axial gaseous velocity are also available.
Both simulations are ignited from the same cold flow, converged as described in the previous sections, with adiabatic boundary conditions on the walls. A sphere of burnt gases of radius $r = 4$ mm is inserted in the outer recirculation zone to trigger combustion.
On the isothermal case, the temperatures measured on the internal side of the quartz wall (see section 2.2.2 and Fig. 2.3) are imposed.

2.6.2.1 Flame shapes

Photographs of the experimental flame are taken with a camera equipped with a OH* filter and with an exposure time of 6 ms. The resulting images therefore show the flame integrated along the line of sight. The Abel transform is a numerical method that infers a longitudinal slice of the flame, so as to enable comparisons with simulations. The resulting image is displayed in the center of Fig. 2.22. The flame of both adiabatic (Fig. 2.22, left image) and isothermal (Fig. 2.22, right image) simulations are visualised through a longitudinal cut coloured by the heat release rate.
The first striking difference between the two simulations is their respective maximum value of the heat release rate, with a gap of almost one order of magnitude: $HR_{max}^{isoT} = 3.60 \times 10^8\ W.m^{-3}$ and $HR_{max}^{adiab} = 3.17 \times 10^9\ W.m^{-3}$. To enable comparisons between the simulations and the experiment, the heat release rates are adimentioned by each simulation's maximum value, so as to obtain fields ranging from 0 to 1. Clearly, the wall boundary condition has a very high impact on the flame shape. With adiabatic walls, the flame is much

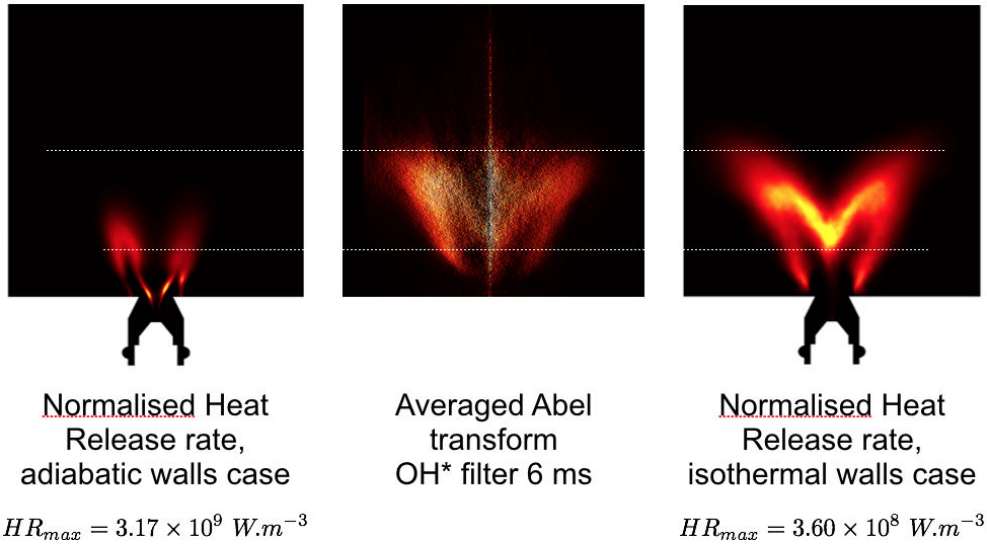

Figure 2.22: *Comparison of the flame shape between the adiabatic walls case (left), the experiment (center) and the isothermal walls case (right).*

more compact than with isothermal walls, as was also indicated by the much higher value of the maximum heat release rate. Moreover, with isothermal walls, the flame is no longer stabilised inside the swirler and its shape is much more similar to that of the experimental flame. As is evidenced by the two white dashed lines, the iso-thermal simulation is the only one that is able to correctly predict the flame shape: the central foot as well as the top are satisfactorily retrieved. The adiabatic case, however, gives a flame shape completely different from the experimental one, showing that an adiabatic wall hypothesis is not adapted to the studied burner and operating conditions.

2.6.2.2 Pressure oscillations in the chamber

When the boundary condition on the walls was first changed from adiabatic to isothermal, some strong oscillations of pressure were observed in the chamber. This section details this acoustic phenomenon, as well as the method used to remove it in order to obtain the results presented in the previous section. As is detailed in section 2.6.5, the propagation of the initial flame kernel stemming from the ignition sphere leads to the stabilisation of a flame attached to the swirler exit, similar to the adiabatic flame, which then detaches itself to take up its definitive position.

The temporal evolution of the pressure obtained through a probe placed in the outer recirculation zone is displayed in Fig. 2.23, at point (x = 10 mm, y = 17.5 mm, z = 0 mm). At t = 0 ms, a flame kernel is introduced in the converged cold flow and propagates until a flame is stabilised around the swirler exit (around t = 30 ms). The lifting of the flame, described in details in

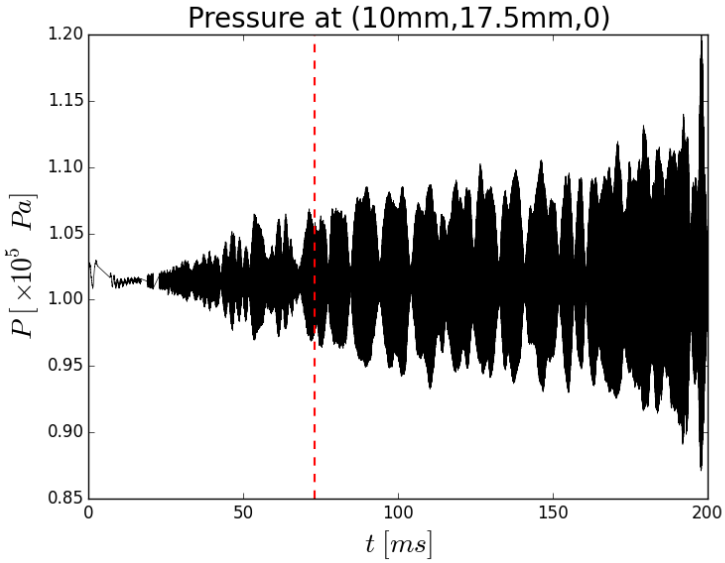

Figure 2.23: *Temporal evolution of the local pressure at a probe located at $x = 10$ mm, $y = 17.5$ mm and $z = 0$ mm. The red dashed line marks the instant of the flame lifting.*

section 2.6.5, is marked by the vertical red dashed line. The oscillations, which are not present at the beginning of the simulation, appear when the flame stabilises and then grow continuously. After 200 ms of simulated physical time, these oscillations have an amplitude of 20 kPa, which corresponds to 180 dB. Such a sound level, equivalent to that of a rocket engine, is not observed in the experiment and is probably due to some numerical issue. The frequency of the wave, 17 kHz, does not either correspond to any physical phenomenon observed in the experiment.

The spatial shape of the acoustic wave can be observed in Fig. 2.24, on the left, where a cut at $z = 0$ in an instantaneous solution is coloured by the pressure. The position of the flame is evidenced by an iso-line of the heat release rate at $HR = 1 \times 10^8$ W.m^{-3}. The acoustic mode is localized in the bottom quarter of the chamber and seems to be a combination of a standing mode and a rotating mode. These oscillations have a strong impact on the instantaneous shape of the flame: the right image in Fig 2.24 is an instantaneous iso-surface of the heat release rate at $HR = 1 \times 10^8$ W.m^{-3} and the flame is clearly stretched along a rotating axis. The deformation evolves with the modification of the pressure field in the chamber, but the flame is never instantaneously axi-symmetric, though its average is.

The understanding of this phenomenon is not within the scope of the present work, however, the presence of such oscillations could be explained by interactions between the flow and the lower external branches of the flame, that

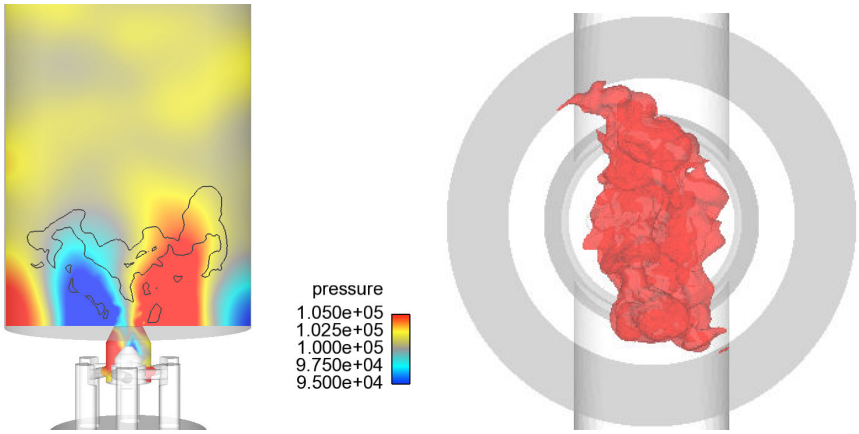

Figure 2.24: *Left: Visualisation of the pressure field on a $z = 0$ plane. The flame position is highlighted by an iso-line of the heat release rate $hr = 1 \times 10^8$ $J.s^{-1}.m^{-3}$. Right: top view of an iso-surface of the heat release rate $hr = 1 \times 10^8$ $J.s^{-1}.m^{-3}$.*

are partially extinguished by the heat losses at the bottom of the chamber and exhibit a flapping motion which could be responsible for the phenomenon. In any case, the oscillations appear to be an undesirable numerical event than prevents correct predictions of the flame behaviour. The method that was chosen to deal with the oscillations is to evacuate them through the walls by imposing there a relax coefficient on the normal velocity component. This needs to be done carefully so that the isothermal wall law is still imposed, otherwise the flame reattaches to the burner. Instantaneous pressure field and flame shape for the case with relaxed walls are shown in Fig. 2.25. The pressure oscillations have disappeared and classical swirled spray characteristics can be observed, such as a pressure drop in the inner recirculation zone. The pressure variations are also much lower than in the previous case. Finally, the flame has a roughly axi-symmetrical shape that is more consistent with the experimental observations.

The average flame shape obtained with the relaxed boundary conditions is displayed in Fig. 2.26 (middle image), compared to the experimental flame shape (left) and the one obtained in the first simulation, with pressure oscillations (right). The removal of the acoustic mode, which was rotating around the chamber axis, does not seem to impact the average flame shape, which remains very similar to the experiment in terms of width and length. The stabilisation point of the lifted flame, whose height is highlighted by the lower dashed white line, is also still well predicted. The outer flame branches' intensity seems to be somewhat overestimated at the foot of the flame in the simulations.

Once the pressure oscillations have been removed from the flow, the simulation is able to predict the formation of a double precessing vortex core (PVC) at the exit of the swirler. It is evidenced in Fig. 2.27 by an iso-surface of the pressure at $P = 99800$ Pa. Like in experimental results, two separate branches

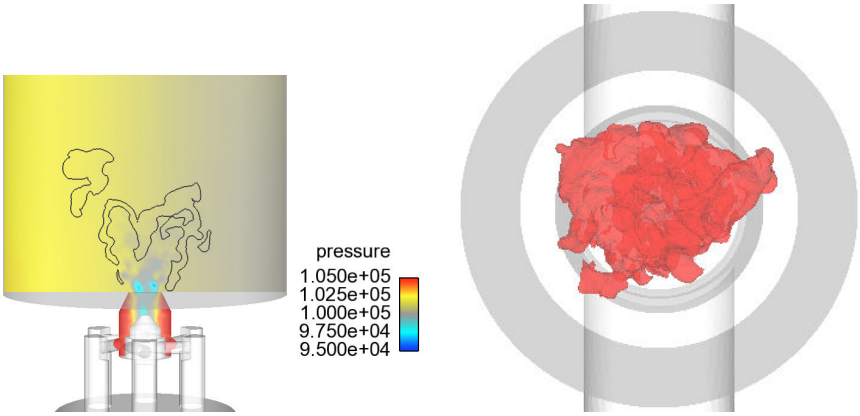

Figure 2.25: *Left: Visualisation of the pressure field on a $z = 0$ plane for the case with relaxed walls. The flame position is highlighted by an iso-line of the heat release rate $hr = 1 \times 10^8\ J.s^{-1}.m^{-3}$. Right: top view of an iso-surface of the heat release rate $hr = 1 \times 10^8\ J.s^{-1}.m^{-3}$.*

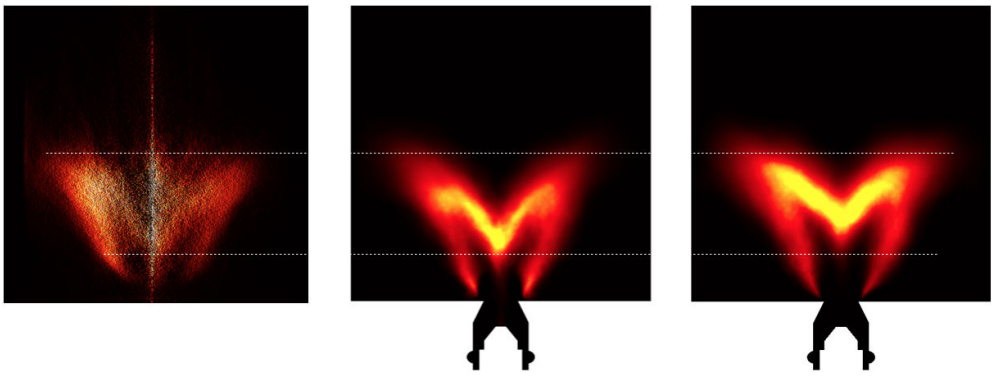

Figure 2.26: *Comparison of the flame shape between the experiment (left), the iso-thermal relaxed walls simulation (center) and the iso-thermal walls non-relaxed case (right).*

are visible, forming a double PVC. A probe placed inside the PVC yields a frequency $f_{PVC} \approx 7000$ Hz, while in the experiment, a double PVC is also observed, with a frequency $f_{PVC}^{exp} \approx 6000$ Hz, which is reasonably close.

2.6.2.3 Velocity profiles

Figure 2.28 displays the axial gaseous velocity average (left) and instantaneous (right) fields extracted from the simulation with iso-thermal boundary conditions on the walls. The position of the flame is highlighted by black iso-lines of the heat release rate at $HR = 1 \times 10^8$ W.m^{-3}. Due to the acceleration of the gases through the flame front, the velocity peaks are more intense and both wider and longer than in the cold flow (see Fig. 2.20). The central recirculation zone is however shorter and does not go beyond the half of the chamber, so

Figure 2.27: *Visualisation of the precessing vortex core in an instantaneous solution with relaxed walls, highlighted by an iso-surface of the pressure at $P = 99800$ Pa.*

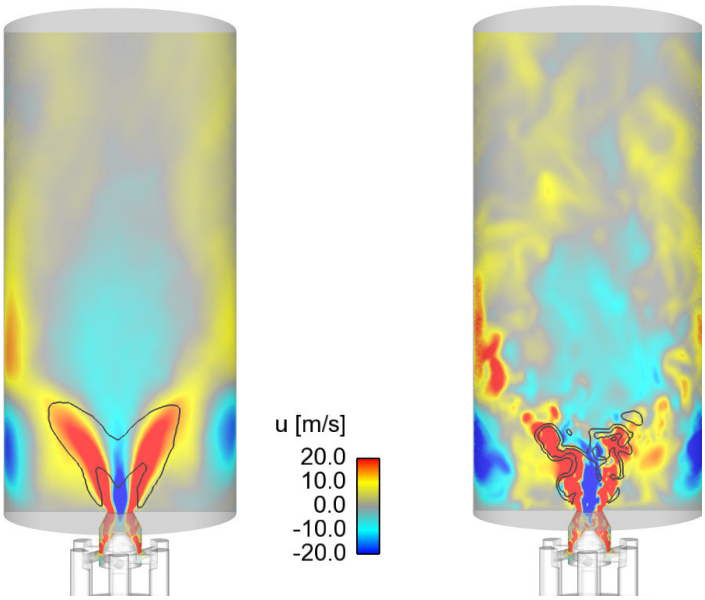

Figure 2.28: *Tangential cuts at $z = 0$ mm of the average (left) and instantaneous (right) axial gaseous velocity fields in the simulation with iso-thermal boundary conditions on the chamber walls. The same color scale in used, from $u = -20$ $m.s^{-1}$ in blue to $u = 20$ $m.s^{-1}$ in red. Black iso-lines of the heat release rate $HR = 1 \times 10^8$ $W.m^{-3}$ are added.*

that there is no longer any dilution by the air from the atmosphere. An intense outer recirculation zone is still present that recirculates the burnt gases towards the foot of the flame.
On the average field, the CRZ is very intense towards the bottom and seems to go down to the fuel injection whereas the flame remains, in the center,

around 10 mm from the chamber bottom. The instantaneous solution shows that the CRZ is actually divided in two and that the flame front is located in the separation, where small axial velocities are found. This separation's axial position fluctuates a lot, so that it cannot be seen on average solutions, leading to the observed flame stabilisation, which is quite surprising with regards to the velocity field.
PIV (Particle Image Velocimetry) measurements have been carried out on solid particles injected along with the air in the ignited burner, enabling the measurement of gaseous axial and radial velocity profiles. Due to the low intensity of the radial velocity, the corresponding profiles are not of a good enough quality to be properly compared to the numerical results.

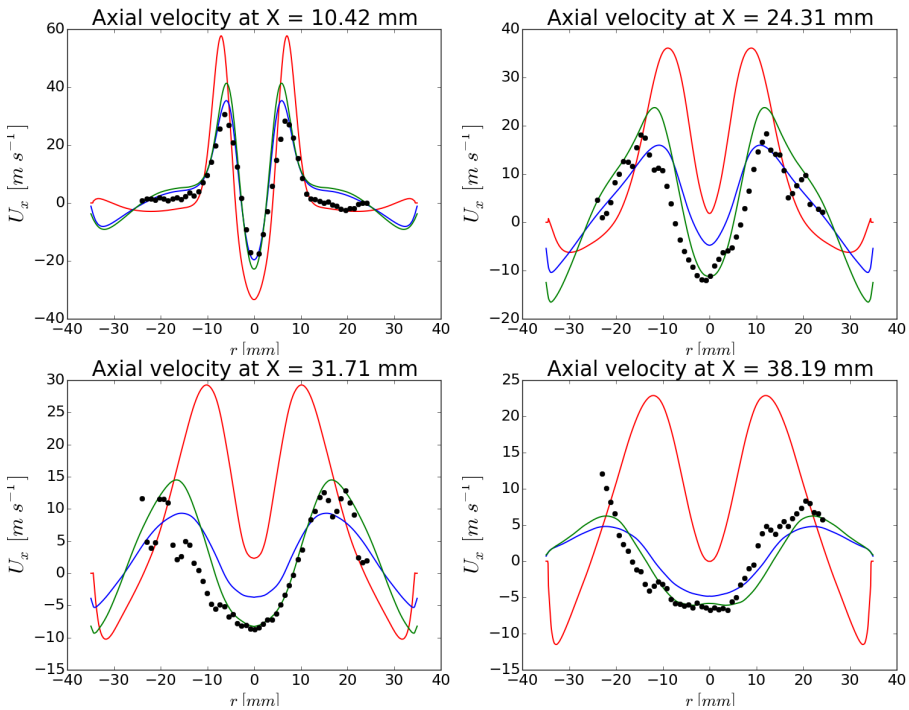

Figure 2.29: *Mean axial velocity profiles for the gas phase at different heights.* —*: adiabatic walls simulation;* —*: isothermal non-relaxed walls;* —*: isothermal relaxed walls;* • *: Experimental data.*

Figure 2.29 shows profiles of the axial velocity for four different heights: $x = 10.42$ mm (top left), $x = 24.31$ mm (top right), $x = 31.71$ mm (bottom left) and $x = 38.19$ mm (bottom right). On theses plots the experimental results (in black dots) are compared to the simulations with adiabatic boundary conditions on the chamber walls (red lines), with isothermal conditions without relax and therefore with pressure oscillations (blue lines) and with isothermal conditions and a relax coefficient (green lines). The change of boundary condition from adiabatic to isothermal, in modifying the position of the flame, has

a great impact on the velocity field, especially further downstream, where the central recirculation zone disappeared in the adiabatic case. The isothermal cases shows results much closer to the experimental measurements, confirming the observations made on the flame shapes. The differences between the simulations with and without the relax are not so striking, mainly because the flame position is not much altered on average. The central recirculation zone is better captured with the relaxed walls, particularly for the highest cuts, in terms of both magnitude and width. The position of the swirled hollow cone is also very well predicted in this case, since the radial position as well as the intensity of the velocity peaks are accurately captured for the three highest cuts. Some discrepancy is present on the $x = 6.71$ mm plot regarding the intensity of the peaks, but overall, the experimental profile is still satisfactorily retrieved.

2.6.3 Impact of the heat losses

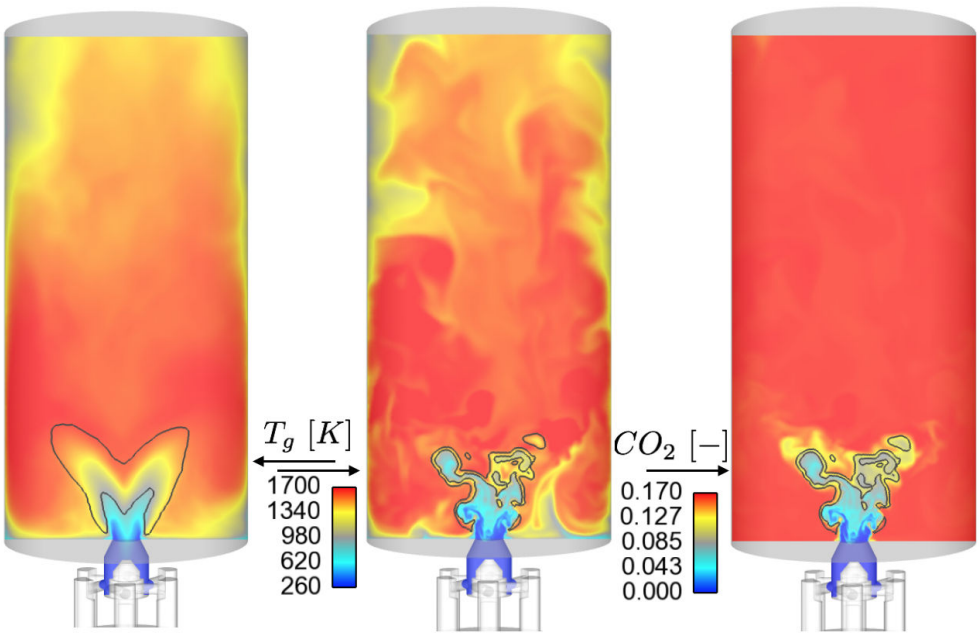

Figure 2.30: *Tangential cuts at $z = 0$ mm of the average (left) and instantaneous (middle) the axial gaseous temperature and of the instantaneous CO_2 mass fraction (right) in the simulation with iso-thermal boundary conditions on the chamber walls. The same color scale in used for the temperature, from $T_g = 260$ K in blue to $T_g = 1700$ K in red. Black iso-lines of the heat release rate $HR = 1 \times 10^8$ $W.m^{-3}$ are added.*

The imposed temperatures at the walls being much lower than the adiabatic flame temperature, the burnt gases are cooled down when they come in contact with the walls. Average and instantaneous fields of the gaseous temperature are displayed on Fig. 2.30, as well as the field of CO_2 mass fraction on the same instantaneous solution. The outer recirculation zone leads the cooled burnt

gases towards the bottom of the chamber and the foot of the flame. The heat losses at the bottom of the chamber prevent the flame front to be attached, so that these gases can go through, creating a region below the flame front where the fresh gases are diluted by burnt gases, the temperature increases as well as the CO_2 mass fraction though no reaction is taking place.

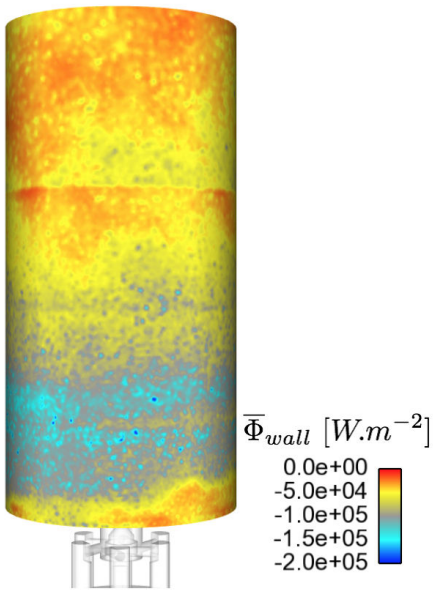

Figure 2.31: *Average normal energy flux on the chamber internal wall.*

Figure 2.31 presents the average normal heat flux on the internal quartz wall. Since energy is lost by the fluid, it is negative everywhere. As could be expected, the heat losses are maximum in the region where $x \in [10; 50]$ mm, which corresponds to the area the jet impacts the wall. From the temporal evolution of the total flux on the internal wall and the bottom of the chamber once an equilibrium has been reached, an mean wall flux $\overline{\Phi}_{wall}$ can be retrieved. In the present case, $\overline{\Phi}_{wall}$ was averaged over $t_{ave} = 15$ ms, starting from a simulated physical time of $t = 250$ ms:

$$\overline{\Phi}_{wall} = \overline{\int_{\mathcal{A}_{wall}+\mathcal{A}_{bottom}} \mathbf{\Phi}_{wall}(\mathbf{x}, t) \cdot \mathbf{n_{wall}} \, dS} = -2381 \text{ W} \tag{2.11}$$

The obtained value for the heat losses is to be compared with the global power of the configuration. In the present case, with an equivalence ratio $\Phi = 0.89$, the power is $\mathcal{P} = 4.96$ kW. This means that the heat losses represent 48 % of the global power. This is another proof, in addition to the flame shape, that the heat losses have a very important impact in the considered configuration and have to be accounted for in order to retrieve the steady-state behaviour of the flame.

2.6.4 Flame analysis

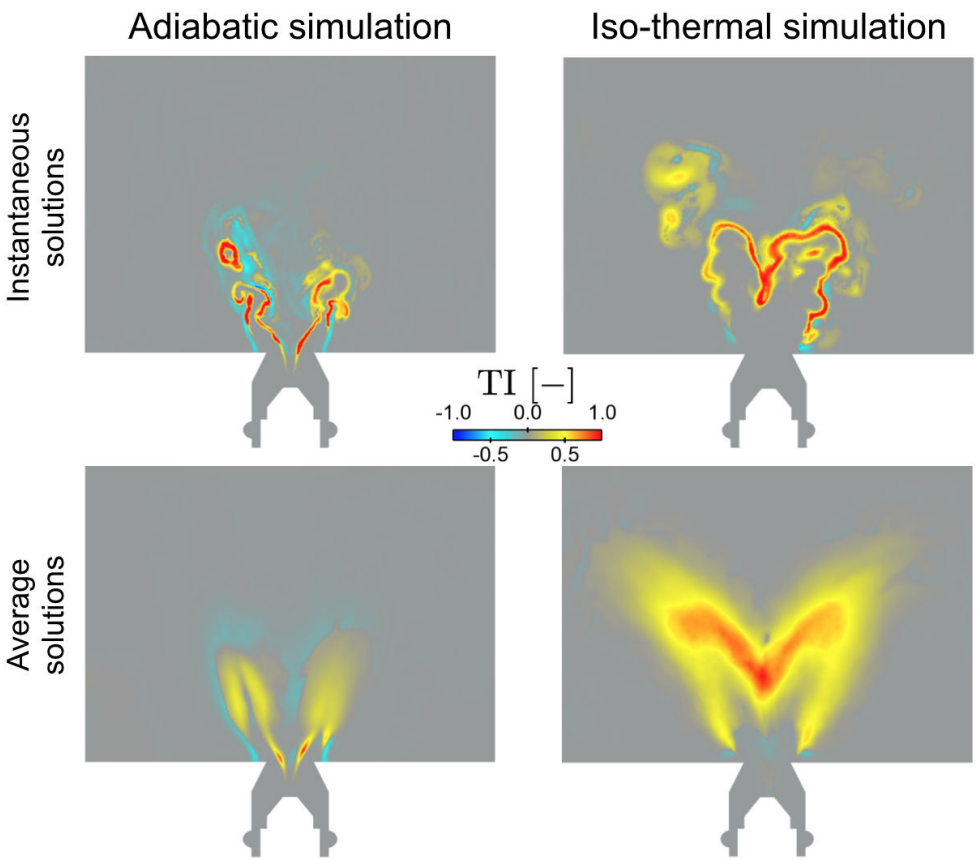

Figure 2.32: *Non-dimensional Takeno's index multiplied by the local heat release rate. Top: TI on instantaneous fields, bottom: TI on average fields; left: adiabatic simulation, right: iso-thermal simulation. Red stands for positive values (premixed regime), blue for negative values (diffusion regime) and grey for zero (no combustion).*

In order to further investigate the local combustion regimes that can be encountered in the flame, and following the methodology proposed by Yamashita et al. (1996) and Reveillon and Vervisch (2005), an interesting indicator is Takeno's index. Considering that in a premixed one-dimensional flame, the gradients of the oxidizer and the fuel mass fractions have the same sign while it is the opposite in a diffusion flame, Takeno's index (TI), defined by Eqn. 2.12, varies between -1 in the diffusion flame zones and 1 in the premixed flame zones.

$$\mathrm{TI} = \frac{\nabla Y_{C_7H_{16}} \cdot \nabla Y_{O_2}}{|\nabla Y_{C_7H_{16}} \cdot \nabla Y_{O_2}|} \tag{2.12}$$

To highlight combustion areas, TI can be multiplied by the absolute value of the heat release rate and normalised. Figure 2.32 shows the TI fields for the

adiabatic walls case (left) and the isothermal relaxed walls case (right), calculated on an instantaneous solution (top) and on an average field (bottom). Both combustion regimes coexist in the adiabatic case, the outer branches attached to the bottom of the chamber are diffusion flames, while the top of the flame burns in the premixed mode. The injection system allows the air and the fuel to mix before the fuel, hence the mostly premixed combustion, but some liquid fuel accumulates at the foot of the flame, which generates some locally rich gases that burn with the recirculation leaner gases, creating the diffusion branch. In the isothermal case, the combustion is even more dominated by the premixed regime. While some diffusion areas are present on the instantaneous solution, the averaged field shows that they are insignificant compared to the premixed zones and are totally erased by the averaging procedure.
The flame structure is further analysed with Fig. 2.33, which displays scatter plots of the local temperature against the mixture fraction Z, defined in Eq. 2.13, for several heights in the chamber, plotted as black dots (left graphs) to highlight dot concentration and coloured by the value of the reaction progress variable (center graphs), defined from mass fractions of CO and CO_2 in Eq. 1.188. Scatter plots of the heat release rate against the mixture fraction are displayed on the right to differentiate the combustion areas from the mixing areas. To ease comparison, the heat release rate was normalised by its global maximum in the chamber. On each plot, the two red vertical lines represent the global injected mixture fraction ($Z_{inj} = 0.056$) and the stoichiometric mixture fraction ($Z_{st} = 0.062$).

$$\mathrm{Z} = \frac{Y_{N2}^{ox} - Y_{N2}}{Y_{N2}^{ox} - Y_{N2}^{fuel}} \tag{2.13}$$

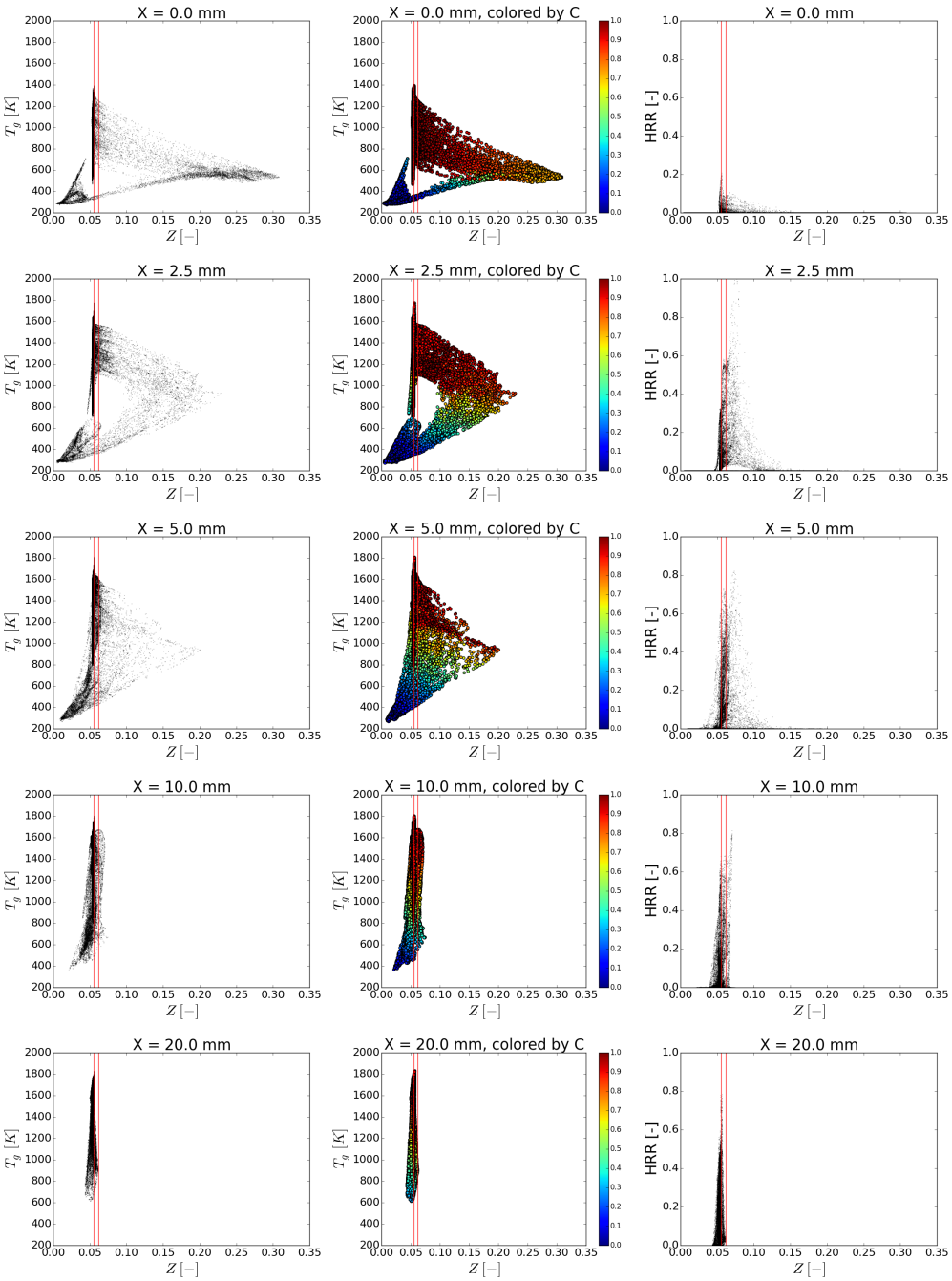

Figure 2.33: *Scatter plots of temperature (left and middle) and heat release rate normalised by the global maximum (right) against mixture fraction for heights x = 0 mm, x = 2.5 mm, x = 5 mm, x = 10 mm and x = 20 mm. The temperature plot is displayed without any colouring (left), coloured by the local progress variable C (right). On each plot, the two red lines represent the global injected mixture fraction ($Z_{inj} = 0.056$) and the stoichiometric mixture fraction ($Z_{st} = 0.062$).*

The analysis of the scatter plots allow to identify several areas that complement the observations made from the field of Takeno's Index.
From $x = 0$ mm to $x = 5$ mm, the denser region on the (T, Z) plots corresponds low mixture fraction and low temperature mixing of the unburnt air and droplets. As they evaporate, the droplets increase the local mixture fraction. At $x = 0$ mm and to a lesser extent at $x = 2.5$ mm and $x = 5$ mm, the presence of recirculating burnt gases in the ORZ creates a mixing branch where the mixture fraction increases at moderate temperatures (below 800 K). In this region, the progress variable increases (middle plots) due to the dilution by burnt gases but the heat release rate plot shows that no combustion is taking place. This corresponds to the mixing below the flame front at moderate temperatures ($T \approx 700$ K) that was also observed on the temperature field displayed on Fig. 2.30.
The heat release rate scatter plots show that the large majority of the combustion takes place around the global injected mixture fraction, meaning that even though large disparity of mixture fraction exist in the unburnt region, the mixture that reaches the flame is quite homogeneous. The warm mixture previously described promotes the evaporation of the droplets by increasing the gaseous temperature below $x = 5$ mm (bottom right region of the (T,Z) scatter plots that was already mentioned) and upon reaching the flame front, which stabilises around $x = 7.5$ mm in the experiment and the simulation, the unburnt gases react and the temperature increases at a constant mixture fraction, as is evidenced by the vertical branch on the (T,Z) plots, which is a typical feature of premixed flames.

2.6.5 Flame lifting process

It was observed in the simulation with isothermal walls that, prior to taking its steady-state lifted position, the flame first stabilises in a position close to that in the adiabatic case. It appears that numerically, the thermal losses at the walls have a characteristic time larger than the stabilisation time, which leads to these two flame shapes.
The ignition is triggered by inserting a sphere of burnt gases in a cold solution that was converged with adiabatic walls. Once the initial flame kernel is added, the boundary conditions are immediately changed to iso-thermal with the steady-state experimental temperatures. Hence, the numerical ignition sequence neither corresponds to an *ignition* event, where the walls are initially at ambient temperature (no preheating of the fresh mixture from hot walls) and are gradually heated as the heat transfers at the walls reach their steady-state, nor to a *re-ignition* event, where the walls are already at thermal equilibrium due to prolonged operation and the mixture is therefore pre-heated before the ignition is triggered. The experimental data that is presented hereafter corresponds to *ignitions*. The numerical prediction of the exact lifting process in these cases, with initially cold walls, would require coupled simulations to cap-

ture the transient heating of the walls. However, since the walls are either at ambient temperature (in the experiment) or steady-state temperature (in the simulation, between 400 K and 900 K), energy is lost by the burnt gases in both cases and the gases are cooled down. The correct physical phenomenon is therefore captured, though not necessarily with the correct magnitude.

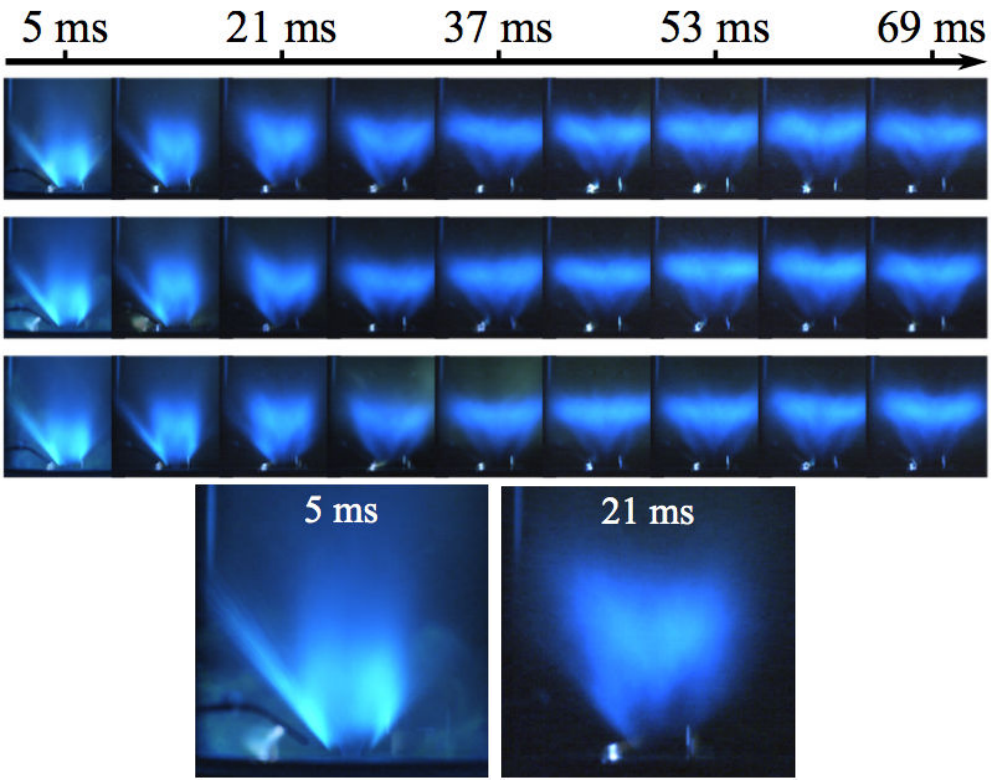

Figure 2.34: *Top: true-color experimental images from three ignition sequences in SICCA-Spray. Bottom: close-up images at $t = 5$ ms and $t = 21$ ms. The images are extracted from Prieur et al. (2018).*

Figure 2.34 presents true-color images of ignition sequences of SICCA-Spray, extracted from Prieur et al. (2018). The images were recorded using a high-speed camera Phantom V2512, providing 16-bit images covering 1280×800 pixels, at a sampling rate of 6000 frames per second, with a shutter duration of 166 μs. The images presented in Fig. 2.34 correspond to the average of 50 images (approximately 8 ms), so as to remove most turbulence in the flame. The top images presents three different successful ignition sequences, triggered by a spark placed towards the bottom of the chamber. Around 5 ms (see bottom left image), the flame is attached to the burner lips and much more compact than at its final shape. After 15 to 20 ms (see bottom right image), the flame expands and lifts, to take the "M" shape presented in section 2.6.2.1. Saturated images presented in Prieur et al. (2018) show that the flame is at

first clearly attached to the burner lips and even enters the swirler through the central recirculation zone. The same behaviour is also observed experimentally on MICCA-Spray, during the light-round sequence.
Several explanations are proposed in Prieur et al. (2018) to explain this behaviour, among which is the impact of the thermal losses at the walls, that take some time to reach their steady-state values. This hypothesis is strengthened by the results from both adiabatic and isothermal walls simulations.

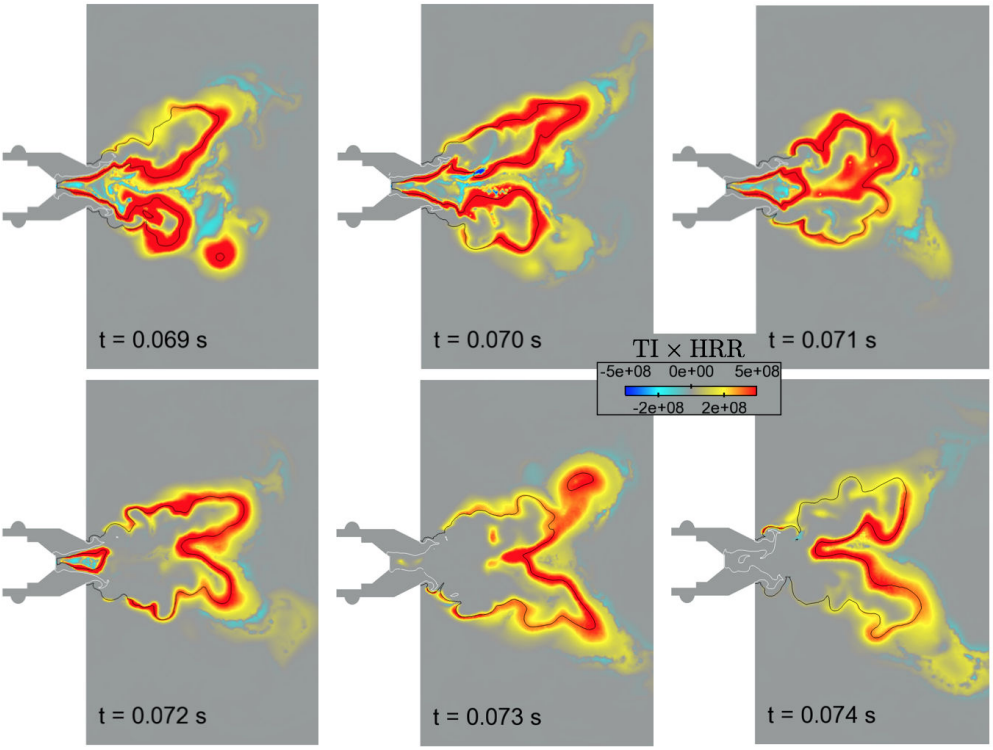

Figure 2.35: *Instantaneous fields of TI × HRR at six instants between $t = 69$ ms (top left) and $t = 74$ ms (bottom right), $t = 0$ ms corresponding to the insertion of the burnt gases sphere. Two iso-lines of the progress variable $c = 0.1$ (in white) and $c = 0.9$ in black are added. These instants are chosen to show the lifting of the flame in the simulation.*

Figure 2.35 presents simulation's fields of Takeno's index multiplied by the heat release rate (TI × HRR) for different instants around the time of the lifting of the flame. Two iso-lines of the progress variable $c = 0.1$ (in white) and $c = 0.9$ (in black) are added.
When the flame is still attached ($t = 69$ ms and $t = 70$ ms), it is anchored inside the swirler unit, up to the fuel injection. The flame has stabilised at this position around $t = 35$ ms. At $t = 71$ ms, the flame branches in the inner shear layers come in contact and form two separate flame fronts, an external one that starts to lift and an internal one that propagates towards the fuel injection

($t = 72$ ms). The internal flame kernel travels upstream and is extinguished, and the flame stabilises into its second and definitive position, as an "M" flame ($t = 73$ ms and $t = 74$ ms)
The progress variable iso-lines allow to highlight some dilution mechanisms by the burnt gases that occur when the flame lifts: at $t = 73$ ms and $t = 74$ ms, the $c = 0.1$ iso-line goes up to the liquid injection while TI $\times$ HRR $= 0$ there, meaning that the presence of burnt gases in this region is due to dilution by recirculation burnt gases rather than combustion.
The lifting process appears to be similar between the simulation and the experiment, with the merging of the flame branches and the creation of a flame kernel that travels upwards and is extinguished. In the simulation, the addition of heat losses at the walls through isothermal boundary conditions, imposing the experimental steady-state temperatures, have triggered the position transition, which is never observed in simulations with adiabatic conditions. This strongly suggests that the same phenomenon is responsible for the flame shape behaviour in the experiment. The transient evolution of the walls temperature would have to be simulated in order to obtain a definitive answer.

2.7 Influence of the injected diameter

The simulation has been successfully compared to the experimental results and the choice of injected diameter has proven able to retrieve the main features of the flame. It is interesting to look at the results obtained with different injected diameters, to a posteriori evaluate the choice of diameter. Two additional simulations were carried out with iso-thermal walls and with two particular diameters that are often used to represent a polydisperse spray: the mean diameter D_{10} and the Sauter mean diameter D_{32}. For these simulations, the pressure oscillations observed with the optimal diameter D_{opt} were also present, so the same modification of the boundary condition was used.

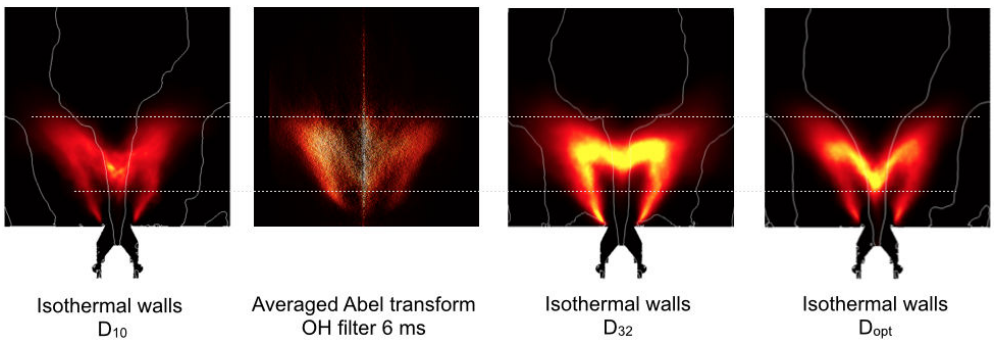

Figure 2.36: *Average flame shapes for several values of the injected diameter, for $d_{inj} = D_{10} = 8$ μm (left), $d_{inj} = D_{32} = 20$ μm (center right), and $d_{inj} = D_{opt} = 15.3$ μm (right), compared to the experimental averaged Abel transform (center left). The white lines are iso-lines of the gaseous axial velocity at $u = 0$ $m.s^{-1}$.*

Average flame shapes for these two new cases are shown in Fig. 2.36 ($d_{inj} = D_{10}$ in the far left $d_{inj} = D_{32}$ in the center right) and compared with the experimental Abel transform (center left) and the previous simulation where the optimal diameter was injected (far right). Regarding the numerical results, the heat release rate is normalised by its maximum value for the sake of comparison and varies from 0 in black to 1 in yellow. Overall, the addition of the isothermal boundary condition seems to have had a greater effect on the position and the shape of the flame than the value of the injected diameter. The simulation with the Sauter mean diameter ($d_{inj} = D_{32}$) yields the poorer results, while the outer branches at the foot of the flame are similar to the other simulations, the stabilisation of the flame around the central axis is not as well predicted as in the other two cases. The height of the flame is well captured by all three simulations.
The D_{opt} and D_{10} cases exhibit flame shapes and positions that are very close to each other and to the experimental flame. They can be further compared through the gaseous axial velocity field, for which experimental measurements are available.

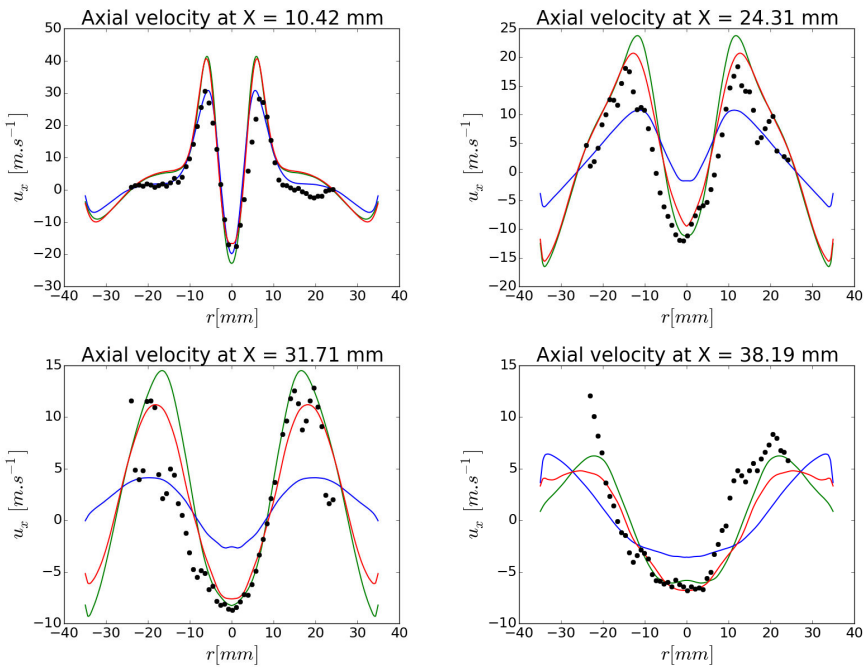

Figure 2.37: *Mean axial velocity profiles for the gas phase at different heights for different values of the injected diameter.$D_{inj} = D_{opt}$; —: iso-thermal relaxed walls, $D_{inj} = D_{opt}$; —: iso-thermal relaxed walls, $D_{inj} = D_{32}$; —: iso-thermal relaxed walls, $D_{inj} = D_{10}$; • : Experimental data (provided by K. Prieur and D. Durox).*

Figure 2.37 compares the velocity profiles at different heights above the injection for the two additional simulations (D_{10} in red and D_{32} in blue), compared

with the cases where the optimal diameter is injected, without the pressure oscillations (in green). The numerical profiles are compared to the experimental PIV measurements, in symbols. At $x = 10$ mm, little difference can be seen between all the cases, they all retrieve fairly well the position of the peaks and the recirculation zones. Except for the D_{32} case, the magnitude of the peaks is slightly overestimated by all cases. In the higher heights however, the D_{32} profiles are not at all able to retrieve the experimental velocities, while the D_{opt} and D_{10} cases predict very well the central recirculation zone and the radial position of the peaks. Surprisingly, even though $D_{10} < D_{opt} < D_{32}$, the D_{opt} curves are not located between D_{10} and D_{32} curves.
Due to the noise in the experimental data, it is difficult to see which of the D_{opt} and D_{10} cases gives the best results for the magnitude of these peaks, but on $x = 31$ mm and $x = 38$ mm, D_{opt} seems to be more accurate.

2.8 Conclusion

In this chapter, the results from simulations of the mono-burner SICCA-Spray as well as the methodology that led to the different choices that were made have been presented. The main objective of the study of this configuration was to be able to test on a reduced scale geometry the numerical set-up later used on MICCA-Spray. Validation cases were conducted depending on the available experimental data. Simulations were first run on the unconfined version of SICCA-Spray, without combustion, and successfully compared with the corresponding experimental velocities. A parametric study, using Uncertainty Quantification tools, has also been carried out to look in more details into the influence of the injected diameter in an Eulerian mono-disperse simulation that aims at representing a polydisperse spray. The conclusions from this study were then applied to the simulation of the confined version of the burner, with and without combustion.
The first simulation with adiabatic boundary conditions on the walls was not able to predict the correct steady-state flame shape. Instead, the flame was attached to the injector lips and much more compact than in the experiment. The addition of isothermal boundary conditions on the chamber walls, using temperatures measured experimentally, evidenced the importance of the heat losses at the walls by predicting the correct flame shape and velocity profiles. In addition, experimental and numerical observations show that prior to taking its final lifted position, the flame is first anchored to the injector exit, in a shape close to that obtained in the adiabatic walls simulation. Consequently, an adiabatic wall assumption is valid for the ignition and first instants of the flame stabilization on a single injector.
The numerical set-up that has been gradually assessed and validated in this chapter, can now be applied to the full scale configuration MICCA-Spray, which is done in the next chapter.

Chapter 3

Large eddy simulation of light-round in MICCA-Spray and comparison with experiments

This chapter presents the simulations of relight sequences of the MICCA-Spray combustor, using the numerical set-up defined and validated on the simpler configuration SICCA-Spray in chapter 2. The liquid n-heptane injection is accounted for by an Eulerian mono-disperse representation of the spray and the combustion is modelled through the Thickened Flame model for LES (TFLES). The pre-heated quartz walls condition studied experimentally is approximated through an adiabatic boundary condition in the simulation. Three operating points are considered, for three values of the equivalence ratio. The establishment of the cold flow is carefully assessed to ensure that a steady-state has been reached that can be compared to the experiment. Validations with experimental data are performed that include comparison of the direct visualisations of the flame, as well as quantitative comparisons of the different flame propagation durations, in the whole chamber (light-round duration) and between injectors (sector ignition delays). Very good agreement is found for two of the three cases, while the propagation speed appears to be less well retrieved for the third case. These good results validate the ability of the simulation to predict the light-round sequence in an annular combustor with liquid injection, thus enabling further analysis, presented in chapter 4.

Contents

3.1 Introduction **128**
3.2 MICCA-Spray: experimental configuration **130**
3.2.1 Presentation of MICCA-Spray 130
3.2.2 Sensors and imaging instrumentation 130
3.2.3 Experimental ignition procedure 131
3.3 Numerical configuration and initial solution **133**
3.3.1 Simulation procedure 133
3.3.2 Numerical set-up 134
3.3.3 Cold flow convergence on the bi-sector 135
3.4 Light-round simulation and results **142**
3.4.1 Initial solutions on the annular chamber 142
3.4.2 Light-round durations 144
3.4.3 Flame shape comparison 145
3.4.4 Heat release rate evolution 150
3.4.5 Sector ignition delays 154
3.5 Conclusion **157**

3.1 Introduction

As was indicated in the general introduction of the manuscript, ignition constitutes one of the critical design issues of any aero-engine combustors. It has to be performed in a smooth, safe and reliable manner over a wide operability range. For a multiple injector combustor, a successful ignition can typically be decomposed into three main stages as done by Lefebvre and Ballal (2010). The first two stages correspond to the flame kernel initiation and the kernel's expansion and propagation to stabilize a flame on a single burner. In a combustor with multiple injectors, the last stage of the ignition process involves the flame propagation from each ignited burner to the next until the full system is ignited. In the case of an annular chamber, this phase is called the light-round. Compared to single burner studies (Marchione et al. (2009), Jones and Tyliszczak (2010), Subramanian et al. (2010), Esclapez et al. (2015) and Marrero Santiago et al. (2017)), this stage has been less well documented in the past. The interest in the need to cope with burner to burner initiation has recently led to a number of studies of ignition on multiple injector systems.
Results of the first large-eddy simulation (LES) of the ignition of a helicopter combustion chamber reported by Boileau et al. (2008) have shown the strong impact of burnt gases volumetric expansion on the flame propagation velocity but with no comparison with experiments. Flame propagation has been studied experimentally in a linear array of injectors with varying inter-injector spacing

with gaseous premixed injection by Barré et al. (2014) and liquid n-heptane injection by Marrero Santiago et al. (2017). Inter-injector distance was found to modify the pattern of flame motion giving rise to two propagation modes. This feature has been retrieved in LES by Barré et al. (2014) and also observed in an annular combustor in Machover and Mastorakos (2016) and Machover and Mastorakos (2017). Nonetheless, such linear configurations do not account for specific phenomena arising in annular geometries.

In 2013, two experimental studies have been reported on successful light-round sequences in idealized annular systems, with premixed propane-air injection (Bourgouin et al. (2013)) and methane-air injection (Bach et al. (2013)). Both studies highlight the influence of the mixture equivalence ratio and bulk velocity on the light-round duration. Later on, investigations have reported the effects of non-premixed injection (Machover and Mastorakos (2016)), inter-injector spacing (Machover and Mastorakos (2016) and Machover and Mastorakos (2017)), and liquid fuel injection (Prieur et al. (2017)), bringing new insights into the ignition of realistic gas turbines.

The first comparisons of light-round simulations with experiments carried out by Philip et al. (2015a) and Philip et al. (2015b) have demonstrated the ability of LES to successfully predict the light-round duration and flame propagation behaviour in an annular fully premixed propane-air combustor and for several operating points. A first analysis of the flame propagation pattern has distinguished several stages in the light-round, thus refining the classical three phase decomposition of the process described by Lefebvre and Ballal (2010).

Accounting for the spray of droplets presents an additional complexity, but is essential when dealing with realistic aeronautical configurations. Prieur et al. (2017) and Prieur et al. (2018) carried out the first experimental visualisation and characterisation of ignition in the laboratory scale annular combustor MICCA-Spray, fed with liquid spray.

In the present chapter, large-eddy simulations of the light-round process in MICCA-Spray with liquid n-heptane injection are presented, along with comparisons with the corresponding experimental data. The design of MICCA-Spray, carried out at EM2C, was a compromise between representativity of industrial aero-combustors and simplicity to allow detailed experimental diagnostics to characterise the system and enable validations of the simulations. With this in mind, MICCA-Spray has some characteristics typical of industrial configurations, such as sixteen swirl injectors fed with liquid fuel arranged in an annular pattern. The lateral walls are made of transparent quartz that allow full optical access for detailed visualisations of the flame.

This chapter is organised as follows, the experimental set-up is detailed in section 3.2, along with the available diagnostics. The simulations are then carried out using the numerical set-up validated in SICCA-Spray and presented in chapter 2, for three different operating points. Close attention is paid to the establishment of the cold flow in the chamber prior to the triggering of the ignition (section 3.3). The simulations are finally compared to the corre-

sponding experimental data in terms of light-round duration, flame macroscopic behaviour and sector ignition delays in section 3.4.

3.2 MICCA-Spray: experimental configuration

3.2.1 Presentation of MICCA-Spray

The MICCA-Spray set-up (Fig. 3.1) is a laboratory-scale combustor representative of a helicopter combustion chamber (Prieur et al. (2017)). It is composed of sixteen swirled injectors placed in the backplane of an annular chamber made of two cylindrical coaxial quartz walls. These injectors are fed with air and liquid n-heptane. The air is injected at ambient temperature into an annular plenum by eight identical channels and then into the chamber through the sixteen injectors. The fuel is fed to sixteen simplex atomizers placed after the swirlers (see the sketch in Fig. 3.1) and positioned with a 6 mm recess with respect to the chamber backplane. The measured swirl number is 0.68. The outer and inner quartz walls that compose the chamber have a diameter of, respectively, 400 mm and 300 mm and are both 200 mm high. The burnt gases are exhausted into the atmosphere. The MICCA-Spray chamber is able to reach a maximum power of 120 kW.
The association of two swirl devices, one sixteenth of the volume of the chamber and one air supply channel forms a periodic pattern that is repeated eight times to make up the whole set-up. This pattern is later used in the simulation to obtain steady-state fields and the geometry is called *bi-sector*. To ease post-processing, the chamber is divided into two halves, designated as H+ and H-, that are defined in Fig. 3.2. Sixteen sectors are also identified in Fig. 3.2. Sector S0 is the one where the ignition is initiated and sector S8 is located on the opposite side, where the flame front merging is expected. The sectors in between are respectively labelled S_i if on the H+ side of the chamber and S_{-i} on the H- side of the chamber, with i ranging from 1 to 7.

3.2.2 Sensors and imaging instrumentation

The walls of the chamber are fully transparent, which allows an optical access to the flame. The evolution of the flame during the ignition sequence is recorded by a high-speed camera Phantom V2512 with a resolution of 1280×800 pixels. The frame rate and shutter speed are respectively 6000 Hz and 166 μs. The camera, equipped with a CH* filter featuring a bandwidth of 420-440 nm, is located opposite the spark igniter, behind the S_8 sector in low-angle shot. MICCA-Spray also features five pressure taps, placed as shown in Fig 3.2. Each pressure tap is connected to a microphone flush mounted in a waveguide, with an acquisition frequency of $32,768$ Hz. Finally, eight photo-multipliers (PM) are installed on the H- side of the chamber, each focused on one injector and equipped with a filter that is sensitive to the light emission of the OH* chemical

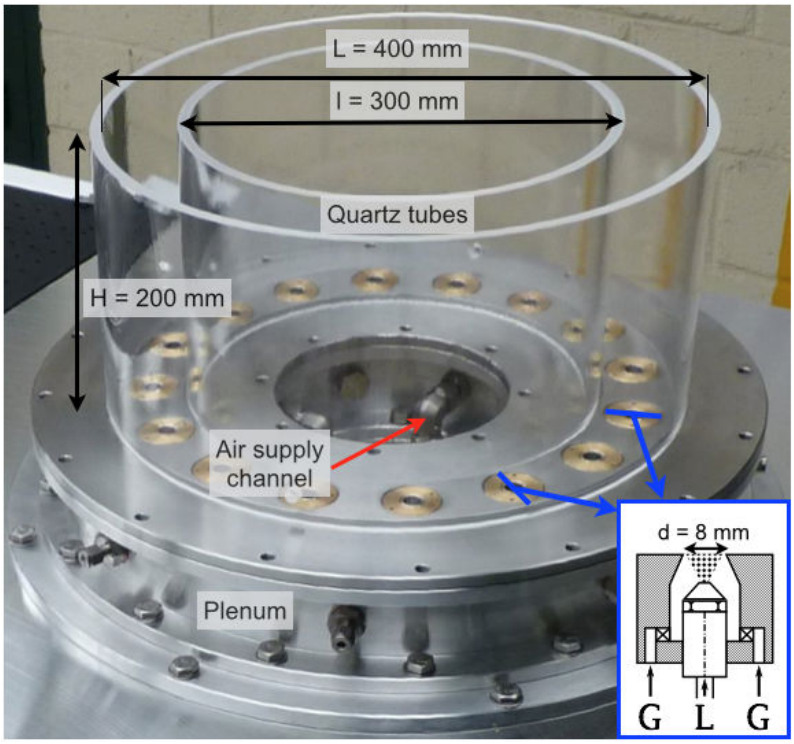

Figure 3.1: *Direct view of the MICCA-Spray combustion chamber. The sketch at the bottom right represents a cut of the swirler unit showing the gaseous (G arrows) and liquid (L arrow) injection.*

radical.

3.2.3 Experimental ignition procedure

To compare experimental and numerical results, it is primordial to achieve similar conditions. In this respect, one central issue is the numerical treatment of the boundary conditions. The impact of temperature on the ignition delay is significant as shown in Bourgouin et al. (2013), Prieur et al. (2017) and Lancien et al. (2017), and is detailed in chapter 5. As a first approximation, the choice is made to first neglect wall heat transfer in the numerical simulation and assume that the walls are adiabatic. In order to match as closely as possible this condition experimentally, one must reduce the difference in temperature between the burnt gases and the walls. As in previous combined experimental and numerical studies (Philip et al. (2015a) and Philip et al. (2015b)), the ignition is then examined under *relight* conditions, when the walls are at a temperature corresponding to the steady-state stabilized flame regime. With such hot walls, heat losses are minimal. In practice, MICCA-Spray is first operated for approximately 10 minutes until the steady-state is reached. Measurements of the external wall temperature evolution with premixed propane-air injec-

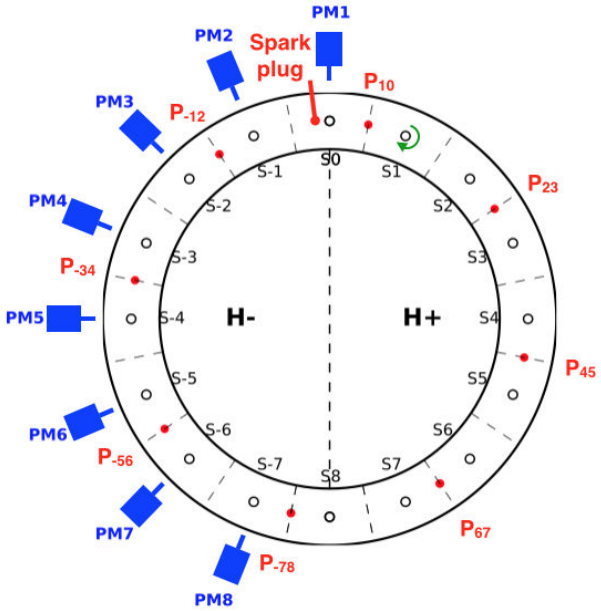

Figure 3.2: *Schematic top view of the MICCA-Spray backplane showing the swirlers positions, photo-multipliers (PM), spark plug and swirl direction.*

tion, displayed in Fig. 3.3, show that after this time, a plateau has appeared. The liquid supply is then turned off so that combustion is stopped and the air injection evacuates the burnt gases from the chamber. Before the walls have time to cool, the liquid injection is turned back on and the relight ignition sequence can be triggered. In the practical operation of an industrial combustor, ignition is initiated as soon as fuel begins to flow in the chamber, however, the transient ramping of the fuel mass flow rate to the nominal value is not well controlled and this would complicate comparisons of ignition simulations since the light-round would then occur in an unknown fuel-air mixture. To allow a consistent comparison, the ignition in experiments is initiated once a permanent regime has been reached for the unburnt two-phase mixture in the chamber. This requires a few seconds, a duration that exceeds the residence time in the combustor, so that the air that had chased the burnt gases is fully replaced by the fresh two-phase mixture, while the change of wall temperature remains negligible (see Fig. 3.3).

In the present study, three operating points are considered, for three different global equivalent ratios: $\Phi = 0.8$, $\Phi = 0.89$ and $\Phi = 1.0$, which are summarized in Table 3.1. In chapter 2, the validations that were carried out on the single burner SICCA-Spray are detailed and an optimal value for the injected diameter is selected for the case $\Phi = 0.89$. In order to keep these conclusions as relevant as possible for the other two cases, the choice was made to vary the equivalence

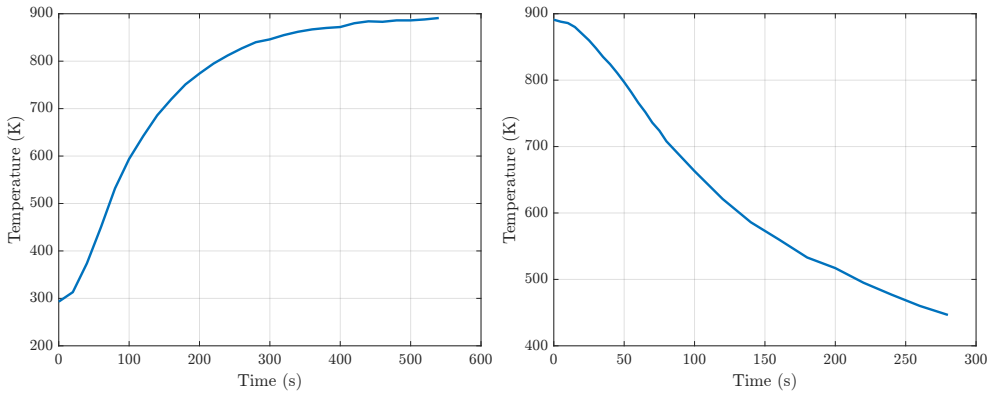

Figure 3.3: *Temporal evolution of the external quartz wall temperature between two injectors and at $x = 40$ mm with premixed propane-air injection. Left: evolution after the triggering of the ignition, $t = 0$ s corresponds to the ignition of the chamber. Right: temperature evolution after extinction of the chamber at $t = 0$ s. The temperatures were measured by applying a thermocouple against the wall.*

Equivalence Ratio		0.8	0.89	1.0
Liq. fuel flowrate	[g.s^{-1}]	1.778	1.778	1.778
Air flowrate	[g.s^{-1}]	33.57	30.19	26.85

Table 3.1: *Summary of the considered operating points with liquid n-heptane injection.*

ratio for a constant combustor power $\mathcal{P} = 79.3$ kW. The liquid fuel flowrate is therefore kept identical while the air flowrate is modified. The assumption is made that in that way, the droplet size distribution does not vary significantly between the operating points, so that the same value of the injected diameter can be used in all three simulations.

3.3 Numerical configuration and initial solution

3.3.1 Simulation procedure

In order to enable reliable comparisons with the experiment, it is primordial to ensure that the simulation is carried out with conditions that are as close as possible to the experimental ones. In particular, some care has to be put into the generation of the initial solution of the light-round sequence. Due to computational cost, it is not possible to simulate the few seconds used in the experiment to ensure that the flow is fully developed in the chamber before triggering the ignition. Instead, as detailed in Section 3.3.3, a criterion is defined to check that steady-state mixture conditions are approximately met on

the reduced configuration called *bi-sector*. Moreover, as mentioned previously, the ignition is experimentally initiated by means of a plug generating a series of sparks until a flame kernel forms with sufficient energy to be able to propagate. This first phase involves complex non-equilibrium physics and is not examined here. The present work focuses on the cases where the plug has succeeded in creating a stable kernel, which is therefore numerically represented by a sphere of burnt gases placed in the vicinity of the first injector in the converged cold flow solution.

3.3.2 Numerical set-up

The numerical set-up is identical to the one that was validated on SICCA-Spray. Simulations are carried out with the AVBP (Schönfeld and Rudgyard (1999)) code, jointly developed by Cerfacs and IFPEN, which solves the three-dimensional Navier-Stokes equations for reactive and compressible flows on unstructured meshes. This software is based on a two-step Taylor-Galerkin weighted residual central distribution scheme (TTGC), third order in time and space (Colin and Rudgyard (2000)), for both gaseous and liquid phases. The subgrid scale turbulence is described with the Wall Adapting Local Eddy model (Nicoud and Ducros (1999)). As indicated previously, the liquid phase is modelled using an Eulerian-Eulerian mono-disperse approach. The evaporation of the uniform temperature droplets is described by the Abramzon-Sirignano (AS) model (Abramzon and Sirignano (1989)). In Sect. 1.3.5 two variations of the AS evaporation model were distinguished, the *simplified* version, which was used for the first $\Phi = 0.89$ simulation and the *complex* version, used for the second $\Phi = 0.89$ as well as for the $\Phi = 0.8$ and $\Phi = 1.0$ cases.
The n-heptane chemistry is described using the two-step mechanism described in Paulhiac (2015) and Shum-Kivan et al. (2016) called 2S_C_7H_{16}_DP and obtained using the methodology proposed in Franzelli et al. (2010) to reproduce the laminar flame speed and the adiabatic temperature for a wide range of operating conditions. The large eddy simulation combustion model describing the unresolved small scale flame structures, the propagation of the flame and its interaction with turbulence relies on the Thickened Flame scheme (TFLES, Colin et al. (2000)), described in Section 1.4.1. This model is based on the artificial thickening of the flame fronts so as to be able to resolve it on the mesh, coupled with an efficiency function $\mathcal{E}$ that accounts for the subgrid scale flame wrinkling lost with the thickening. The thickening of the flame front is defined dynamically according to Legier et al. (2000) so that the combustion model only impacts the flame region. This is used in combination with the efficiency function derived in Charlette et al. (2002).
The only adaptation of the TFLES model, which is initially derived for gaseous premixed flames, to describe spray flames is the application of the thickening to the evaporation source terms, as recommended by Boileau (2007).This choice of combustion modelling will allow to investigate the adequacy of such a robust

set-up before considering more advanced models in the future.

3.3.3 Cold flow convergence on the bi-sector

In order to reduce the computational cost by taking advantage of the periodic patterns in MICCA-Spray, the convergence of the initial cold flow was carried out on the bi-sector, which corresponds to one-eighth of the chamber. As will be detailed in the following, special attention was given to the establishment of the velocity and species fields.

3.3.3.1 Geometry and mesh

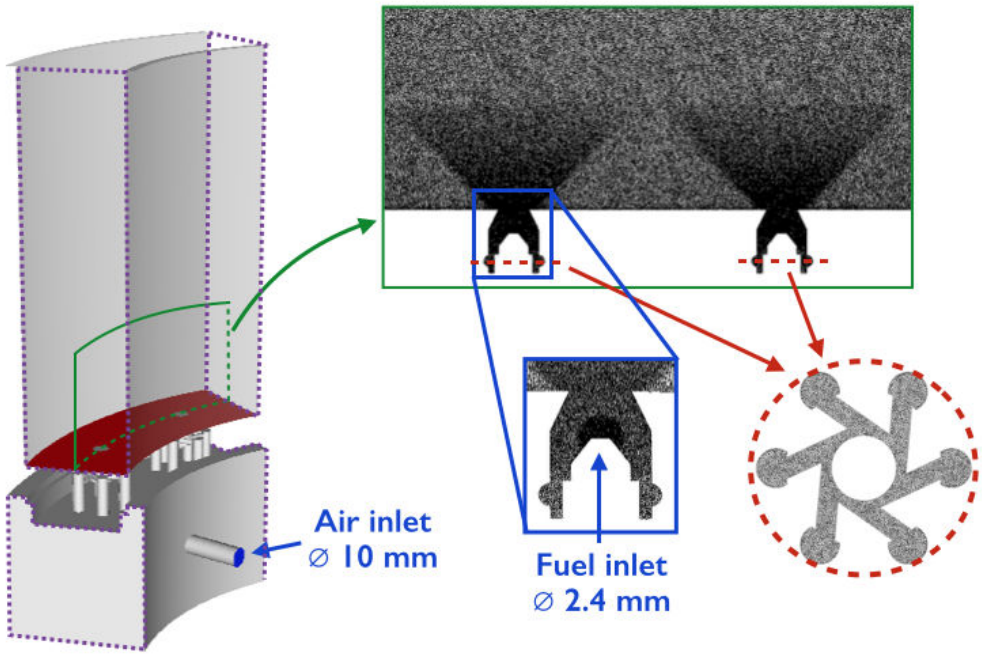

Figure 3.4: *Visualisation of the geometry and mesh of a bi-sector. The mesh is shown through a cylindrical slice at the middle of the chamber.*

The two-phase injection of the annular chamber is composed of 16 swirler units, 16 fuel hollow cone injectors and 8 air inlets. In consequence, the chamber can be divided into eight identical portions, called hereafter *bi-sectors*, whose geometry is shown in Fig. 3.4. Thanks to the axi-periodicity of the chamber, the simulation of one portion of the chamber is sufficient in order to capture steady-state phenomena, and in particular the cold aerodynamic flow.
The geometry used in the simulation of a bi-sector is therefore composed of:

- A 45 deg portion of the chamber, the plenum and the atmosphere (the latter is not shown in Fig. 3.4).
- Two swirler units (see the green insert in Fig. 3.4).

- Two fuel injectors that generate hollow cone sprays of n-heptane droplets.
- One air injector, in the form of a 10 mm-diameter duct in the plenum.
- Two pairs of periodic lateral boundary conditions, for the chamber and the plenum, highlighted with violet dashed lines in Fig. 3.4.

In the experiment, the exit of the chamber is free and the exhaust gases are released in the atmosphere. To avoid numerical issues, it is often best to put the boundary conditions as far away as possible from the area of interest, namely the inside of the chamber. To that end, and similarly to what was done for the burner SICCA-Spray, a large atmosphere is added at the exit and around the chamber. The bottom boundary condition of this atmosphere is an inlet with an inlet velocity of 1 m.s^{-1} that mimics entrainment phenomena. The geometry of the complete chamber is obtained by replication of that of the bi-sector.

Element and node counts	**Bi-sector**	**360**
Number of nodes	6.3 Million	50.7 Million
Number of cells	36.2 Million	290 Million

Table 3.2: *Mesh characteristics for the bi-sector and MICCA-Spray*

The mesh for the bi-sector, and then the full chamber, is generated according to the conclusions drawn from the simulation of SICCA-Spray in terms of mesh refinement. This leads to grids composed of, respectively, 36 million and 290 million elements, as is summarised in Tab. 3.2. As can be seen on the mesh slices in Fig. 3.4, the regions where high concentrations of liquid, high levels of turbulence, high velocity gradients or combustion are present are refined. The cell sizes for each region are also given in Tab. 3.3. The swirler region is particularly refined to capture the turbulence and the mixing between the air and the liquid. A truncated cone of refined cells is placed at the location of the swirled hollow cone. Finally, since a vertical flame front is expected to propagate in the chamber, combustion in the top half of the chamber needs to be accurately captured, so the cell size ratio between the bottom and the top of the chamber is limited to 2.

Mesh region	**Cell size Δx**
Liquid injection	0.13 mm
Swirler	0.2 mm
Bottom of swirling spray	0.2 mm
Top of swirling spray	0.5 mm
Bottom of the chamber	0.5 mm
Top of the chamber	1 mm

Table 3.3: *Summary of cell sizes for the bi-sector and annular grids.*

3.3.3.2 Converged solution for the three cases

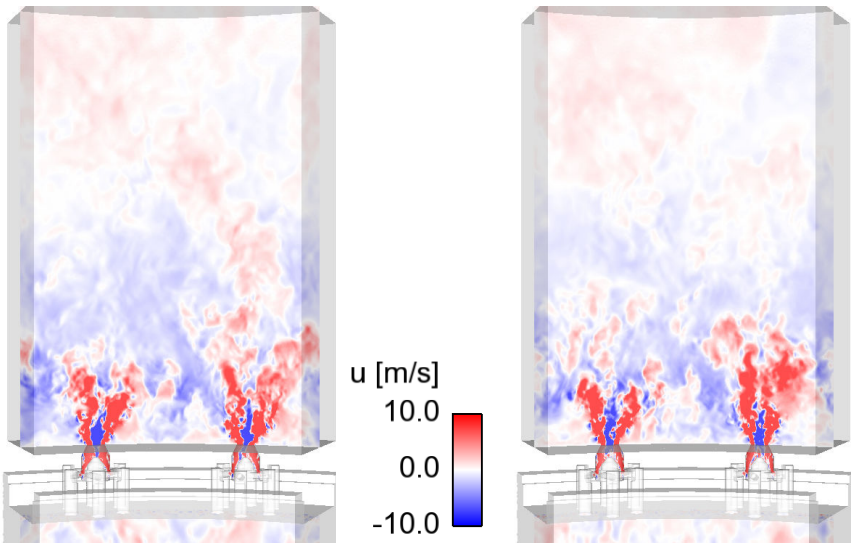

Figure 3.5: *Visualisation of the instantaneous axial velocity u on a slice at $r = 175$ mm for case $\Phi = 0.89$, at instants $t = 0.3$ s (left) and $t = 0.4$ s (right).*

As mentioned previously, three operating points are considered here, hereafter referred to as cases $\Phi = 0.8$, $\Phi = 0.89$ and $\Phi = 1.0$. For each case, one has to ensure that the flow field are sufficiently converged. While the velocity fields are usually converged within 10 to 100 ms, the gaseous species fields, that are modified by the evaporation of the liquid droplets and subsequent mixing, present a larger characteristic time. Figures 3.5, 3.6 and 3.7 present instantaneous visualisations of the axial velocity (Fig. 3.5), the fuel mass fraction $Y_{C_7H_{16}}$ (Fig. 3.6) and the liquid mass density $\alpha_l \rho_l$ (Fig. 3.7) for the case $\Phi = 089$ at two different instants $t = 0.3$ s (left) and $t = 0.4$ s (right), on a cut at $r = 175$ mm.
These snapshots illustrate the fact that while the axial velocity field seems to have reached its steady-state regime, the fuel mass fraction is clearly still evolving. The evaporation of the liquid droplets appears to take place at the bottom of the chamber, where low-speed recirculation zones are present, particularly in the inter-injector region (see axial velocity fields), and lead to a transient accumulation of fuel vapour, which is then gradually pushed downstream.
It is necessary to select a criterion that allows to evaluate the convergence of the flow fields while keeping the computational cost reasonable. Since the species mass fractions appear to be the limiting quantities, the mean gaseous equivalence ratio was used as such criterion, defined as $\Phi_{gas}^{mean} = \mathrm{s}\, M_{C_7H_{16}}/M_{O_2}$, with $M_{C_7H_{16}}$ and M_{O_2} the total masses of gaseous n-heptane and oxygen in the chamber and s = 3.52 the stoichiometric coefficient associated to the reaction of n-heptane and air. The evolution of Φ_{gas}^{mean} for the three cases is plotted in Fig. 3.8 as dots. The previous observations are here confirmed, the mean gas

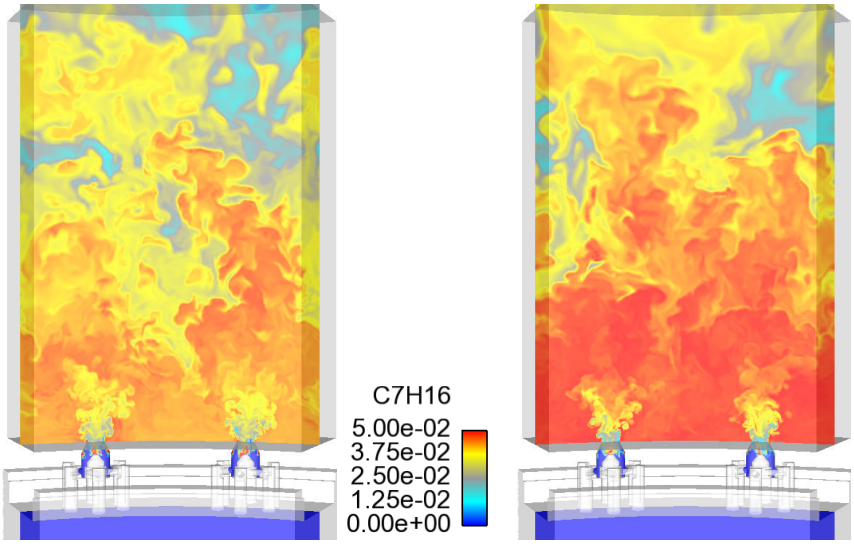

Figure 3.6: *Visualisation of the instantaneous n-heptane mass fraction $Y_{C_7H_{16}}$ on a slice at $r = 175$ mm for case $\Phi = 0.89$, at instants $t = 0.3$ s (left) and $t = 0.4$ s (right).*

equivalence ratio evolves quite slowly. For each data set, a fitting is realized on a and λ in the function $a(1 - e^{-\lambda x})$ and is plotted in solid lines of the corresponding color.

For the three cases, 95% of its estimated final value (highlighted by the left vertical dashed lines) is reached after approximately 1 second of simulated physical time. The simulations were launched on the super-computer TURING, on which one iteration of the cold flow in the bi-sector lasts 0.18 s on 1024 nodes that are each composed of 16 processors. The timestep in the present cases being $dt = 8 \times 10^{-8}$, the simulation of one second of physical time cost 36.9 million CPU hours on TURING. Obtaining 99% (right vertical dashed lines) would have necessitated approximately 0.5 s more of simulated physical time for each case, which was unaffordable considering the computational cost and the available resources.

Instantaneous snapshots of these converged bi-sector solutions are displayed in Figs. 3.9 and 3.10, where slices at $r = 175$ mm are coloured by the liquid density $\alpha_l \rho_l$ (Fig. 3.7) and the local gaseous equivalence ratio Φ_{gas} (Fig. 3.10). The liquid density fields show that for $\Phi = 0.8$ and $\Phi = 0.89$, the n-heptane is fully prevaporised before the chamber's exit and no liquid remains in the upper half of the chamber. Logically, the local gaseous equivalence ratio is higher for $\Phi = 0.89$ than for $\Phi = 0.8$.

For case $\Phi = 1.0$ however, a saturated state is reached and some liquid remains everywhere in the chamber.

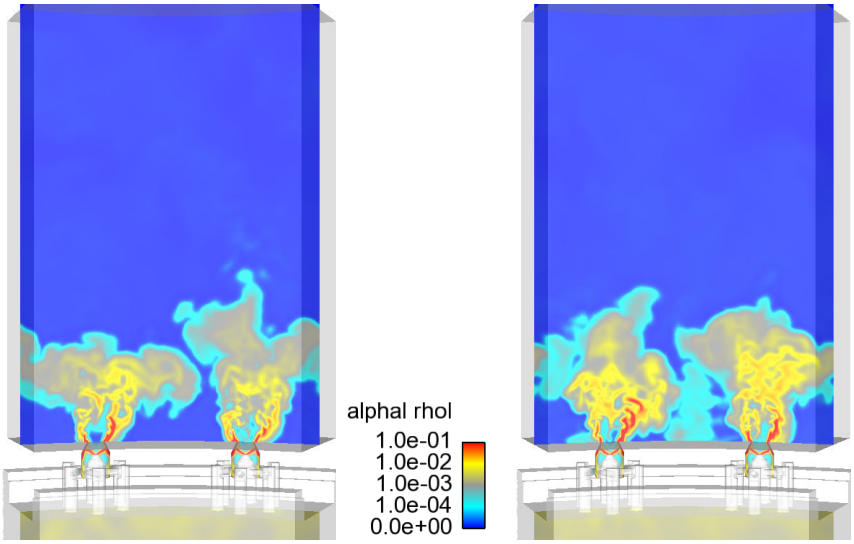

Figure 3.7: *Visualisation of the instantaneous liquid density $\alpha_l \rho_l$ on a slice at $r = 175$ mm for case $\Phi = 0.89$, at instants $t = 0.3$ s (left) and $t = 0.4$ s (right).*

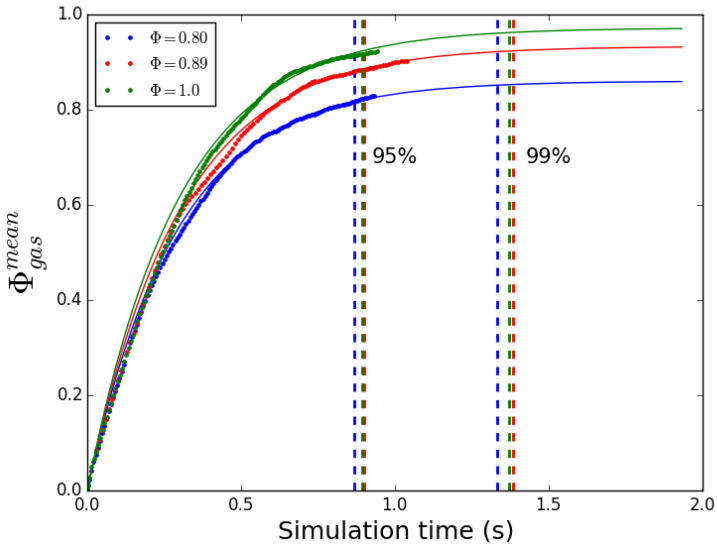

Figure 3.8: *Transient evolution of the mean gaseous equivalence ratio in the bi-sector chamber Φ_{gas}^{mean} for all three cases, each represented by a different color. The dots stand for the numerical data, which is approximated by an exponential curve in full lines. The left and right series of vertical lines respectively mark 95% and 99% of the estimated final values.*

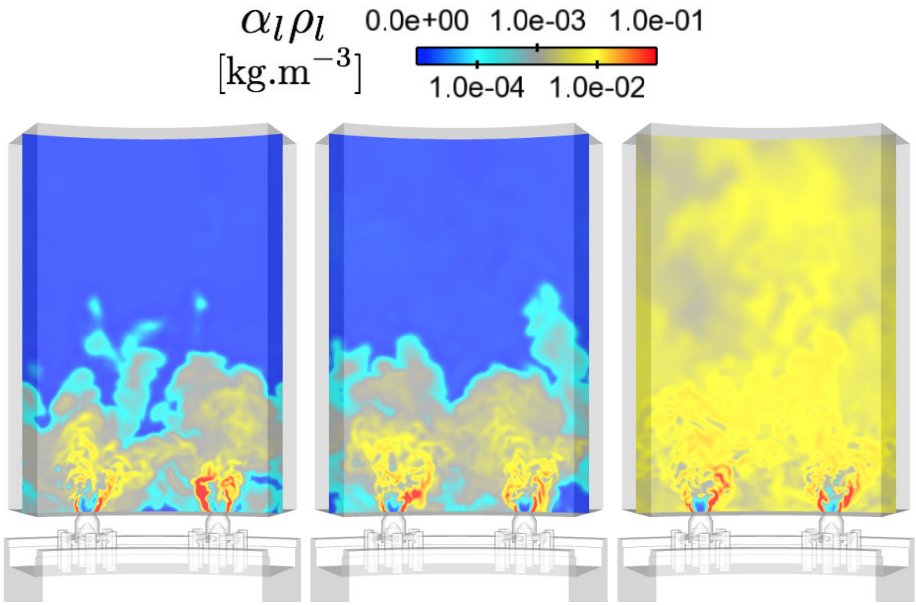

Figure 3.9: *Visualisation of the instantaneous liquid density $\alpha_l \rho_l$ on a slice at $r = 175$ mm for cases $\Phi = 0.8$ (left), $\Phi = 0.89$ (middle) and $\Phi = 1.0$ (right), on a solution at 95% of the estimated final value.*

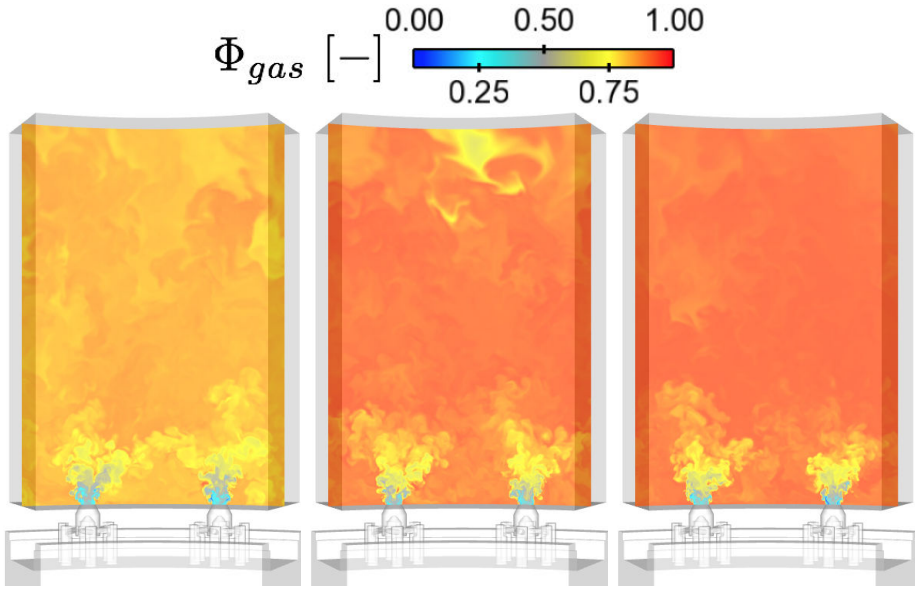

Figure 3.10: *Visualisation of the local gaseous equivalence ratio Φ_{gas} on a slice at $r = 175$ mm for cases $\Phi = 0.8$ (left), $\Phi = 0.89$ (middle) and $\Phi = 1.0$ (right), on a solution at 95% of the estimated final value.*

3.3.3.3 Evaporation model for case $\Phi = 0.89$

The simulation of the light-round sequence for the case $\Phi = 0.89$ was initially carried out with a simplified evaporation model which does not take into ac-

count the local gaseous composition for thermodynamic quantities calculations. Results from this light-round simulation were published in Lancien et al. (2017). The same case was simulated anew with the recommended more complex model, which showed great differences in the prediction of the steady-state two phase flow field. In particular, the liquid density field, displayed in Fig. 3.11, shows that the simplified model underestimates the evaporation and predicts a saturated state. As will be shown later with the light-round duration comparisons, this has an impact on the accuracy of the simulation.
The evaporation model was corrected to the complex variant for the simulations of cases $\Phi = 0.8$ and $\Phi = 1.0$, and, unless explicitly mentioned, all the results presented for case $\Phi = 0.89$ come from the second simulation, i.e. with the complex model.

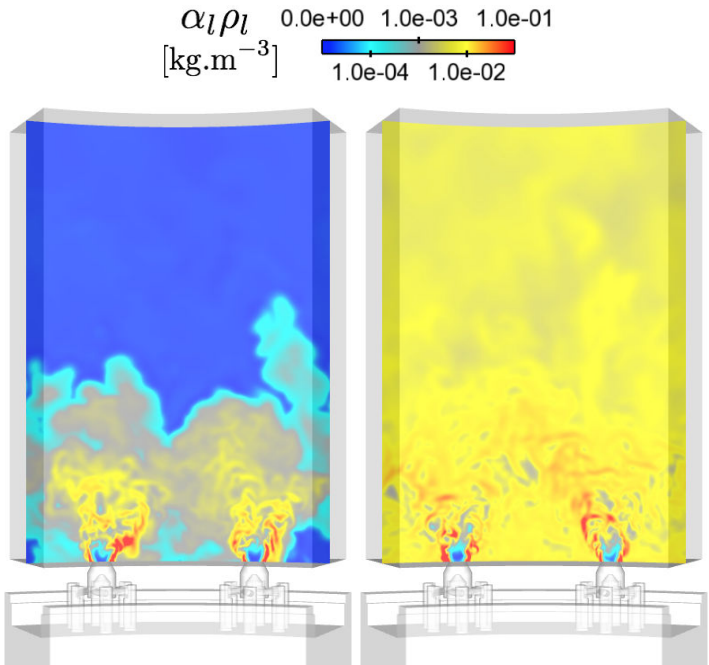

Figure 3.11: *Visualisation of the instantaneous liquid density $\alpha_l \rho_l$ on a slice at $r = 175$ mm for case $\Phi = 0.89$ on a solution at 95% of the estimated final value, with a simplified evaporation model (right) and the more complex one (left).*

3.3.3.4 Mean flow on the bi-sector

The quite reasonable size of the bi-sector mesh enables the simulation of greater physical times than would the annular configuration. In particular, an average solution was retrieved than gives information on the mean velocity fields in the chamber. The swirling sprays generated by each injector, evidenced in Fig. 3.12 by visualisations of the axial velocity, are not axi-symmetrical around their respective injector's axis, but rather inclined in the same tangential direction,

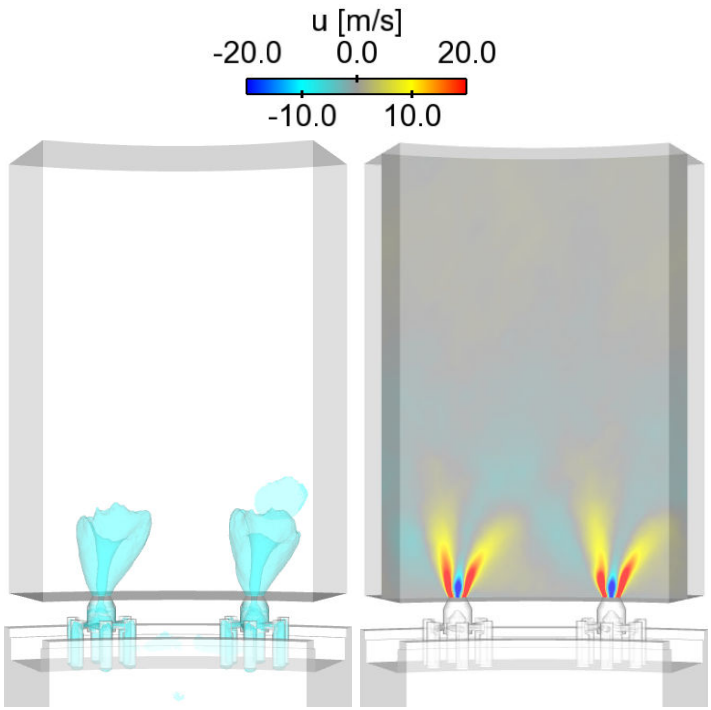

Figure 3.12: *Fields extracted from a solution averaged over* $\Delta t = 0.12$ *s for case* $\Phi = 0.89$. *Left: iso-surface of the axial velocity* $u = 5$ $m.s^{-1}$. *Right: Slice at* $r = 175$ *mm coloured by the axial velocity* u.

indicating that a mean clockwise tangential flow is present in the annulus.
This phenomenon is further evidenced by the visualisation of the tangential velocity, computed using the cylindrical coordinates associated to the annular chamber, plotted on axial cuts in the bisector chamber, shown in Fig. 3.13, where the blue color corresponds to clockwise velocities and the red color to counter-clockwise. All over the length of the chamber, the average field is largely dominated by blue, highlighting the presence of a tangential flow.

3.4 Light-round simulation and results

3.4.1 Initial solutions on the annular chamber

Before the simulation of the light-round sequence can be carried out, the converged cold flow solution has to be transformed into an annular cold flow solution. This is done by replicating 7 times the bi-sector solution. In order to remove the axi-periodicity that is introduced at the lateral walls, 6 ms of physical time was additionally simulated for the cold flow in the annular chamber, a duration which was estimated from autocorrelation considerations on the velocity.
During the convergence of the bi-sector cases, probes have been placed on the

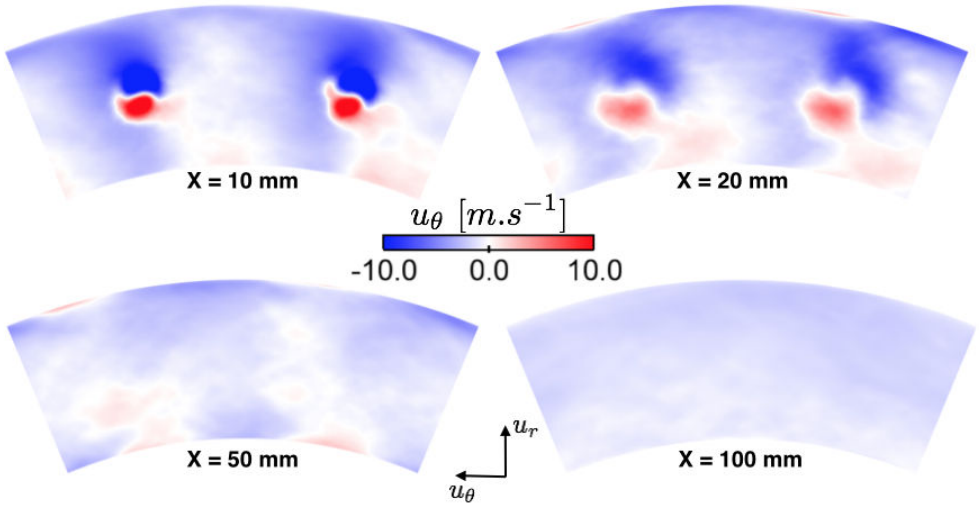

Figure 3.13: *Axial cuts extracted from a solution averaged over* $\Delta t = 0.12$ *s for case* $\Phi = 0.89$ *coloured by the tangential gaseous velocity* u_θ.

lateral periodic patches to record the evolution of the velocity at several heights. For each component of the velocity, u, v and w, the average values $\overline{u}$, $\overline{v}$ and $\overline{w}$ are deduced, and from that the fluctuations u', v' and w', with $u' = u - \overline{u}$. The autocorrelation rates R_{uu}, R_{vv} and R_{ww} are computed from the velocity fluctuations as given in Eq. 3.1.
If the set of data was taken from times t_0 and t_1, $R_{uu}(\tau)$ with $\tau \in [0, t_1 - t_0]$ represents how much $u(t_0 + \tau)$ depends on $u(t_0)$.

$$R_{uu}(\tau) = \frac{\sum_{t=\tau}^{t=t_1} u'(t)u'(t-\tau)}{\sum_{t=0}^{t=t_1} u'(t)u'(t)} \tag{3.1}$$

An example of the autocorrelation rate is given on the left plot of Fig. 3.14, for the axial gaseous velocity at $x = 7.5$ mm of case $\Phi = 0.89$. At $\tau = 0$ ms, $R_{uu}(\tau = 0) = 1$ and then decreases towards 0. The decrease can be approximated by an exponential function $f(\tau) = e^{-\tau/a}$, where a is the slope of the tangent at the origin and is here called the autocorrelation time. This is the time that is chosen to estimate the duration required in the 360° simulation to remove most of the periodicity. The plot on the right of Fig. 3.14 displays the values of the autocorrelation times for u, v and w at heights $x = 2.5$ mm, $x = 5.0$ mm, $x = 7.5$ mm, $x = 10$ mm, $x = 15$ mm and $x = 20$ mm for case $\Phi = 0.89$.
Except for v and w at $x = 2.5$ mm, after a physical time of 6 ms, most of the autocorrelation on the velocities have disappeared, so this was the duration chosen for all three cases. A sphere of burnt gases of radius $r_{sphere} = 4.0$ mm is inserted in the recirculation zone between two injectors to trigger the ignition and the light-round sequences.

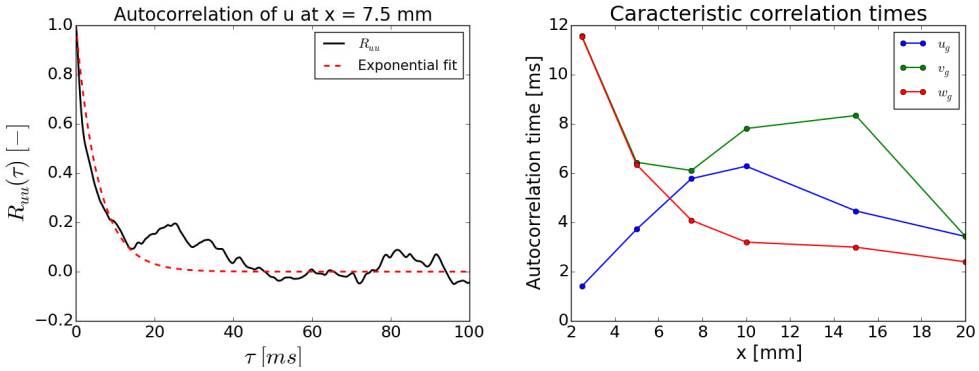

Figure 3.14: *Left: Evolution of the autocorrelation for the axial gaseous velocity fluctuations on the axi-periodic patch at $x = 7.5$ ms (in black) and the corresponding exponential approximation (in red). Right: autocorrelation times for the three component of the velocity against the height on the chamber, for case $\Phi = 0.89$.*

3.4.2 Light-round durations

The simulations of the light-round sequences were carried out over physical times of 50 to 60 ms, depending on the merging delay. Each simulation requires approximately 2.5 million CPU hours for the cold flow convergence of the bisector and 1 million for the light-round sequence. The simulation of the light-round sequences were run on 6144 processors on the French national cluster CURIE.

After completion of the simulations, it is first natural to compare the light-round durations with those of the experimental sequences. However, this duration needs to be carefully defined. Due to the camera sensitivity, it is difficult to precisely identify the instant the series of sparks generated by the plug becomes a propagating flame kernel. Moreover, the numerical ignition through the introduction of a spherical kernel does not represent the physics of these initial moments, introducing further uncertainty in the estimation of the time duration. It is then more suitable to consider the process after the ignition of the injector in sector S_1 and this instant is used as the beginning of the light-round sequence. The merging of the flame fronts is easier to identify, and simply corresponds to the first image in which an overlapping of the fronts is observed. The light-round duration, written τ^{lr}, is finally defined as the time difference between these two instants.

The experimental and numerical values for the light-round durations are shown in Fig. 3.15. The experimental data points are plotted as blue diamond symbols while the red dots stand for the three simulations. Very good results are achieved for cases $\Phi = 0.89$, for which the predicted duration falls in the experimental scatter of points, and $\Phi = 0.8$, where the duration is overestimated by 5%, which remains acceptable. However, the relative error of 30% in the $\Phi = 1.0$ simulation indicates that this calculation is less adequate. One ex-

planation could be the presence of locally rich conditions at the leading point, which is discussed in Chapter 4. The light-round duration predicted for case $\Phi = 0.89$ with the simplified evaporation model is marked as a green square and exhibits a 10% error, indicating that the model that accounts for the local species composition is indeed necessary to capture the flame propagation velocity.

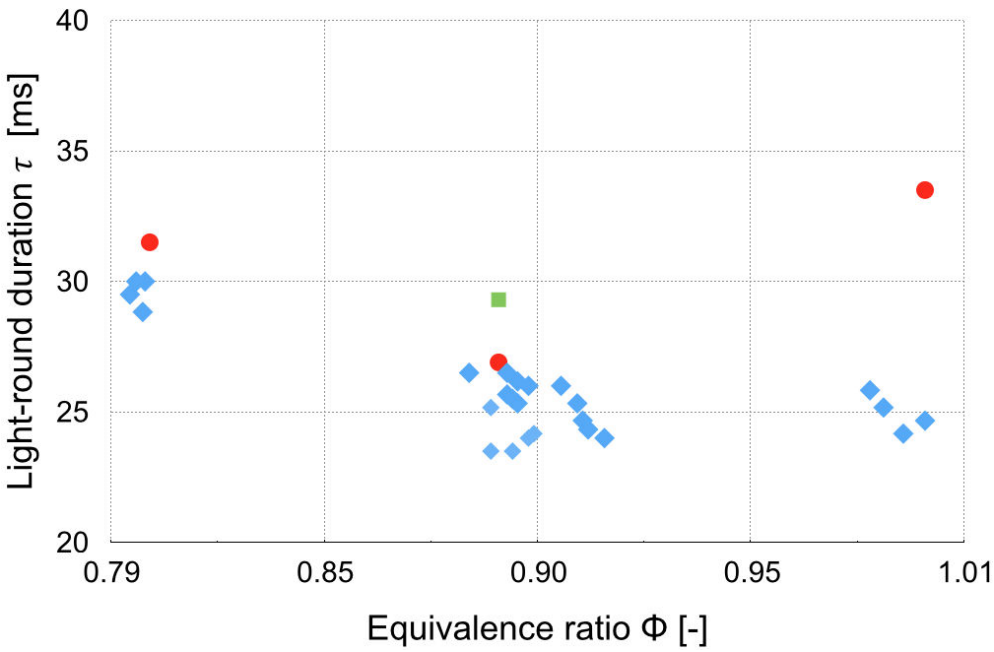

Figure 3.15: *Light-round durations as a function of the global injected equivalence ratio. Diamond symbols stand for experimental results. The durations predicted by the simulations are represented by red circles. The green square indicates the light-round simulated before fixing the evaporation model.*

3.4.3 Flame shape comparison

The experimental images of the propagating flame front generated by the Phantom camera, initially in levels of grey, are represented on a scale of colors from yellow to red for better clarity. It is worth noting that the globally lean operating conditions lead to blue flames without noticeable soot emission. To be able to draw comparisons, an iso-surface of the progress variable $c = 0.9$[1] defined

[1]This value for the progress variable was chosen because it is close to the maximum value of the reaction rate in the Arrhenius law. The impact of the selected value fro the progress variable on the flame front shape and behaviour was investigated and showed no significant differences. Some comparisons are shown in chapter 4, sect. 4.4.

as:

$$c = \frac{Y_{CO_2} + Y_{CO}}{Y^{eq}_{CO_2} + Y^{eq}_{CO}} \tag{3.2}$$

is used in the numerical simulations to represent the flame front. This iso-surface is coloured by the axial gaseous velocity, from -10 m.s^{-1} in yellow to 25 m.s^{-1} in black. For better visualization, iso-surfaces of the axial gaseous velocity at $u = 25$ m.s^{-1} are added to highlight the presence of each injector as well as the interaction between the flame and the flow field.

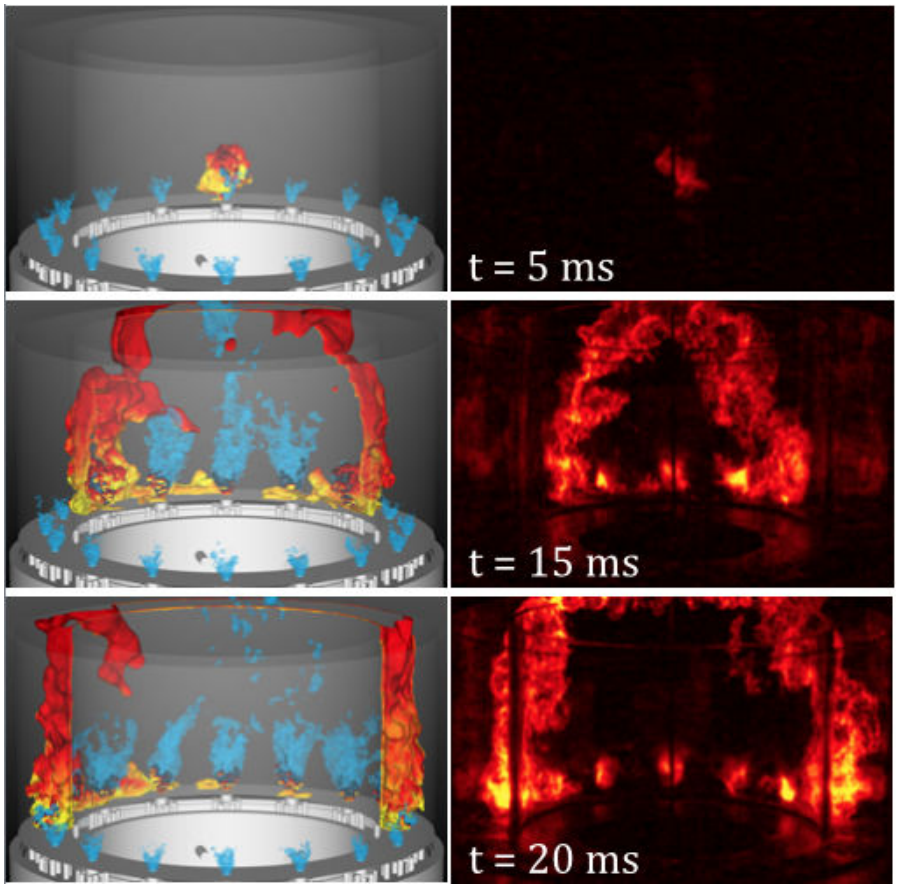

Figure 3.16: *Comparison between experimental and numerical flame configurations at three instants during the light-round sequence for case* $\Phi = 0.8$, $t = 5$ *ms (top),* $t = 15$ *ms (middle) and* $t = 20$ *ms (bottom).*

Figures 3.16 to 3.21 display comparisons between the experimental and numerical evolutions of the flame fronts for the three operating points. For each case, and similarly to what was done for the global durations, experimental images and numerical visualizations are synchronized using the first burner ignition as reference, and the time-scale is set as that of the simulation.

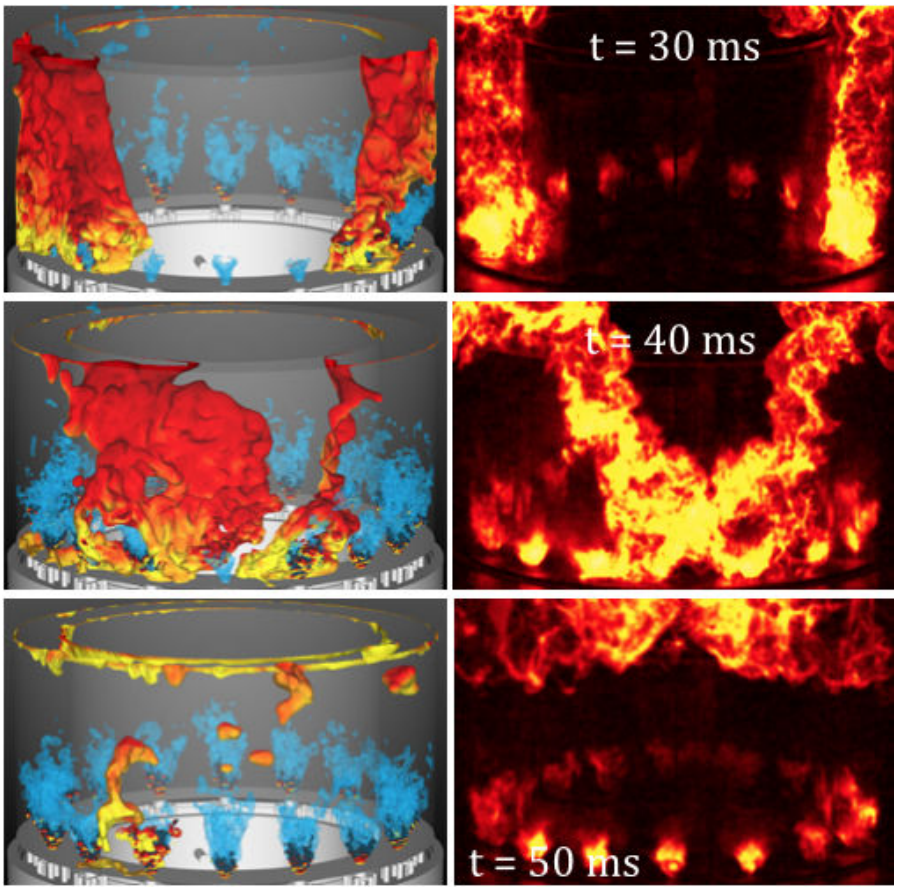

Figure 3.17: *Comparison between experimental and numerical flame configurations at three instants during the light-round sequence for case* $\Phi = 0.8$*,* $t = 30$ *ms (top),* $t = 40$ *ms (middle) and* $t = 50$ *ms (bottom).*

The comparison of the instantaneous snapshots confirms the observations made by analysing the global light-round durations. Figures 3.16, 3.17, 3.18 and 3.19 show that for $\Phi = 0.8$ and $\Phi = 0.89$, the evolution of the flame in the simulation (left images) is in very good agreement with that of the experiment (right images), up to the merging point. However, in case $\Phi = 1.0$, presented in Figs. 3.20 and 3.21, as soon as the flame reaches the exit of the chamber and two separate fronts are formed, a steadily increasing delay appears between the experiment and the simulation, leading to the observed difference in the light-round duration. This is further analysed in sect. 3.4.5, along with the flames propagation delays.

Regardless of the propagation velocities, the three snapshot series indicate that the simulation is able to reproduce the different stages of the ignition of MICCA-Spray. As in previous studies Philip et al. (2015a) and Philip et al. (2015b), several phases can be identified in the experimental and numerical images:

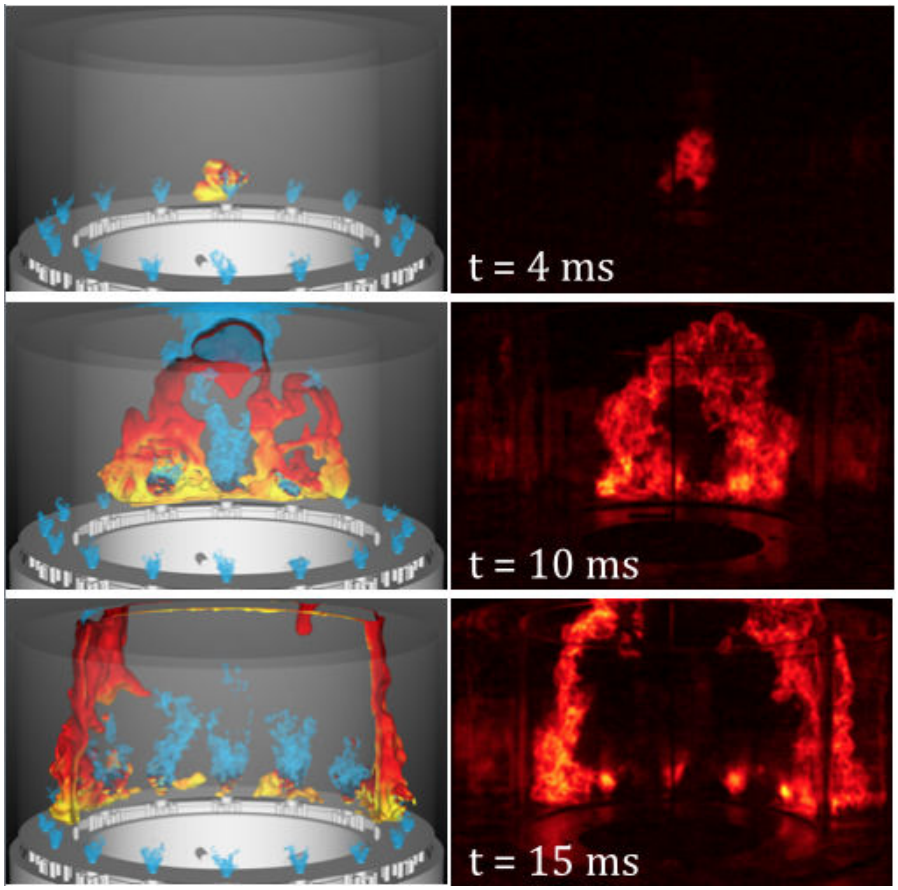

Figure 3.18: *Comparison between experimental and numerical flame configurations at three instants during the light-round sequence for case* $\Phi = 0.89$*,* $t = 4$ *ms (top),* $t = 10$ *ms (middle) and* $t = 15$ *ms (bottom).*

(I) During the first instants after the initiation of ignition, the kernel is convected by the flow exhausted by the first swirler and distorted by turbulence. Once it meets an area with favorable conditions, the flame starts to propagate around and towards the first injector (top images on Figs. 3.16, 3.18 and 3.20).
(II) The flame front takes the form of an arch that rapidly expands sideways towards the neighbouring burners and the exit plane of the chamber (middle images on Figs. 3.16, 3.18 and 3.20).
(III) During the third phase, the longest of the five, the arch, upon reaching the exit of the chamber, separates into two distinct flame fronts that propagate in their respective half chamber in a mostly vertical form (bottom images on Figs. 3.16, 3.18 and 3.20). When these two fronts get closer to each other on the other side of the chamber, a distant interaction takes place that changes their shape: in all three cases, the bottom part of the flame travels faster and the fronts incline backwards (top images on Figs. 3.17, 3.19 and 3.21), so that

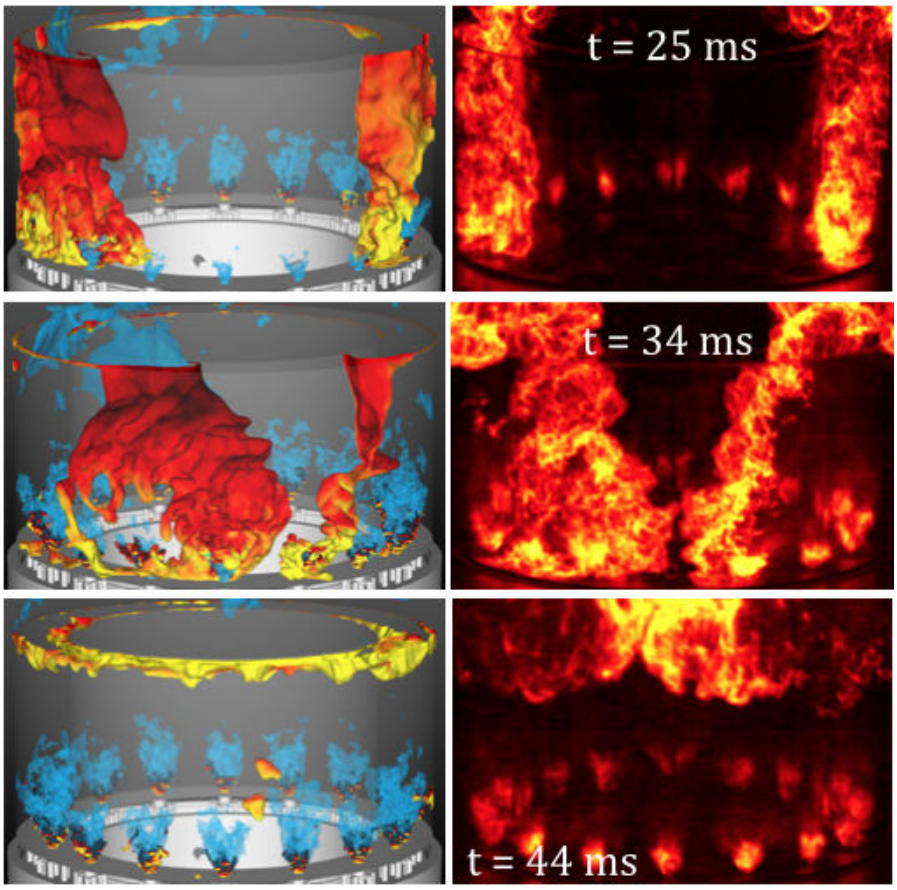

Figure 3.19: *Comparison between experimental and numerical flame configurations at three instants during the light-round sequence for case* $\Phi = 0.89$, $t = 25$ *ms (top),* $t = 34$ *ms (middle) and* $t = 44$ *ms (bottom).*

the merging occurs in the bottom half of the chamber.
(IV) The head on collision takes place and the interaction of the flame fronts leads to the fast burning of the remaining fresh mixture (middle images on Figs. 3.17, 3.19 and 3.21).
(V) Once all the fresh two-phase mixture in the chamber has been consumed, a flame is stabilised around each injector and the steady-state regime is reached (bottom images on Figs. 3.17, 3.19 and 3.21).
These phases, already observed in gaseous premixed cases (Philip et al. (2015a) and Philip et al. (2015b)) and now in two-phase flow simulations and experiments, show the ability of the simulation to predict the flame propagation behaviour during a successful ignition sequence.

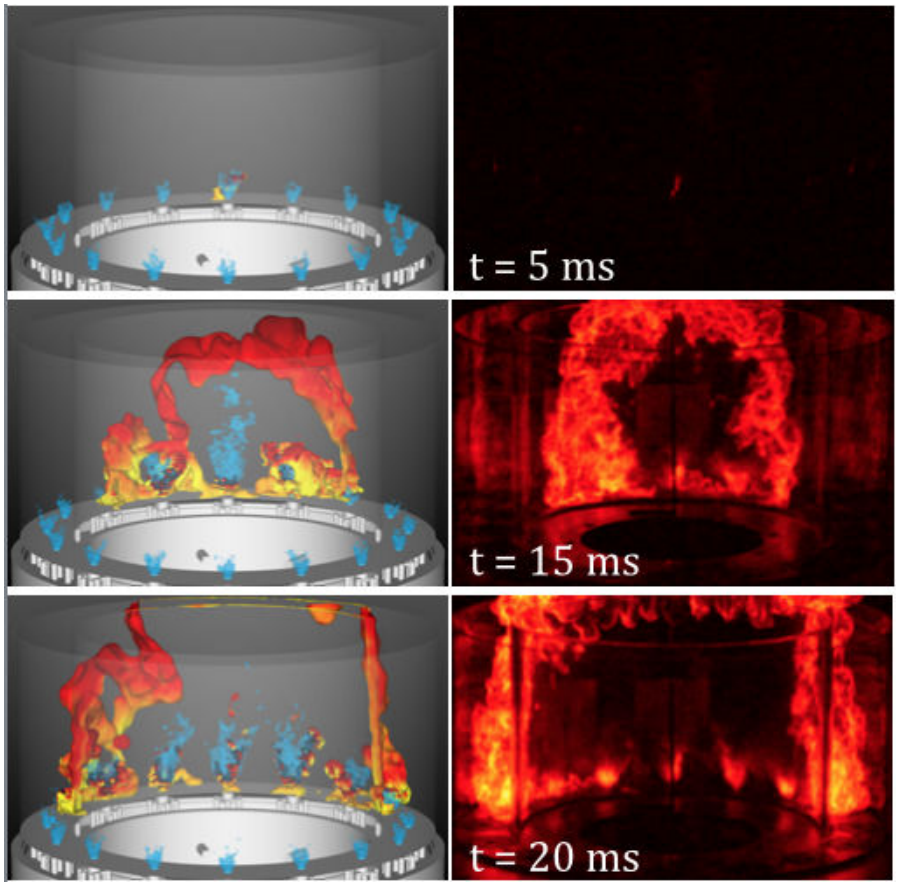

Figure 3.20: *Comparison between experimental and numerical flame configurations at three instants during the light-round sequence for case* $\Phi = 1.0$, $t = 5$ *ms (top),* $t = 15$ *ms (middle) and* $t = 20$ *ms (bottom).*

3.4.4 Heat release rate evolution

Another way to examine the flame evolution is to consider the temporal records of the integrated heat release rate over the whole chamber. This is done experimentally by integrating the flame light intensity on each image. The relationship between heat release rate and light intensity is well established for gaseous premixed flames and was verified in Philip et al. (2015b), where the line-of-sight integrated light intensity from experimental images of a light-round sequence was successfully compared to the numerical integrated heat release rate, for two different gaseous premixed combustion models. However, this is not true in general for two-phase flames which can exhibit complex reaction layers with premixed and non-premixed combustion modes. The analysis of the simulated flame structure (detailed in chap. 4) reveals that the reaction zone mainly behaves like a premixed flame front. This observation justifies the use of light intensity to characterize the rate of heat release in the spray flame. The

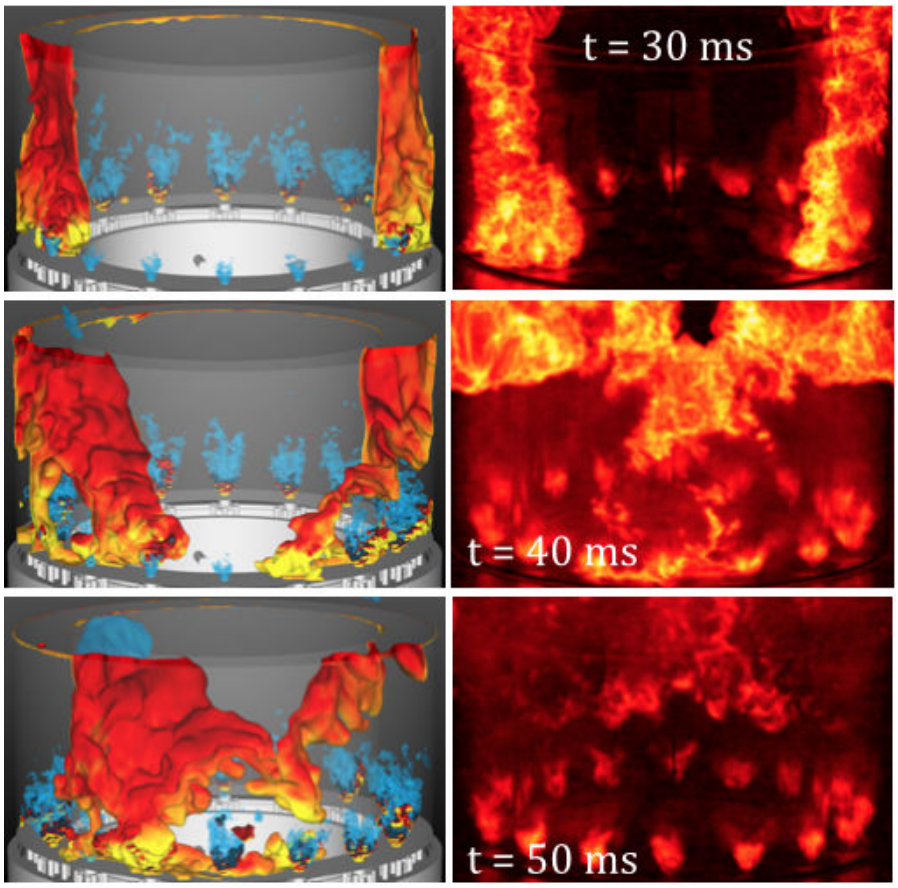

Figure 3.21: *Comparison between experimental and numerical flame configurations at three instants during the light-round sequence for case* $\Phi = 1.0$*,* $t = 30$ *ms (top),* $t = 40$ *ms (middle) and* $t = 50$ *ms (bottom).*

two-phase nature of the flow nonetheless prevents a quantitative comparison. Besides, the visual integration of the light emission can introduce some error when some parts of the flame hide one another. The presence of the quartz tube also leads to a damping of the light intensity, especially during the first instants when the flame is in the back of the chamber.

To compare the different cases with each other and similarly to the other sets of data, the time-scales of the experimental sequences have all been adjusted so as to synchronise the ignition of the first injector (in S_1). Figure 3.22 presents all the experimental sequences (thin coloured lines), compared to the numerical simulations (thick blue line), for the three considered operating points, $\Phi = 0.8$, $\Phi = 0.89$ and $\Phi = 1.0$. All the curves have been normalised by their maximum. Contrary to the numerical data, all the experimental curves are not at zero at the beginning of the ignition, but rather at a value that varies depending on the cases due to the normalisation by the maximum. This is due to the fact that

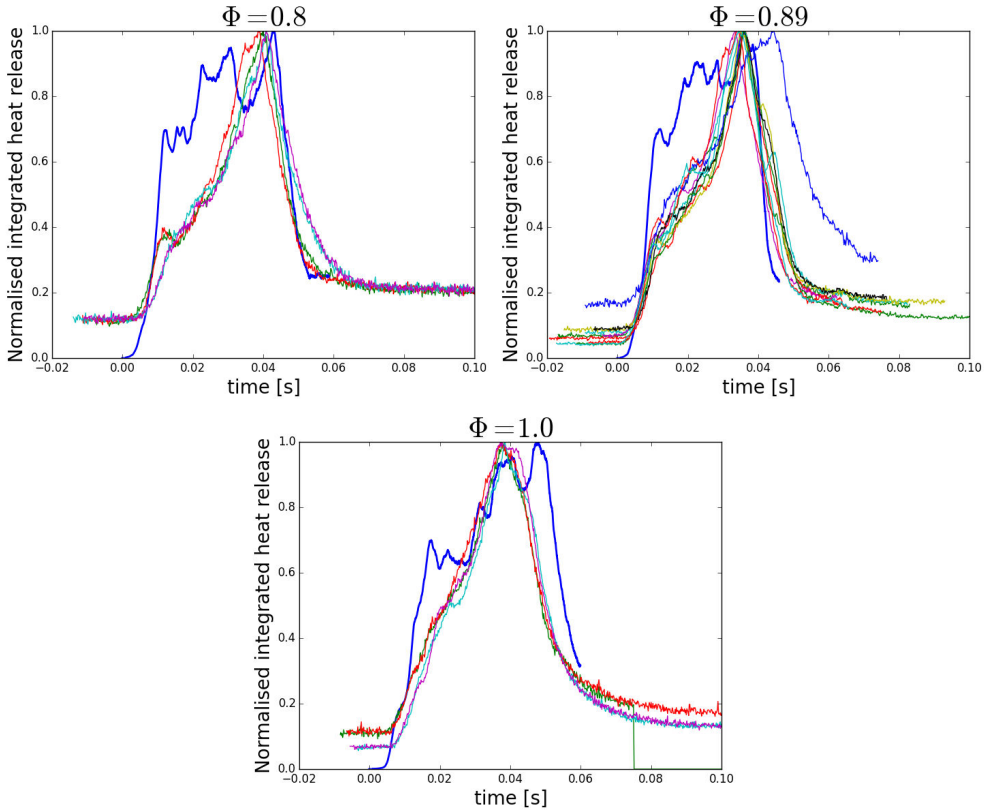

Figure 3.22: *Comparison between the integrated heat release rate in the chamber and the total light intensity obtained from the experimental images. Top left:* $\Phi = 0.8$*, top right:* $\Phi = 0.89$*, bottom:* $\Phi = 1.0$*.*

total darkness is not achieved in the experimental room, so that residual light is captured by the camera. This light pollution being constant throughout the ignition, it does not affect the slopes and shapes of the experimental data sets. Similarly to what is observed on the global merging delays, the experimental integrated light intensity shows little scattering in its temporal evolution. The slopes, as well as the local or global maxima, are roughly consistent for each series of measurements, giving a similar shape to all the curves corresponding to one given equivalence ratio.

In order to ease comparison with the simulation, one single experimental sequence has been chosen for each operating condition, shown in Fig. 3.23, where, in addition to the numerical integrated heat release rate (in blue) and the selected experimental light intensity (in black dots), the two blue and black solid vertical lines highlight the instants of the merging of the flame fronts, making the previously described errors ($err_{\Phi=0.8} = 5\%$, $err_{\Phi=0.89} = 2\%$, $err_{\Phi=1.0} = 30\%$) in the numerical prediction of the light-round duration apparent. Vertical blue dashed lines have been added to mark the beginning and

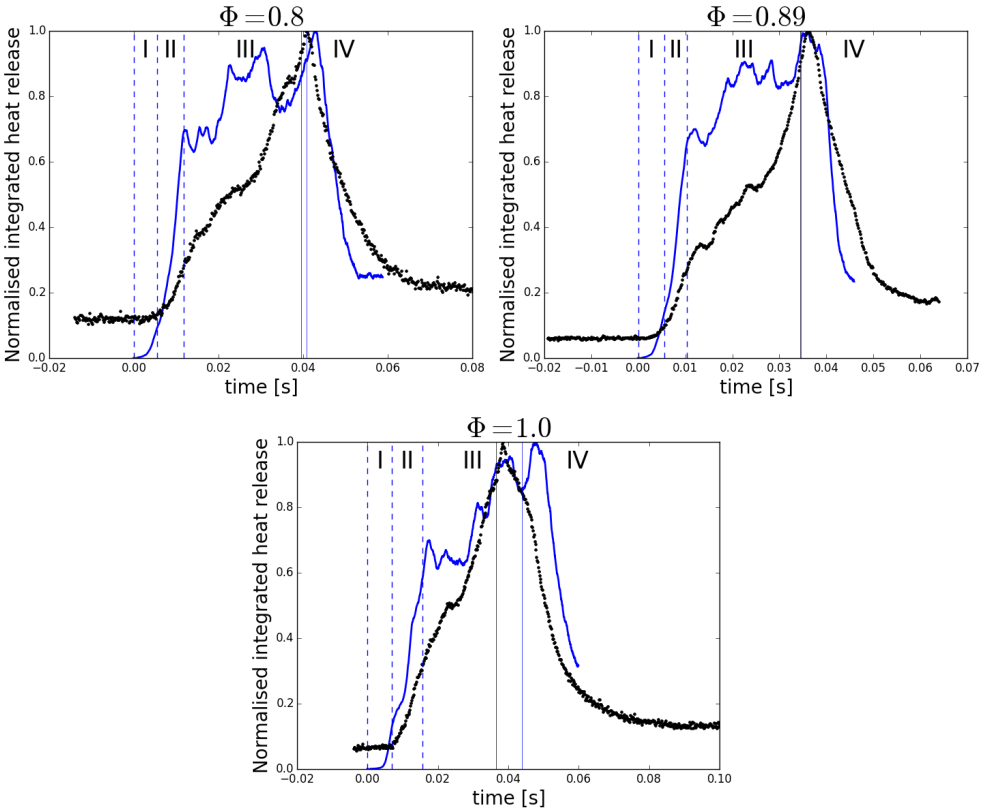

Figure 3.23: *Comparison between the integrated heat release rate in the chamber and the total light intensity obtained from the experimental images. •: Experimental data from one sequence, –: numerical data. Top left:* $\Phi = 0.8$*, top right:* $\Phi = 0.89$*, bottom:* $\Phi = 1.0$*. The black and blue solid lines mark the merging instant of the experimental and numerical sequences, respectively. The blue dashed lines highlight the beginning and the end of the numerical phases, identified by Roman numbers.*

the end of the phases identified on the images of the numerical propagation sequence, labelled in Roman numbers.

In the numerical profiles, phase I is characterised by a stagnation of the flame kernel which is looking for a favourable region, so that the heat release rate increase does not start until the second half of the phase. At this point, and during all of phase II, where the kernel has formed an arch that expands radially, the heat release rate growth follow an exponential trend. At the instant the flame reaches the chamber exit, marking the transition between phases II and III, the growth of heat release rate halts and a plateau is reached for a few instants before increasing again, but with a less regular behaviour. A global behaviour is reached at the end of phase III, when the two fronts come in contact and the merging takes place. After that, the remaining fresh gases are gradually burnt and evacuated from the chamber, leading to a rapid decrease

of the heat release rate until its steady-state value which corresponds to the 16 stabilized flames. This evolution is similar to that observed in gaseous premixed cases by Philip et al. (2015b), though phase III showed more linear behaviour. The experimental profiles, which were matched very well by the numerical profiles in Philip et al. (2015b), do not seem at first glance to agree with the numerical data other than in terms of global trends for any of the cases. The images of the flame propagation presented in section 3.4.3 showed however that the simulations are able to capture the flame fronts behaviour, particularly in terms of shape and propagation mechanism. This leads to think that perhaps the observed differences are more due to the fact that the plotted quantities are not strictly proportional in the case of a two-phase injection rather than to a discrepancy between the simulation and the experiment. In particular, strong oscillations are present in the simulation, due to swirler ignitions, that are not consistent with the experimental signal.
Nevertheless, upon closer look, some common features can be identified that show that, though it is less conclusive than in a gaseous premixed case, the comparison is still relevant. First of all, all three cases exhibit a break in the slope, around $t = 0.02$ s, which corresponds to the end of phase II, when the flame exits the chamber and two flame fronts are created. Though it is less marked in the experimental data, a halt in the rapid increase of the heat release rate is apparent on all curves and around the same time. On all cases, the global maximum is reached a few milliseconds after the merging (indicated by the vertical solid lines). At this time, a flame has stabilised or is in the process of stabilising around each injector, and the two mostly vertical fronts are still present in the chamber, which explains the maximum of heat release rate in the simulation and light emission in the experiment. After the maximum that follows the merging, the combustion and evacuation of the burnt gases lead to the observed sharp decrease in all cases towards the steady-state value. During its ignition, the chamber emits an instantaneous global power up to $\mathcal{P}_{max} \approx 300-350$ kW, depending on the operating point, which is much greater than the steady-state power $\mathcal{P}_{st} = 79.3$ kW (see section 3.2.3).

3.4.5 Sector ignition delays

In the simulation, the passage of the flame in a given sector can be observed through the volume integral of the heat release rate in that sector, as shown in Fig. 3.24, for side H+ (right graphs) and H- (left graphs). All three cases exhibit similar features, which was expected from the analogous behaviour observed on the flame fronts propagation. For each sector, a clear global maximum is present and this instant is used to define the ignition time of the sector. This will be further described later on. The value of the maximum of heat release rate is of the same order of magnitude for sectors S_1 to S_7 and S_{-1} to S_{-7}, where a flame front has formed that crosses the domain in a vertical like manner. All curves exhibit a quite broad shape that is due to the fact that the whole height

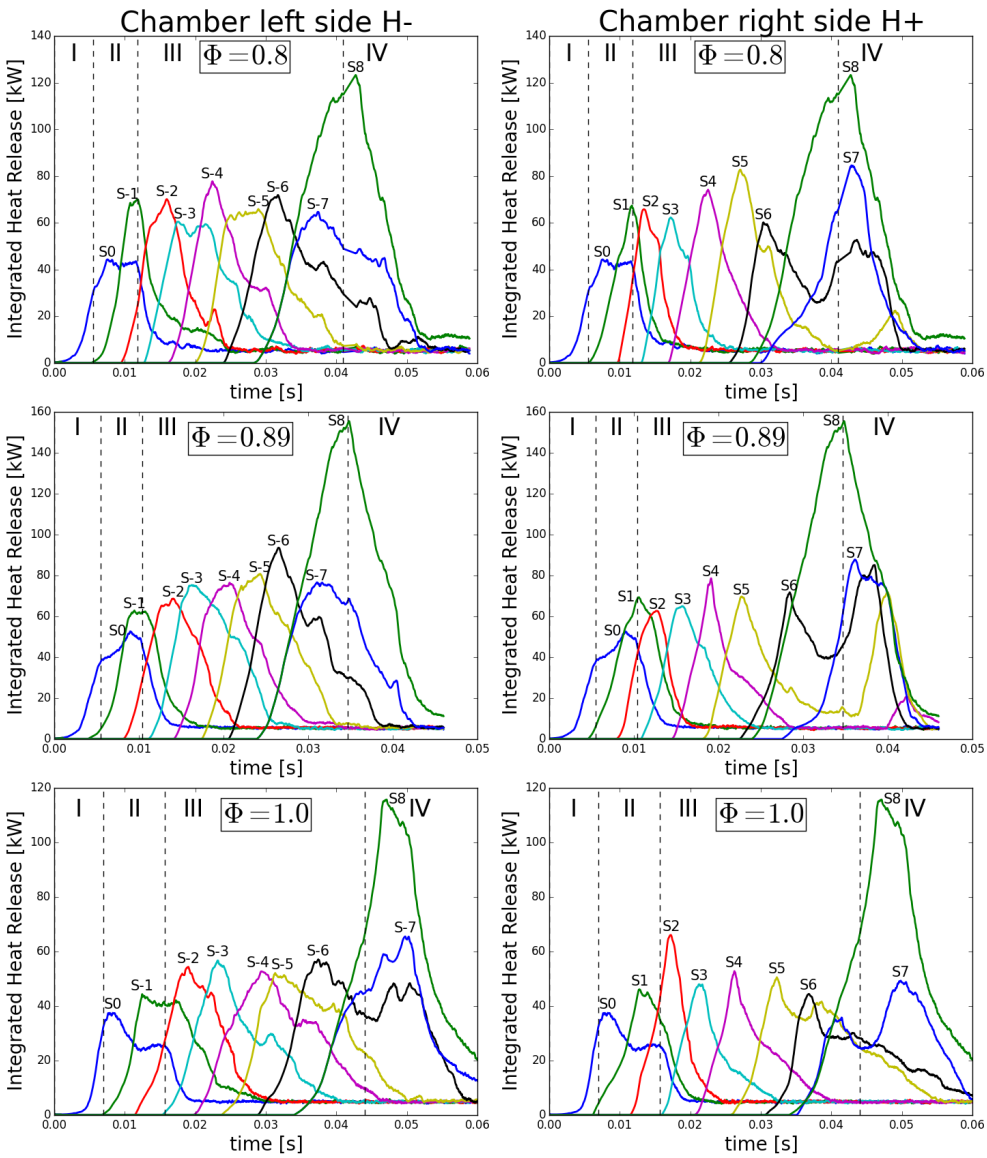

Figure 3.24: *Evolution of the integrated heat release rate in each sector of the H+ side of the chamber (right) and the H- side (left) for cases* $\Phi = 0.8$ *(top),* $\Phi = 0.89$ *(middle) and* $\Phi = 1.0$ *(bottom). The beginning and the end of the phases identified on the numerical images are marked through black vertical dashed lines. The phases are labelled by Roman numbers.*

of the chamber is considered for the integration, so that the fronts, not being perfectly vertical nor perpendicular to the azimuthal direction, do not cross the sectors at the same time depending on the considered height. The heat release rate in S_0 corresponds to the formation of the arch and its radial expansion, which can explain its different shape (lower maximum and broader curve). In

the final sector, S_8, the heat release rate peak is twice higher than in the other sectors because both fronts are present for the merging, so that the amount of flame surface in the sector is doubled.
On each plot in Fig. 3.24, the phases beginning and ending times, identified on the numerical images presented in section 3.4.3, are reported as vertical lines. On the three cases, the transition between phases I and II, when the flame kernel forms an arch and begins to expand laterally towards the neighbouring injectors, corresponds to a change of slope in the S_0 curve.
Additionally, it is interesting to note that at any given time t during phase III, three different sectors are being ignited: if at this instant, the highest curve is that of sector S_i, meaning that most of the flame front is located there, then sector S_{i-1} is still evacuating some flame elements while combustion is already beginning in sector S_{i+1}.
Finally, and consistently to what was observed on the normalised heat release rate in Figs. 3.22 and 3.23, the beginning of the merging phase, phase IV, takes place a few instants before the maximum of heat release rate in sector S_8.

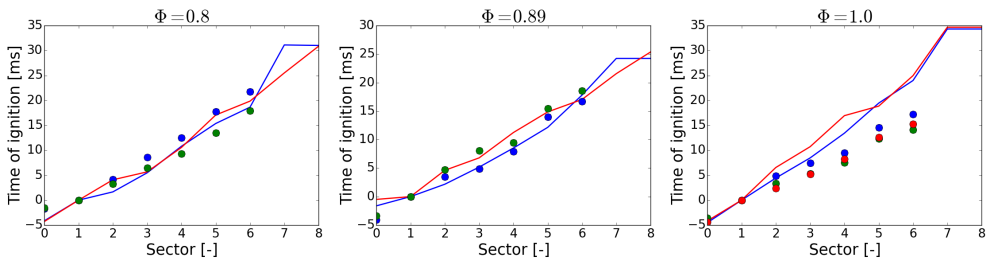

Figure 3.25: *Comparison of sectors ignition times for cases* $\Phi = 0.8$ *(left),* $\Phi = 0.89$ *(center) and* $\Phi = 1.0$ *(right),* $-$*: Simulation, H+,* $-$*: Simulation, H-,* $\bullet\bullet$*: Experimental measurements on the H- side of the chamber, each color stands for a different sequence.*

Another assessment of the simulation consists in comparing durations between the ignition of two consecutive burners. As mentioned previously, the maximum of heat release rate in a sector can also be used as an indicator of its ignition. In the experiment, the photo-multipliers (PM) placed in front of each injector on the H- side measure the evolution of the light intensity around them, and the maximum of the signal gives an estimation of the experimental ignition times. Contrary to the numerical integration, a mask is placed in front of each PM in which a slit allows to focus laterally and axially on the corresponding injector's light emission. In consequence, the measured signal does not account for emissions from the propagation fronts located above the injector. For each operating point, two or three sets of measurements are plotted in Fig. 3.25 as symbols, each color standing for one set of measurements, highlighting some variability in the experimental results. Values from the simulations are plotted as solid lines for both H+ (blue lines) and H- (red lines). As was done for the global light-round duration, the numerical and experimental results are

synchronized with respect to the ignition of the first sector (S_1 or S_{-1}), that sets the origin of times.
Cases $\Phi = 0.8$ (Fig. 3.25 left) and $\Phi = 0.89$ (Fig. 3.25 center) show an excellent agreement between experiment and simulation. Both H+ and H- evolutions are close to that of the experimental sequences, indicating that the accuracy observed in the global light-round duration is linked to the ability of the simulation to capture the flame propagation velocity. On the H+ side of case $\Phi = 0.8$, the plot shows that the flame front slows down between sectors S_6 and S_7, indicating that the 5% difference observed in the light-round duration is due to a deceleration of one of the flame fronts towards the end of the sequence, when the two fronts collide head on and the flow is notably modified by the flame. Finally, the plot on the right in Fig. 3.25 allows to identify the source of error for the case $\Phi = 1.0$ for both sides of the chamber. The simulation systematically overestimates the ignition delay between sectors, leading to a gradually increasing error in ignition time, which explains the larger error in the light-round duration. Contrarily to the previous case, the error does not arise towards the end of the sequence, but is formed by an accumulation throughout the simulation, indicating that the propagation mechanisms are less well captured under these conditions.

3.5 Conclusion

The present chapter reports large eddy simulations of the light-round sequence in a laboratory scale annular combustor equipped with multiple swirl spray injectors. This experimental system MICCA-Spray is dimensionally similar to a typical helicopter gas turbine combustor and is operated in a liquid injection mode in an effort to achieve a better representativity of aero-engine combustion chambers. The chamber is equipped with quartz walls that allow full optical access to the combustion region and detailed visualizations of the flame during light-round sequence allow precise comparisons between experiments and simulations. The LES simulation accounts for the liquid disperse phase with an Eulerian framework and a mono-disperse representation of the spray, whose parameters have been carefully determined and assessed in chapter 2. Three different cases with varying global equivalence ratios and constant power are considered here and compared to experimental data. Attention is focused on relight conditions, meaning that experimentally, the walls have been preheated and are at their steady-state temperature when the ignition is triggered. This condition is approximated numerically by adiabatic boundary conditions on all the walls.
To ensure comparability of the simulation with the experimental sequences, the cold aerodynamic flow is first converged on a reduced geometry called *bi-sector* by making use of the periodic pattern present in MICCA-Spray. The convergence of both phases is carefully evaluated.

Direct visualisation of the flame fronts and light intensity signals measurements from photo-multipliers focused on one injector are used to access the different experimental flame propagation delays. Cases $\Phi = 0.8$ and $\Phi = 0.89$ indicate that the simulation is able to accurately predict the light-round duration as well as the ignition delay between the injectors, while the case $\Phi = 1.0$ is less accurately described, with an underestimation of the absolute flame velocity, leading to a 30 % error in the global light-round delay. In all three cases, and setting aside the error in flame propagation speed for case $\Phi = 1.0$, the global dynamics and the flame geometry are very well predicted by the simulation.
These results show the ability of the present numerical set-up in conjunction with the TFLES model to accurately predict the flame evolution during a light-round sequence in an annular combustor with liquid injection. These unique simulations can now be further post-processed for a more detailed analysis of the propagation mechanisms and the coupling between the combustion and the liquid phase. This is done in chapter 4.

Chapter 4

Detailed analysis of light-round in MICCA-Spray with liquid n-heptane and air injection

This chapter presents the detailed analysis of the numerical simulation of the light-round for the three operating points presented in chapter 3. Specific post-processing is applied in order to identify the key mechanisms that drive the flame fronts propagation and the light-round process. Calculations indicate that the volumetric expansion due to the chemical reaction at the flame induces a strong azimuthal flow in the fresh stream at a distance of several sectors ahead of the flame, which modifies conditions in this region and has a large impact on the flame fronts propagation velocity. The turbulent flame dynamics is then studied in terms of flame surface evolution and propagation velocities. The observation of the flame structures shows that combustion occurs mainly in the premixed regime, allowing the use of premixed flames considerations and quantities as a first approximation. The propagation of the turbulent flame fronts in the two-phase mixture is examined through the local behaviour of its leading points, shown to be relevant quantities for the study of the whole sequence, which leads to the identification of some phenomena responsible for the flame behaviour, such as the influence of the liquid droplet spray and its vaporization in the chamber. Interactions between the propagating flames, the flow in the chamber and the sprays at the injectors create heterogeneities in the gas composition and in the liquid repartition, and wakes appear on the downstream side of the swirling jets formed by the injectors, with notable effects on the motion of the leading point and on the absolute flame velocity.

Contents

4.1 Introduction **160**
4.2 Volumetric expansion of the burnt gases **161**
4.2.1 Flow field modifications due to the propagating flame 161
4.2.2 Flow field dynamics evolution at fixed azimuthal positions 165
4.2.3 Flow field dynamics at the chamber exhaust 168
4.3 Flame fronts dynamics: global point of view **173**
4.3.1 Analysis of the flame structure 173
4.3.2 Evolution of the flame surface 176
4.3.3 Flame velocities 184
4.4 Behaviour of the leading points of the flame fronts **191**
4.4.1 Leading points position and trajectory 193
4.4.2 Ignition delays and velocities 196
4.4.3 The leading point and its surrounding flow field . . . 199
4.5 Flame-spray interactions **202**
4.5.1 Interactions between the flame and the swirling sprays 203
4.5.2 Local effects of flame crossing on the flow 204
4.6 Conclusion **206**

4.1 Introduction

In the previous chapter, large-eddy simulations of the light-round sequence in the annular combustion chamber MICCA-Spray, operated with liquid n-heptane and air injection, were presented in the case of successful re-ignition sequences. Three operating conditions were considered for varying global equivalence ratios and compared with experimental data in terms of flame shape evolution, global light-round duration and burner-to-burner ignition delays. Results showed that while the three simulations were able to predict the correct global flame shape behaviour, only cases $\Phi = 0.8$ and $\Phi = 0.89$ also retrieved accurate ignition delays. An error of 30% was observed on the global duration in case $\Phi = 1.0$.
The ignition sequence in an annular multi-burner combustor equipped with two-phase swirl injectors is a highly complex phenomenon to understand and to predict. The mechanisms involved are intrinsically multi-physical, three-dimensional, turbulent and transient. The objective of the present chapter is to further analyse the three simulation cases ($\Phi = 0.8$, $\Phi = 0.89$ and $\Phi = 1.0$, with the complex evaporation model) in order to better understand the local dynamics of the chamber in response to the triggering of the ignition.
The expansion of the burnt gases in the semi-confined chamber during the light-round in first studied and quantified in section 4.2. The evolution of the flame

front is then considered from a global point of view through its behaviour in the whole chamber in section 4.3. Further analyses highlight the existence of a leading point for each flame front whose influence on the whole dynamics is investigated in section 4.4. Finally, attention is focused on the interactions between the flame propagation and the liquid spray in section 4.5.

4.2 Volumetric expansion of the burnt gases

It was already observed in previous studies of the light-round in annular combustion chambers (Boileau et al. (2008); Philip et al. (2015b); Philip et al. (2015a)) that the acceleration and the expansion of the burnt gases had a notable impact on the whole flow field in the chamber, even on the fresh gases in regions that have not yet been reached by the flame.
This section aims at characterizing and quantifying this effect on the three simulated operating points.

4.2.1 Flow field modifications due to the propagating flame

In order to observe the evolution of the flow field during the light-round, it is convenient to take cylindrical cuts of the chamber at a given radius r^{cut} and to unfold it as shown in Fig. 4.1 for better visualisation.

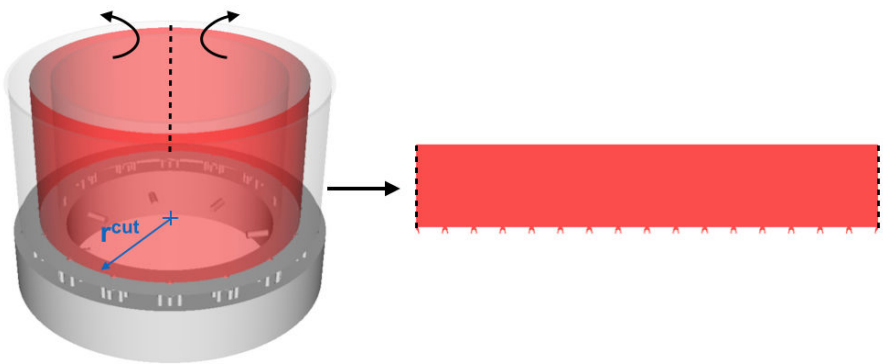

Figure 4.1: *Schematic description of the unfolded surface for a given radius r^{cut}. The cylindrical cut is divided at sector S_0 and unfolded as shown.*

A modification of the flow in the fresh gases ahead of the flame can be observed everywhere in the chamber during the light-round sequence. Unfolded cylindrical cuts inside the chamber at the medium radius $r^{cut} = 175$ mm are considered in Fig. 4.2. In this representation the spark plug corresponds to the left and right boundaries of the unfolded cylindrical surface and the flames propagate towards the center of the image. In Fig. 4.2, the sections are coloured by the gaseous azimuthal velocity u_θ, for several instants of the flame propagation in case $\Phi = 0.89$. The tangential velocity evolution being very close in

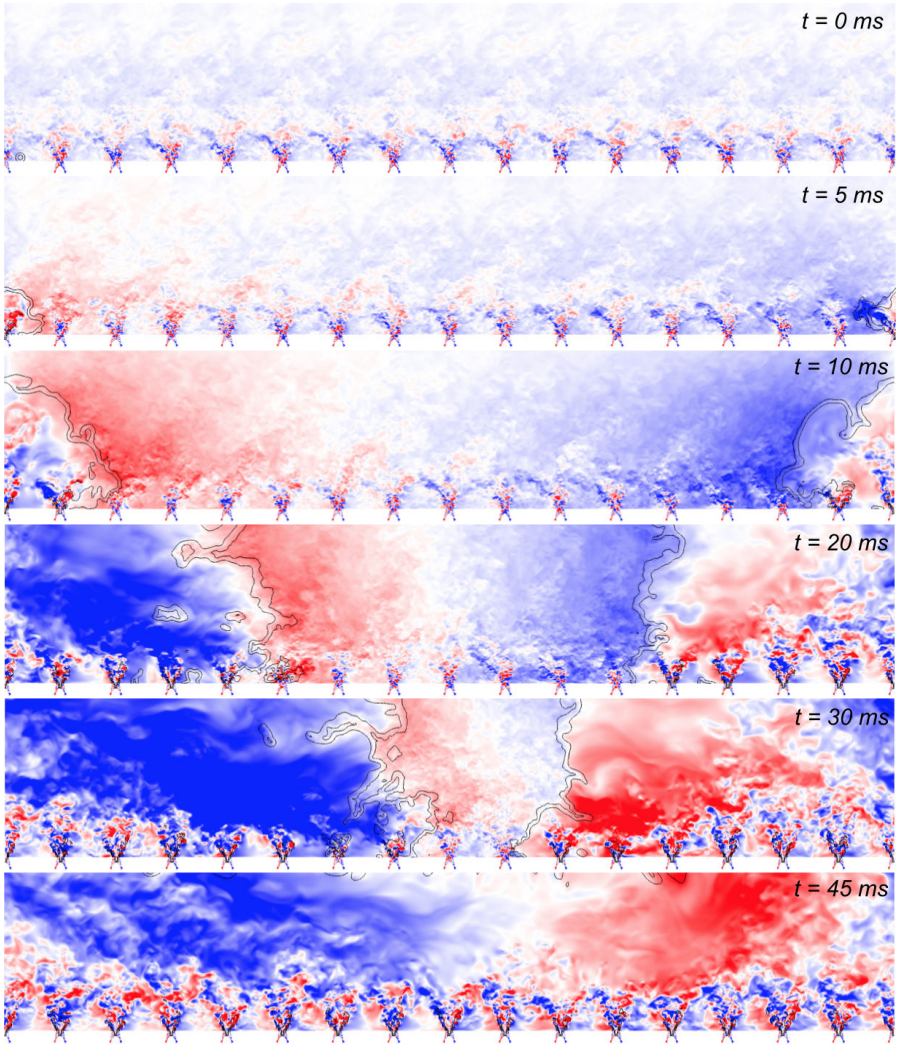

Figure 4.2: *Visualization of the tangential gaseous velocity on a cylinder of radius $r^{cut} = 175$ mm, crossing the injectors' centerlines, unfolded on a plane surface for the case $\Phi = 0.89$ at different instants. The lateral sides of the unfolded cylinder correspond to the location of the first ignited injector. Tangential velocities are counted positive from left to right and range from $u_\theta = -20$ m.S^{-1} in blue to $u_\theta = 20$ m.S^{-1} in red. Two iso-lines of the progress variable $\widetilde{c} = 0.1$ and $\widetilde{c} = 0.9$ (in black) highlight the position of the flame fronts.*

the three cases, only one case is presented here. The flame front positions are evidenced by two iso-surfaces of the progress variable, at $\widetilde{c} = 0.1$ and $\widetilde{c} = 0.9$. The azimuthal velocity is counted positive from left to right and varies between $u_\theta = -20$ m.s^{-1} in blue and $u_\theta = +20$ m.s^{-1} in red, the white standing for no azimuthal velocity.

At $t = 0$ ms, a sphere of burnt gases is inserted into a converged cold flow,

obtained following the procedure detailed in 3.4.1. The swirling motion generated by each injector is apparent and the tangential velocity in the chamber is mostly negative due to the global rotative flow that was evidenced on the bisector in section 3.3.3.4. The flow generated by each injector is similar to that of its neighbours and no asymmetry is observed.
At $t = 5$ ms, the flame kernel has begun to propagate outwards in the form of an arch and already alters the azimuthal velocity distribution. The rapid expansion of the arch creates an additional tangential flow that impacts the first two injectors. This flow increases until the flame reaches the exhaust plane of the chamber at $t = 10$ ms and two separate fronts are formed. At this point, the generated azimuthal flow has reached a limit state and its intensity remains constant throughout all of phase III, from $t = 10$ ms to $t = 30$ ms, impacting up to four injectors upstream.
When the flame fronts have crossed most of the chamber and are getting close to one another, at $t = 30$ ms, the tangential flows generated by the two fronts come in contact and seem to cancel each other out, diminishing the intensity of the observed velocity.
Finally, at $t = 45$ ms, the merging has taken place, a flame has stabilized around each injector and all the fresh gases in the chamber have been consumed, a steady state it reached for the combustion and the tangential flow created by the light-round is gradually evacuated until the velocity field becomes symmetric once again. This is estimated to require 10 to 20 additional milliseconds of physical time, which was not simulated due to computational cost.
During the propagation of the flame fronts, the gases are accelerated upon crossing the flame, which leads to strong azimuthal velocities on the burnt gases side away from the flame. There is therefore a point close to the flame front where the tangential velocity goes to zero and changes sign (from positive to negative or the opposite, depending on the half-chamber H+ or H-). As can be seen on Fig. 4.2, the zero-velocity region, however, is not located inside the flame fronts nor directly behind them, but rather further behind, so that the whole region where there is combustion has a tangential gaseous velocity that goes in the direction of the flame propagation. The burnt gases volumetric expansion then plays a major role in the flame fronts absolute velocities by generating an azimuthal flow that entrains the whole fronts.
This was expected since mass conservation through the flame front implies an acceleration of the gases as the density drops. This effect leads to this strong backwards azimuthal velocity as well as a large increase of the axial velocity, meaning that the burnt gases are expelled from the chamber faster during the light-round sequence than at the ignited steady-state. We are in the presence of two phenomena that feed each other, the burnt gases tend to expand, which generates an azimuthal flow in the burnt and fresh gases. This flow in turn entrains the flame fronts which propagate much faster, producing more burnt gases that need to expand. This retro-action develops during phase II and seems to reach a limit behaviour at the beginning of phase III.

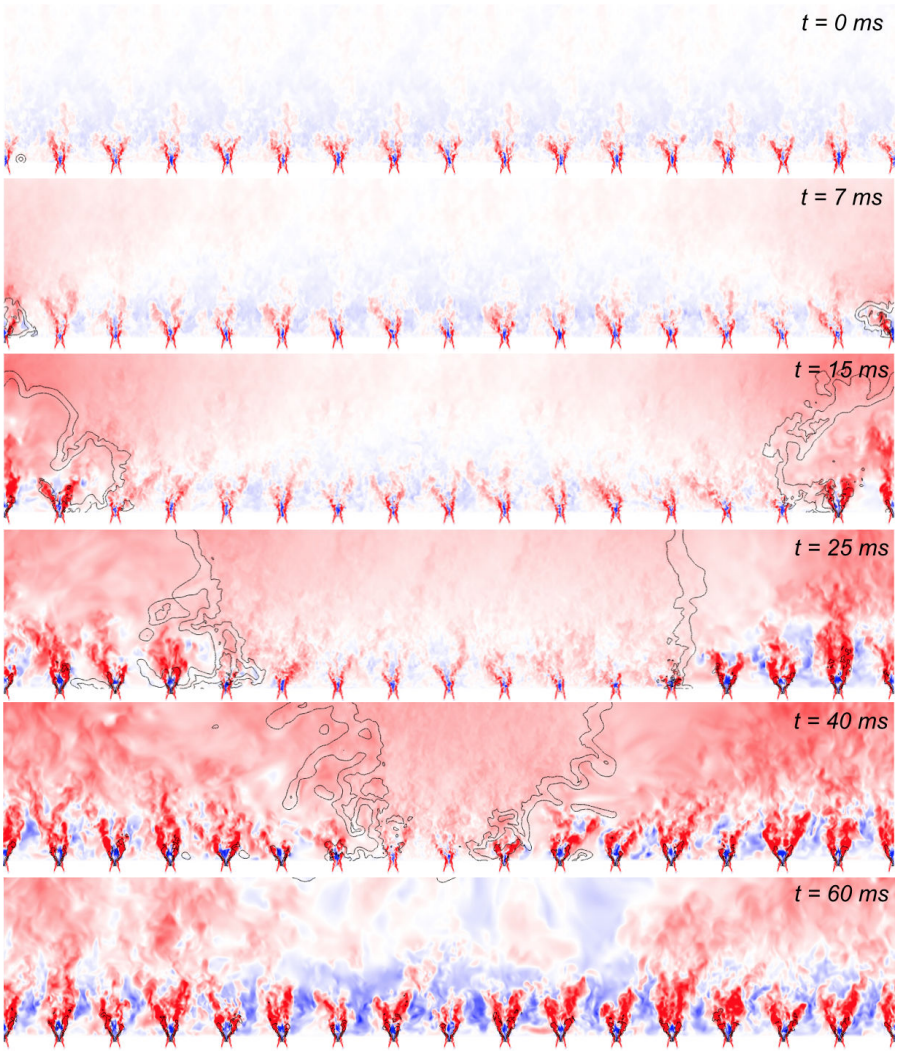

Figure 4.3: *Visualization of the axial gaseous velocity on a cylinder of radius* $r^{cut} = 175$ *mm, crossing the injectors' centerlines, unfolded on a plane surface for the case* $\Phi = 1.0$ *at different instants. The lateral sides of the unfolded cylinder correspond to the location of the first ignited injector. The velocity varies between* $u_x = -30$ $m.s^{-1}$ *in blue and* $u_x = +30$ $m.s^{-1}$ *in red. Two iso-lines of the progress variable* $\widetilde{c} = 0.1$ *and* $\widetilde{c} = 0.9$ *(in black) highlight the position of the flame fronts.*

The burnt gases volumetric expansion also has a great impact on the axial velocity, which can be observed in Fig. 4.3 for case $\Phi = 1.0$. The same cylindrical developed cuts as in Fig. 4.2 are coloured by the axial gaseous velocity, ranging from $u_x = -30$ m.s^{-1} in blue to $u_x = +30$ m.s^{-1} in red.
On the top image, at $t = 0$ ms, the cold flow axial velocity can be observed and typical multi-injector swirling flow features can be identified. As was observed on SICCA-spray and on the bi-sector simulations, a strong central recirculation

zone (CRZ) is present above each injector, surrounded by two very intense positive velocity branches that correspond to the hollow cones generated by the swirlers. Between two injectors, a negative velocity region is present, called outer recirculation zone (ORZ), that is less intense but much wider and expands up to the middle of the chamber. At the instant a flame kernel is inserted in the simulation, besides the spray regions, the axial velocity field is dominated by rather low intensities, negative in the lower half and positive in the upper half of the chamber.
Once the kernel starts to propagate, at $t = 7$ ms and then $t = 15$ ms, similarly to the tangential velocity, the axial velocity field is modified. The stabilisation of a flame around the injector in S_0 generates burnt gases that are accelerated and push the arch-like front upwards. The fresh mixture above the arch is therefore propelled towards the outlet of the chamber, hence the positive values that appear. At first, the axial velocity in the rest of the chamber is not affected.
During the two flame fronts propagation, at $t = 15$ ms or $t = 40$ ms, the flow is logically strongly accelerated above the ignited burners, but fresh gases are also entrained towards the outlet and the velocity field is globally positive everywhere in the chamber. The effect that was observed on the tangential velocity seems to result in the fresh gases being chased from the chamber ahead of the flames. This is particularly marked during the last instants of the propagation, just before the merging of the flame fronts, at $t = 40$ ms, where the axial velocity reaches up to $u_x = 20$ m.s^{-1}.
Once the flame fronts have merged and all the fresh gases have been consumed, the velocity field relaxes towards its ignited steady-state. Due to combustion, the velocity peaks around each injector are much more intense than in the cold configuration. The CRZ is still present and the ORZ that had disappeared during the light-round sequence is back with a greater magnitude than before the ignition.

4.2.2 Flow field dynamics evolution at fixed azimuthal positions

The evolution of the flow inside the chamber can also be observed from fixed positions, and in particular on planes at fixed azimuthal positions, as shown in Fig. 4.4. The average of quantities over these radial cuts gives information on the response of chamber slices during the light-round sequence.
Figure 4.5 presents the temporal evolution of the mean values of the tangential axial gaseous velocities u_θ and u_x, averaged over three radial cuts, for $\theta^{cut} = 78.75°$, $\theta^{cut} = 90°$ and $\theta^{cut} = 101.25°$, which respectively correspond to the frontier between sectors S_3 and S_4 (or S_{-3} and S_{-4}), to the middle of sector S_4 (or S_{-4}), and to the frontier between sectors S_4 and S_5 (or S_{-4} and S_{-5}). Results are presented for both H+ (blue curves) and H- (red curves) and are extracted from case $\Phi = 0.8$. Conclusions being similar for the other two cases, the corresponding plots are not shown here. In order to ease comparison, u_θ is

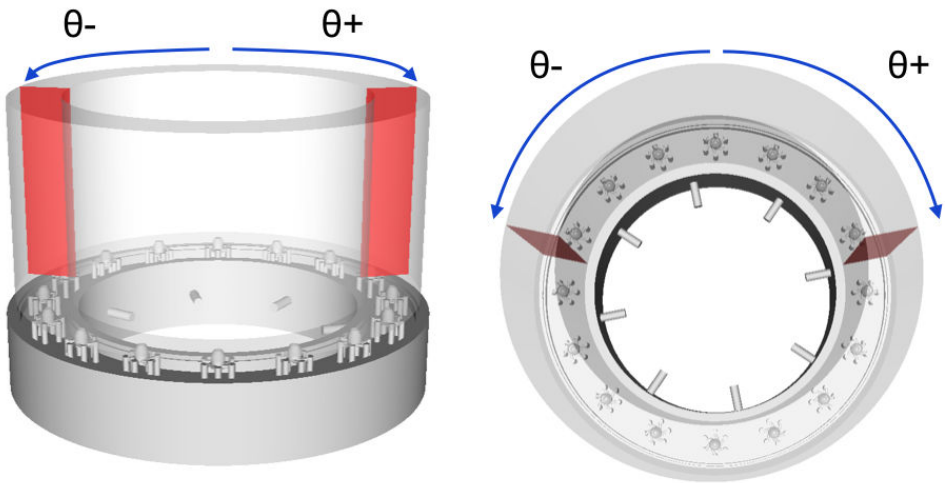

Figure 4.4: *Schematic description of the radial cuts, for fixed azimuthal positions θ^{cut}. Two cuts are displayed for $\theta^{cut} = 78.25°$ on the H+ and H- sides as well as the definition of the angles. A lateral and a top view of the chamber are presented*

plotted for H+ (in blue) and $-u_\theta$ for H- (in red) so that they appear to have the same sign while really being opposite (as is for instance seen on Fig. 4.2). Additionally, the crossing of the flame is highlighted by dashed vertical lines. These lines mark the instant the most forward point on each flame front, based on iso-surfaces at $\widetilde{c} = 0.9$, reaches the chosen θ, so the instants really correspond to the beginning of the crossing of the flame fronts, since they are not perfectly vertical. This most forward point, called the *leading point* of the flame, will be defined and discussed in details in Sec. 4.4. The averaged heat release rate is also displayed on the plots in dashed lines, associated to the axis on the right. The same post-processing has been done on the liquid velocities but due to the relatively small size of the droplets, the liquid velocity is identical to the gaseous velocity, so no further information can be extracted. The liquid velocities are therefore not presented here.

On the selected tangential positions, $\theta^{cut} = 90°$ crosses an injector centerline while the two others are located in between two injectors. As a consequence, the $\theta^{cut} = 90°$ cut is the only one where some heat release remains after the flame fronts have passed, while for the other two, the heat release rate drops to zero since the stabilised flames in the adiabatic walls case are compact and do not interact with their neighbours.

It was observed in section 3.3.3.4 that on a mean cold solution, an azimuthal flow was created in the chamber due to the direction of rotation of the swirlers. At the beginning of the simulation, for all three cases, the averaged azimuthal velocity is not null, it is instead positive in both halves (u_θ is positive in H+ and $-u_\theta$ is negative in H-), meaning that the tangential motion is also present in the full chamber and can clearly be observed on the instantaneous solutions. Even

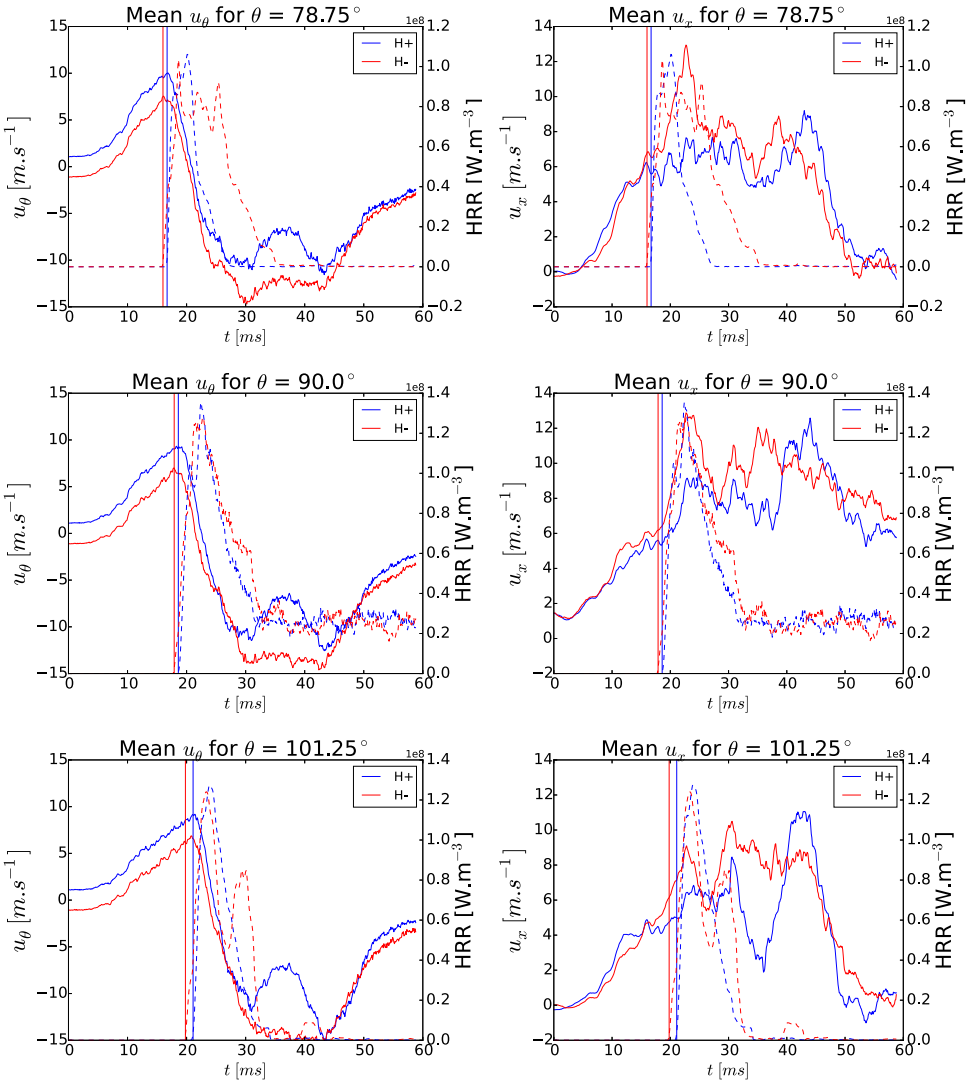

Figure 4.5: *Temporal evolution of the mean tangential gaseous velocity (u_θ for H+ in blue and $-u_\theta$ for H- in red) on the left and the mean axial gaseous velocity on the right (full lines), averaged over cuts for several values of θ^{cut}. The dashed lines represent the averaged heat release rate, associated to the right axis. Data from H+ cuts is presented in blue and data from H- in red. The vertical lines mark the instant of the flame crossing, based on the leading points position. The data presented here is extracted from case $\Phi = 0.8$.*

though the full velocity convergence was not attained at the end of the light-round in the simulations, it seems that this rotational motion is also present in the ignited state: the H+ and H- mean velocities tend towards their steady-state value with a difference that is the result of a global motion.
Shortly after the triggering of the light-round, the mean tangential velocity

increases as a result of the volumetric expansion of the burnt gases evidenced in the previous section, going from a relatively low magnitude of $u_\theta \sim 1$ m.s^{-1} to a much greater one $u_\theta \sim 10$ m.s^{-1}. This constitutes a quantification of the induced flow in the fresh gases, the tangential gaseous velocity is gradually increased by one order of magnitude and reaches a maximum as the leading point passes, which marks the beginning of the crossing of the flame.
An interesting observation is the fact that the maximum of azimuthal velocity is reached at the time of the leading point crossing and not, for instance, at the maximum of averaged heat release on the cut, which occurs a few millisecond later. This will be further analysed in Sec. 4.4.3 with the study of the flow field surrounding the leading point.
Once the leading point has crossed the considered tangential position, the averaged tangential velocity drops sharply towards very strong negative values, around $u_\theta \sim -10$ m.s^{-1}. This does not mean that the whole cut sees negative u_θ, but rather that, as the flame progresses, an increasing proportion is covered by burnt gases that expand away from the flame fronts, as was seen on Fig. 4.2.
Similarly to the tangential speed, the axial velocity increases gradually approximately 15 ms before the flame crossing, but the leading point position does not appear to determine the velocity maximum. During the crossing of the flame, that is to say when the heat release rate is not zero, and for some time afterwards, the axial velocity reaches a plateau which corresponds to the expulsion from the chamber of the accelerated burnt gases. In the cuts taken between two injectors ($\theta^{cut} = 78.75°$ and $\theta^{cut} = 101.25°$), the mean axial velocity drops towards zero at the end of the light-round sequence, while in the cut $\theta^{cut} = 90°$ which crosses an injector, it remains at high levels due to the presence of the stabilised flame.

4.2.3 Flow field dynamics at the chamber exhaust

In the previous section the effect of the flame propagation on the velocity field was shown, resulting in the fresh gases being pushed away from the flame and outside of the chamber. The magnitude of this chasing of the fresh gases can be observed more quantitatively through the analysis of the mass flowrates through the exit plane of the chamber. The total mass flowrate $\dot{m}_{tot}^{out}$ can be divided into two contributions, a flow of unburnt mixture $\dot{m}_u^{out}$ and a flow of burnt gases $\dot{m}_b^{out}$, computed in Eqs. 4.1 to 4.3, using the progress variable $\widetilde{c}$ defined in Eq. 3.2.

$$\dot{m}_b^{out} = \int_{A^{out}} \widetilde{c}\overline{\rho}\widetilde{u}_x \; dS \tag{4.1}$$

$$\dot{m}_u^{out} = \int_{A^{out}} (1-\widetilde{c}) \left(\overline{\rho}\widetilde{u}_x + \overline{\alpha}_l \rho_l \widehat{u}_{l,x}\right) \; dS \tag{4.2}$$

$$\dot{m}_{tot}^{out} = \dot{m}_b^{out} + \dot{m}_u^{out} \tag{4.3}$$

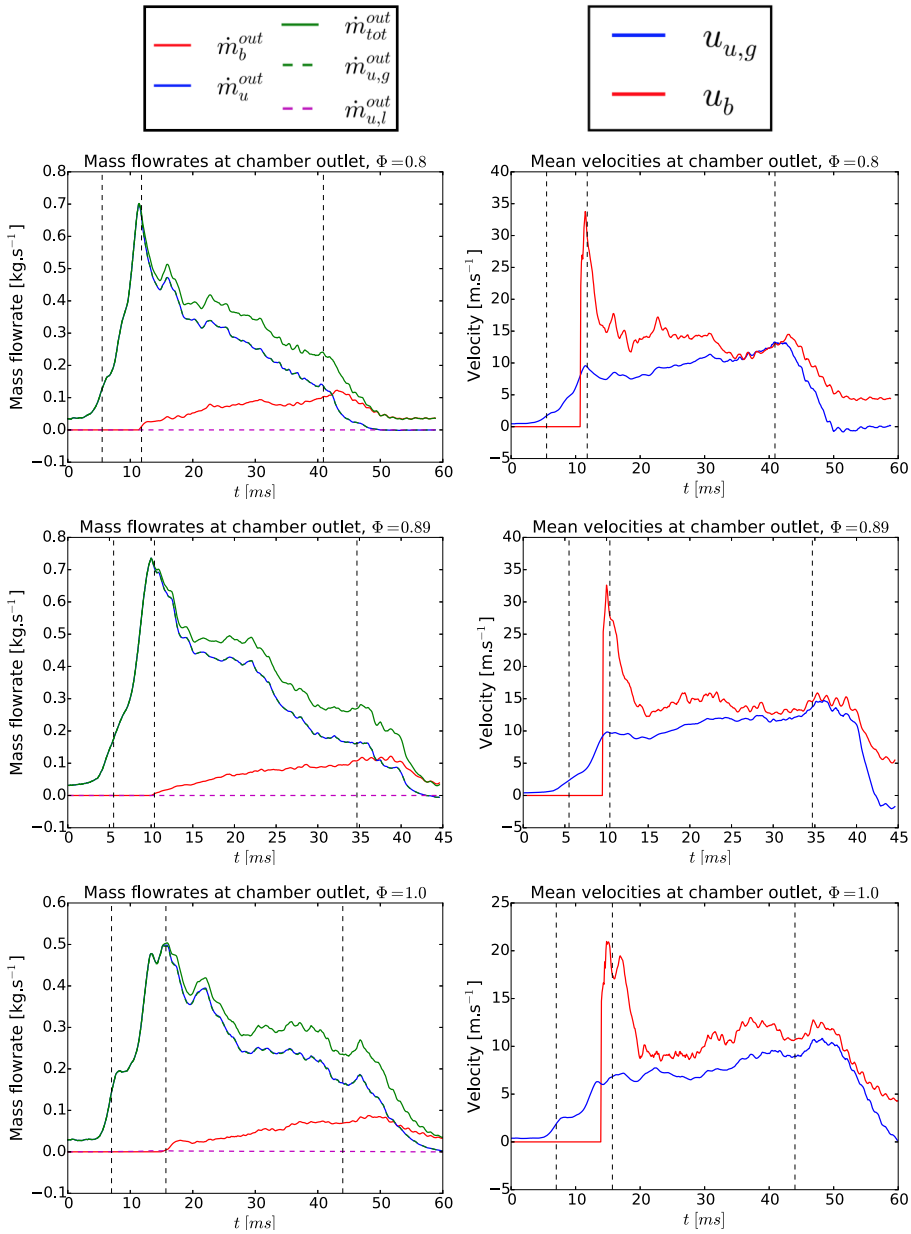

Figure 4.6: *Evolution of the mass flowrates (left) and mean velocities (right) at the chamber exit for the three cases. Left plots: -: burnt gases, -: total unburnt mixture, -: total mixture. The unburnt gases exiting the chamber are divided into: - -: unburnt gaseous mixture, - -: unburnt liquid. Right plots: -: burnt gases mean velocity, - : unburnt mixture mean velocity.*

As is apparent in Eq. 4.2, the unburnt mixture mass flowrate is composed of a

gaseous flow and a liquid flow. Two additional flowrates are therefore defined:

$$\dot{m}_{u,g}^{out} = \int_{A^{out}} (1-\widetilde{c})\overline{\rho}\widetilde{u}_x \; dS \tag{4.4}$$

$$\dot{m}_{u,l}^{out} = \int_{A^{out}} (1-\widetilde{c})\overline{\alpha}_l \rho_l \widehat{u}_{l,x} \; dS \tag{4.5}$$

The integrals are computed on the exit surface of the chamber, noted A_{out}, located at height $X = 195$ mm. Similarly, mean velocities for the burnt and unburnt mixtures can be computed as:

$$u_{u,g}^{out} = \frac{\int_{A^{out}} (1-\widetilde{c})\widetilde{u}_x \; dS}{\int_{A_{out}} (1-\widetilde{c}) dS} \tag{4.6}$$

$$u_b^{out} = \frac{\int_{A^{out}} \widetilde{c}\widetilde{u}_x \; dS}{\int_{A_{out}} \widetilde{c} dS} \tag{4.7}$$

Figure 4.6 presents the temporal evolution of each of the previously defined flowrates for the three considered cases on the left plots and of the burnt and unburnt mean velocities on the right plots. Vertical dashed lines have been added to mark each case's phases, delimiting phases I, II, III and IV.
At $t = 0$ ms, the chamber is at equilibrium and the unburnt and total mass flowrates at the exit are equal and correspond to the total injected mass. Since the global power was kept constant for all three cases, the injected liquid mass flowrate is identical $\dot{m}_l^{in} = 1.776 \times 10^{-3}$ kg.s^{-1}. The injected air flow was adjusted to obtain the desired equivalence ratio: $\dot{m}_{air}^{in,\Phi=0.8} = 33.57 \times 10^{-3}$ kg.s^{-1}, $\dot{m}_{air}^{in,\Phi=0.89} = 30.10 \times 10^{-3}$ kg.s^{-1} and $\dot{m}_{air}^{in,\Phi=1.0} = 26.85 \times 10^{-3}$ kg.s^{-1}.
The three cases exhibit similar features on the evolution of the flow at the exit of the chamber. During the first few instants of the simulation, the flame kernel stagnates before it can encounter favourable conditions and, similarly to the velocity fields, the flow at the exit is not yet affected. Once the kernel is able to expand, the generation of additional axial velocity that was observed on Fig. 4.3 begins to impact the fresh gases flow at the chamber exit and its mass flowrate as well as its velocity increases. The formation of the arch-like flame front marks the transition between phase I and phase II, identified as the first vertical line. Phase II is characterised by a sharp increase of the fresh mixture flowrate and velocity at the exit, due to the rapidly expanding arch that pushes the unburnt mixture downstream. The flame being still confined inside the chamber, the burnt gases flowrate is null. For all cases, a maximum of the unburnt mixture flowrate is reached at the end of phase II, when the arch reaches the exit of the chamber. At this point, the total mass flowrate is comprised between 0.5 and 0.7 kg.s^{-1}, which is approximately 20 times the value of the injected flowrate. At this instant, the burnt gases reach the exit with a very high velocity which is due to some build-up effect inside the arch, the burnt gases, being less dense than the fresh gases, are limited in their expansion by the flame fronts, so the pressure builds up and is released in contact with the

atmosphere. This causes the peak in burnt gases velocity observed in all cases around the transition between phases II and III, u_b^{out} increases up to 30 m.s^{-1} for a brief instant before dropping back down to half that value.
The second and third vertical lines mark the beginning and the end of phase III, during which the two fronts formed by the division of the arch propagate in their respective half-chamber. The burnt gases have reached the exit and the corresponding mass flowrate increases in a linear manner with a slightly increasing velocity. In the meantime, the fresh gases flowrate decreases regularly, though with the mean velocity does not, as the fronts progress in the chamber and the surface available for their expulsion is reduced. The corresponding velocity increases slightly, indicating that the effect of the burnt gases volumetric expansion on the fresh stream remains as strong throughout all of phase III. The unburnt mixture flowrate decreases faster than the burnt gases flowrate increases, resulting in the total flowrate being divided by two between the beginning and the end of phase III.

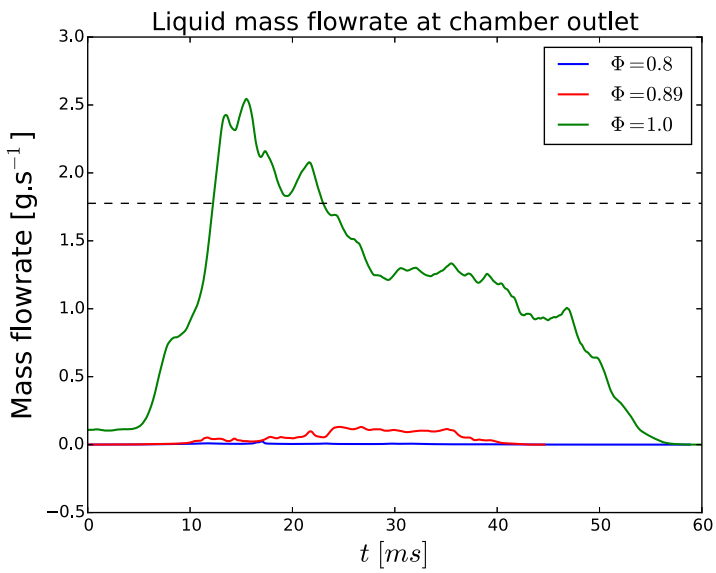

Figure 4.7: *Evolution of the liquid mass flowrate at the chamber exit for each case,* $\Phi = 0.80$ *in blue,* $\Phi = 0.89$ *in red and* $\Phi = 1.0$ *in green. The black horizontal dashed line marks the total liquid mass flowrate injected in the chamber through the swirlers.*

The last vertical lines, on the right of the plots, marking the transition between phase III and phase IV, correspond to the head-on collisions between the two fronts. During phase IV, some fresh gases remain in the chamber since the front collide in the bottom of the chamber and are rapidly consumed or expelled, so $\dot{m}_u^{out}$ drops to zero. At the same time, the total flowrate also decrease sharply towards its steady-state value, which is logically equal to the burnt gases flowrate and to the unburnt gases flowrate at the beginning of the light-

round.
Both gaseous and liquid unburnt flowrates are plotted on Fig. 4.6, in green and magenta dashed lines, respectively. For all cases, the liquid mass flowrate is negligible before the gaseous one. However, some differences had been observed on the converged cold flow on the bi-sectors in section 3.3.3 that can be evidenced by comparing the liquid flowrates for the three cases. This is done in Fig. 4.7 where each color stands for one case, $\Phi = 0.80$ is plotted in blue, $\Phi = 0.89$ in red and $\Phi = 1.0$ in green. As a reference, the horizontal dashed line marks the value of the liquid mass flowrate injected in the chamber, identical for all cases.
For cases $\Phi = 0.8$ and $\Phi = 0.89$, the cold flow convergence showed that the liquid was fully prevaporised in the chamber, no or a negligible amount of liquid is left to exit the chamber and $\dot{m}_{u,g}^{out} = \dot{m}_{u}^{out}$. In case $\Phi = 1.0$, a saturated state was reached on the cold flow, meaning that some liquid is present up the whole height of the chamber. Throughout the light-round sequence, Fig. 4.7 shows that for this last case the liquid mass flowrate exhibits a behaviour similar to the gaseous mass flowrate, with a much lower order of magnitude: during phase I and II, the flowrate increases sharply up to a maximum and then decreases regularly in phase III. Finally, after the merging, during phase IV, the flowrate drops towards zero, since the chamber is fully ignited and all the liquid is evaporated in the flames stabilised around each injector.

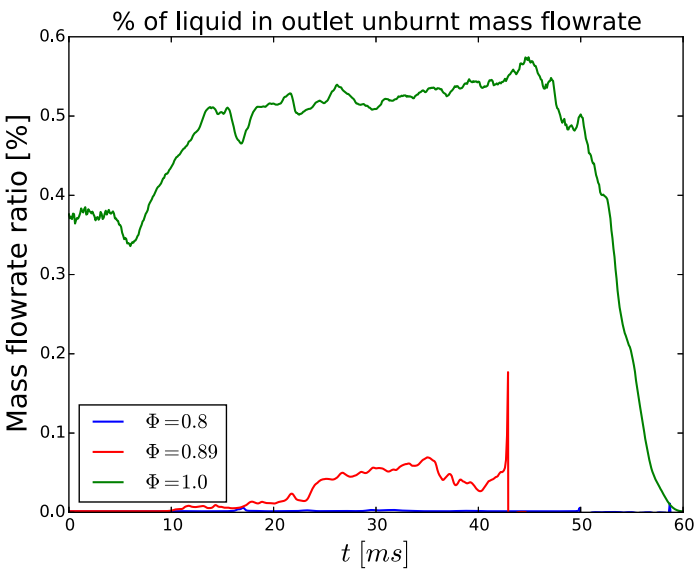

Figure 4.8: *Evolution of the percentage of liquid mass flowrate at the chamber exit for each case,* $\Phi = 0.80$ *in blue,* $\Phi = 0.89$ *in red and* $\Phi = 1.0$ *in green.*

Figure 4.8 displays the evolution of the ratio of liquid in the fresh gases mass flowrate at the outlet, in percentage, defined as $\dot{m}_{u,l}^{out}/(\dot{m}_{u,g}^{out} + \dot{m}_{u,l}^{out})$.

As expected, the liquid proportion at the outlet is negligible on cases $\Phi = 0.8$ and $\Phi = 0.89$. In case $\Phi = 1.0$ however, the ratio of liquid in the fresh gases is roughly constant during the light-round and drops at the end once the merging has occurred. This value, of around 0.5 %, is much lower than at the injection (for $\Phi = 1.0$, 5.8 % of liquid mass is injected). The fact that it remains constant means that the flame fronts propagation and the azimuthal flow that they generate do not modify significantly the composition of the fresh mixture that exits the chamber and that the gas and the liquid are equivalently impacted. This is consistent with observations made on the single burner SICCA-Spray and the bi-sector, where the size of the droplets led them to be completely entrained by the gaseous flow after few millimeters in the chamber.

4.3 Flame fronts dynamics: global point of view

The evolution of the flame can first be observed from a global point of view, considering the system formed by the entire chamber. In this approach, the global evolution of the flame fronts is characterised and analysed to identify the key aspects of the light-round sequence for the three considered cases. The flame is identified by considering the progress variable defined in Eq. 3.2 and reminded here:

$$c = \frac{Y_c}{Y_c^{eq}} = \frac{Y_{CO_2} + Y_{CO}}{Y_{CO_2}^{eq} + Y_{CO}^{eq}} \tag{4.8}$$

4.3.1 Analysis of the flame structure

In order to observe more closely the structure of the flame fronts, it is interesting to look at their evolution on sections along their direction of propagation. To that end, cylindrical cuts are taken in the chamber at radius $r^{cut} = 0.175$ m, in the middle of the chamber, and unfolded as shown in Fig. 4.1 for a better visualisation.

The local combustion regime in a flame front can be characterised through the instantaneous Takeno's Index (TI), defined in Eq. 2.12. To highlight combustion regions, and using the methodology proposed in Yamashita et al. (1996) and Reveillon and Vervisch (2005), the TI is multiplied by the absolute value of the heat release rate (TI × HRR, see Eq. 4.9).

$$\text{TI} \times \text{HRR} = \text{TI} \cdot |\text{HRR}| = \frac{\nabla Y_{C_7H_{16}} \cdot \nabla Y_{O_2}}{|\nabla Y_{C_7H_{16}} \cdot \nabla Y_{O_2}|} \cdot |\text{HRR}| \tag{4.9}$$

Figures 4.9 and 4.10 present the fields of TI × HRR at different instants of the flame propagation for cases $\Phi = 0.89$ (Fig. 4.9) and $\Phi = 1.0$ (Fig. 4.10). The legend is added on the top image. From the definition of Takeno's Index, it comes that positive values (from yellow to red) indicate premixed combustion

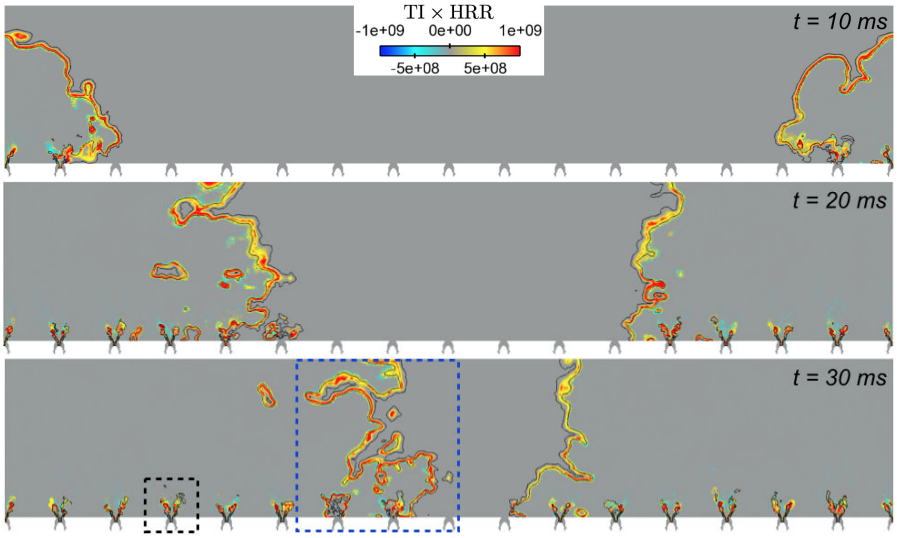

Figure 4.9: *Visualisation of TI× HRR during the flame propagation in case* $\Phi = 0.89$ *on a cylinder of radius* $r^{cut} = 175$ *mm, crossing the injectors' centerlines, unfolded on a plane surface. Data is presented for* $t = 10$ *ms (top),* $t = 20$ *ms (middle) and* $t = 30$ *ms (bottom). Positive values (from yellow to red) indicate premixed combustion areas while negative values (in shades of blue) non-premixed reaction areas. Two iso-lines of the progress variable* $\widetilde{c} = 0.1$ *and* $\widetilde{c} = 0.9$ *(in black) highlight the position of the flame fronts.*

areas while negative values (in shades of blue) correspond to non-premixed reaction layers. Regions where no combustion is taking place are coloured in grey.

Figures 4.9 and 4.10, show that the flame that stabilises around each injector has a structure that is logically close to that observed on the simulation of SICCA-Spray with adiabatic walls. One flame that is in the process of stabilising around an injector during the light-round is compared in Fig. 4.11 with the stabilised flame in SICCA-Spray. Very close structures are observed, with the flame entering the swirler in the central recirculation zone and a V-shape with approximately the same height. The encountered combustion regimes are also similar, with a premixed dominance while some diffusion flame fronts are present in particular at the foot of the flame. As was observed experimentally by Prieur et al. (2018) on SICCA-Spray and MICCA-Spray, the flame first stabilises in this more compact and attached position before lifting and reaching its steady-state lifted form.

Focusing on the propagating flame fronts, for which a zoom is also displayed in Fig. 4.11 for case $\Phi = 0.89$, it appears that only positive TI $\times$ HRR are present, which means that the fronts propagation during the light-round sequence is largely dominated by premixed combustion. This validates the premixed flame assumptions that have been made several times during the set-up of the simulation, in particular in the use of the TFLES combustion model. The analysis

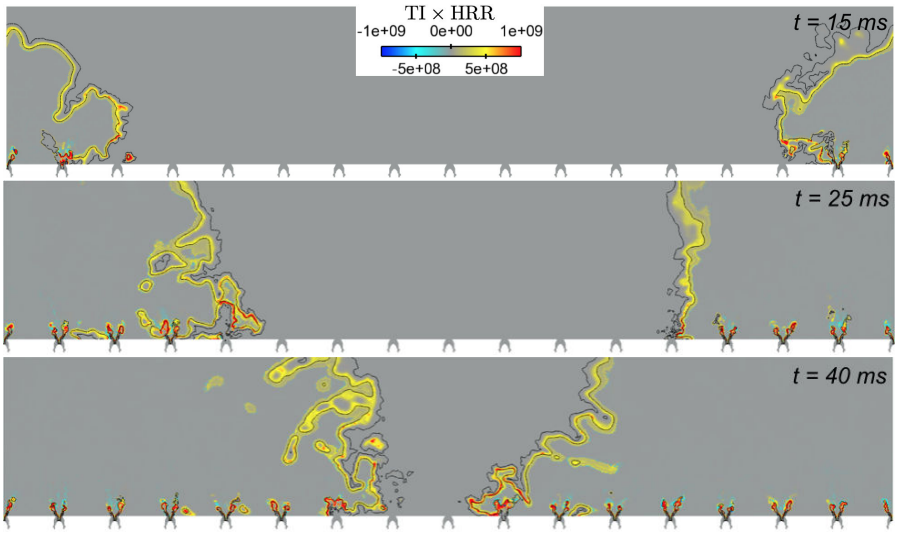

Figure 4.10: *Visualisation of TI× HRR during the flame propagation in case* $\Phi = 1.0$ *on a cylinder of radius* $r^{cut} = 175$ *mm, crossing the injectors' centerlines, unfolded on a plane surface. Data is presented for* $t = 15$ *ms (top),* $t = 25$ *ms (middle) and* $t = 40$ *ms (bottom). Positive values (from yellow to red) indicate premixed combustion areas while negative values (in shades of blue) non-premixed reaction areas. Two iso-lines of the progress variable* $\widetilde{c} = 0.1$ *and* $\widetilde{c} = 0.9$ *(in black) highlight the position of the flame fronts.*

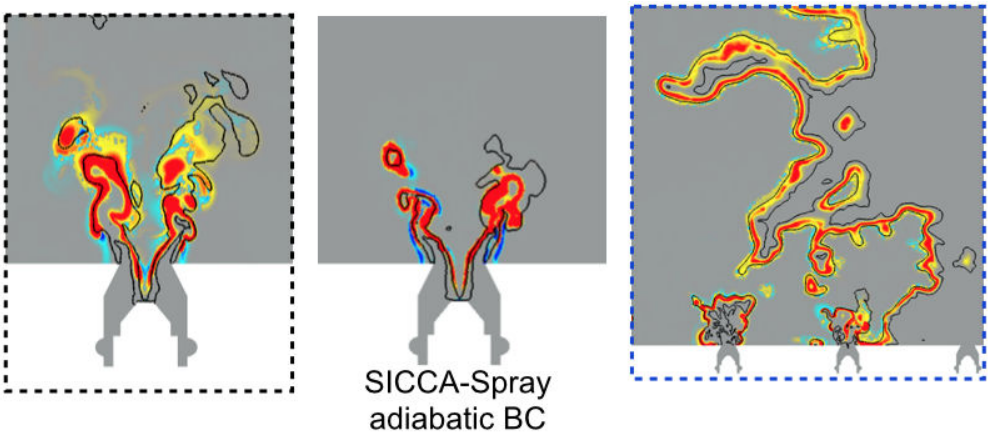

Figure 4.11: *Left: zoom on one injector during the light-round of case* $\Phi = 0.89$ *at* $t = 30$ *ms, the zoom area is identified by the black dashed line rectangle in Fig. 4.9. Centre: instantaneous solution of the stabilised flame in SICCA-Spray with adiabatic boundary conditions. Right: zoom on the propagating flame during the light-round of case* $\Phi = 0.89$ *at* $t = 30$ *ms, the zoom area is identified by the blue dashed line rectangle in Fig. 4.9. All images are coloured by TI* $\times$ *HRR with the colour scale displayed in Fig. 4.9.*

of the fronts propagation can also be carried out using premixed flame considerations, as will be done later in this chapter.

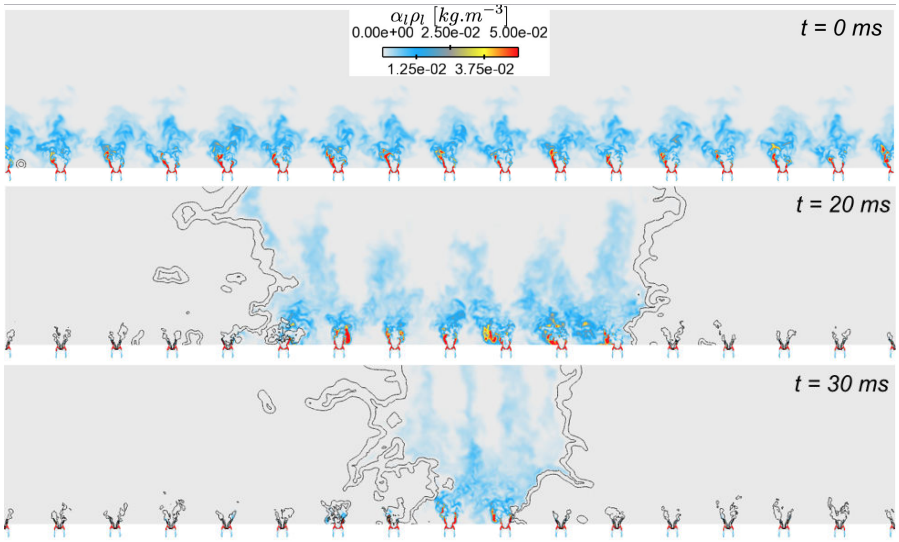

Figure 4.12: *Visualisation of the liquid density $\alpha_l \rho_l$ during the flame propagation in case $\Phi = 0.89$ on a cylinder of radius $r^{cut} = 175$ mm, crossing the injectors' centerlines, unfolded on a plane surface. Data is presented for $t = 0$ ms (top), $t = 20$ ms (middle) and $t = 30$ ms (bottom). Two iso-lines of the progress variable $\widetilde{c} = 0.1$ and $\widetilde{c} = 0.9$ (in black) highlight the position of the flame fronts.*

The predominance of premixed combustion inside the propagation flame fronts suggests that the liquid evaporates and mixes with the air before or at the beginning of the combustion regions. more detail can be obtained by looking at the fields of the liquid mass during the light-round sequence on the $r^{cut} = 175$ mm unfolded cut: Figs. 4.12 and 4.13 display fields of the liquid density $\alpha_l \rho_l$ for cases $\Phi = 0.89$ and $\Phi = 1.0$ at three different instants of the flame propagation.
The difference in liquid mass repartition in the fresh gases depending on the case was already evidenced and commented on the bisector cold flow in Sec. 3.3.3.2, but even in case $\Phi = 1.0$ where some liquid is present up the whole height of the chamber, it appears that it is completely evaporated in front of the flame front. Indeed, no liquid is present behind the first black line, the one that is on the fresh gases side, which stands for $\widetilde{c} = 0.1$, and where little reaction occurs. Inside the flame front, between the two iso-lines, all the liquid has evaporated and mixed with the air, thus explaining the premixed regime.

4.3.2 Evolution of the flame surface

A global point of view of the light-round sequence can be obtained by considering the evolution of the flame surface in the chamber. For a flame front that

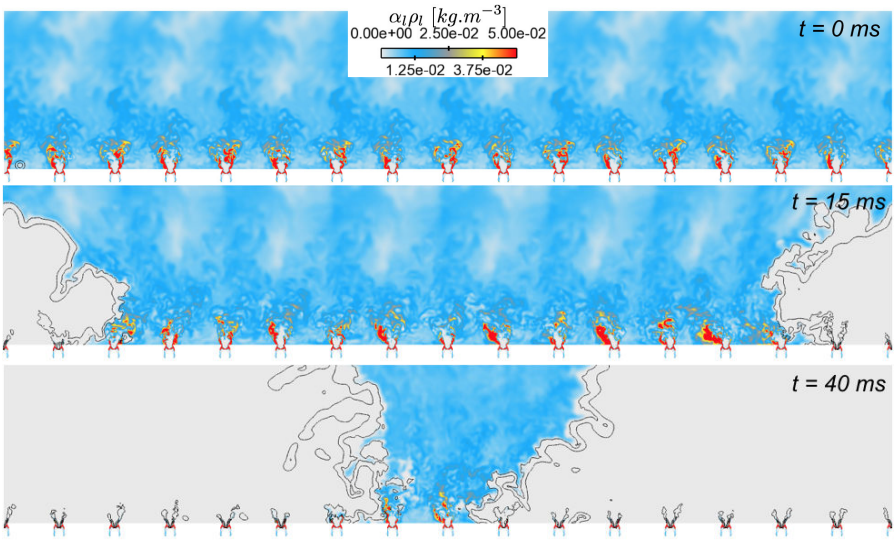

Figure 4.13: *Visualisation of the liquid density $\alpha_l \rho_l$ during the flame propagation in case $\Phi = 1.0$ on a cylinder of radius $r^{cut} = 175$ mm, crossing the injectors' centerlines, unfolded on a plane surface. Data is presented for $t = 0$ ms (top), $t = 15$ ms (middle) and $t = 40$ ms (bottom). Two iso-lines of the progress variable $\widetilde{c} = 0.1$ and $\widetilde{c} = 0.9$ (in black) highlight the position of the flame fronts.*

is not infinitely thin, the resolved flame surface can be computed from the resolved flame surface density $\Sigma_{res} = |\boldsymbol{\nabla}\widetilde{c}|$ (as defined in Veynante and Vervisch (2002)) integrated over the chamber volume V_{cc}, where $|\boldsymbol{\nabla}\widetilde{c}|$ is the norm of the local gradient of the filtered progress variable $\widetilde{c}$:

$$A_{res} = \int_{V_{cc}} \Sigma_{res} \mathrm{d}V = \int_{V_{cc}} |\boldsymbol{\nabla}\widetilde{c}| \mathrm{d}V \tag{4.10}$$

The loss of flame wrinkling due to the thickening procedure of the TFLES model and due to the filtering of the LES model is compensated through the use of the subgrid scale wrinkling Ξ_Δ, with Δ the local LES filter size (see section 1.4.1.2). The total flame surface density Σ_{tot}, as well as the subgrid scale flame surface density Σ_{sgs}, can therefore be estimated as:

$$\Sigma_{tot} = \Xi_\Delta \ |\boldsymbol{\nabla}\widetilde{c}| \tag{4.11}$$

$$\Sigma_{sgs} = \Sigma_{tot} - \Sigma_{res} = (\Xi_\Delta - 1) \ |\boldsymbol{\nabla}\widetilde{c}| \tag{4.12}$$

These expressions lead to the following formulations for the total and subgrid scale surfaces in the chamber, A_{tot} and A_{sgs}:

$$A_{tot} = \int_{V_{cc}} \Sigma_{tot} \mathrm{d}V = \int_{V_{cc}} \Xi_\Delta \ |\boldsymbol{\nabla}\widetilde{c}| \mathrm{d}V \tag{4.13}$$

$$A_{sgs} = \int_{V_{cc}} \Sigma_{sgs} \mathrm{d}V = \int_{V_{cc}} (\Xi_\Delta - 1) \ |\boldsymbol{\nabla}\widetilde{c}| \mathrm{d}V = A_{tot} - A_{res} \tag{4.14}$$

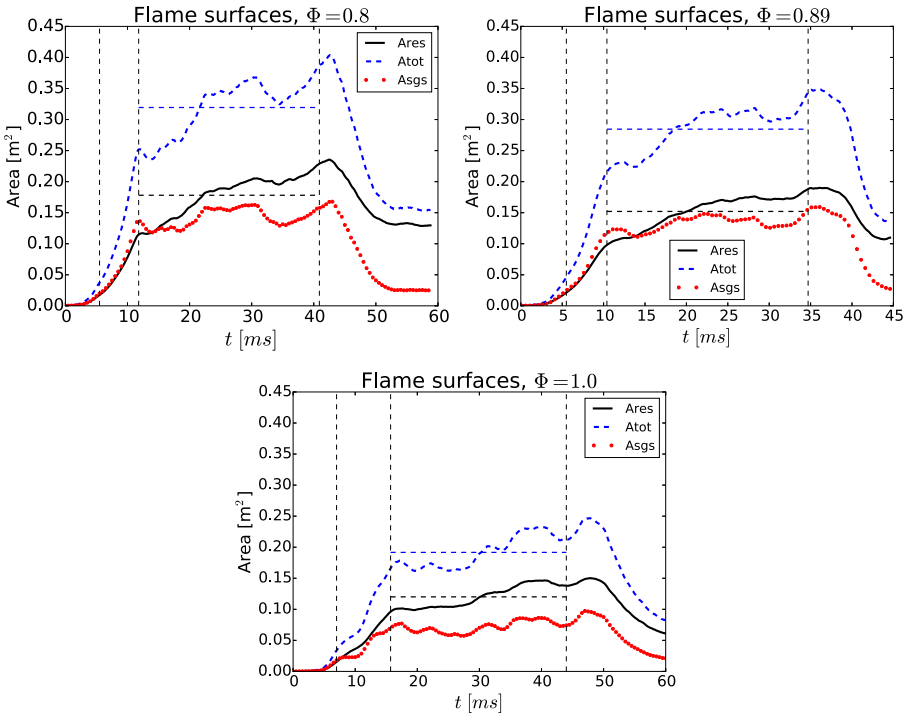

Figure 4.14: *Temporal evolution of the resolved flame surface A_{res} in full black lines, the total flame surface A_{tot} in dashed blue lines and the subgrid scale flame surface A_{sgs} in red dots. Results for the three cases are displayed: top left for case $\Phi = 0.8$, top right for case $\Phi = 0.89$ and bottom for case $\Phi = 1.0$. For each case, vertical dashed lines mark the beginning and the end of phases I to IV.*

The temporal evolution of these three surfaces throughout the light-round sequence is reported on Fig. 4.14. Each plot corresponds to one of the studied operating conditions, with A_{tot} plotted in dashed blue lines, A_{res} in full black lines and A_{sgs} in red dots. Vertical dashed lines have been added to mark the beginning and the end of phases I to IV and the average of A_{tot} and A_{res} during phase III in each case are respectively represented by the blue and black horizontal dashed lines.

The total flame surface evolution looks very similar to that of the integrated heat release rate that was presented in section 3.4.4. This is confirmed through Fig. 4.15 which presents a comparison between the chamber-integrated heat release rate (full lines) and the total flame surface in the chamber (dashed lines), each normalised by its maximum to enable comparison. The blue curves stand for case $\Phi = 0.8$ data, the red for case $\Phi = 0.89$ and the green for case $\Phi = 1.0$. While the three curves have the same origin of times, their maximum, which approximately corresponds to the merging of the flame fronts, does not occur at the same instants. The differences in light-round durations (that were compared to experimental data in Fig. 3.15) is here retrieved, with case

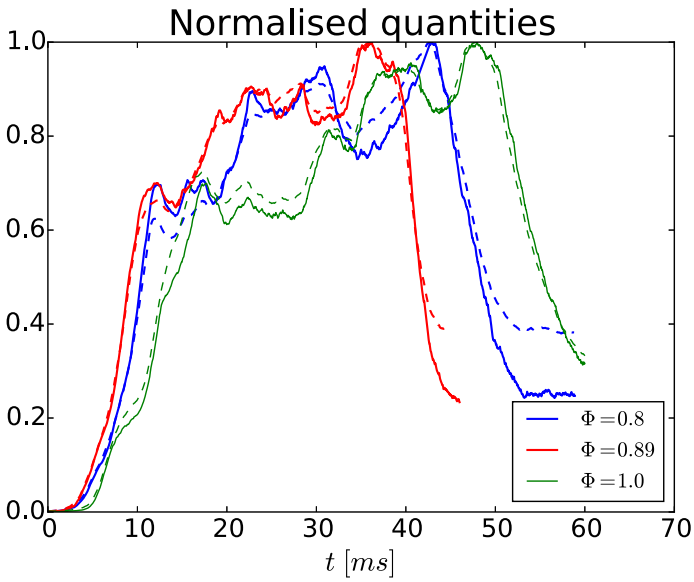

Figure 4.15: *Evolution of normalised quantities for the three cases. Full lines: normalised integrated heat release rate, dashed lines: normalised total flame surface. Each quantity has been normalised by its maximum for the sake of comparison.*

$\Phi = 0.89$ being the fastest, followed by case $\Phi = 0.8$ and then case $\Phi = 1.0$, for which the light-round duration τ^{lr} is overestimated in the simulation compared to the experiment.

The total flame surface and the heat release rate evolutions are, as expected, strongly correlated. In purely gaseous premixed combustion, the flame surface is proportional to the total heat release rate in a system. In the case of two-phase combustion, the relation between the two is less obvious. However, as was evidenced on the cold flow convergence in section 3.3.3, the liquid is largely pre-vaporised in the chamber before the ignition and section 4.3.1 showed that the structure of the two-phase propagating flame fronts is very close to that of premixed gaseous fronts, and that they therefore tend to behave as such. This is consistent with the observed similitude between flame surface and heat release rate.

On Fig. 4.14, the flame surfaces evolution is similar for the three cases, all surfaces increase exponentially during phases I and II, until the beginning of phase III, clearly visible through the break in the smooth evolution, after which the curves have a more erratic behaviour, with some oscillations around a mean value that increases linearly as each individual burner is ignited one after the other. The total flame surface is approximately twice greater than the resolved flame surface, which shows the importance of the subgrid scale and of the corresponding models.

It is interesting to compare the evolution of the average flame surfaces, total

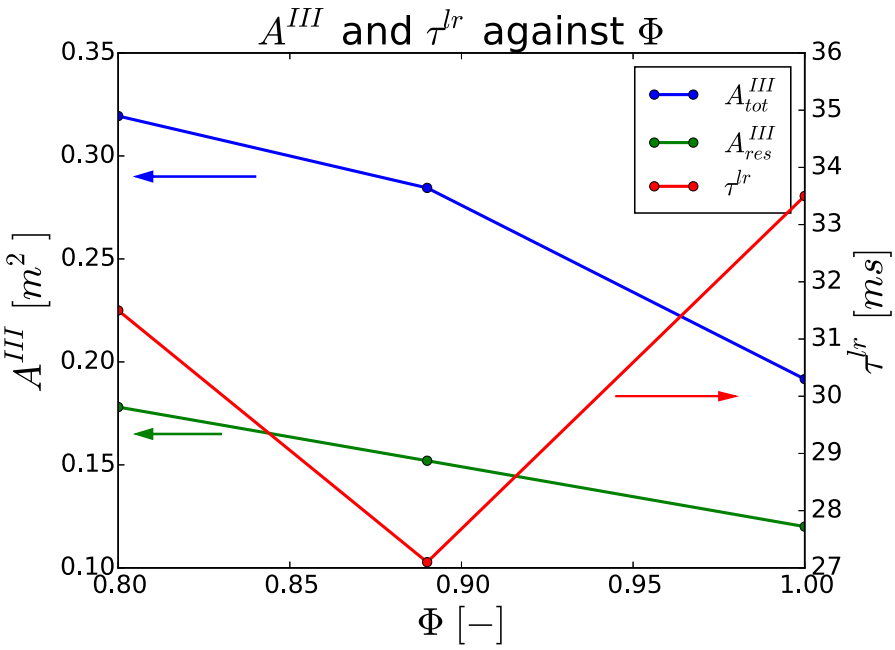

Figure 4.16: *Average total and resolved flame flame surfaces over phase III, A^{III}_{tot} in blue and A^{III}_{res} in green, as displayed on Fig. 4.14, against the global equivalence ratio Φ, associated to the left axis. Light-round delay τ^{lr} in red against the global equivalence ratio Φ, associated to the right axis.*

and resolved, during phase III, that were displayed on Fig. 4.14 for each case. The values are reported in Fig. 4.16, in blue for A^{III}_{tot} and in red for A^{III}_{res}, against the injected global equivalence ratio Φ, associated to the axis on the left. Additionally, the light-round duration is added in red, associated to the axis on the right. Both the total and resolved average flame surfaces decrease with the equivalence ratio, however, this is not consistent with the evolution of the light-round delay, which decrease between $\Phi = 0.8$ and $\Phi = 0.89$ but increase between $\Phi = 0.89$ and $\Phi = 1.0$. This is surprising since the flame surface is linked to the consumption speed of the reactants, and therefore to the flame propagation speed.

For fixed injection conditions (and in particular fixed equivalence ratio), a decrease of the flame surface means that less reactants are consumed and therefore that the flame absolute velocity decreases (the acceleration of the flame due to its increased surface was for instance observed experimentally by Masri et al. (2012) and through the simulation of the same experimental set-up by Vermorel et al. (2017)). One would then expect an increase of the light-round duration with the decrease of the flame surface in phase III. This is however balanced by the increase of the equivalence ratio which, up to $\Phi = 1.1$, increases the laminar flame speed. In the experimental observations by Prieur et al. (2017),

this effect is the strongest and τ^{lr} systematically decreases when Φ increases. This tendency is here retrieved for the two first cases ($\Phi = 0.8$ and $\Phi = 0.89$), but not for $\Phi = 1.0$.
The question that arises is that of the phenomenon responsible for the much lower propagation in case $\Phi = 1.0$. Obviously, no explanation can be found from the flame surfaces. This is further analysed in terms of consumption speed in Sec. 4.3.3.

It is now convenient to look at the wrinkling of the flame fronts during their propagation.

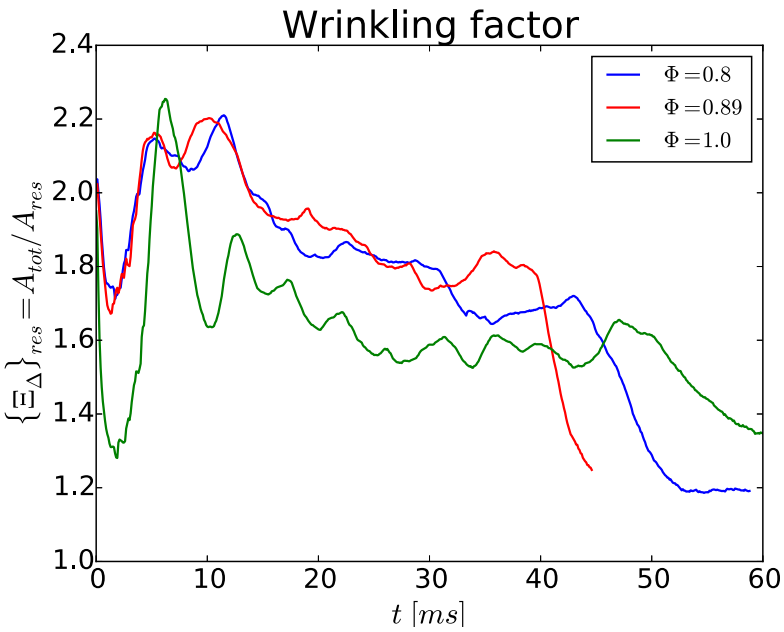

Figure 4.17: *Evolution of the wrinkling factor* $\{\Xi_\Delta\}_{res}$ *for cases* $\Phi = 0.8$ *in blue,* $\Phi = 0.89$ *in red and* $\Phi = 1.0$ *in green during the light-round sequence.*

Following notations from Philip (2016), the average of a quantity Ψ on the resolved flame surface is noted $\{\Psi\}_{res}$ and is defined as:

$$\{\Psi\}_{res} = \frac{\int_{V_{cc}} \Psi |\nabla \widetilde{c}| dV}{\int_{V_{cc}} |\nabla \widetilde{c}| dV} = \frac{\int_{V_{cc}} \Psi |\nabla \widetilde{c}| dV}{A_{res}} \tag{4.15}$$

The impact of the flame surface contained by the subgrid scale can be quantified by the observation of the wrinkling factor averaged over the resolved flame front, noted $\{\Xi_\Delta\}_{res}$:

$$\{\Xi_\Delta\}_{res} = \frac{\int_{V_{cc}} \Xi_\Delta \, |\boldsymbol{\nabla} \widetilde{c}| \mathrm{d}V}{\int_{V_{cc}} |\boldsymbol{\nabla} \widetilde{c}| \mathrm{d}V} = \frac{A_{tot}}{A_{res}} \tag{4.16}$$

The mean wrinkling factor is plotted for each case on Fig. 4.17. Cases $\Phi = 0.8$ and $\Phi = 0.89$, in blue and red, respectively, exhibit very similar trends, with a translation in time due to the longer ignition delay in case $\Phi = 0.8$: $\{\Xi_\Delta\}_{res}$ varies between 1.7 and 2.2 during the first two phases and then decreases throughout phase III from a value of 2.2 down to 1.7 in a roughly linear manner. This could already be seen in Fig. 4.14 where the two cases seemed to have very similar flame surface evolutions. This means that during phase III, between 45% (for $\{\Xi_\Delta\}_{res} = 2.2$) and 59% (for $\{\Xi_\Delta\}_{res} = 1.7$) of the total flame surface is captured by the resolved flame front. The subgrid scale flame surface therefore corresponds to 41% to 55% of the total flame surface, evidencing the crucial importance of the subgrid scale models. After the merging has taken place, the mean wrinkling factor drops to a final state value located around $\{\Xi_\Delta\}_{res} = 1.2$ meaning that at the steady-state, 83% of the flame surface is resolved. This difference with the values encountered during the propagation is explained by the fact that the stabilised flames are located in the bottom of the chamber where the cell size is the smallest, so that the grid is able to capture a larger proportion of the flame and the sub-grid scale has therefore less impact. It appears from this figure that the difference of light-round duration between cases $\Phi = 0.8$ and $\Phi = 0.89$ is not due to differences at the sub-grid scale, but probably to consumption speed effects.

Figure 4.14 shows that for case $\Phi = 1.0$, the total flame surface is approximately 10 % lower than in the other two cases throughout the whole sequence, while the resolved surface seems similar. Indeed, on Fig. 4.16, the average of the total flame surface during phase III decreases faster for this case than the resolved flame surface. This is also retrieved on the mean wrinkling factor: the part played by the subgrid scale is almost always lower than in the other cases. In particular, during phase III, $\{\Xi_\Delta\}_{res}$ varies between 1.8 (55% resolved flame surface) and 1.6 (63% resolved flame surface) with a less linear evolution.

A different vision of the flame wrinkling can be obtained through the resolved wrinkling Ξ_{res}, defined as the ratio of resolved flame surface A_{res} over a reference surface A_0. In the present case, the propagating flame fronts during phase III can be assimilated to vertical fronts, so that the reference surface is that of a radial cut in the chamber perpendicular to the direction of propagation (illustrated in Fig. 4.4) and $A_0 = 2h\Delta r$, with $\Delta r = 0.05$ m the width of the chamber and $h = 0.195$ m its height. A_0 being a constant, Ξ_res is actually simply a scaling of the resolved surface previously shown in Fig. 4.14. Ξ_{res} is plotted for each case on Fig. 4.18. As for the previous plots, the phases are indicated by vertical dashed lines. The choice of reference surface makes Ξ_{res} relevant only during phase III, that is for each case between the second and third lines.

As for the wrinkling factor, the resolved wrinkling is very similar between cases $\Phi = 0.8$ and $\Phi = 0.89$, with a difference in the merging instant, showing that the shape of the propagating flame fronts is similar between these cases and that the difference of propagation velocity would rather come from the consumption

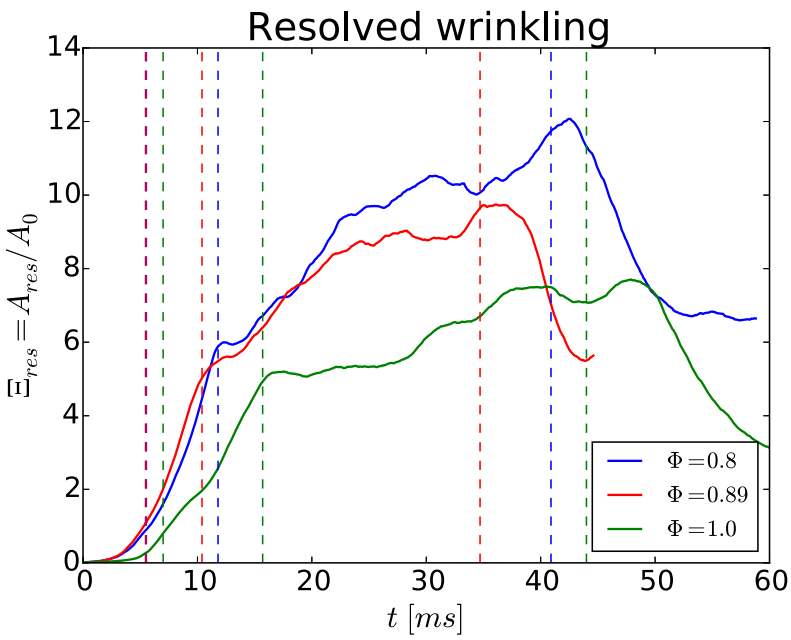

Figure 4.18: *Evolution of the resolved wrinkling* $\Xi_{res} = A_{res}/A_0$ *for cases* $\Phi = 0.8$ *in blue,* $\Phi = 0.89$ *in red and* $\Phi = 1.0$ *in green during the light-round sequence.*

speed, which will be analysed in the next section. In both cases, Ξ_{res} varies between 6 and 12, which highlight the importance of the wrinkling of the front that is captured by the simulation.

The resolved wrinkling is however very different in case $\Phi = 1.0$, it varies between 5 and 7, which is much lower than in the other two cases, but is consistent with the previous observations on the total, resolved and sub-grid scale flame surfaces which were also smaller.

Finally, some more information can be extracted from the average value of the gaseous equivalence ratio on the resolved flame front, $\{\Phi\}_{res}$, following the formula given in Eq. 4.15. As was done previously, the equivalence ratio is computed on the carbon atoms of the gaseous species so that it is conserved through the flame front and can be averaged on the $\widetilde{c} = 0.9$ iso-surface. The evolution of $\{\Phi\}_{res}$ during the light-round in each case is plotted on Fig. 4.19, in blue for $\Phi = 0.8$, red for $\Phi = 0.89$ and green for $\Phi = 1.0$.

Several observations can be made front Fig. 4.19. First of all, even though the amount of flame surface and its shape vary a lot during the light-round, $\{\Phi\}_{res}$ remains quite constant throughout the whole ignition sequence. The largest variations occur at the beginning of the propagation, during the first 10 milliseconds, when the flame kernel is looking for favourable conditions for its propagation. In particular, a large peak is present on the $\Phi = 1.0$ curve, which might be due to an encounter between the flame kernel and a local pocket of

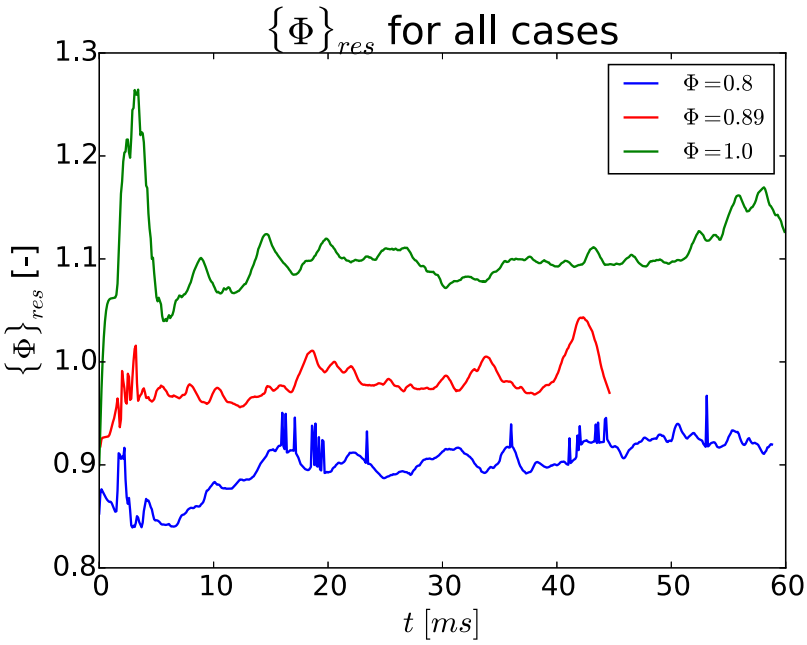

Figure 4.19: *Evolution of the equivalence ratio averaged on the resolved flame front* $\{\Phi\}_{res}$ *for cases* $\Phi = 0.8$ *in blue,* $\Phi = 0.89$ *in red and* $\Phi = 1.0$ *in green during the light-round sequence.*

rich (with gaseous or liquid fuel) mixture. On the whole, the mean equivalence ratio encountered by the resolved flame fronts can be considered constant for each case, with small variations around the mean value: $\{\Phi\}_{res}(t) \approx \{\Phi\}_{res}^{mean}$. The other striking feature is the value of $\{\Phi\}_{res}^{mean}$ for each case, which is systematically almost 10% greater than the global injected equivalence ratio. On average, the flame evolves in a mixture that is richer than was expected from the injected equivalence ratio. This is bound to have an impact on local quantities such as the consumption speed, which is analysed in the next section. The origin of the increased equivalence ratio is identified in Secs. 4.4 and 4.5.

4.3.3 Flame velocities

The velocity of the flame fronts in the chamber can be defined in several ways, representing different physical quantities.
A global propagation velocity can be computed from the light-round delay τ^{lr}, defined in section 3.4.2, knowing the distance covered by the flame in each half-chamber $7/8\pi r_{ch}$ (τ^{lr} is measured from the ignition of the first injector):

$$V^{lr} = \frac{7}{8}\frac{\pi r_{ch}}{\tau^{lr}} \tag{4.17}$$

This gives an average global velocity for the whole light-round sequence, which

in reported in Fig. 4.20 against the global injected equivalence ratio.

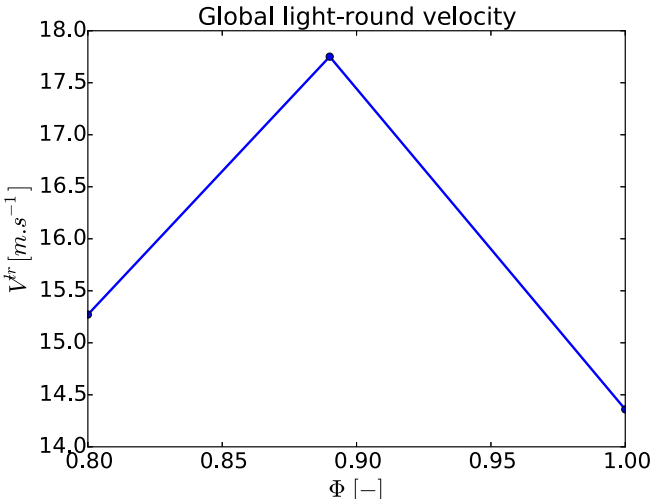

Figure 4.20: *Global light-round velocity as defined in Eq. 4.17 against the global injected equivalence ratio.*

The influence of the injected equivalence ratio on the light-round duration is logically retrieved here, the flame fronts in case $\Phi = 0.89$ have an average propagation speed that is greater than in cases $\Phi = 0.8$ and $\Phi = 1.0$. Experimentally, Prieur et al. (2017) found that the global velocity increases with the equivalence ratio, at constant power. The large error in the prediction of τ^{lr} at $\Phi = 1.0$ is here responsible for the break in the slope of V^{lr} between $\Phi = 0.89$ and $\Phi = 1.0$.

Potential fluctuations during the propagation, in particular during the different phases, cannot be seen with this formulation. Different expressions for the flame velocity have to be adopted in order to observe transient processes and are presented hereafter.

In all the following expressions, the flame is represented by the filtered progress variable $\widetilde{c}$, defined in Eq. 3.2, but other definitions could be used with the same conclusions.

The *absolute velocity* of a flame front element S_a represents its speed relatively to a fixed reference flame. It is written as:

$$S_a = \mathbf{w} \cdot \mathbf{n} = \frac{1}{|\nabla \widetilde{c}|} \frac{\partial \widetilde{c}}{\partial t} \tag{4.18}$$

with $\mathbf{w}$ the absolute velocity (in a fixed referential) of a $\widetilde{c}$-iso-surface and $\mathbf{n}$ the vector normal to the flame front. All the $\widetilde{c}$-iso-surfaces are supposed to have the save velocity, so that $\mathbf{w}$ does not depend on the chosen iso-surface.

The *displacement velocity* S_d is the velocity of the flame front relatively to its

surrounding flow, which has a velocity $\mathbf{u}$:

$$S_d = (\mathbf{w} - \mathbf{u}) \cdot \mathbf{n} = \frac{1}{|\nabla \widetilde{c}|} \frac{\mathrm{d}\widetilde{c}}{\mathrm{d}t} \tag{4.19}$$

Finally, the *consumption speed* S_c corresponds to the rate of consumption of the reactants by the flame. For a fully resolved flame front in a flamelet regime and with moderate wrinkling and curvature effects, S_c is defined from the integrated chemical source term of the progress variable, the flame surface $A(t)$ and the fresh gases density ρ_u as:

$$S_c^{1D} = \frac{1}{\rho_u A_{tot}(t)} \int_V \dot{\omega}_c dV \approx S_l^0 \tag{4.20}$$

with S_l^0 the laminar flame speed. In the large-eddy simulations with the TFLES combustion model, the flame front is filtered and thickened, so the consumption speed, written S_c^{TF}, is obtained as:

$$S_c^{TF} = \frac{1}{\rho_u A_{res}(t)} \int_{V_{cc}} \frac{E}{F} \dot{\omega}_c dV \tag{4.21}$$

with V_{cc} the volume of the combustion chamber, A_{res} the resolved flame surface defined in Eq. 4.10 and $\dot{\omega}_c$ the progress variable chemical source term predicted by the Arrhenius law.

S_c^{1D} and S_c^{TF} correspond to two different quantities. While S_c^{1D} is the consumption speed of the fully resolved (DNS) flame front, S_c^{TF} is the consumption speed of the LES resolved flame front. It is therefore expected that S_c^{TF} should be greater than S_c^{1D} by a factor $\{\Xi\}_{res}$, the sub-grid scale wrinkling.

Contrarily to the absolute and displacement velocities that are local quantities, the two consumption speeds S_c^{1D} and S_c^{TF} are global measures that are computed using data from the whole chamber.

S_c^{1D} and S_c^{TF} are displayed in Fig. 4.21, for the three cases ($\Phi = 0.8$ in blue, $\Phi = 0.89$ in red and $\Phi = 1.0$ in green) against the simulated time. S_c^{1D} is plotted as full lines and S_c^{TF} as dashed lines. Additionally, horizontal dot-dashed lines are added to mark the gaseous 1D laminar flame speed at the global injected equivalence ratio for each case.

On the consumption speed taken on the resolved front, S_c^{TF}, the order observed on the light-round durations is retrieved, the velocity is greater in case $\Phi = 0.89$ than in case $\Phi = 0.8$ and case $\Phi = 1.0$, where S_c^{TF} is the lowest.

For all cases, S_c^{TF} has a similar evolution, with an increase at the beginning of the simulation, during phases I and II, and a slightly decreasing trend during phase III. Its value evolve between 0.5 and 0.7 m.s^{-1}, which is as expected much lower than the light-round flame speeds V^{lr} 15 m.s−1, presented in Fig. 4.20, but higher than the gaseous laminar flame speeds (horizontal lines).

The consumption speed based on the total flame surface, S_c^{1D}, plotted in full lines, is logically closer to the values of S_l^0. Contrarily to S_c^{TF}, after a first

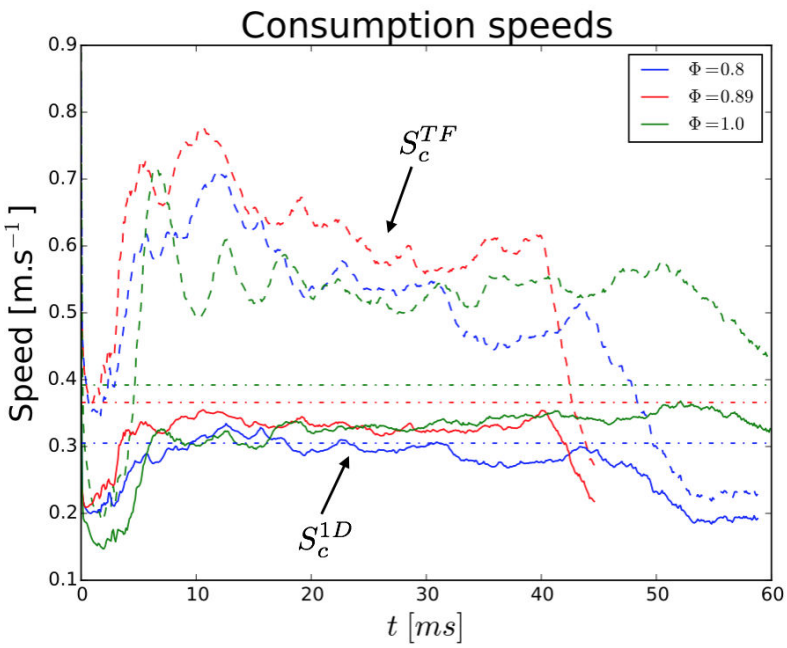

Figure 4.21: *Consumption speeds in the large-eddy simulations of the light-round for the three cases, $\Phi = 0.8$ in blue, $\Phi = 0.89$ in red and $\Phi = 1.0$ in green. S_c^{TF} is plotted in dashed lines, S_c^{1D} in full lines, and the laminar flame speed S_l^0 of the global injected equivalence ratio for each case is added as horizontal dot-dashed lines.*

increase at the beginning of the simulation, S_c^{1D} remains constant throughout the whole light-round sequence, though at different values for each case. For case $\Phi = 0.8$, S_c^{1D} is very close to $S_l^0(0.8) = 0.305$ m.s^{-1}, while in the other two cases, though it is higher than in case $\Phi = 0.8$, S_c^{1D} remains lower than the corresponding laminar flame speed. The difference with the laminar flame speed values would be even greater if the equivalence ratios actually observed on the flame fronts were taken. Indeed, Fig. 4.19 showed that the propagation flame fronts burn on average at a greater gaseous equivalence ratio than the global injected one. The laminar flame speed increases up to $\Phi = 1.1$, so the effective values of S_l^0 should be higher on Fig. 4.21. On the other hand, Ballal and Lefebvre (1981a) showed that the laminar flame speed in a two-phase mixture decreases with the size of the droplets. As has been previously shown, some non-evaporated liquid is still present everywhere in the fresh mixture in case $\Phi = 1.0$ and a large amount of droplets are present at the bottom of the chamber in all three cases. This would effectively decrease the laminar flame speed of the mixture and could explain the difference with S_c^{1D}.
Furthermore, the fact that the $\Phi = 0.89$ and $\Phi = 1.0$ have equal values during most of the flame propagation, until the merging is reached for case $\Phi = 0.89$ couls also be explained by the largest amount of liquid in the fresh mixture in case $\Phi = 1.0$, which decreases the value of the laminar flame speed. This

similarity is however not consistent with the light-round durations, since the greatest difference in τ^{lr} is observed between $\Phi = 0.89$ and $\Phi = 1.0$, which have similar consumption speeds.
Figure 4.21 shows that the flame propagation velocity cannot be explained by only considering combustion, since the consumption speeds' orders of magnitudes are much lower than the global propagation velocities. It was already shown that the volumetric expansion of the burnt gases created a thrust effect on the flame. This is further confirmed hereafter.

In order to compare the absolute flame speed S_a defined in Eq. 4.18, which is a local quantity, to global quantities like S_c^{TF} and V^{lr}, an average expression needs to be defined.
The volume of burnt gases in the chamber, noted $V_b(\widetilde{c})$, can be defined as the volume delimited by the bottom and the exit plane of the chamber, the quartz walls and the iso-surface $\mathcal{A}_f(\widetilde{c})$ of the progress variable. It therefore depends on the chosen value of $\widetilde{c}$. The variation of $V_b(\widetilde{c})$ can be written, using the transport theorem and using the fact that all surfaces but $\mathcal{A}_f(\widetilde{c})$ are fixed:

$$\frac{dV_b(\widetilde{c})}{dt} = \frac{d}{dt}\int_{V_b(\widetilde{c})} 1\ dV \tag{4.22}$$

$$= \int_{V_b(\widetilde{c})} \frac{\partial}{\partial t}(1) dV + \int_{\mathcal{A}_f(\widetilde{c})} 1 \times \mathbf{w}\cdot\mathbf{n}\ dA \tag{4.23}$$

$$= 0 + \int_{\mathcal{A}_f(\widetilde{c})} S_a dA \tag{4.24}$$

The integral of dV_b/dt over all the $\widetilde{c}$ iso-surfaces gives: :

$$\int_{\widetilde{c}=0}^{1} \frac{dV_b}{dt}(\widetilde{c}) d\widetilde{c} = \int_0^1 \int_{\mathcal{A}_f(\widetilde{c})} S_a dA\ d\widetilde{c} \tag{4.25}$$

$$\tag{4.26}$$

The RHS term can be transformed using the formula for the integral of modulus of the gradient given by Maz'ja (1985): let Φ and u be two functions defined on Ω an open subset of $\mathbb{R}^n$, one can write:

$$\int_\Omega \Phi(x)\ |\nabla u(x)|\ dx = \int_{t=0}^{\infty}\int_{\epsilon_t} \Phi(x)\ ds(x)\ dt \tag{4.27}$$
$$\text{with:}\quad \epsilon_t = \{x \in \Omega : |u(x)| = t\}$$

In consequence, combining Eqs. 4.25 and 4.27 with $u = \widetilde{c}$, $\Omega = V_{cc}$ and $\Phi = S_a$, one obtains:

$$\int_{\widetilde{c}=0}^{1} \frac{dV_b}{dt}(\widetilde{c}) d\widetilde{c} = \int_0^\infty \int_{\mathcal{A}_f(\widetilde{c})} S_a dA\ d\widetilde{c} = \int_{V_{cc}} S_a |\nabla \widetilde{c}| dV \tag{4.28}$$

Finally, the variation of $V_b(\widetilde{c})$ with $\widetilde{c}$ is due to the thickness of the flame, which is negligible before the dimensions of the chamber. The volume of burnt gases can therefore be considered independent of the progress variable: $V_b(\widetilde{c}) \approx V_b$. Equation 4.28 then becomes:

$$\frac{dV_b}{dt} \approx \int_{\widetilde{c}=0}^{1} \frac{dV_b}{dt}(\widetilde{c})d\widetilde{c} = \int_{V_{cc}} S_a|\nabla\widetilde{c}|dV \tag{4.29}$$

An expression can then be obtained for the average of the absolute velocity over the resolved flame surface $\{S_a\}_{res}$, using the average defined in Eq. 4.15

$$\{S_a\}_{res} = \frac{\int_{V_{cc}} S_a|\nabla\widetilde{c}|dV}{A_{res}} = \frac{1}{A_{res}}\frac{dV_b}{dt} \tag{4.30}$$

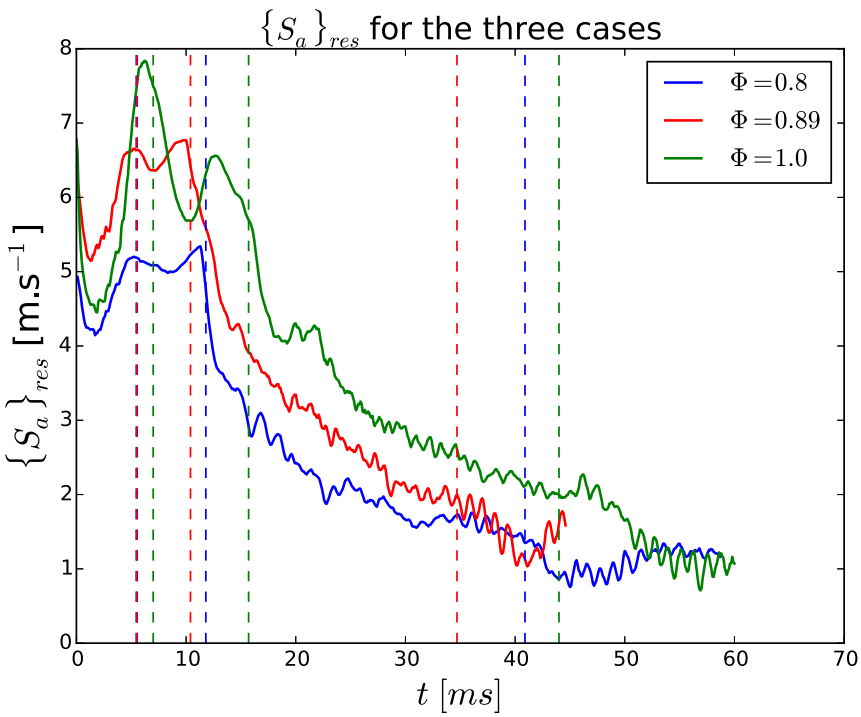

Figure 4.22: *Absolute flame speed averaged on the resolved LES flame surface for the three cases $\Phi = 0.8$ in blue, $\Phi = 0.89$ in red and $\Phi = 1.0$ in green. The beginning and the end of phases I to III are added for each case as vertical dashed lines. The horizontal lines mark the value of the global light-round velocity V^{lr} for each case.*

The evolution of $\{S_a\}_{res}$ during the light-round in the three cases is displayed in Fig. 4.22. The vertical dashed lines correspond to the transitions between phases I and II, II and III, and III and IV, each color standing for one case ($\Phi = 0.8$ in blue, $\Phi = 0.89$ in red ans $\Phi = 1.0$ in green). Here also, the three cases exhibit similar trends. At the beginning of the propagation, $\{S_a\}_{res}$

increases sharply up to a first maximum, which is reached around $t = 10$ ms and in each case corresponds to the end of phase I. $\{S_a\}_{res}$ then stabilises and keeps roughly constants for a few milliseconds, which corresponds to the arch-like propagation in phase II. At this point the velocity evolves between 5 and 8 m.s^{-1}. Afterwards, and during all of phase III, when two vertical fronts are present, $\{S_a\}_{res}$ drops progressively until the merging of the fronts and reaching of a steady-state.

It is worth noting that, contrarily to other previously plotted quantities, the evolution of $\{S_a\}_{res}$ with respect to the global equivalence ratio is consistent with what would be expected from the evolution of the laminar flame speed: $\{S_a\}_{res}^{\Phi=1.0} > \{S_a\}_{res}^{\Phi=0.89} > \{S_a\}_{res}^{\Phi=0.8}$. This was for instance not the case with the global light-round velocity V^{lr} plotted in Fig. 4.20, or the consumtion speeds plotted in Fig. 4.21.

The values obtained for $\{S_a\}_{res}$, between 1 and 8 m.s^{-1}, though they are greater than the consumption flame speeds, are still much lower than the observed global light-round velocities. As is detailed by Philip (2016), $\{S_a\}_{res}$ is an average of the absolute velocity of all the flame elements, which do not all have the same orientation, so the expression in Eq. 4.30 cannot be expected to retrieve the azimuthal propagation of the flow.

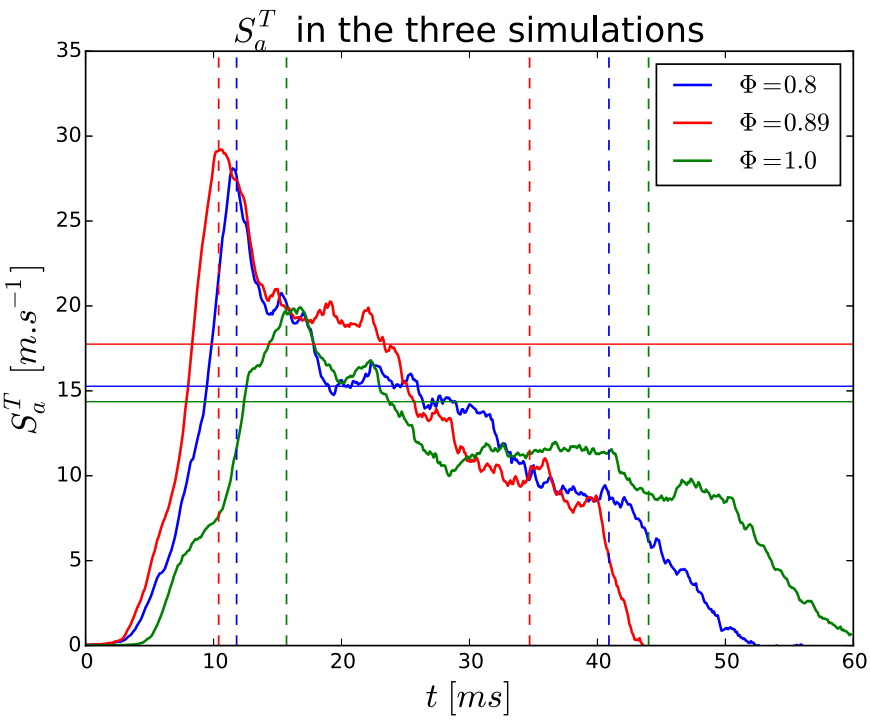

Figure 4.23: *Absolute turbulent flame speed S_a^T for the three cases $\Phi = 0.8$ in blue, $\Phi = 0.89$ in red and $\Phi = 1.0$ in green. The beginning and the end of phases I to III are added for each case as vertical dashed lines.*

As was done to obtain an expression for the resolved wrinkling plotted in Fig. 4.18, the flame fronts can be assimilated during phase III to vertical surfaces $A_0 = 2h\Delta r$ perpendicular to the azimuthal direction, as illustrated in Fig. 4.4, that propagate in the fixed referential at S_a^T, called the *absolute turbulent velocity*, following notations used by Philip (2016). Following the same reasoning as was used to derive Eq. 4.30, and using a control volume delimited by A_0 instead of A_{res}, the balance of burnt gases in the chamber gives:

$$\frac{dV_b}{dt} = S_a^T A_0 \tag{4.31}$$

The absolute turbulent flame speed S_a^T is plotted for each case ($\Phi = 0.8$ in blue, $\Phi = 0.89$ in red and $\Phi = 1.0$ in green) in Fig. 4.23 against the simulated time. Two vertical dashed lines are added for each case to mark the beginning and the end of phase III, where the expression for S_a^T is valid. Additionally, the horizontal lines mark the values of the global light-round velocities V^{lr}, computed from the light-round delay.
For all cases, the absolute turbulent velocity appears as a relevant estimation of the propagation velocity, since the orders of magnitude are consistent with the values of V^{lr}. Indeed, the global light-round velocity is a rough average of S_a^T during phase III. In all cases, S_a^T decreases strongly between the beginning and the end of phase III, a trend which was already observed $\{S_a\}_{res}$, and shows that the velocity based on the light-round is not representative of the transient evolution of the flame fronts.
A large difference is observed between case $\Phi = 1.0$ and the two other cases, in particular at the beginning of phase III, where $S_a^T(\Phi = 1.0)$ is 30% lower. Though S_a^T drops quickly in the first milliseconds of phase III, the absolute turbulent velocity remains higher in cases $\Phi = 0.8$ and $\Phi = 0.89$, which is consistent with the difference observed on $\{\Xi\}_{res}$ and could be an explanation to the difference in light-round duration.

4.4 Behaviour of the leading points of the flame fronts

In the previous section, analyses of the flame propagation from a macroscopic point of view were presented, considering the system formed by the whole chamber. In order to get a more local point of view of the flame behaviour, a different approach is here adopted. During the propagation of the flame in the chamber, the turbulent fronts do not take a regular shape that would make it easy to characterize the propagation mechanisms at stake, and that would in particular be responsible for the propagation speeds. In their study of the light-round with two-phase injection ans gaseous premixed, Boileau et al. (2008) and Philip et al. (2015b) showed that on the flame fronts, a most forward point in the azimuthal direction was clearly defined, called the *leading point* of the flame.

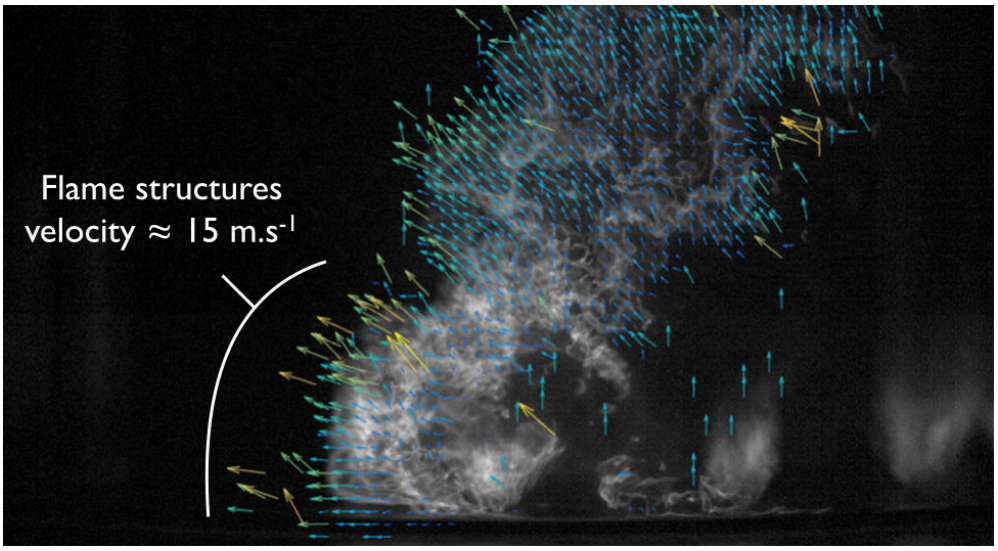

Figure 4.24: *Instantaneous snapshot of the propagating flame for a case with preheated walls at* $\Phi = 0.89$*. The camera is positioned behind sector* S_4*. The flame front propagates from right to left. Extracted from Prieur et al. (2018).*

On MICCA-Spray, a camera positioned on the H+ side, behind the injector in sector S_4 (see Fig. 3.2) is able to capture the shape of the experimental flame when it crosses its field of vision. An instantaneous image is displayed in Fig. 4.24, extracted from Prieur et al. (2018), taken on a case with preheated walls at $\Phi = 0.89$. On this image, the flame front crosses the chamber from right to left. The flame front is divided into two regions, the lower part, in the bottom third of the chamber, is more forward in the azimuthal direction than the top region, which is additionally inclined backwards. A leading point appears to be located in the bottom region.
In addition, results published by Prieur et al. (2017) and Prieur et al. (2018) show that during the light-round with liquid n-heptane injection in MICCA-Spray, the propagation mechanism between injectors follows the azimuthal pattern observed by Bourgouin et al. (2013) with premixed injection and described in the general introduction of the manuscript. In the present case, the two-phase nature of the injection therefore does not change the global propagation behaviour.
The Phantom camera used by Prieur et al. (2018) for these images captures consecutive snapshots on which PIV (Particule Image Velocimetry) algorithms can be used (Prieur (2017)). Though the camera framerate (6000 images per second) is too low to study the displacement of PIV particles, it is enough for the motion of the large structures of the flow and the flame. The velocity vectors obtained by the algorithms are superimposed onto the snapshot in Fig. 4.24. The two previously identified regions are also apparent on the velocity vectors, in the bottom region the flame structures have a rather horizontal motion, with

a tangential velocity comprised between 15-20 m.s^{-1}, while in the top region the flame propagates tangentially and axially at the same time due to burnt gases expansion, which will be investigated in section 4.2, with a tangential velocity comprised between 10-15 m.s^{-1}. This suggests that the bottom part of the flame is driving the propagation of the flame fronts by igniting the injectors one after the other and "pulling" the rest of the front.
These observations reinforce the idea that the leading point is an important element of the whole flame propagation and its study could provide useful information regarding the light-round process.

4.4.1 Leading points position and trajectory

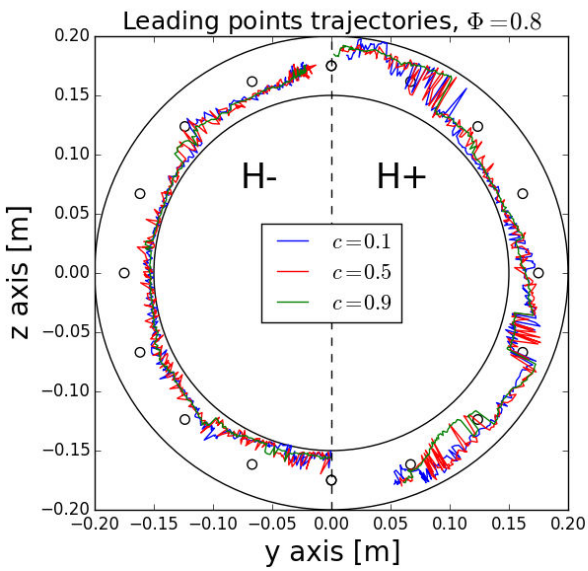

Figure 4.25: *Leading points trajectories projected on the chamber backplane for different value of the progress variable $\widetilde{c}$, for case $\Phi = 0.8$. The LP is defined on three different iso-surfaces, $\widetilde{c} = 0.1$ (blue), $\widetilde{c} = 0.5$ (red) and $\widetilde{c} = 0.9$ (green).*

For each half chamber, the leading point (LP) is defined as the most forward point in the azimuthal direction on an iso-surface of the progress variable $\widetilde{c}$, defined in Eq. 3.2 to ensure its monotony through the flame front. Figure 4.25 displaysthe trajectory of the LP in the case $\Phi = 0.8$, for three different iso-surfaces $\widetilde{c} = 0.1$, $\widetilde{c} = 0.5$ and $\widetilde{c} = 0.9$. For this case, the choice of the iso-surface for the definition of the leading point does not impact the shape of its trajectory, though more discontinuities are observed on $\widetilde{c} = 0.1$ and $\widetilde{c} = 0.5$ than on $\widetilde{c} = 0.9$. Similar results were observed for cases $\Phi = 0.89$ and $\Phi = 1.0$, which are not presented here.
In the following, the LP is then taken on the $\widetilde{c} = 0.9$ iso-surface because it is close to the peak of heat release in the flame based on the Arrhenius law.

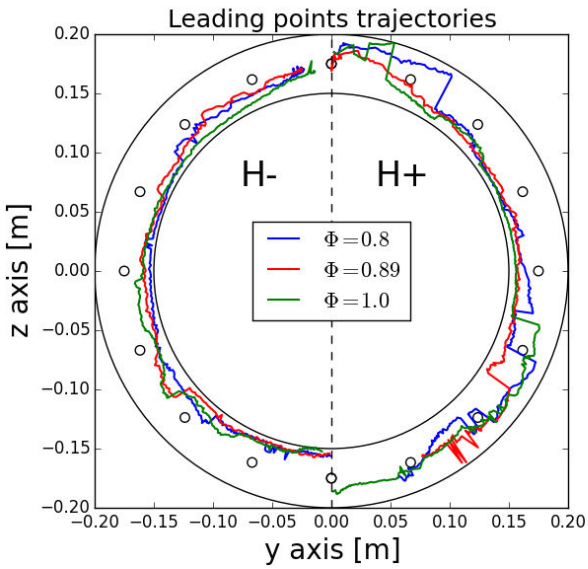

Figure 4.26: *Leading points trajectories projected on the chamber backplane for the three cases: the blue, red and green lines respectively stand for* $\Phi = 0.8$*,* $\Phi = 0.89$ *and* $\Phi = 1.0$ *with the LP defined on the* $\widetilde{c} = 0.9$ *iso-surfaces.*

Similarly to the trajectories, this choice does not impact the post-processing results and the conclusions presented hereafter.
Figure 4.26 displays the trajectory of the LP for both halves of the chamber and for all three cases ($\Phi = 0.8$ in blue, $\Phi = 0.89$ in red and $\Phi = 1.0$ in green). Despite the differences in equivalence ratios, and the fact that the $\Phi = 1.0$ simulation is not able to predict the propagation speed (as shown in chapter 3), the same behaviour is observed for all three conditions. On the H- side (left side), the leading point is systematically located close to the inner wall of the chamber, which indicates that a preferential path exists in this area, probably due to the presence of the swirling flow generated by each injector. In the right half H+ however, the trajectories are more complex. For the first quarter-chamber, the preferential path seems to be located along the inner wall of the chamber. In the second quarter-chamber, the LP is not pinned to the inner wall anymore, and within one sector, moves to the middle of the chamber and evolves thereafter close to the radius of the injector axes. The shorter path is no longer followed, suggesting that the clockwise swirling motion generated by the injectors plays an important role in the radial position of the leading point, and therefore in the flame propagation path.
It is interesting to note that the trajectories observed in this two-phase n-heptane case are similar to that observed by Philip (2016) on MICCA with gaseous premixed propane injection. The path followed by the leading points could therefore be a consequence of the geometry of the chamber and the ori-

entation of the swirling flows.

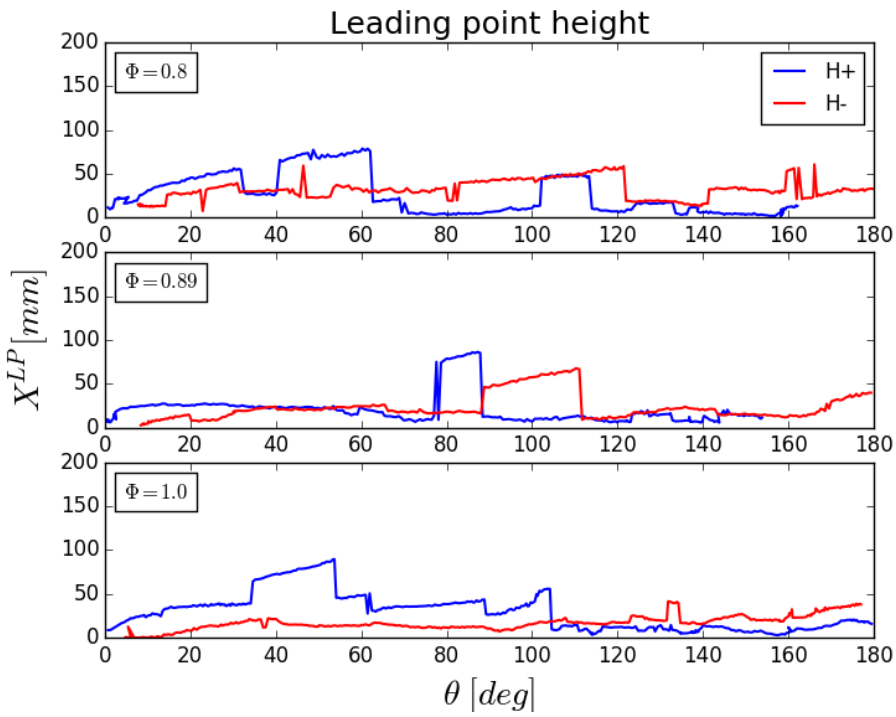

Figure 4.27: *Leading points height against their azimuthal position for H+ (blue lines) and H- (red lines) and all three cases:* $\Phi = 0.8$ *at the top,* $\Phi = 0.89$ *in the middle and* $\Phi = 1.0$ *at the bottom.*

The shape of the flame fronts is strongly influenced by the local flow field, and there can be some local competition between several flame elements, which explains the discontinuities observed on the trajectories when one element overtakes another. This is further evidenced on Fig. 4.27 which shows the axial position of the LP for both halves of the chamber and for all three cases with respect to the LP azimuthal position. For each case and during the whole propagation, the LP is located below 50 mm, which corresponds to the bottom 25% of the chamber. The LP in H- (red lines) exhibits a relatively smoother behaviour, with fewer discontinuities, which is consistent with the smoother trajectory observed in Fig. 4.26. On the H+ side (blue lines), some common features can be identified. At the beginning of the azimuthal propagation, corresponding to phase II, the LP is lifted up due to the arch-like flame. After the separation into two distinct fronts, the distance of the LP with respect to the chamber backplane gradually increases until it is suddenly brought back. This trend is repeated several times, until some point after the half of the trajectory, which varies depending on the case, where the LP definitely drops down near the backplane. The azimuthal propagation pattern observed experimentally is

here retrieved, since the LP height remains roughly constant. In the case of a *sawtooth* propagation, some arch-like patterns where the LP goes up in the chamber before being brought back down would be observed. In the present cases, the LP height and radial trajectory show that the flame fronts tend to go around the swirlers and that the propagation is azimuthal.
The LP appears to evolve in the swirlers outer recirculation zones, where favourable conditions are often found due to local increases of the equivalence ratio by the droplets that are trapped there. This point will be investigated in Sec. 4.5.

4.4.2 Ignition delays and velocities

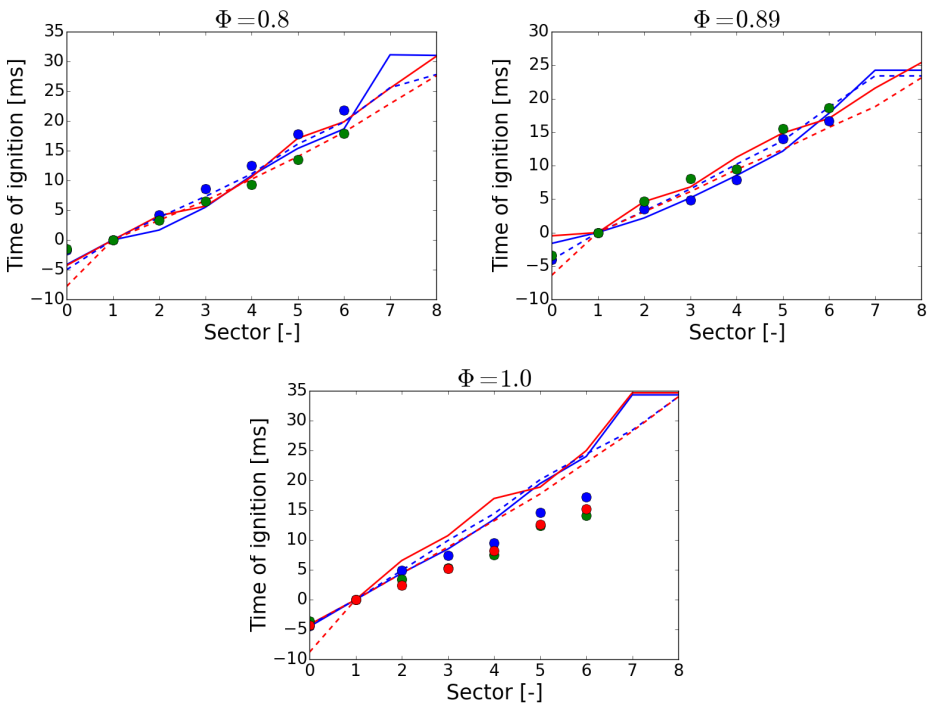

Figure 4.28: *Comparison of sectors ignition times for cases* $\Phi = 0.8$ *(left),* $\Phi = 0.89$ *(center) and* $\Phi = 1.0$ *(right), in the simulation for H+: −: from sector-integrated heat release, −−: from the leading point position, for H-: −: from sector-integrated heat release, −−: from the leading point position, ••: Experimental measurements on the H- side of the chamber, each color stands for a different sequence. The origin of times is set for all sequences at the instant of ignition of sector* S_1 *(or* S_{-1}*).*

The instants the leading point crosses each injector azimuthal position can be used as another indicator of the ignition delay between the sectors. In addition to the data already described in Fig. 3.25, these instants are reported for each sector in Fig. 4.28 as dashed lines (blue lines for H+ and red lines for H-), synchronized at sector S_1 or S_{-1} as with the other data sets, which instant is

set as $t = 0$ s.
For all cases, the largest discrepancy between the ignition delay measurements in the simulation and the experiments is located between sectors S_0 and S_1.
In the experiment and the simulation, the delay between the initiation of the ignition (a series of sparks or the insertion of a sphere of burnt gases) and the propagation of a flame kernel largely depends on the local conditions and is characterised by a large variations (shown experimentally by Prieur et al. (2017)). An efficient and more reliable numerical treatment of this first phase would require ignition probability considerations. The datasets obtained from the experimental measurements of the light intensity and from the numerical sector-integrated heat release are global quantities and the ignition of sector S_0 is less influenced by this initial stochastic behaviour. The data presented here was however extracted from the leading points position, which cannot really be considered as a crossing instant as is done for the other sectors since no vertical flame front has yet formed. The ignition delays obtained from the LP should then only be considered from sectors S_1 and S_{-1}.
For all the other sectors, the LP-based delays are very close to the heat release ones. In cases $\Phi = 0.8$ and $\Phi = 0.89$, the good agreement between the simulation and the experimental data that was observed through the images in chapter 3, Figs. 3.16 to 3.19, is further evidenced on Fig. 4.28, while for case $\Phi = 1.0$, the discrepancy is still present and increases gradually with time.
The consistency between the data extracted from the LP and from the sector-integrated heat release, which is a more global measure, shows that the LP position can be used as an indicator of the flame progress in the chamber and that its evolution is strongly linked to the evolution of the amount of reaction in the chamber. This confirms that one possible scenario for the flame propagation involves the leading-point entraining the turbulent flame brush.
Using the leading points spatial position at each instant, it is also possible to retrieve their absolute velocity. The absolute velocity is the velocity of the leading point in the laboratory fixed reference frame, its tangential component is defined from the radial and azimuthal positions r^{lp} and θ^{lp} as:

$$v_\theta^{lp} = r^{lp} \frac{d\theta^{lp}}{dt} \tag{4.32}$$

In order to remove some of the largest discontinuities that were present on v_θ^{lp} due to *jumps* of the LP between two flame elements, the derivative of the tangential position is computed in two different ways, $v_{\theta,1}^{lp}$ and $v_{\theta,2}^{lp}$, defined in Eqs. 4.33 and 4.34, and the selected value for v_θ^{lp} is the one whose absolute value is the smallest.

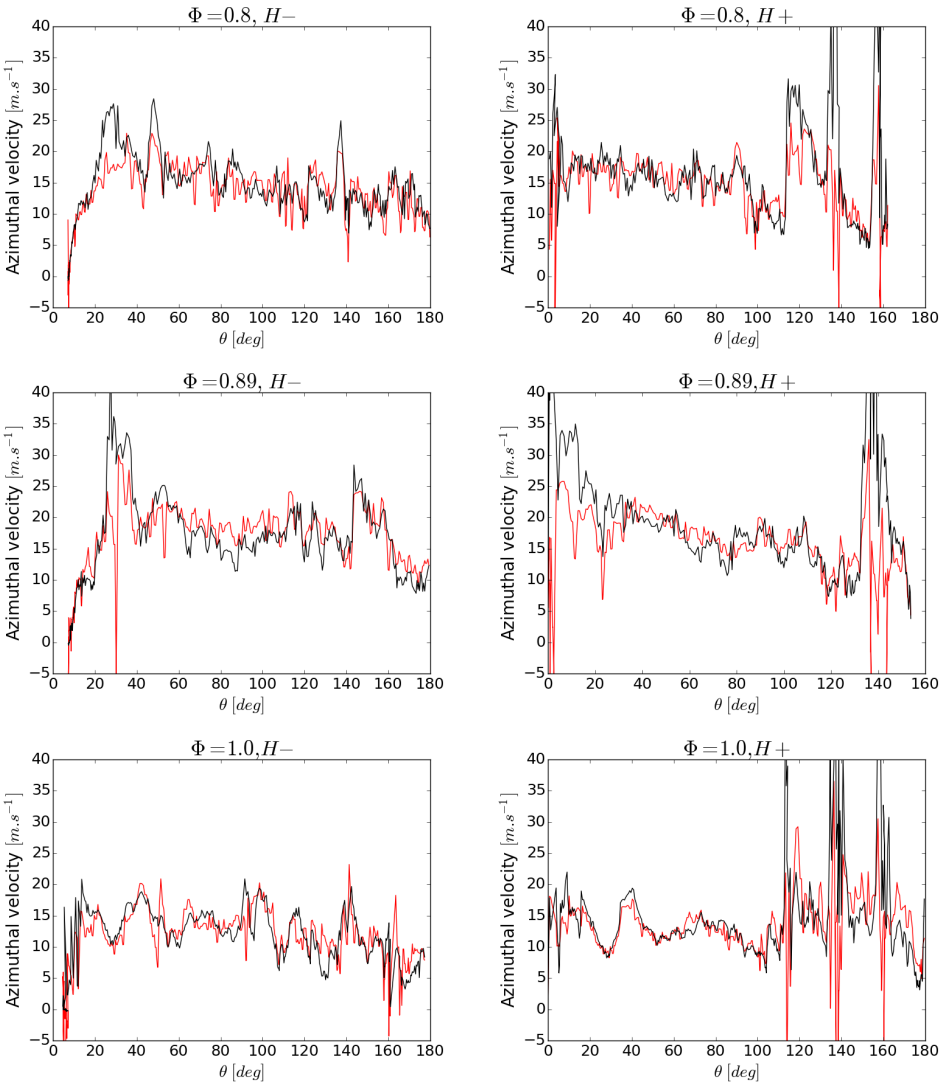

Figure 4.29: *Comparison of the azimuthal speed v_θ^{lp} of the leading point (in red) and the flow azimuthal velocity at the same point (in black) plotted with respect to the leading point angular position for H+ (right) and H- (left). Results are given for the three cases $\phi = 0.8$ (top), $\phi = 0.89$ (middle) and $\phi = 1.0$ (bottom).*

$$v_{\theta,1}^{lp}(i) = r^{lp}(i)\frac{\theta(i+1)-\theta(i)}{t(i+1)-t(i)} \tag{4.33}$$

$$v_{\theta,2}^{lp}(i) = r^{lp}(i)\frac{\theta(i)-\theta(i-1)}{t(i)-t(i-1)} \tag{4.34}$$

This formulation leads to somewhat smoothest curves, though some large swings are still present.

Figure 4.29 compares the LP absolute tangential velocity, in red, with the local tangential velocity of the flow, v_θ^{flow} at the leading point, in black. For all three cases, a similar behaviour is observed for the leading point: after an acceleration phase which corresponds to the arch-like expansion of the flame, the velocities oscillate between 10 and 25 m.s^{-1}, depending on the case, with a slightly decreasing trend on the average value, during phase III, when the two distinct fronts propagate in their respective half-chamber.
The ignition sphere having been placed on the H- side of the injector in sector S_0 (see Fig. 3.2 for the location of the spark), the acceleration phase that appears clearly on all H- plots is mostly hidden on the H+ plots by the fact that it partly occurs before the flame reaches the H+ half, and therefore before a leading point can be defined for this half-chamber. For the same reason, the curves for the H- side do not begin at $\theta = 0$ deg.
The observed values for the flame propagation speed are one order of magnitude higher than typical values for the turbulent flame consumption velocity ($\sim$ 1 m.s^{-1} in the present cases), indicating that the burnt gases volumetric expansion evidenced in Sec. 4.2 also largely impacts the leading points. Moreover, the average value of the leading point absolute tangential velocity during the fronts propagation in case $\Phi = 0.89$, approximately $v_\theta^{lp,mean} \approx 16$ m.s^{-1}, is consistent with the values obtained from by the PIV algorithms on the experimental images, as shown in Fig. 4.24.
In all three cases, the surrounding flow and the LP velocities are strongly correlated, v_θ^{lp} follows the global evolutions of v_θ^{flow}, which indicates that the leading point is mostly convected by the flow. The relationship between the leading point and its immediate surroundings is more closely studied in the next section.

It is finally interesting to compare the leading points velocity to global velocities obtained in Sec. 4.3.3. Figure 4.30 compares the H+ and H- leading point velocities v_θ^{lp+} and v_θ^{lp-}, respectively plotted in green and red lines, to the absolute turbulent velocity S_a^T in blue lines and to the global light-round velocity V^{lr}, in cyan dashed line. In all cases, the LP velocities have magnitudes that are comparable to that of S_a^T and more importantly to V^{lr}, which further show the relevance of studying the leading points of the flame fronts to understand their propagation. This similitude was expected from the injectors ignition delays which were already similar to the rate of progress of the flame fronts through the chamber. This is further demonstrated here.

4.4.3 The leading point and its surrounding flow field

Figure 4.31 displays a zoom around the H+ flame front on a cylindrical cut, as defined in Fig. 4.1, for case $\Phi = 0.80$ and at $t = 25$ ms, taken at the radius occupied by the leading point at this instant: $r^{cut} = r^{lp}(t = 25 \text{ ms})$. The section is coloured by the gaseous phase tangential velocity, counted positive in the direction of the flame propagation, from right to left, and ranging from $u_\theta = -20$ m.s^{-1} in blue to $u_\theta = +20$ m.s^{-1} in red. On the fresh gases side,

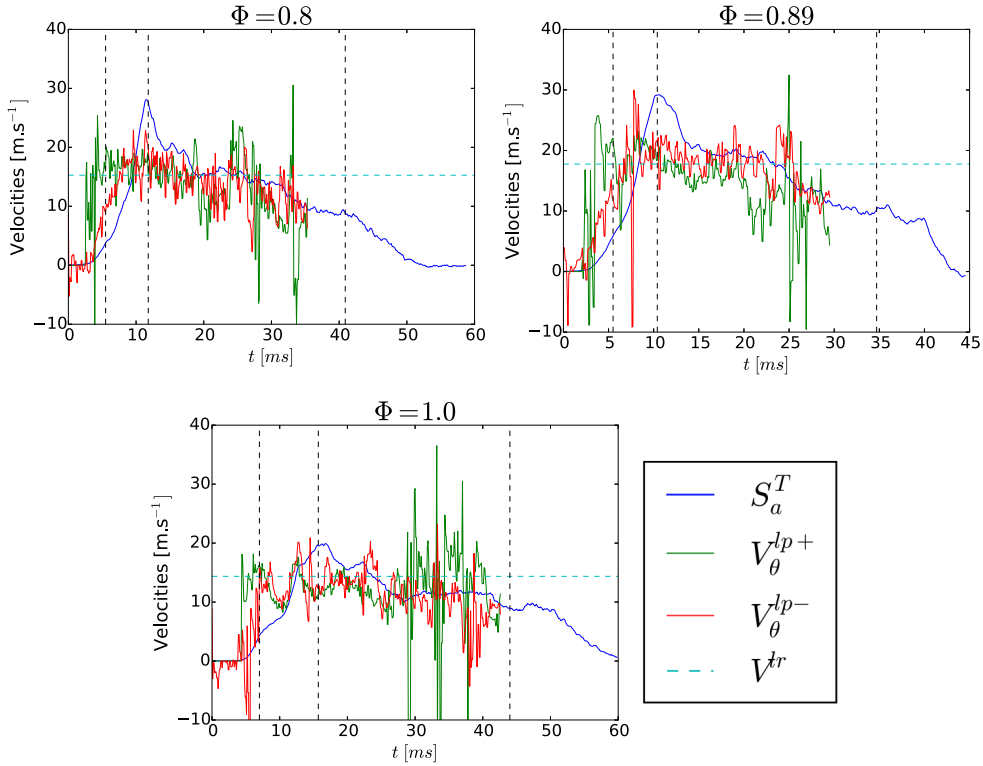

Figure 4.30: *Flame velocities for all three cases, top left:* $\Phi = 0.8$*, top right:* $\Phi = 0.89$ *and bottom:* $\Phi = 1.0$*. Several velocities are plotted: the light-round velocity* V^{lr} *in cyan dashed lines, the flame absolute turbulent velocity* S_a^T *in blue lines and the H+ and H- leading points absolute velocities in green and red lines, respectively. The phases are indicated through vertical black dashed lines.*

the tangential velocity is positive, with a rather homogeneous value around $u_\theta = +10$ m.s^{-1}. The remarkable feature in Fig. 4.31 is that the leading point, evidenced by a black circle, is located inside a region of greater velocity, where u_θ is twice higher than everywhere else in the fresh gases. This explains the high absolute tangential velocity of the leading point and further validates the idea of the leading point being convected by its surrounding flow, thus greatly increasing its speed. One possible scenario would then be that the leading point, being located is regions of higher velocities, entrains the whole flame fronts during the light-round and influences its speed.

This increased positive azimuthal velocity in front of the flame, on the fresh gases side, is accompanied by a strong negative velocity on the burnt gases side, which is due to the acceleration of the flow through the flame by mass conservation. The effect of the volumetric expansion, which was observed from the point of view of the whole chamber in Sec. 4.2, appears to be emphasized around the leading point position: the generated azimuthal velocities in the

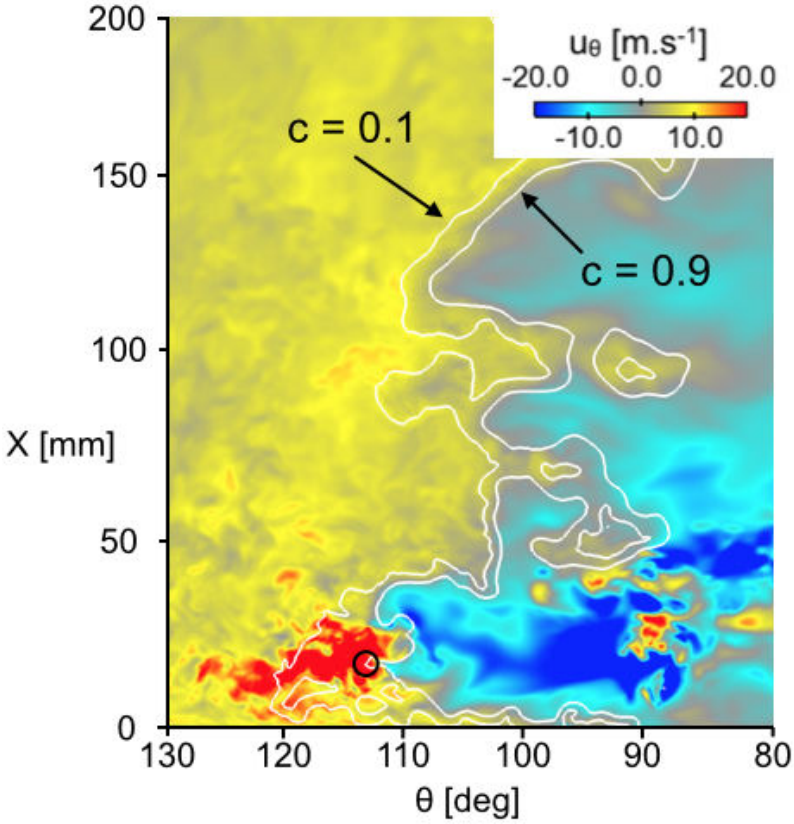

Figure 4.31: *Zoom on the flame front in the leading point area on an unfolded cylindrical cut at $r^{cut} = r^{lp}$, coloured by the tangential velocity, for case $\Phi = 0.80$ and at $t = 25.0$ ms. The flame is evidenced by white iso-lines of the progress variable $c = 0.1$ and $c = 0.9$. The LP is highlighted by the black circle. The tangential velocity is counted positive from right to left. The flame propagates from right to left.*

fresh and burnt gases are both much greater than in the rest of the chamber. The presence of this region of higher velocity suggests that other quantities might also exhibit a particular behaviour around the leading point position. In particular, the local gaseous equivalence ratio at the leading point is plotted in Fig. 4.32, for the three cases, $\Phi = 0.8$ at the top, $\Phi = 0.89$ in the middle and $\Phi = 1.0$ at the bottom. The equivalence ratio is computed based on the gaseous species atoms balance so that it remain constant with the reaction of the reactants and is presented for H+ in blue and H- in red. On each plot, a horizontal black dashed line highlights the injected global equivalence ratio Φ. For all cases and during the whole propagation, the LP is systematically located in a mixture that is richer than Φ. Excepting the last third in H+, fewer discontinuities are observed here than on the LP position, indicating that the equivalence ratio does not vary much in the LP propagation region and therefore that the competing flame tips burn at similar Φ. When the flame fronts are

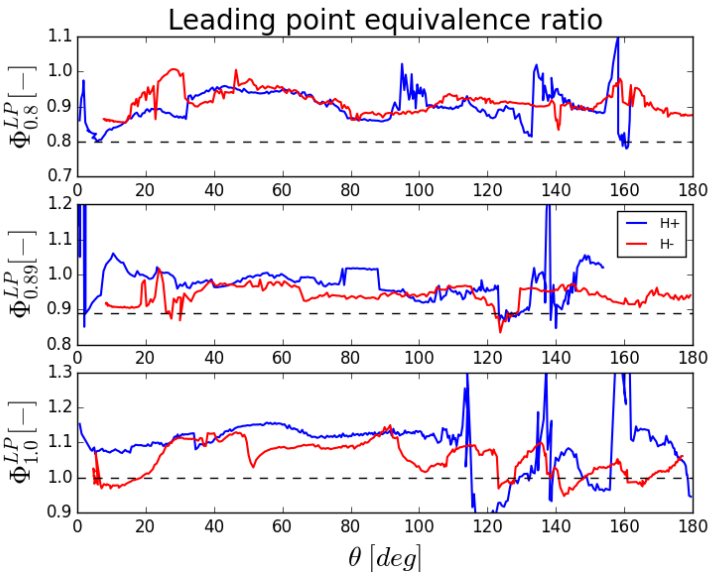

Figure 4.32: *Time evolution of the gaseous equivalence ratio, computed on the carbon atoms, at the leading point in H+ (blue lines) and H- (red lines) and for* $\Phi = 0.8$ *(top),* $\Phi = 0.89$ *(middle) and* $\Phi = 1.0$ *(bottom). The horizontal black dashed lines mark the global equivalence ratio injected for each case.*

located in the last third of the chamber on the H+ side (blue curves), during which the LP evolves around the injectors' centrelines, some large swings occur in the local equivalence ratio evolution that can be surprising. The tangential positions where these events take place correspond to the positions of the injectors, suggesting that in the presence of the highly turbulent sprays, the flame fronts encounter large Φ variations, due in particular to the presence of pockets of liquid fuel, as will be shown later.
The fact the the gaseous equivalence ratio at the leading point is higher than in the rest of the chamber explains its higher propagation speed (see Fig. 1.9 for the laminar flame speed S_L^0, the maximum is located around $\Phi = 1.1$) and strengthens the hypothesis of the existence of a preferential path in the bottom of the chamber.
The presence of such heterogeneities of equivalence ratio suggests that specific interactions are taking place between the propagating flame fronts and the sprays generated by each injector. This is further investigated in the next section.

4.5 Flame-spray interactions

The creation of a gaseous flow in the fresh gases induced by the propagation of the two flame fronts in the chamber was evidenced in Sec. 4.2. The cold

flow analyses on SICCA-Spray in Sec. 2.4.3 showed that the size of the droplets led them to be largely entrained by the gaseous flow, leading to close velocity fields. The impact of the propagating fronts on the gaseous velocity should therefore be retrieved on the liquid velocities. This section aims at identifying the particular evolution of the liquid repartition in the chamber as the flame fronts propagate and ignite the injectors one by one, as well as the interactions between the flame and the spray.

4.5.1 Interactions between the flame and the swirling sprays

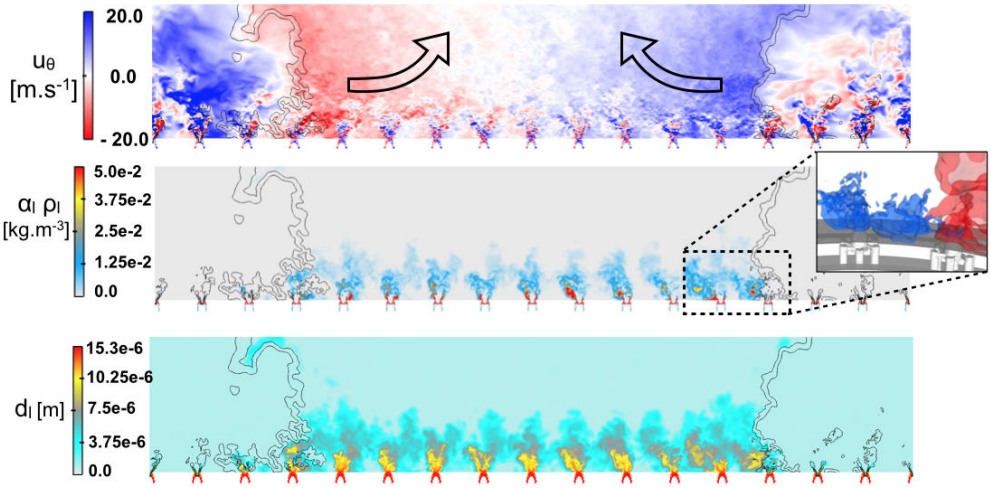

Figure 4.33: *Visualisations of the unfolded cylindrical cut taken at $r^{cut} = 175$ mm unfolded on a plane surface for case $\Phi = 0.8$ at instant $t = 17$ ms. The cut is coloured by the tangential gaseous velocity (top), the liquid mass density (middle) and the liquid droplet diameter (bottom). Tangential velocities are counted positive from left to right. Two iso-lines of the progress variable $\widetilde{c} = 0.1$ and $\widetilde{c} = 0.9$ (in black) highlight the position of the flame fronts. The insert on the right represents the impact of the flame progress (red iso-surface) on the liquid spray, evidenced by a blue iso-surface at $\alpha_l \rho_l = 0.01$ $kg.m^{-3}$.*

Figure 4.33 presents the developed cylindrical cut at the middle of the chamber, as defined in Fig. 4.1, at the same instant $t = 17$ ms chosen to observe phase III of case $\Phi = 0.8$ and coloured by different quantities: the tangential gaseous velocity u_θ at the top, the liquid mass density $\alpha_l \rho_l$ at the middle and the droplet diameter d_l at the bottom. The azimuthal flow visible on the u_θ field that pushed the fresh mixture towards sector S_8 and the exit of the chamber, as shown by the black arrows, also strongly perturbs the liquid phase distribution: on the $\alpha_l \rho_l$ and d_l fields, the sprays generated by the un-ignited injectors are inclined away from the flame. Additionally, some pockets of droplets are created and pushed away from the flame fronts, forming patterns similar to those found in the case of jets in cross-flows (as can be seen on the insert on the right in

Fig. 4.33 and in Fig. 4.34).

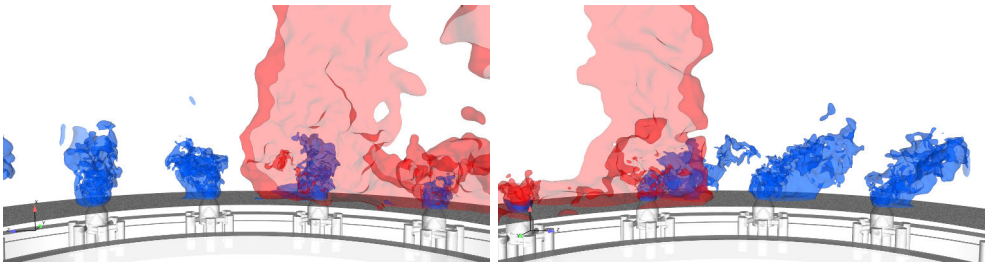

Figure 4.34: *Visualisation of the effect of the flame fronts on the liquid sprays, evidenced by blue iso-surfaces of the liquid mass density* $\alpha_l \rho_l = 0.01$ *kg.m*$^{-3}$*. The flame fronts are represented by iso-surfaces of the progress variable* $\widetilde{c} = 0.9$*. Snapshots are taken for H- (left) and H+ (right) at* $t = 25$ *ms from case* $\Phi = 0.8$*.*

When the chamber is in its un-ignited steady-state, the droplets injected by the swirler units form a hollow cone that is symmetric around the vertical axis of the injectors. The fuel mass fraction generated by the evaporated droplets is partly captured by the recirculation zones and mostly ejected through the chamber exit. During the light-round sequence, this axi-symmetry is broken by the azimuthal flow and the droplets are pushed and trapped in the outer recirculation zones between the injectors. This is further illustrated on Fig. 4.34 which displays iso-surfaces of the liquid density at $\alpha_l \rho_l = 0.01$ kg.m^{-3} in blue that highlight the sprays and iso-surfaces of the progress variable at $\widetilde{c} = 0.9$ in red that represent the flame fronts. The two images are taken from the simulation of case $\Phi = 0.8$ at $t = 25$ ms, for H- on the left and H+ on the right. This representation allows to visualise the mass of liquid that is deviated by the fresh gases flow away from its injector axis. Strong modifications are observed up to three injectors ahead of the flame fronts.
The images in Figs. 4.33 and 4.34 are all taken from case $\Phi = 0.8$ but, as could be seen on Figs. 4.12 and 4.13 which presented $\alpha_l \rho_l$ fields from the two other cases, the impact of the azimuthal flow on the liquid mass repartition is similar in the three cases.

4.5.2 Local effects of flame crossing on the flow

The excess of liquid in the bottom of the chamber explains the higher gaseous equivalence ratios observed throughout the propagation, as shown in Fig. 4.32. The induced flow impact on the liquid phase can be further evidenced by observing the temporal evolution of relevant quantities at selected points in the chamber. Figure 4.35 displays the evolution of $\alpha_l \rho_l$ in full black lines (axis and scale on the right) and the local gaseous equivalence ratio ϕ_g in blue dashed lines (axis and scale on the left), for the three cases, at the point $[x = 2.5$ mm, $r = 0.175$ m, $\theta = 9\pi/8]$, which corresponds to a point located near the chamber back-plane at the frontier between S_4 and S_5, on the H+ side. This

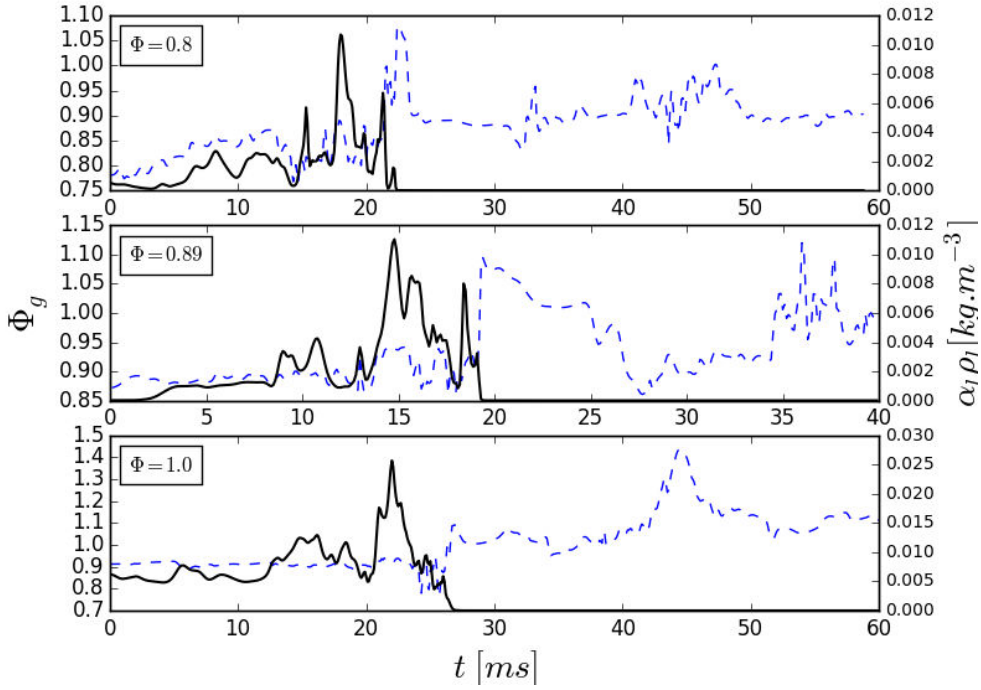

Figure 4.35: *Temporal evolution of the liquid mass density $\alpha_l\rho_l$ (black solid lines, right axis) and the gaseous equivalence ratio Φ_g (blue dashed lines, left axis) for the three cases $\Phi = 0.8$ (top), $\Phi = 0.89$ (middle) and $\Phi = 1.0$ (bottom) at point [$x = 2.5$ mm, $r = 0.175$ m, $\theta = 9\pi/16$]. The crossing of the flame can be evidenced by the decrease of the liquid density to zero.*

point is chosen to be near the leading point trajectory during its passage at $\theta = 9\pi/8$. The gaseous equivalence ratio is computed using the carbon atoms in the gaseous species as was done in Fig. 4.32. The crossing of the flame can be identified as the instant the liquid mass density $\alpha_l\rho_l$ drops to zero.

During the first instants on each case, some features already observed are retrieved. In cases $\Phi = 0.8$ and $\Phi = 0.89$, the liquid is mostly pre-vaporised before the ignition, so that, even this low in the chamber, almost no liquid is present at this point located in the outer recirculation zone between two injectors. This is not the case for $\Phi = 1.0$, the bottom plot shows that in the steady-state cold flow, the liquid density evolves around $\alpha_l\rho_l \approx 0.007$ kg.m^{-3}. This is also consistent with previous observations, on the cold converged bi-sector flows in particular.

In all cases, the same trend is observed: although a steady state regime had been reached before the ignition, the local liquid mass density begins to increase approximately 10 ms before the crossing of the flame (evidenced by the sharp decrease towards zero of the liquid density). This shows that an accumulation

of liquid is created by the azimuthal flow generated ahead of the flame fronts, so that the local conditions seen by the flame differ from those corresponding to the steady-state cold two-phase flow field. The density of liquid is for each case several order of magnitude greater than in the un-perturbed cold flow, which obviously has an impact on the flame propagation. The maximum levels of liquid density reached in front of the flame are similar for cases $\Phi = 0.8$ and $\Phi = 0.89$, with $[\alpha_l \rho_l]^{max}_{\Phi=0.8,0.89} \approx 0.01$ kg.m^{-3}, for which very little liquid was available in the cold flow in the first place, however, levels are more than twice greater in case $\Phi = 1.0$, at $[\alpha_l \rho_l]^{max}_{\Phi=1.0} \approx 0.025$ kg.m^{-3}, showing that the pre-vaporisation and the liquid accumulation before the flame are two effects that add up during the light-round sequence.
As a consequence to this added presence of liquid fuel, the local gaseous equivalence ratio is increased close to the flame front, when the accumulation of droplets evaporates in the vicinity of the flame. This shows that this excess of liquid, which was first evidenced in section 4.5.1, is not negligible and is responsible for the larger gaseous equivalence ratio observed at the leading point throughout the whole light-round sequence in Fig. 4.32 and section 4.4.3.
This increase is expected to be even larger for fuels that are less volatile than n-heptane. The larger error of the simulated case $\Phi = 1.0$ as evidenced in chapter 3 could be due to a more pronounced heterogeneity with rich conditions prevailing in the leading point region, a situation that is less well tackled by the retained combustion model.

4.6 Conclusion

This chapter continues the analysis of the three simulated light-round sequences that were validated against experimental results in chapter 3. The sequence is analysed from several perspectives. It is first found that the volumetric expansion resulting from chemical conversion in the flame induces an azimuthal velocity in the fresh stream at a distance of several sectors ahead of the flame, a phenomenon that was already observed in previous experimental and numerical studies with gaseous injection. This induced flow modifies conditions in the fresh stream. A global point of view is then adopted through the study of the evolution of integrated quantities over the chamber. Flame velocities and flame surfaces are defined in order to characterise the propagation and to compare it with gaseous injection simulations conclusions. The progress of the flame fronts is also observed through the definition of a leading point for each flame front and the local dynamics of the flow. The three cases investigated present similar preferential leading point trajectories in the combustor. Analysis of local values at these leading points indicates that the flow induced by the flame interacts with the liquid phase, modifying the liquid volume fraction in the wakes of the swirling jets established by the various injectors. This gives rise to a heterogeneity in composition and higher equivalence ratios in the fresh stream

in front of the flames. These two features influence the leading point motion and trajectory in the chamber and affect the absolute flame velocity. The study of the local dynamics around the leading point shows that its evolution is strongly correlated to that of the surrounding flow, and that it is in particular located in an area of much greater velocity, linked to the volumetric expansion of the burnt gases, which is responsible for its high absolute propagation speed.
The liquid field heterogeneity is greater in case $\Phi = 1.0$, for which the ignition delay predicted by the simulation is different from the experimental value. In the un-ignited flow, the larger proportion of injected liquid fuel leads to a saturated state in the fresh mixture, and therefore to pockets of higher liquid concentration that are formed and chased away from the flame fronts. This could be an explanation to the much larger error that is observed. In the experiment, the *relight* conditions are studied by recording the light-round in the chamber with walls at thermal equilibrium. The adiabatic wall conditions that are imposed in the simulations as a substitute to these hot walls do not allow to account for pre-heating of the fresh gases before the ignition. This does not appear to have a great impact for cases $\Phi = 0.8$ and $\Phi = 0.89$, for which the liquid is fully pre-vaporised even with adiabatic walls. However, the liquid that remains in the fresh mixture of the simulation with adiabatic walls for case $\Phi = 1.0$ is probably pre-vaporised in the experiment due to the increase of the fresh gases temperature close to the walls. To answer this question, simulations with iso-thermal walls are necessary. Such simulations were successfully carried out in chapter 2 on SICCA-Spray, leading to the correct prediction of the flame shape and the velocity fields. The next chapter attempts to apply this numerical set-up to the simulation of the light-round in MICCA-Spray with iso-thermal boundary conditions on the chamber walls.

Chapter 5

Impact of the walls temperature on the light-round in MICCA-Spray

In this chapter is presented preliminary work on the light-round simulation carried out accounting for heat losses at the walls when they are initially at ambient temperature. This is represented numerically by an iso-thermal boundary condition at $T_{wall} = 300\ K$. Experimental data shows that the temperature of the walls has a large impact on the global light-round duration. Although a marked slowing down of the flame is observed in the simulation, it is not enough to retrieve the experimental durations. Some analysis of the transient evolution of the fluxes and the temperature field is presented to provide some explanation for this result.

Contents

5.1 Impact of the walls temperature in the experimental results 210
5.2 Numerical set-up of the light-round with cold walls 211
5.2.1 Geometry and mesh 212
5.2.2 Numerical schemes and models 212
5.2.3 Iso-thermal boundary condition 213
5.3 Light-round simulation and results 216
5.3.1 Initial solution for the light-round 216
5.3.2 Light-round durations 218
5.3.3 Flame shape comparison 219
5.4 Analysis of the flow field modifications 225
5.4.1 Wall fluxes and temperature evolution 225
5.4.2 Evolution of the burnt gases volumetric expansion . 230
5.5 Addition of radiative effects 232
5.6 Conclusion 232

5.1 Impact of the walls temperature in the experimental results

As was explained in chapter 3, the experimental data that was used to validate all the previous simulations were extracted from *re-ignition* cases, meaning that the walls are at their operating equilibrium temperature at the time of the triggering of the ignition. Specifically, to ensure these conditions, MICCA-Spray is first operated for approximately 10 minutes so as to heat up the walls, the fuel supply is then switched off while the air is kept flowing in order to shut off the combustion while evacuating the burnt gases. The fuel supply is finally turned back on and, after a few seconds, the cold flow is established in the chamber and the sparking device is started.
In the joint numerical and experimental study of MICCA under premixed gaseous propane and air injection conducted by Philip et al. (2015a), it was already shown that the temperature of the walls have a large impact on the light-round delay. In particular, the authors showed that the light-round duration was 60 % greater in the cases where the walls were initially at ambient temperature compared to cases where the walls had been pre-heated.
Figure 5.1 presents experimental measurement of the light-round duration τ^{lr} against the global injected equivalence ratio with n-heptane and air injection, with pre-heated walls, in red diamonds, for the three studied operating points (these measurements were also presented in Fig. 3.15 from chapter 3) and with walls at ambient temperature (also referred to as *cold walls*), in blue circles, for

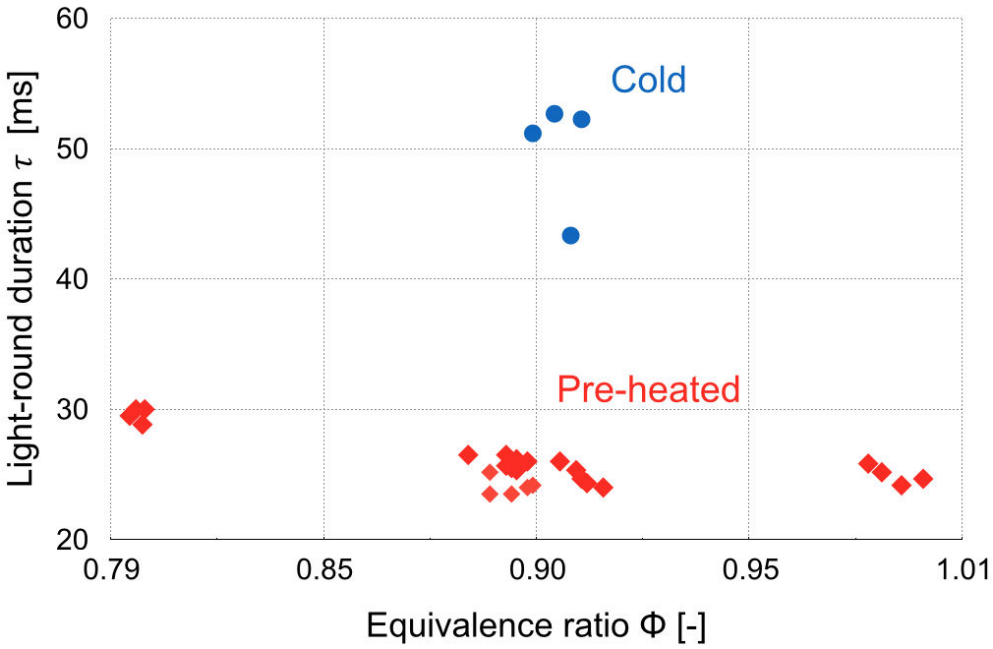

Figure 5.1: *Experimental values of the light-round durations as a function of the global injected equivalence ratio for n-heptane and air injection. The red diamond symbols stand for the experimental measurements carried out with pre-heated walls and the blue circles stand for measurements with walls at ambient temperature.*

an injected equivalence ratio around $\Phi = 0.89$. The dispersion in the equivalence ratio is due to the response time of the flowrate-meter that controls the fuel injection.
These experimental measurements show that the light-round duration is twice greater in the cases where the walls are at ambient temperature than when the walls have been pre-heated. In addition, images of the flame propagation in the cold walls cases captured by the CMOS camera, compared to the pre-heated walls case, exhibit similar flame shapes.
The flame fronts propagation speed therefore appears to be greatly reduced by the change of wall temperature, but the propagation mechanisms, and in particular the five-phase process that was identified on the pre-heated walls cases, are not altered.

5.2 Numerical set-up of the light-round with cold walls

Chronologically, the simulation of the light-round with iso-thermal boundary conditions at ambient temperature was carried out after the first simulation with adiabatic boundary conditions at $\Phi = 0.89$, with the *simplified* evapora-

tion model, and before that of the two additional operating points, $\Phi = 0.8$ and $\Phi = 1.0$, with the *complex* evaporation model, which prompted the second $\Phi = 0.89$ simulation.
In consequence, the light-round simulation with cold walls was also carried out with the *simplified* evaporation model, and the bi-sector converged cold flow solution that was used to obtain the initial 360° MICCA-Spray flow field is that of the first $\Phi = 0.89$ adiabatic walls simulation.

5.2.1 Geometry and mesh

The geometry used for the light-round simulations was already presented in details in chapters 2 and 3, so only a summary of the important facts is given here.

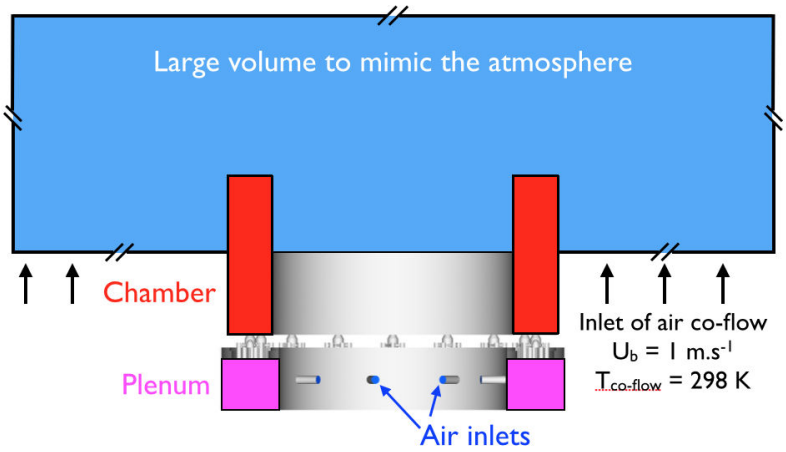

Figure 5.2: *Axial slice of the computational domain, with the plenum coloured in pink, the chamber in red and the outer atmosphere in blue. The axial co-flow is represented by black arrows.*

As with the other cases, the whole geometry of the chamber is included in the numerical domain, which is composed of the air plenum, the 16 swirlers geometry, the chamber itself and a large surrounding atmosphere, illustrated in Fig. 5.2/
The full MICCA-Spray mesh comprises 288 million elements and 50.0 million nodes.

5.2.2 Numerical schemes and models

Apart for the treatment of the chamber walls and bottom, the numerical set-up is identical to the ones presented in chapters 2 and 3 for the simulation of the adiabatic walls cases, with the *simplified* Abramson-Sirignano evaporation model (Abramzon and Sirignano (1989)).

A two-step Taylor- Galerkin weighted residual central distribution numerical scheme (TGCC), third order in time and space (Colin and Rudgyard (2000)- is used for both liquid and gaseous phases. The subgrid scale turbulence is described with the Wall Adapting Local Eddy model developed by Nicoud and Ducros (1999).
The Thickened Flame model for LES (TFLES, Colin et al. (2000)) is used to describe the unresolved small scale flame structures and the propagation of the flame as well as its interaction with turbulence. As in the other light-round simulations, the flame fronts are thickened so that they are captured by 7 grid points. The thickening of the flame front is defined dynamically according to Legier et al. (2000) so that the combustion model only impacts the flame region. This is used in combination with the efficiency function derived in Charlette et al. (2002).
Standard Navier-Stokes characteristic boundary conditions (NSCBC, Poinsot and Lele (1992)) are used at the inlets and outlet of the system. The air injection is represented by eight injection patches at the end of tubes leading to the plenum with imposed mass flow rates, temperatures and gaseous species mass fractions. The pressure at the outlet is set to 101325 Pa. With the exception of the internal chamber walls and the chamber bottom, all walls are considered adiabatic, with a slip condition on the liquid velocity and a wall law on the gaseous velocity. The numerical treatment of the cold walls through the iso-thermal boundary condition in detailed in Sec. 5.2.3.
The sixteen fuel injection patches need a more detailed treatment since the internal geometry generating the swirled hollow cone is not known and therefore not simulated. As was done with good results on the other simulated cases, the experimental profiles for the droplets velocities and the particle number density, measured 2 mm downstream the injector, are directly scaled and imposed. The mono-disperse diameter imposed at the injection patch is $d_l^{inj} = 15.3$ μm, as chosen in Sec. 2.5.
The overall equivalence ratio considered for the simulation corresponds to the target value in the cold walls experiments (see Fig. 5.1): $\Phi = 0.89$, so that the total air mass flow rate is $\dot{m}_{air}^{in} = 30.10$ g.s^{-1} and the liquid mass flow rate for each injector $\dot{m}_{fuel}^{in} = 0.111$ g.s^{-1}.

5.2.3 Iso-thermal boundary condition

For large Reynolds-number flow, Wall-Resolved LES (WRLES), i.e. capturing the energetic turbulent eddies through the boundary layer, is impractical. Figure 5.3 shows the wall-normal distance y^+ of the first cell for the considered mesh. y^+ is introduced later in Eqs. 5.1 and 5.3 and can be seen here as a metric of the boundary layer resolution on the LES mesh. The calculated field of y^+ from a law-of-the-wall (introduced hereafter) shows values larger than 5, highlighting that the mesh is too coarse for WRLES. This issue is classically tackled by a Wall-Modelled LES (WMLES) approach where the boundary layer pro-

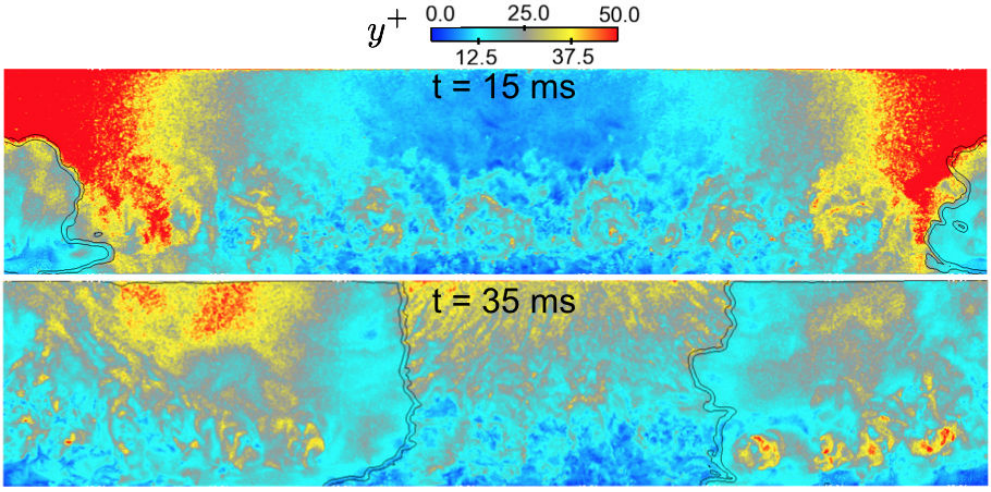

Figure 5.3: *Visualisation of the field of y^+ at the wall on the internal chamber wall at instants $t = 15$ ms (top) and $t = 35$ ms (bottom). The flame fronts position is highlighted by two iso-lines of the progress variable at $c = 0.1$ and $c = 0.9$.*

files are modelled instead of being calculated by the LES. In the present work, a law-of-the-wall is used: the boundary layer profiles are analytical functions obtained in classical boundary layer theory.
In practice, the wall heat loss due to the ambient wall temperature is modelled with the AVBP boundary condition WALL_LAW_ISOT_COUPLED, with an imposed wall temperature $T_{wall} = 300$ K.
The system of equations used by this boundary condition is similar to that of the *non-coupled* boundary condition that was applied on the walls in SICCA-Spray in Sec. 2.6.2, which allowed the prediction of the correct steady-state flame shape as well as an accurate flame lifting mechanism. It has derived by Cabrit and Nicoud (2009) to account for large temperature and density variations.
Physically, the boundary layer is the internal zone, close to the wall, where molecular and turbulent diffusion phenomena are in competition. It can be divided into several regions, characterised by a range of the non-dimensional wall coordinate y^+, defined in Eq. 5.1, and where the non-dimensional velocity profile u^+ follows a particular behaviour:

$$y^+ = \frac{y u_\tau}{\nu} \tag{5.1}$$

$$u^+ = \frac{u}{u_\tau} \tag{5.2}$$

where u^+, the dimensionless velocity, is defined as the ratio of u the mean velocity tangential to the wall and u_τ the friction velocity, which depends on

the wall shear stress τ_w and the gaseous density ρ:

$$u_\tau = \sqrt{\frac{\tau_w}{\rho}} \tag{5.3}$$

Additionally, in the case of a thermal boundary layer, the dimensionless temperature T^+ is introduced:

$$T^+ = \frac{T_w - T}{T_\tau} \tag{5.4}$$

$$T_\tau = \frac{q_w}{\rho C_p u_\tau} \tag{5.5}$$

with T_w, q_w, C_p and ρ respectively the temperature and the heat flux at the wall, the gaseous heat capacity and density, and T the mean temperature of the fluid. The heat flux at the wall, q_w, is the flux transferred from the fluid to the wall, computed as:

$$q_w = -\lambda \frac{\partial T}{\partial y} \tag{5.6}$$

where the y coordinate varies from 0 at the wall to positive values in the fluid. Three regions can be classically identified in the inner layer of the boundary layer:

- The **viscous sub-layer**, for $y^+ < 5$, located closest to the wall, where molecular diffusion dominates and linear laws can be applied to the dimensionless velocity and temperature:

$$u^+ = y^+ \tag{5.7}$$

$$T^+ = \mathrm{Pr} y^+ \tag{5.8}$$

- The **inertial sub-layer**, or logarithmic sub-layer, for $y^+ > 30$, where the turbulent diffusion dominates over the molecular one, and the following system, derived by Cabrit and Nicoud (2009), is applied:

$$\frac{2}{\alpha}\left(\sqrt{D} - \sqrt{D - \alpha u^+}\right) = \frac{1}{\kappa}\ln\left(y^+\right) + C \tag{5.9}$$

$$T^+ = \frac{1-D}{B_q} + \frac{\alpha}{B_q} u^+ \tag{5.10}$$

$$\frac{1-D}{B_q} = K\left(\mathrm{Pr}\right) \tag{5.11}$$

with, in the absence of combustion in the boundary layer:

$$\alpha = B_q \mathrm{Pr}_t \tag{5.12}$$

$$\text{and } B_q = \frac{q_w}{\rho_w C_{p,w} u_\tau T_w} \tag{5.13}$$

Pr is the molecular Prandtl number, defined in Eq. 4. κ, C and $K(\mathrm{Pr})$ are integration constants whose expressions can be found in Cabrit and Nicoud (2009).
In isothermal cases, the classical logarithmic expressions derived by Kader (1981) are retrieved for the velocity:

$$u^+ = \frac{1}{k}\ln\left(Ey^+\right) \tag{5.14}$$

$$\text{with} \quad k = 0.41 \text{ and } \quad E = 9.2 \tag{5.15}$$

and the temperature:

$$T^+ = 2.12\ln\left(y^+\right) + \beta(\mathrm{Pr}) \tag{5.16}$$

$$\text{with } \beta(\mathrm{Pr}) = \left(3.85\mathrm{Pr}^{1/3} - 1.3\right)^2 + 2.12\ln(\mathrm{Pr}) \tag{5.17}$$

- In the intermediate region, a **buffer layer** is found, for $5 < y^+ < 30$, where molecular and turbulent diffusion are of the same magnitude.

In practice, a test is applied to the value of the non-dimensional wall coordinate y^+ in AVBP to determine which expression should be used for the velocity and the temperature in the near-wall region. A cut-off value $y_c^+ = 11.445$ is used, so that if at the first cell center $y^+ < y_c^+$, Eqs. 5.7 and 5.8 are used, and Eqs. 5.14, 5.16 otherwise. These equations constitute algebraic equations solved for the unknowns τ_w and q_w from the provided values u and T on the LES grid.

5.3 Light-round simulation and results

5.3.1 Initial solution for the light-round

As was indicated before, the cold iso-thermal walls simulation is carried out with the *simplified* evaporation model. The initial solution for the light-round simulation is extracted from the first bi-sector convergence at $\Phi = 0.89$.
This solution was also presented in Sec. 3.3.3. Instantaneous fields of the liquid density $\alpha_l\rho_l$ and the gaseous equivalence ratio Φ_g on a slice at $r = 175$ mm are displayed on Fig. 5.4. With this evaporation model, the liquid is not completely evaporated when it reaches the chamber exit and the gaseous equivalence ratio is in consequence lower than the injected one ($\Phi_g \approx 0.8$ in the upper part of the chamber.
This solution was obtained by using adiabatic boundary conditions on all the chamber walls. The two-phase mixture being injected at ambient temperature ($T = 300$ K), the flow field in this case is expected to be very close to the one that would be obtained with iso-thermal boundary conditions at $T_{wall} = 300$ K. In consequence, and considering the cost of the bi-sector convergence, the adiabatic-walls solution was used for the iso-thermal walls case.

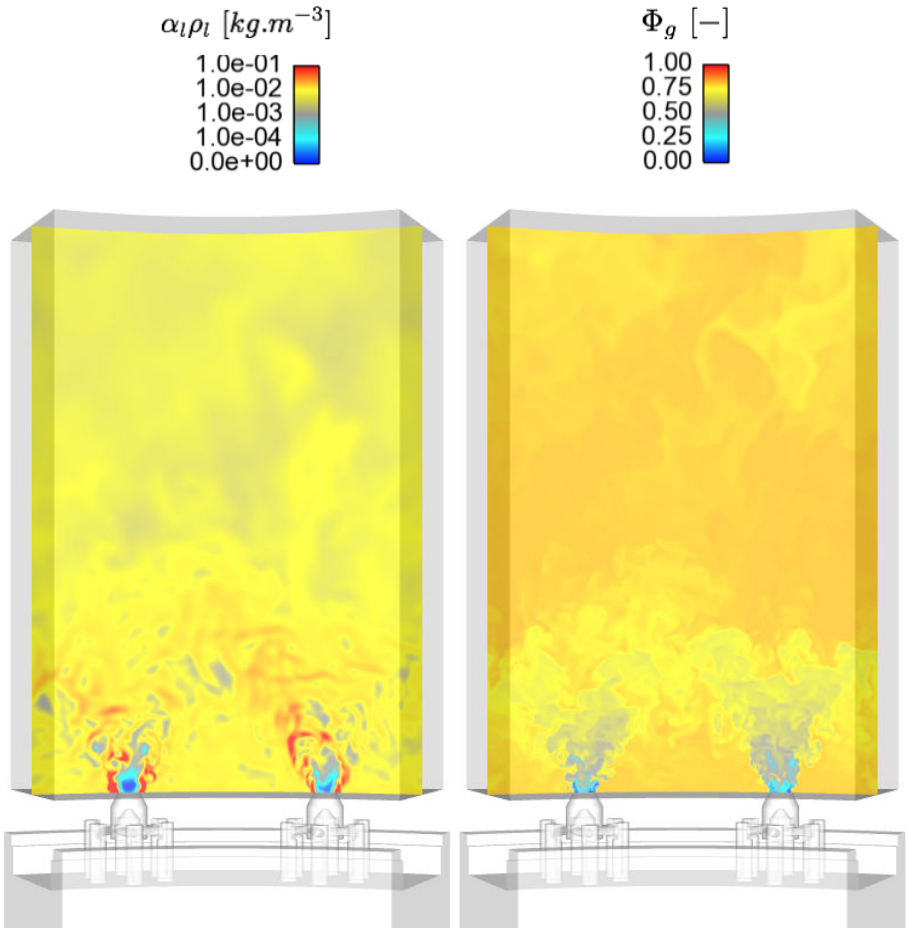

Figure 5.4: *Visualisation of the instantaneous liquid density $\alpha_l \rho_l$ (left) and the gaseous equivalence ratio Φ_g on a slice at $r = 175$ mm for case $\Phi = 0.89$ on a solution at 95% of the estimated final value, with a simplified evaporation model.*

As for the other cases, the converged bi-sector solution is replicated 7 times to retrieve the whole chamber geometry, a few milliseconds are simulated in order to remove some of the periodicity, and a sphere of burnt gases is introduced at the location of the experimental spark.
Due to the iso-thermal condition at the bottom of the chamber, the sphere that was big enough to ignite the chamber in the adiabatic simulation (with a diameter $d = 8$ mm) is not able to propagate before being extinguished in this case. In consequence, the sphere size was increased to an oval of dimensions 8×12 mm. The initial flame kernel can be seen on the initial solution for this case in Fig. 5.5.

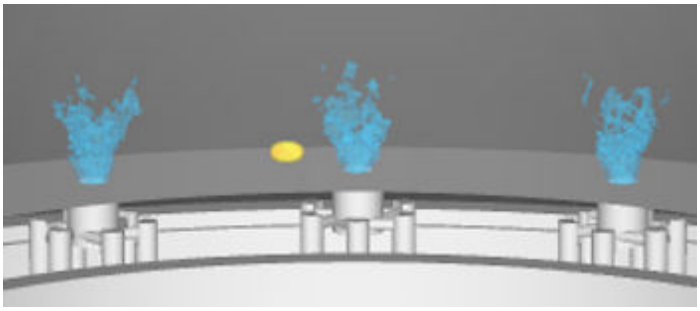

Figure 5.5: *Visualisation of the flame kernel on the initial solution for the light-round with iso-thermal walls at $T_{wall} = 300$ K. The flame kernel is represented by an iso-surface of the progress variable at $c = 0.9$ and the surrounding injectors are highlighted by iso-surfaces of the axial gaseous velocity $u = 25$ $m.s^{-1}$. The initial sphere's size had to be increase to compensate the losses at the bottom of the chamber.*

5.3.2 Light-round durations

The simulation of the light-round with iso-thermal walls was carried out on 3360 processors on the French cluster OCCIGEN located in CINES.
Similarly to the other cases, the light-round duration is retrieved as the time difference between the ignition of the first injector (in S_1 or S_{-1}) and the merging of the two fronts on the other side of the chamber. This value is reported on Fig. 5.6, as a purple cross for the iso-thermal walls case, in addition to the previously computed durations, marked by the green triangles for the *complex* evaporation model and the green square for the *simplified* model. The experimental measurements already presented in Fig. 5.1 are also reported.
With the iso-thermal boundary conditions, the predicted light-round duration is $\tau^{lr}_{cold} = 36.67$ ms. This is higher than the durations obtained with adiabatic conditions for the same global equivalence ratio ($\tau^{lr}_{simplified} = 29.3$ ms and $\tau^{lr}_{complex} = 27.1$ ms). The change of boundary condition therefore increases τ^{lr} by 25 %. The predicted duration is however still lower than the cold walls experimental measurements. Indeed, supposing that the lowest cold experimental point is reliable, the average duration between the four points is $\tau^{lr}_{exp} = 49.86$ ms, which gives an error of 26 %. If the lowest point is excluded, the error of the simulation increases up to 29.5 %.
In terms of global light-round delay, though the addition of the iso-thermal boundary condition greatly increases the duration of the light-round sequence, comparison with experimental data shows that the simulations fails to capture the full magnitude of the slowing down of the flame due to heat losses at the walls.

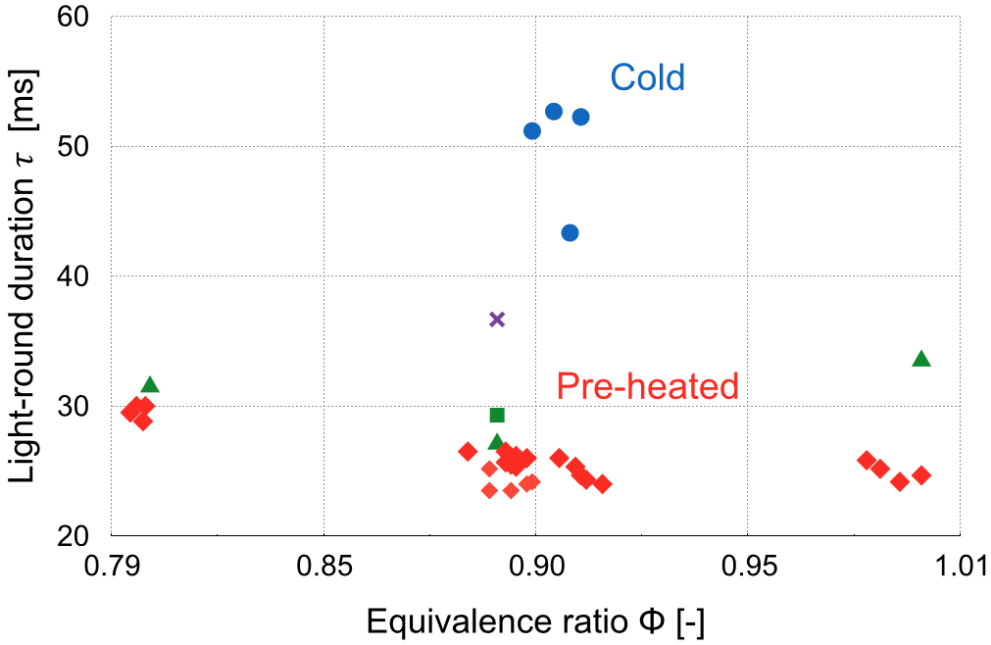

Figure 5.6: *Light-round durations as a function of the global injected equivalence ratio for n-heptane and air injection. Red diamond symbols stand for experimental results with pre-heated walls and blue circles with ambient temperature walls. The durations predicted by the simulations with adiabatic chamber walls are represented by green triangles for the LES with the complex evaporation model and a green square for the LES with the simplified evaporation model. The purple cross indicates the light-round duration predicted by the simulation with iso-thermal walls at* $T_{wall} = 300$ *K and with the simplified evaporation model.*

5.3.3 Flame shape comparison

After the global light-round duration, it is interesting to analyse the behaviour of the flame during the light-round sequence. The iso-thermal walls sequence is first compared to the adiabatic walls one (using the *simplified* evaporation model case). Let us remind that both simulations start from the same field of fresh gases. This comparison therefore outlines the effect of the modified boundary condition.

Figures 5.7 and 5.8 present visualisations of the flame progress in the chamber at different instants. The flame front is evidenced by an iso-surface of the progress variable c, defined in Eq. 3.2, at $c = 0.9$, coloured by the axial gaseous velocity, ranging from $u = -10$ m.s^{-1} in yellow to $u = 25$ m.s^{-1} in black. The presence of each individual injector is highlighted by blue iso-surfaces of the axial gaseous velocity at $u = 25$ m.s^{-1}. Time is measured as the simulated physical time, $t = 0$ ms for both simulations being the instant the sphere of burnt gases is introduced in the fresh mixture. Instants $t = 5$ ms, $t = 15$ ms and $t = 20$ ms are displayed in Fig. 5.7 and $t = 30$ ms, $t = 40$ ms and $t = 47$ ms

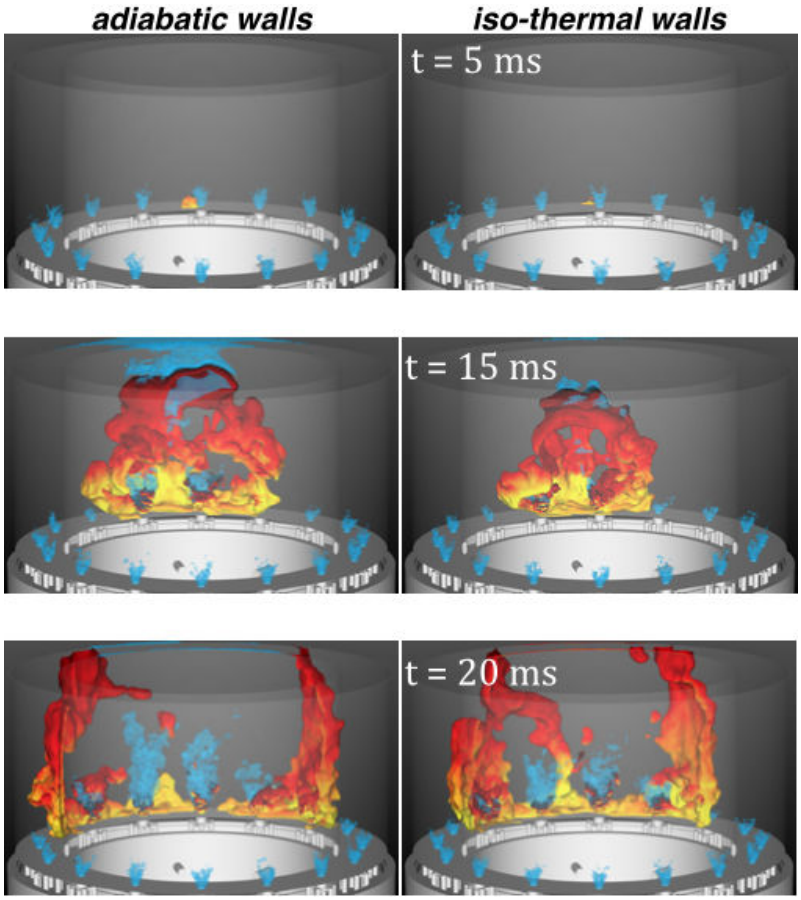

Figure 5.7: *Comparison between the adiabatic and iso-thermal walls numerical sequences at three instants during the light-round sequence for case* $\Phi = 0.89$*,* $t = 5$ *ms (top),* $t = 15$ *ms (middle) and* $t = 20$ *ms (bottom).*

in Fig. 5.8.

In the first instants ($t = 5$ ms, Fig. 5.7, top), even though the initial flame sphere was bigger, the flame kernel is smaller in the iso-thermal walls case, and in particular is not able to come in contact with the bottom due to the strong heat losses. This explains the greater difficulty that is encountered, both experimentally and numerically, in the ignition of the chamber with cold walls (experimentally, a larger number of sparks are necessary to trigger the ignition and numerically the sphere had to be bigger).

During the whole light-round sequence, the different snapshots show that the propagation pattern is not modified by the change of boundary condition. Indeed, the phases identified in previous studies and retrieved on the adiabatic walls sequences are also present here. After the initial propagation of the kernel (phase I), an arch-like flame front is formed that propagates sideways and upwards (phase II), as can be seen at $t = 15$ ms on Fig. 5.7 (middle), in

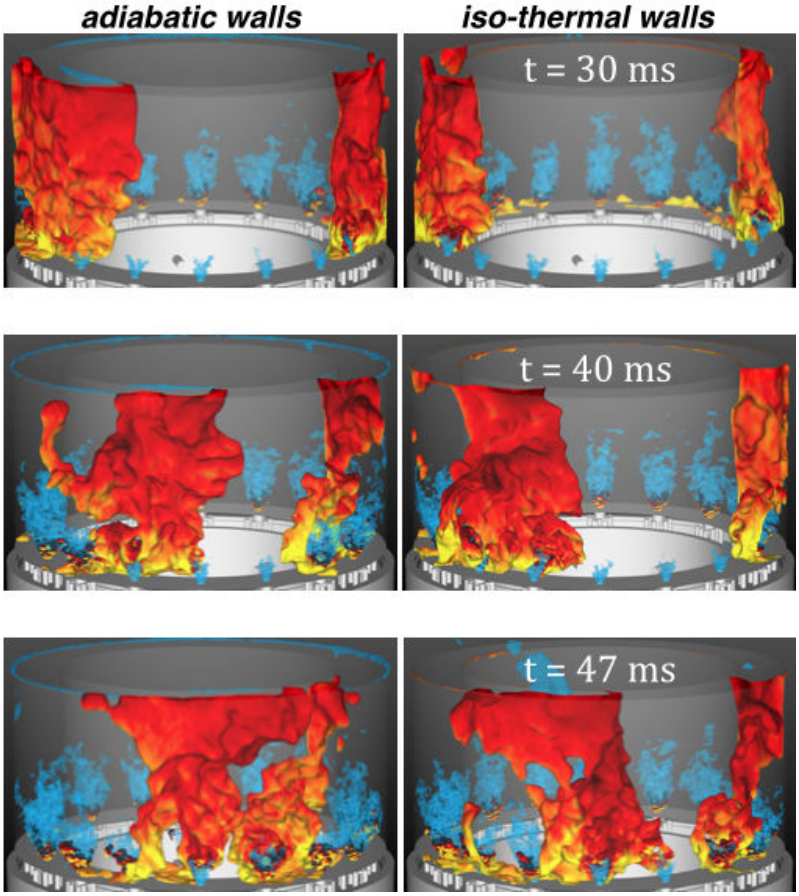

Figure 5.8: *Comparison between the adiabatic and iso-thermal walls numerical sequences at three instants during the light-round sequence for case* $\Phi = 0.89$*,* $t = 30$ *ms (top),* $t = 40$ *ms (middle) and* $t = 47$ *ms (bottom).*

which the iso-thermal walls case is slightly less advanced than the adiabatic walls case. Upon reaching the exit, two fronts are formed in phase III that are mostly vertical and propagate tangentially (see instants $t = 20$ ms, $t = 30$ ms and $t = 40$ ms on Figs. 5.7 and 5.8).

Even though during phase III, the iso-thermal walls case is less advanced than in the adiabatic case, the difference seems to be due to the less favourable conditions encountered by the kernel in phase I rather than to effect of the cold walls. However, close to the instant the flame fronts merge on the other side of the chamber, a marked slowing down is observed in the iso-thermal walls case. At $t = 47$ ms (bottom figures of Fig. 5.8), the fronts in the adiabatic walls case have already encountered each other close to the opposite position of the spark, while in the isothermal walls case, a marked asymmetry is observed, and the fronts do not come in contact until a few seconds later. These instants before the merging are displayed on Fig. 5.9, at $t = 48$ ms, $t = 49$ ms and $t = 50$ ms,

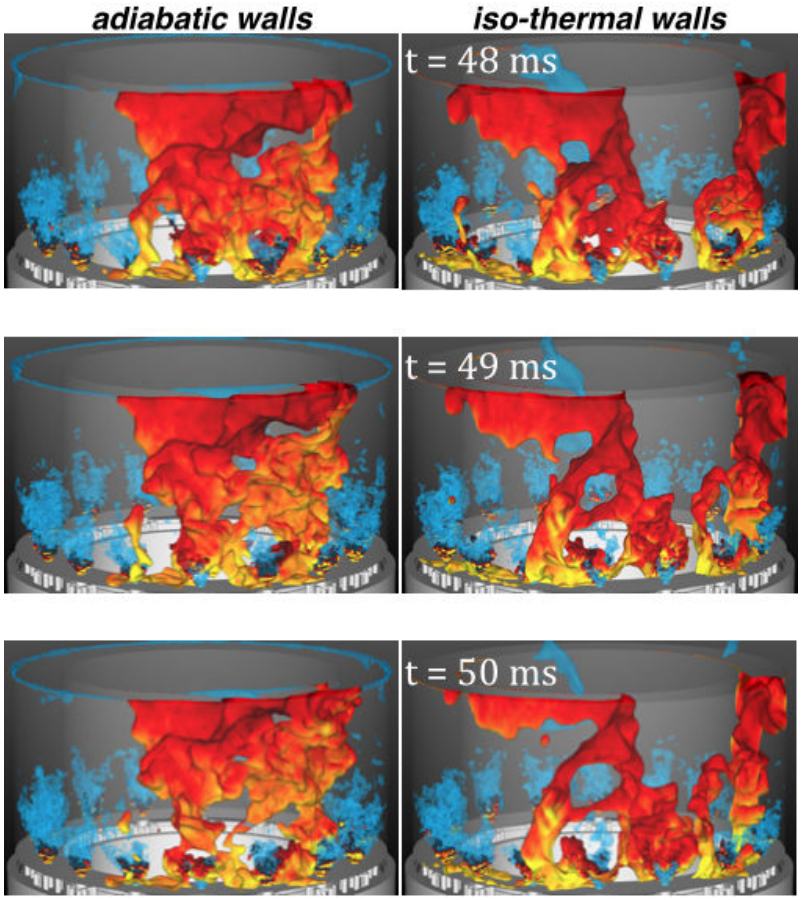

Figure 5.9: *Comparison between the adiabatic and iso-thermal walls numerical sequences at three instants during the light-round sequence for case* $\Phi = 0.89$*,* $t = 48$ *ms (top),* $t = 49$ *ms (middle) and* $t = 50$ *ms (bottom).*

in addition to instant $t = 47$ ms at the bottom of Fig. 5.8. Clearly, though the flame fronts are very close to one another and were progressing regularly before, some distant interaction is taking place that slows their progress and delays the merging. At the same instants, no such interaction is observed on the adiabatic walls case and the whole fronts are going on with the merging.
The large difference that was observed on the light-round duration between the two cases (25 %) appears to be caused by a large deceleration of the fronts in the iso-thermal walls case at the end of phase III.
Comparison with one of the experimental sequences that yielded a light-round duration $\tau_{exp}^{lr} \approx 52$ ms on Fig. 5.6 is presented in Figs. 5.10 and 5.11. The experimental images, captured with a high-speed intensified complementary metal-oxide semiconductor (CMOS) camera, with a resolution of 512×512 pixels. The frame rate and shutter speed are respectively 6000 Hz and 166 μs.
As was done for the images recorded by the Phantom camera and presented in

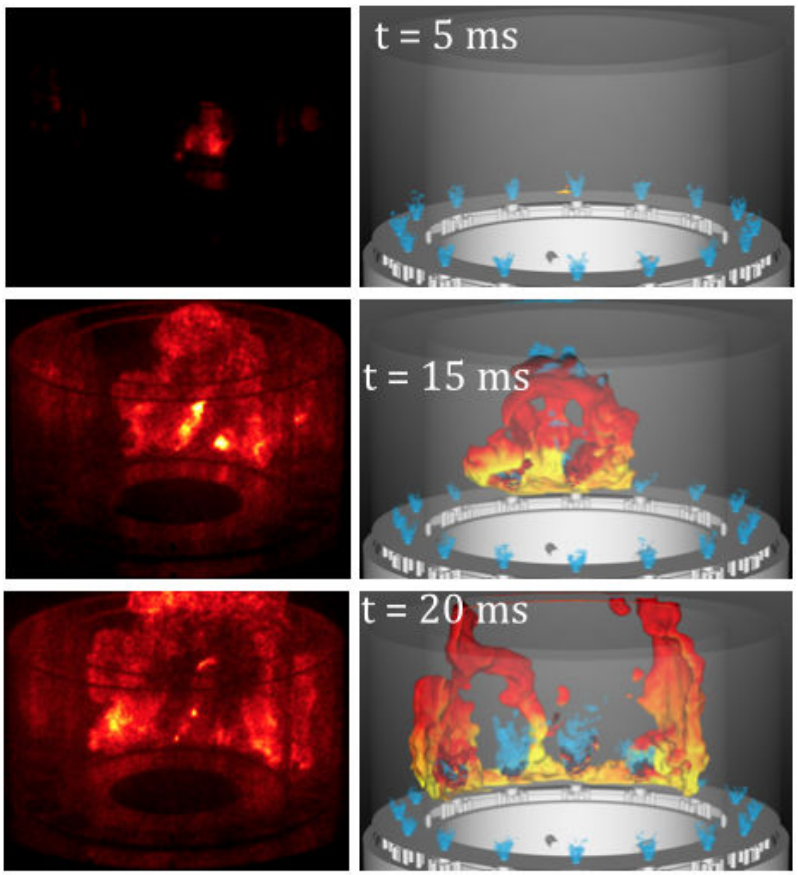

Figure 5.10: *Comparison between experimental and numerical with light-round sequences with walls at ambient temperature. Three instants are displayed, $t = 5$ ms (top), $t = 15$ ms (middle) and $t = 20$ ms (bottom).*

chapter 3, the images of the propagating flame fronts generated by the CMOS camera, initially in levels of grey, are represented on a scale of colors from yellow to red for better clarity.
On these images, the time taken for the snapshots is that of the simulation, and the two sequences were synchronised through the ignition of the first injector (S_1 or S_{-1}, depending on the one that is reached first).
The images of the experimental sequence show that, as is the case in the simulation, the temperature of the walls do not impact the propagation pattern. The five phases are retrieved, although only three are displayed here, due to the much faster propagation in the simulation.
On the first images, on Fig. 5.10, between $t = 5$ ms and $t = 20$ ms, the shape of the flame fronts are very similar between the simulation and the experiment. Even though at $t = 5$ ms, a bigger flame kernel can be seen on the experimental image, the two arches that are formed at $t = 15$ ms are similar in size and shape. At $t = 20$ ms, two fronts have formed in each case that are roughly vertical and

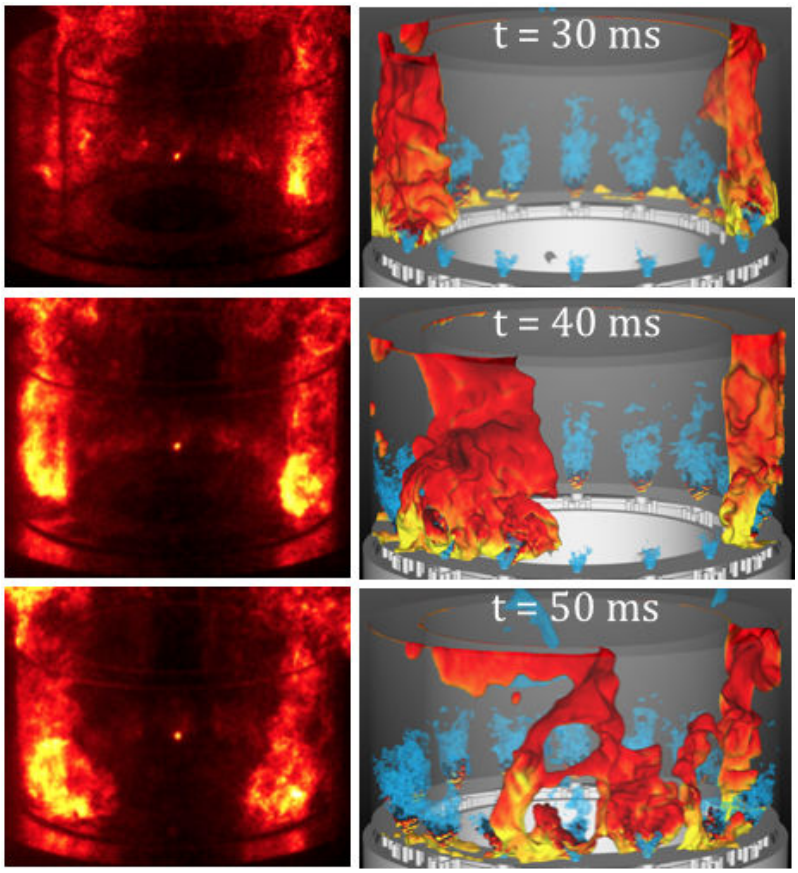

Figure 5.11: *Comparison between experimental and numerical with light-round sequences with walls at ambient temperature. Three instants are displayed, $t = 30$ ms (top), $t = 40$ ms (middle) and $t = 50$ ms (bottom).*

have each crossed around one-third of their respective half-chamber.
The same conclusions can be drawn at $t = 30$ ms, the fronts are approximately at the same azimuthal position. It is also interesting to notice that an asymmetry is observed in both cases, though in the experiment, the right front is more advanced while it is the left in the simulation. In the experimental sequences, the asymmetry was almost always present in the cold walls cases, but with a strong stochastic aspect.
At $t = 40$ ms, the simulated flame fronts are much more forward than in the experiment, indicating that, sometimes in the middle of phase III, the flame fronts in the experiment slow down sooner because of the heat losses at the walls. In the simulation, though some deceleration was observed in the comparison with the adiabatic walls case at the very end of phase III, it appears not to be of the magnitude observed in the experiment. In consequence, when the merging of the flame fronts occurs in the simulation, at $t = 50$ ms, the experimental fronts are still far from merging, thus explaining the 29.5 % error

on the light-round duration.

To conclude, the discrepancy observed on the propagation duration between the simulation with cold iso-thermal walls and the experiment with ambient temperature walls arises from an underestimation of the flame fronts velocity during their propagation in the second half of the chamber, that is to say during the second half of phase III. Even though some deceleration is observed in the simulation, apparently caused by the change of boundary condition, it appears later than in the experiment and is not strong enough to predict the correct propagation delay.

5.4 Analysis of the flow field modifications

5.4.1 Wall fluxes and temperature evolution

In the simulation of SICCA-Spray with hot iso-thermal walls, the analysis of the fluxes at the chamber wall and bottom showed that they were responsible for a heat loss equivalent to 48 % of the global power of the burner. Since SICCA-Spray was designed in terms of geometry and confinement to be representative of one sixteenth of MICCA-Spray, it can be assumed that the heat losses in the annular chamber at its ignited steady-state, with walls at thermal equilibrium, would have a similar proportion. In this case, with an injected equivalence ratio of $\Phi = 0.89$, the chamber power is $\mathcal{P} = 79.3$ kW.

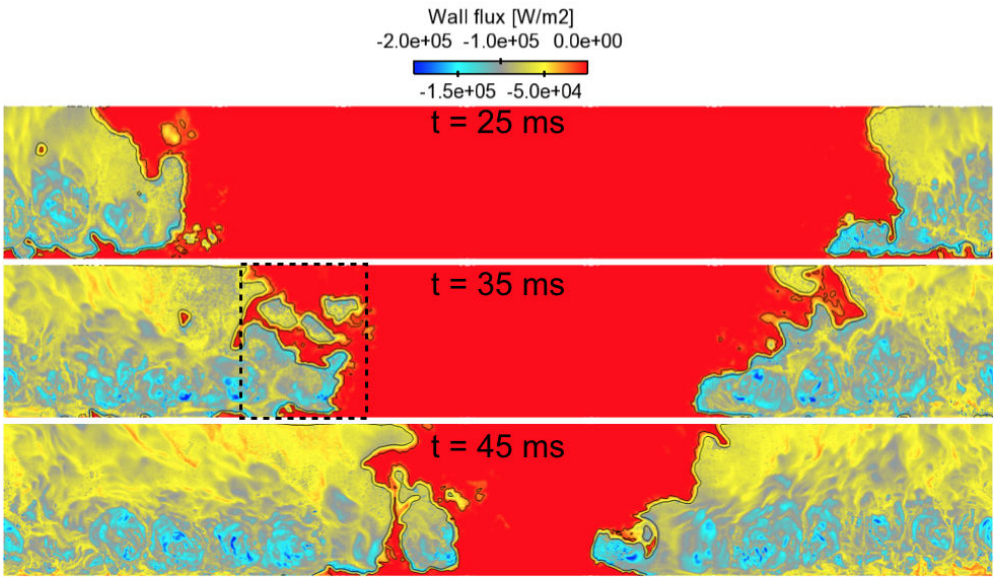

Figure 5.12: *External chamber wall unfolded on a plane surface, coloured by the normal wall flux. Three instants are displayed, $t = 25$ ms (top), $t = 35$ ms (middle) and $t = 45$ ms (bottom).*

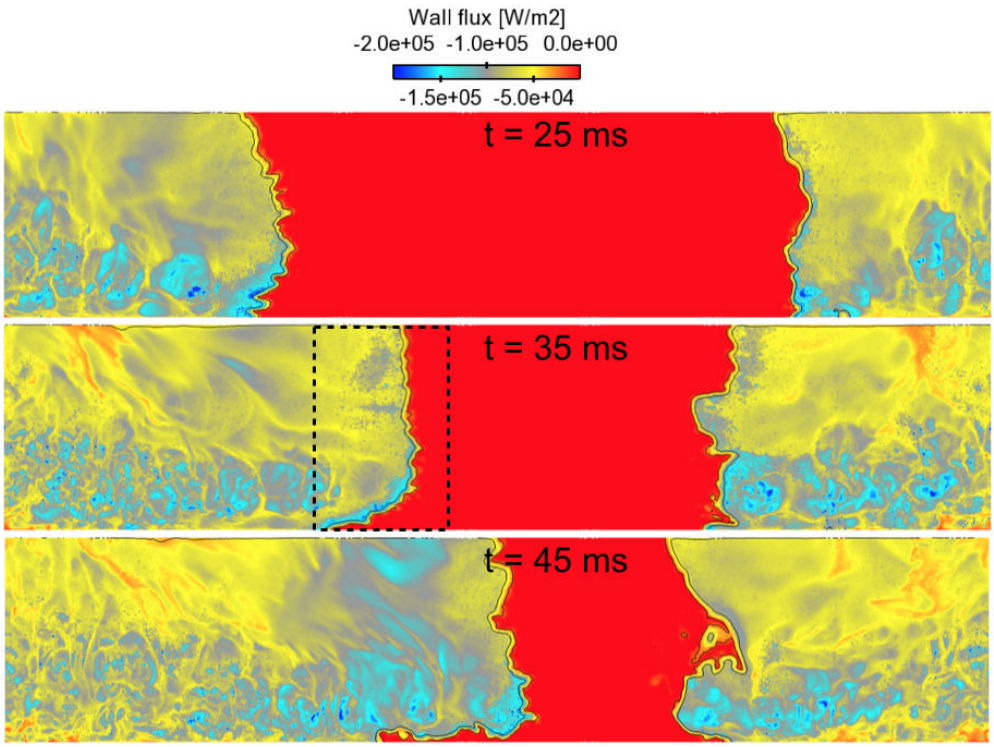

Figure 5.13: *Internal chamber wall unfolded on a plane surface, coloured by the normal wall flux. Three instants are displayed, $t = 25$ ms (top), $t = 35$ ms (middle) and $t = 45$ ms (bottom).*

The evolution of the fluxes at the walls during the light-round sequence are displayed on Figs. 5.12 and 5.13, respectively on the external ($r = 200$ mm) and internal ($r = 150$ mm) walls of the chamber, that have been unfolded on plane surfaces for better visualisation, at the three instants $t = 25$ ms (top images), $t = 35$ ms (middle images) and $t = 45$ ms (bottom images). By convention in AVBP, the fluxes are negative when energy is being taken from the fluid, as is the case here. The flame front is evidenced by two iso-lines, coloured in black, of the progress variable c, at $c = 0.1$ and $c = 0.9$.
First of all, the main observation is that the wall law is working as expected, meaning that in the fresh mixture, which is injected at $T = 300$ K, which is also the walls temperature, no flux is present at the wall (null fluxes are identified by the red color), while as soon as the flame has increased the gases temperature, some heat losses are observed.
On both external and internal walls, the fluxes in the burnt gases appear to be quite constant once the flame front has passed, at least in the duration of the light-round. They are logically greater towards the bottom of the chamber where the convective heat transfer is enhanced due to the stronger turbulent flows around the injectors, and are approximately twice lower in the upper half

of the chamber.

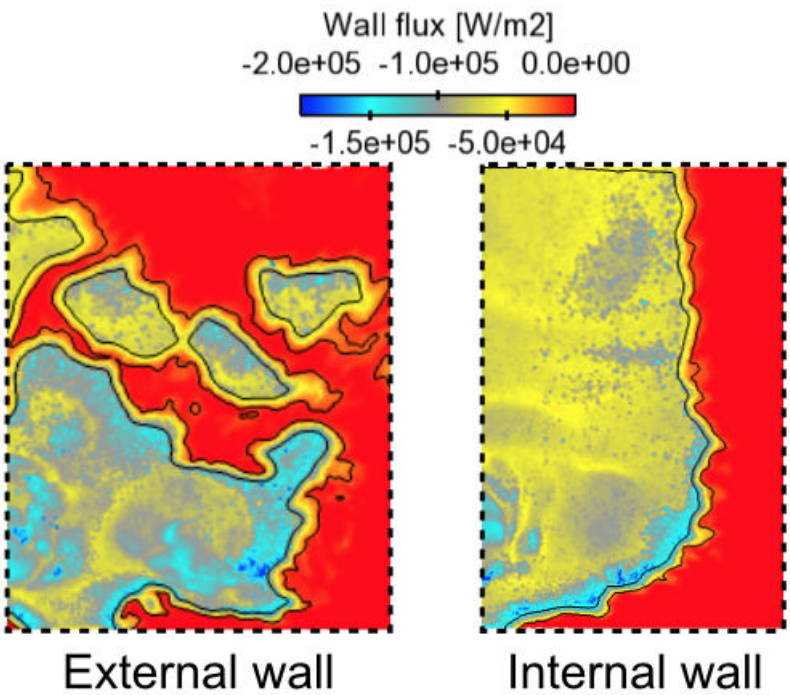

Figure 5.14: *Zoom on the left flame front area on the external wall (left) and the internal wall (right) at $t = 35$ ms and coloured by the normal flux at the wall. The zoom areas are identified by the dashed rectangles on Figs. 5.12 and 5.13.*

Figure 5.14 presents zooms on the left flame front region on the external (left) and internal (right) walls, extracted from instant $t = 35$ ms. The zoom areas are also identified as black dashed rectangles on Figs. 5.12 and 5.13.
The flame fronts are identified by the two c-iso-surfaces, at $c = 0.1$ and $c = 0.9$, and these zooms show that the maximum flux around the flame front is located behind it. In other words, the heat losses at the wall are still quite low at the instant of the flame crossing and only increase largely after it has passed.
On SICCA-Spray, one of the mechanisms that appeared to have an effect in the flame shape with iso-thermal boundary conditions was the suppression of the flame elements that came in contact with the cooled bottom wall. In the case of the simulation of the light-round in MICCA-Spray, it appears that the losses are not important enough to have a direct impact of the flame. Indeed, a flame front is still present in contact with the wall while a usual effect of heat losses, that was observed on SICCA-Spray, is to kill the flame elements directly in contact with the wall.
The impact of the cold boundary condition on the flow field can also be observed on the gaseous temperature T_g. In a steady-state solution of SICCA-Spray with hot iso-thermal walls, a large decrease of T_g was already observed. Figures 5.15

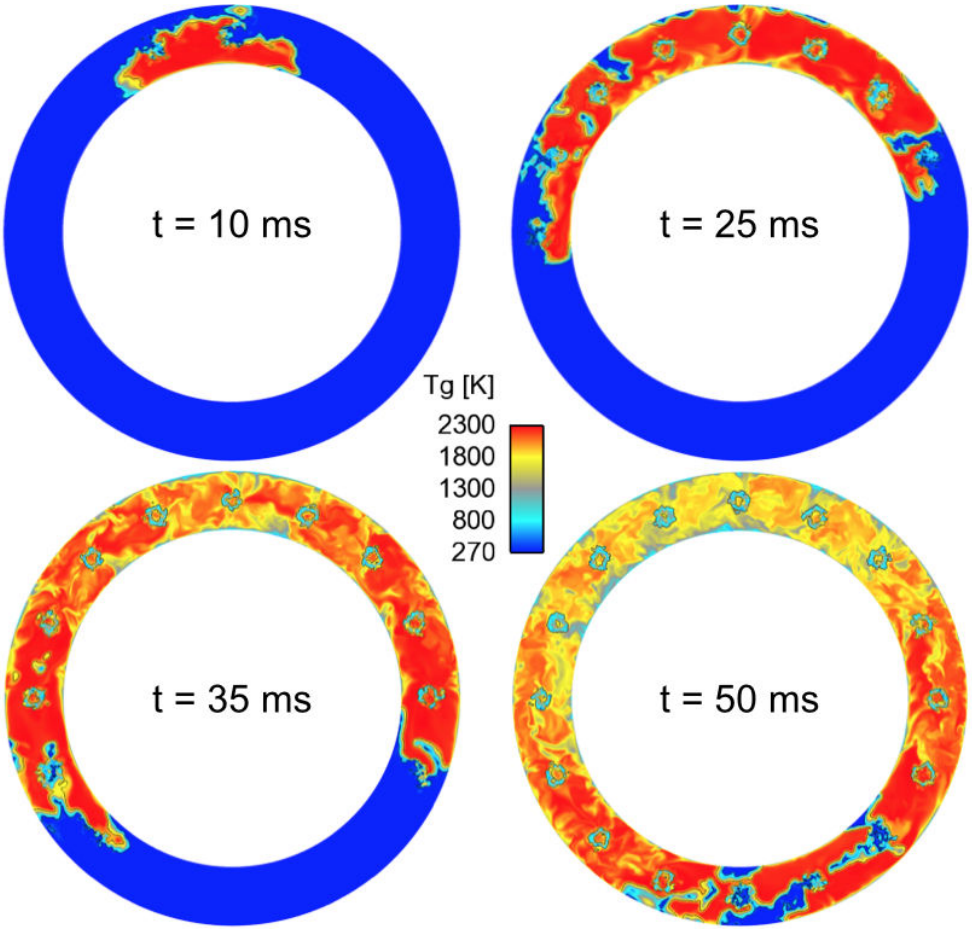

Figure 5.15: *Axial cut of the flow field in the chamber at $X = 10$ mm, coloured by the gaseous temperature T_g, at four instants of the simulation, $t = 10$ ms (top left), $t = 25$ ms (top right), $t = 35$ ms (bottom left) and $t = 50$ ms (bottom right).*

and 5.16 present the evolution of the gaseous temperature during the light-round sequence on axial cuts in the chamber at $X = 10$ mm (Fig. 5.15), which is close to the bottom of the chamber, and at $X = 100$ mm (Fig. 5.16), which corresponds to the middle height of the chamber. Four instants are displayed, $t = 10$ ms (top left), $t = 25$ ms (top right), $t = 35$ ms (bottom left) and $t = 50$ ms (bottom right).

It appears from these axial cuts that the drop of the gaseous temperature in the burnt gases does not occur until well after the crossing of the flame. At $X = 10$ mm, the burnt gases at instants $t = 10$ ms and $t = 25$ ms are still at their adiabatic flame temperature (around $T_g = 2300$ K), and some decrease of T_g begins to appear close to the walls. This decrease is much more marked at $t = 35$ ms, where the burnt gases in sectors S_0, S_1 and S_{-1}, the ones closest to the initial flame kernel, exhibit temperatures $T_g \sim 1800-1900$ K. At $t = 50$ ms,

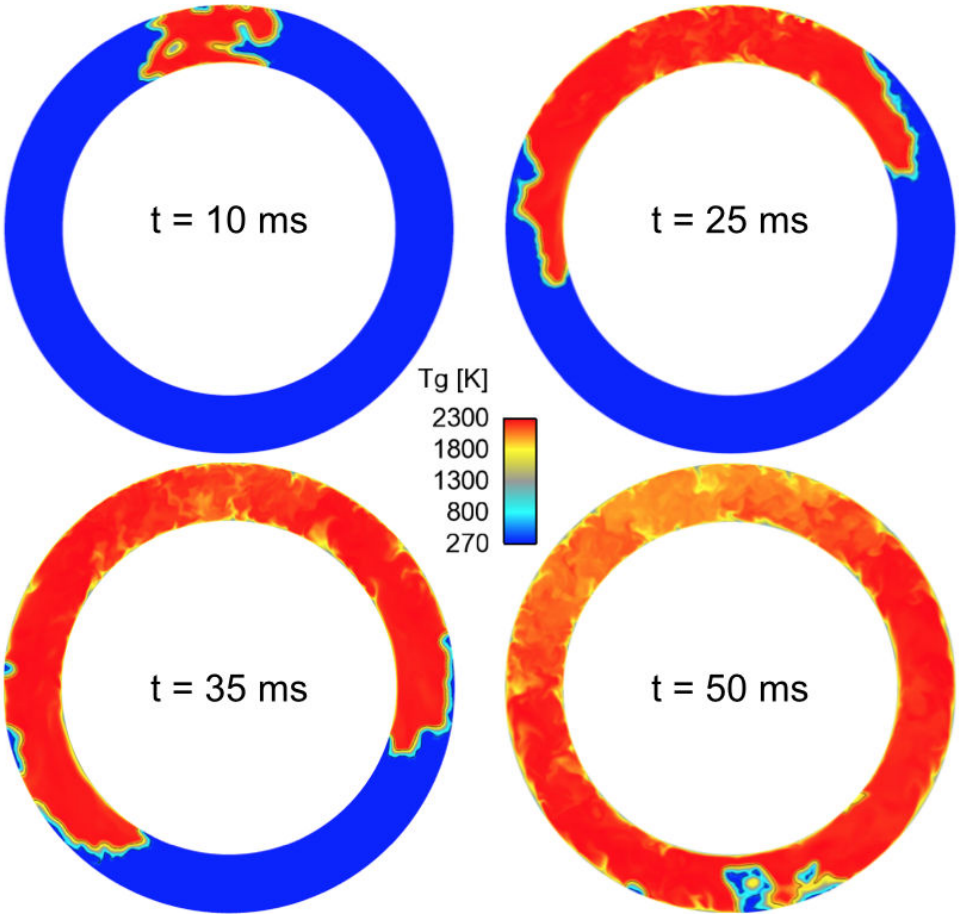

Figure 5.16: *Axial cut of the flow field in the chamber at $X = 100$ mm, coloured by the gaseous temperature T_g, at four instants of the simulation, $t = 10$ ms (top left), $t = 25$ ms (top right), $t = 35$ ms (bottom left) and $t = 50$ ms (bottom right).*

after the flame fronts have merged, the temperature has dropped even more in one half of the chamber (sectors S_0 to S_5 and S_{-5}) but close to the propagating flame fronts, the burnt gases are still at $T_g \sim 2300$ K and the heat losses do not appear to have had an effect yet.
The cut $X = 10$ mm is located close to the bottom of the chamber, where $T_{wall} = 300$ K. Higher in the chamber, for instance at the medium height $X = 100$ mm, the heat losses can only come from the lateral walls, and the temperature field is less impacted during the light-round. Even at $t = 50$ ms, the temperature drop around the initial kernel position is around 400 K, compared to the field at the same instant at $X = 10$ mm, where temperatures have come down to 800 K at some places.
The delay in the effect of the heat losses at the walls can finally be observed on the evolution of power lost at the walls during the light-round sequence. Figure 5.17 presents the evolution of the heat losses at each iso-thermal bound-

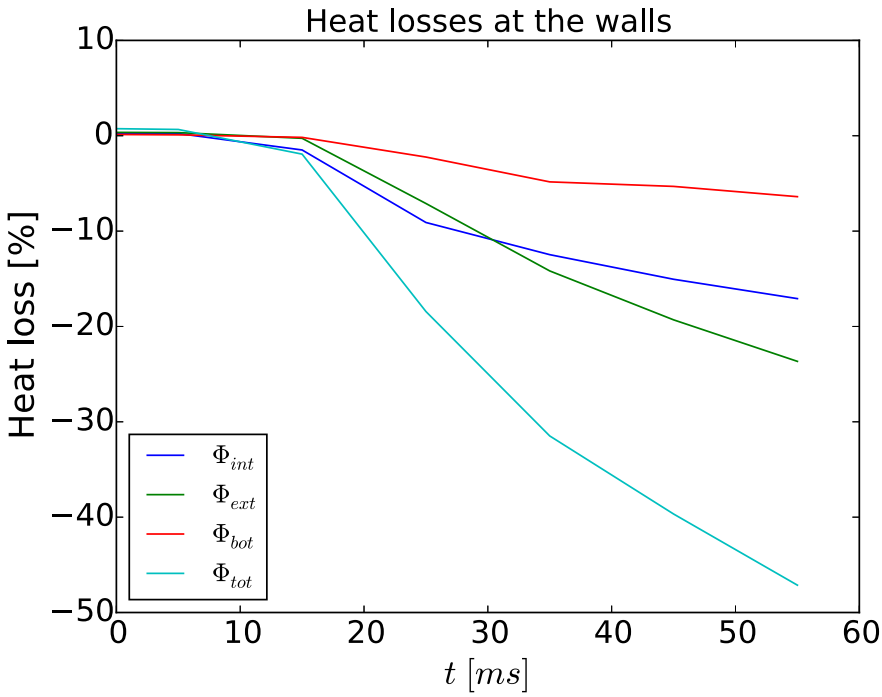

Figure 5.17: *Transient evolution of the heat flux integrated over the different surfaces. The integrated flux on the internal chamber wall is plotted in blue, on the external wall in green and on the chamber bottom in red. The sum of the three contributions is plotted in cyan.*

ary, the internal chamber wall in blue, the external chamber wall in green and the chamber bottom in red. The total heat losses at the walls is also reported in cyan. All quantities have been divided by the chamber nominal power $\mathcal{P} = 79.3$ kW and are presented in percentage. As could be expected, the heat losses look far from having reached a steady-state value, and are at their maximum at the end of the simulated time, when the fronts have merged and the simulation is stopped. The transient heat losses still reach around 50 % of the chamber nominal power.

5.4.2 Evolution of the burnt gases volumetric expansion

As was detailed in chapter 4, Sec. 4.2, the propagating fronts velocity is largely driven by the volumetric expansion of the burnt gases which, due to their increased temperature and lower density, generate an azimuthal flow in the fresh and burnt gases.
Figures 5.18 and 5.19 show comparisons of the gaseous tangential velocity on a radial cut at $r^{cut} = 175$ mm (see Sec. 4.2.1 for more details) between the case with iso-thermal walls (top images) and the one with adiabatic walls (bottom

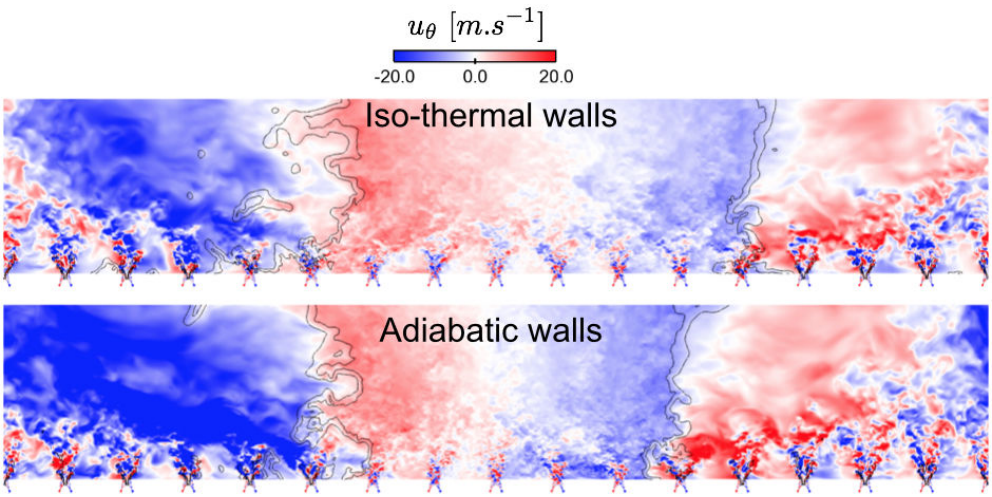

Figure 5.18: *Visualization of the tangential gaseous velocity on a cylinder of radius $r^{cut} = 175$ mm, crossing the injectors' centerlines, unfolded on a plane surface for the case with iso-thermal walls (top) and with adiabatic walls (bottom): $t_{isoT} = 35.0$ ms and $t_{adiab} = 32.0$ ms. The instants were chosen to present similar flame fronts positions in the chamber. Tangential velocities are counted positive from left to right and range from $u_\theta = -20$ $m.s^{-1}$ in blue to $u_\theta = 20$ $m.s^{-1}$ in red. Two iso-lines of the progress variable $\widetilde{c} = 0.1$ and $\widetilde{c} = 0.9$ (in black) highlight the position of the flame fronts.*

images). For comparison's sake, the instants for each case were chosen in order to have similar flame front positions in the chamber, and are therefore not the same.

On both figures, representing two different position of the flame fronts, both during phase III where the deceleration in observed, the azimuthal flow in the burnt and fresh gases is also observed in the iso-thermal walls case, though it seems to have a lower magnitude. In particular, around the position of the initial kernel, at the sides of the unfolded surfaces, the tangential velocity, which is very strong and in one direction in the adiabatic walls case, is disappearing in the cold walls case in favour of the flow generated by the swirlers. In addition, on both figures, the blue and red are less intense in the burnt gases in the iso-thermal walls case.

The lessening of the induced azimuthal flow created by the burnt gases volumetric expansion, probably due to the decrease of the burnt gases temperature through the heat losses at the walls, could explain the significant decrease of the flame fronts propagation velocities. In particular, the observation of the flame images showed that this decrease occurs mainly during the propagation in phase III, where the volumetric expansion plays a crucial role.

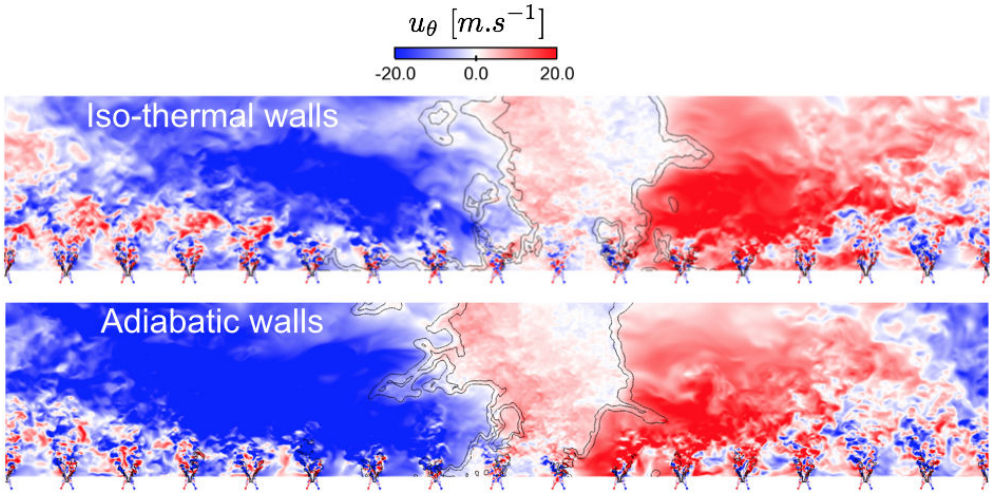

Figure 5.19: *Visualization of the tangential gaseous velocity on a cylinder of radius $r^{cut} = 175$ mm, crossing the injectors' centerlines, unfolded on a plane surface for the case with iso-thermal walls (top) and with adiabatic walls (bottom): $t_{isoT} = 45$ ms and $t_{adiab} = 40$ ms. The instants were chosen to present similar flame fronts positions in the chamber. Tangential velocities are counted positive from left to right and range from $u_\theta = -20$ $m.S^{-1}$ in blue to $u_\theta = 20$ $m.S^{-1}$ in red. Two iso-lines of the progress variable $\widetilde{c} = 0.1$ and $\widetilde{c} = 0.9$ (in black) highlight the position of the flame fronts.*

5.5 Addition of radiative effects

In light of the previously presented results, an additional light-round simulation was carried out with the same numerical set-up and with an activation of radiative heat losses. Since the heat losses appeared not to be important enough in the iso-thermal simulation, radiative heat losses in the burnt gases might lead to an improvement of the results.
The radiative model is the optically thin medium approximation, which does not account for absorption by the gases. In consequence, the loss due to radiative effects are expected to be over-estimated.
The predicted light-round duration in the simulation with cold iso-thermal walls and radiative heat losses was found to be $\tau^{lr}_{rad} = 35.95$ ms, which is very close to the iso-thermal simulation value $\tau^{lr}_{cold} = 36.67$ ms.
The radiative heat losses therefore appear to have a limited impact on the light-round duration and their absence was not the reason for the under-prediction of the light-round delay in the ignition cases with cold walls.

5.6 Conclusion

Experimental results showed a large impact of the walls temperature on the light-round duration. This chapter presents the results obtained from the light-round simulation of case $\Phi = 0.89$ with iso-thermal boundary conditions applied

at the chamber walls and bottom and their preliminary analysis.
Comparisons of the flame propagation showed that, though the predicted duration is larger than in cases with adiabatic boundary conditions, the simulation still under-estimates the propagation velocities. Flame shape analyses showed however that, in both the experiment and the simulation, the flame behaviour, and in particular the five phases of the light-round identified on the hot walls configurations, were retrieved.
From the temperature fields and the evolution of the fluxes at the walls, it appears that the law-of-the-wall allows to account for heat losses when the walls are at ambient temperature, leading in particular to a significant decrease of the burnt gases temperature. A lessening of the magnitude of the azimuthal flow generated by the burnt gases volumetric expansion is also observed, that can explain the slowing down of the flame in the simulation.
The simulation therefore captures qualitatively the physical behaviour of the light-round with cold walls conditions. However, the magnitude of the predicted effects however appear to be too small to have a large enough impact of the flame fronts propagation velocity in order to retrieve the experimental durations.
A possible issue is the fact that the retained wall law, with or without its coupled variant, rely on quasi-steady assumptions. As is shown by Ma et al. (2017a), equilibrium wall laws might not be adequate for the simulation of configurations where large transient variations on the velocity and the density are present near the walls. In this context, it might be necessary to use non-equilibrium laws, such as have been recently developed to predict the cycle-to-cycle behaviour in internal combustion engines, such as was done for instance by Kawai and Larsson (2013) or Ma et al. (2017b).

Conclusion and perspectives

The general objective of this thesis was to provide additional characterisation and understanding of the light-round sequence in a system representative of aeronautic gas turbines. This was done through the numerical study of the MICCA-Spray chamber, designed and studied experimentally at EM2C in an effort to investigate systems whose complexity is closer to industrial combustors. In particular, the two-phase nature of the injection is accounted for by making use of liquid n-heptane.

MICCA-Spray is an annular combustion chamber, comprising sixteen identical swirl injectors and transparent quartz walls to allow optical access It was initially operated with gaseous premixed injection. The PhD work of J. F. Bourgouin provided detailed experimental data on the light-round sequence with perfectly premixed propane and air injection. This data was then used by M. Philip to validate results obtained from large-eddy simulations. Additionally, M. Philip carried out a detailed analysis of the light-round and proposed a model for the absolute flame fronts propagation velocity in the chamber.
The PhD work of K. Prieur included the modification of the injection system in MICCA-Spray in order to allow the use of liquid fuel. The light-round sequence was then studied under different operating conditions, in terms of bulk velocity, global power and equivalence ratio, and with different fuels, including propane, liquid n-heptane and liquid dodecane.

Summary of the thesis results

The quite large dimensions of MICCA-Spray and the transient nature of the light-round process make the large-eddy simulations very expensive in terms of CPU hours and make it necessary to use simplified models. In particular, the presence of a flame front over the entire height of the chamber imposes limitations on the cell sizes. For the first simulations of the light-round in MICCA-Spray with two-phase injection, the Eulerian mono-disperse formalism was retained for the description of the liquid phase, among other reasons because of its good scaling in massively parallel calculations.
In continuity of the work done by M. Philip, attention was focused on successful *re-ignition* cases, where the combustor has just been shut off after a

prolonged operation, so that the whole combustor is at thermal equilibrium. Numerically, this condition was approximated by supposing the chamber walls to be adiabatic. Three operating conditions were retained for the investigation of the light-round, with three values of the global injected equivalence ratio, while keeping the global power constant.

A detailed validation and analysis was first carried out on a simpler configuration, SICCA-Spray, composed of a single injector, identical to the sixteen found on MICCA-Spray, and a cylindrical removable quartz chamber, which provides a confinement equivalent to one-sixteenth of the annular chamber. A large amount of experimental data was available on SICCA-Spray, with and without confinement, on the cold flow and with combustion, that enable the assessment and validation of the numerical set-up step by step.
The choice of the mono-disperse representation for the experimental poly-disperse spray raises the problem of the selection of a relevant value for the injected diameter. Tools from the uncertainty quantification framework were used to estimate the evolution of the variables predicted by the simulation against the injected diameter. Once a criteria has been selected to evaluate the quality of the predicted fields with respect to experimental data, the optimal value for the injected diameter is naturally the one that minimises the associated error.
The selection of the injected diameter was carried out on the un-confined configuration of the single burner. This optimal value was then used for the simulation of the confined configuration, with and without combustion. The first calculation of the steady-state flame with adiabatic boundary conditions on the chamber walls failed to predict the correct flame shape, which was later retrieved by applying iso-thermal conditions on the walls, imposing the steady-state temperatures measured in the experiment. Additional simulations with other values of the injected diameter showed the suitability of the chosen value, in terms of predicted flame shape and velocity fields.

In order to provide the initial solutions for the light-round simulations, the un-ignited flow field was first converged on the *bi-sector* configuration, which corresponds to one eighth of the annular chamber with axi-periodic conditions on the sides, thus making use of the periodic pattern in MICCA-Spray. The species mass fraction fields were found to have a very slow convergence, due to the presence of recirculation zones that trap the droplets and the evaporated fuel. Analyses of the converged fields showed that, while in the two lowest equivalence ratio cases $\Phi = 0.8$ and $\Phi = 0.89$, the liquid was totally vaporised before reaching the chamber exit, in case $\Phi = 1.0$, a saturated state was reached and a large proportion of the injected fuel remained liquid in the fresh mixture. The initial instants of the light-round in the experiment, from the generation of a series of sparks to the formation of an initial expanding kernel are not accounted for in the simulation, and a sphere of burnt gases was directly inserted

at the location of the ignition device.
Comparisons of the light-round duration between the experimental series of measurement and the numerical sequences showed excellent results for cases $\Phi = 0.8$ and $\Phi = 0.89$, while a 30 % error was obtained for case $\Phi = 1.0$. Direct visualisations of the flame fronts evolution however showed that their behaviour was correctly captured by the simulation, in terms of propagation mechanism and shape evolution, even for case $\Phi = 1.0$. In particular, the five-phase process already identified on the gaseous premixed sequences was retrieved here. Burner-to-burner propagation delays confirmed the accurate prediction in the first two cases and showed that the error in the third case comes from an underestimation of the flame propagation velocity throughout the whole sequence.

A detailed analysis of the three simulated light-round sequences has then been carried out in order to further understand the mechanisms at stake during the propagation of the flame fronts in the chamber. A global point of view was first adopted to observe the interaction between the propagating flames and the flow field in the chamber. In particular, the generation of an azimuthal flow in the fresh and burnt gases by the volumetric expansion of the burnt gases was evidenced. This greatly influences the flame absolute velocity and the flow at the exit of the chamber during the light-round sequence.
The observation of the flame structures showed that combustion occurs mainly in the premixed regime, allowing the use of premixed flames considerations and quantities as a first approximation. The turbulent flame dynamics were studied in terms of flame surface evolution and propagation velocities, which allowed comparisons between the three cases.
The propagation of the turbulent flame fronts in the two-phase mixture was also examined through the local behaviour of its leading points, shown to be relevant quantities for the study of the whole sequence, which led to the identification of some phenomena responsible for the flame behaviour, such as the influence of the liquid droplet spray and its vaporization in the chamber.
The interactions between the azimuthal flow in the fresh mixture and the swirling sprays creates heterogeneities in the liquid repartition and therefore in the gas composition. Wakes are formed on the downstream side of the swirling jets formed by the injectors, with notable effects on the motion of the leading point and on its absolute flame velocity.

Finally, a first attempt had been made to account for the influence of the wall temperature on the light-round sequence. Experimental results in both gaseous and two-phase injections have shown that the light-round duration was approximately doubled in *ignition* cases, when the walls are at ambient temperature at the time the ignition is triggered, compared to *re-ignition* cases, where the walls are already at their hot steady-state temperature. The simulations previously presented dealt with *re-ignition cases*, assuming adiabatic

boundary conditions at the walls. A classical iso-thermal law-of-the-wall was here imposed on the chamber walls with a fixed temperature $T_{wall} = 300$ K. It was found that, although the light-round duration was increased by 25 % by the change of boundary condition, it still under-estimates the experimental duration by approximately 30 %. Further analyses showed that the temperature in the simulation is decreased in the burnt gases well after the crossing of the flame, leading to some decrease in the intensity of the induced azimuthal flow by the burnt gases volumetric expansion and therefore a decrease of the propagation velocity of the flame fronts. This decrease, however, seems to occur later than in the experiment, thus explaining the error on the global light-round duration.

Perspectives

Among the main achievements of this work are the successful prediction of the light-round sequence for cases $\Phi = 0.8$ and $\Phi = 0.89$, which match all the datasets that were extracted from the experiment. No definitive conclusion could however be drawn as to the reason for the error in the light-round duration in case $\Phi = 1.0$. Several explanations have been proposed throughout the manuscript. In particular, it was found that the fresh mixture in this case reached a saturated state, with liquid fuel being present everywhere in the chamber, and not only in the bottom as is the case for the other two. The flame fronts therefore propagate in a two-phase mixture, which effectively lowers the flame speed. In this context, the adiabatic boundary condition that is used to represent the experimental hot walls may not be adequate for the simulation of the filling of the chamber with un-burnt mixture. In the experimental set-up, the mixture is pre-heated by the hot walls, which leads to a greater pre-vaporisation of the fuel than what is predicted by the adiabatic walls simulation. Taking into account the increase of temperature of the two-phase mixture in contact with the hot walls before the ignition is triggered might therefore be necessary in order to retrieve accurate initial conditions for the light-round sequence. This is expected to be especially important if the injected liquid fuel is changed to other less volatile ones.

On the other hand, if the change of slope in the propagation delay is due to the presence of liquid droplets, this behaviour might be observed on experimental data from cold walls sequences, where droplets are still present. It cannot be confirmed at present since the experimental light-round duration with ambient temperature walls was only recorded for one operating point. It might be interesting in the future, and in particular with less volatile fuels, to look for a decrease of the propagation velocity linked to the increased presence of droplets.

In any case, the problem posed by the impact of the walls temperature on the whole chamber dynamics remains open. Further work is planned at EM2C on this subject to try to understand which mechanisms are modified by the heat

losses and how to include them in the simulation in order to retrieve the correct propagation delays. This is part of the PhD work of K. Topperwien.

From a simulation point of view, the challenging of the different approaches and models used in the present set-up is a useful exercise that allows to assess their individual impact on the results. Light-round simulations in the Lagrangian framework, which allows in particular to naturally account for the polydispersion of the spray, are being carried out by F. Collin at CERFACS. This work, compared to the simulations that were presented in this manuscript, is expected to provide answers on the influence of the description of the liquid liquid phase on the behaviour of the flame fronts and the flow in the chamber during the ignition sequences.

In addition, some efforts have been done in this thesis to enable two-phase flow simulations with tabulated chemistry in the AVBP solver. In such simulations where the mesh cannot be fine enough to capture the flame front, the turbulent combustion model is bound to have an impact on the description of the flame fronts. The comparison between the TFLES model, used here, and the F-TACLES model, which was successfully applied to the simulation of the light-round sequence with gaseous injection by M. Philip, will provide additional information. The modification of the evaporation routines to make them compatible with tabulated chemistry has been validated on 0D and 1D cases, but could not be applied to SICCA-Spray of MICCA-Spray. Some further work is planned to complete this study.
Another way to challenge the turbulent combustion model is the use of a dynamic formulation for the β constant used in the efficiency function for the TFLES model. The PhD work of P. S. Volpiani provided a new model where this constant is estimated dynamically and locally. In the context of a flame propagating vertically in the chamber and encountering very different cell sizes and mixture conditions, such an approach is relevant. The first results obtained by S. Puggelli indeed show that the values for β computed by this dynamic model are very different from its default constant value. As was shown in chapter 4, the efficiency function plays a role in the flame surface and the sub-grid scale wrinkling, therefore impacting the flame consumption speed. Results from light-round simulations with the dynamic formulation will show whether it also modifies the flame behaviour during the whole sequence.

Perspectives on the medium to long term from a numerical point of view include the study of other liquid fuels, and in particular fuels that are less volatile than n-heptane and that are chemically closer to aeronautic fuels. Experimental data is already available for the injection of liquid dodecane, with pre-heated chamber walls.
All the previously mentioned studies focus on successful ignitions. It is essential to understand such events and to identify the main mechanisms at stake. From such simulations, reduced models, such as was derived by M. Philip for gaseous

premixed injection, can be obtained. With the view of providing tools to design safer and more stable combustors, it will also be interesting to study numerically failed ignition events, where the chamber is for instance only partially ignited. Understanding the difference between a failed and a successful ignition sequence would lead to more certain predictions of the reliability of combustion chambers, and to a faster adoption and adaptation to new clean technologies and biofuels.

References

Abd Al-Masseeh, W., D. Bradley, P. Gaskell, and A. Lau (1991, 12). Turbulent premixed, swirling combustion: Direct stress, strained flamelet modelling and experimental investigation. *23*, 825–833. *(p. 60)*

Abramzon, B. and W. Sirignano (1989). Droplet vaporization model for spray combustion calculations. *International Journal of Heat and Mass Transfer 32*(9), 1605 – 1618. *(p. 47, 67, 86, 134, 212)*

Aggarwal, S. (1998). A review of spray ignition phenomena: Present status and future research. *Progress in Energy and Combustion Science 24*(6), 565 – 600. *(p. 8, 9)*

Aggarwal, S. K. (2014). Single droplet ignition: Theoretical analyses and experimental findings. *Progress in Energy and Combustion Science 45*, 79 – 107. *(p. 8)*

Ahmed, S., R. Balachandran, T. Marchione, and E. Mastorakos (2007). Spark ignition of turbulent nonpremixed bluff-body flames. *Combustion and Flame 151*(1), 366 – 385. *(p. 9)*

Angelberger, C., D. Veynante, F. Egolfopoulos, and T. Poinsot (1998). Large eddy simulations of combustion instabilities in premixed flames. In C. for Turbulence Research (Ed.), *Summer Program*, pp. 61–82. NASA Ames/Stanford Univ. *(p. 56)*

Auzillon, P., O. Gicquel, N. Darabiha, D. Veynante, and B. Fiorina (2012). A filtered tabulated chemistry model for {LES} of stratified flames. *Combustion and Flame 159*(8), 2704 – 2717. Special Issue on Turbulent Combustion. *(p. 59, 62)*

Bach, E., J. Kariuki, J. R. Dawson, E. Mastorakos, and H. joerg Bauer (2013, 2016/03/01). *Spark ignition of single bluff-body premixed flames and annular combustors*. American Institute of Aeronautics and Astronautics. *(p. 13, 129)*

Ballal, D. and A. Lefebvre (1977). Ignition and flame quenching in flowing gaseous mixtures. *Proceedings of the Royal Society of London A: Mathematical, Physical and Engineering Sciences 357*(1689), 163–181. *(p. 9)*

Ballal, D. and A. Lefebvre (1979). Ignition and flame quenching of flowing heterogeneous fuel-air mixtures. *Combustion and Flame 35*, 155 – 168. *(p. 9)*

Ballal, D. and A. Lefebvre (1981a). Flame propagation in heterogeneous

mixtures of fuel droplets, fuel vapor and air. *Symposium (International) on Combustion 18*(1), 321 – 328. Eighteenth Symposium (International) on Combustion. *(p. 102, 187)*

Ballal, D. and A. Lefebvre (1981b). A general model of spark ignition for gaseous and liquid fuel-air mixtures. *Symposium (International) on Combustion 18*(1), 1737 – 1746. Eighteenth Symposium (International) on Combustion. *(p. 9)*

Barré, D., L. Esclapez, M. Cordier, E. Riber, B. Cuenot, G. Staffelbach, B. Renou, A. Vandel, L. Y. Gicquel, and G. Cabot (2014). Flame propagation in aeronautical swirled multi-burners: Experimental and numerical investigation. *Combustion and Flame 161*(9), 2387 – 2405. *(p. 15, 16, 129)*

Birch, A., D. Brown, and M. Dodson (1981). Ignition probabilities in turbulent mixing flows. *Symposium (International) on Combustion 18*(1), 1775 – 1780. Eighteenth Symposium (International) on Combustion. *(p. 10)*

Bird, R., W. Stewart, and E. Lightfoot (1960). *Transport Phenomena*. John Wiley. *(p. 50, 67)*

Boileau, M. (2007, October). *Large eddy simulation of two-phase ignition in aeronautical combustors*. Theses, Institut National Polytechnique de Toulouse - INPT. *(p. xiv, 35, 36, 37, 39, 45, 59, 134)*

Boileau, M., G. Staffelbach, B. Cuenot, T. Poinsot, and C. Bérat (2008). Large eddy simulation of an ignition sequence in a gas turbine engine. *Combustion and Flame 154*(1–2), 2 – 22. *(p. xiv, 15, 16, 128, 161, 191)*

Bourgouin, J.-F., D. Durox, T. Schuller, J. Beaunier, and S. Candel (2013). Ignition dynamics of an annular combustor equipped with multiple swirling injectors. *Combustion and Flame 160*(8), 1398 – 1413. *(p. xiii, 2, 11, 12, 129, 131, 192)*

Bradley, D., P. Gaskell, and X. Gu (1998). The mathematical modeling of liftoff and blowoff of turbulent non-premixed methane jet flames at high strain rates. *Symposium (International) on Combustion 27*(1), 1199 – 1206. Twenty-Seventh Sysposium (International) on Combustion Volume One. *(p. 60)*

Bradley, D., L. Kwa, A. Lau, M. Missaghi, and S. Chin (1988). Laminar flamelet modeling of recirculating premixed methane and propane-air combustion. *Combustion and Flame 71*(2), 109 – 122. *(p. 60)*

Butler, T. and P. O'Rourke (1977). A numerical method for two dimensional unsteady reacting flows. *International Symposium on Combustion 16*(1), 1503 – 1515. *(p. 54)*

Cabrit, O. (2009). *Modélisation des flux pariétaux sur les tuyères des moteurs à propergol solide*. Ph. D. thesis. 2009MON20239. *(p.)*

Cabrit, O. and F. Nicoud (2009). Direct simulations for wall modeling of multicomponent reacting compressible turbulent flows. *Physics of Fluids 21*(5), 055108. *(p. 214, 215, 216, 233)*

Cardin, C., B. Renou, G. Cabot, and A. M. Boukhalfa (2013). Experimental

analysis of laser-induced spark ignition of lean turbulent premixed flames: New insight into ignition transition. *Combustion and Flame 160*(8), 1414 – 1427. *(p. 9)*

CERFACS (2011, dec.). *AVBP Handbook*. *(p. 2, 25, 35)*

Chapman, S. and T. Cowling (1970). *The Mathematical Theory of Non-uniform Gases: An Account of the Kinetic Theory of Viscosity, Thermal Conduction and Diffusion in Gases*. Cambridge Mathematical Library. Cambridge University Press. *(p. 35, 36)*

Charlette, F., C. Meneveau, and D. Veynante (2002). A power-law flame wrinkling model for LES of premixed turbulent combustion part I: non-dynamic formulation and initial tests. *Combustion and Flame 131*(1–2), 159 – 180. *(p. 57, 62, 134, 213)*

Cheneau B, Vié A, D. S. (2015). Large eddy simulations of a liquid fuel swirl burner: Flame characterization for pilot and multipoint injection strategies. In *ASME Turbo Expo: Power for Land, Sea, and Air*, Volume 4A, Combustion, Fuel and Emissions. *(p. 81)*

Chigier, N. (1983). Group combustion models and laser diagnostic methods in sprays: A review. *Combustion and Flame 51*, 127 – 139. *(p. xiii, 5, 6, 7)*

Chiu, H., H. Kim, and E. Croke (1982). Internal group combustion of liquid droplets. *Symposium (International) on Combustion 19*(1), 971 – 980. Nineteenth Symposium (International) on Combustion. *(p. xiii, 5, 6)*

Chiu, H. H. and T. M. Liu (1977). Group combustion of liquid droplets. *Combustion Science and Technology 17*(3-4), 127–142. *(p. 5)*

Chrigui, M., J. Gounder, A. Sadiki, A. R. Masri, and J. Janicka (2012, 8). Partially premixed reacting acetone spray using les and fgm tabulated chemistry. *Combustion and Flame 159*(8), 2718–2741. *(p. 18, 34)*

Clenshaw, C. W. and A. R. Curtis (1960, Dec). A method for numerical integration on an automatic computer. *Numerische Mathematik 2*(1), 197–205. *(p. 97)*

Colin, O., F. Ducros, D. Veynante, and T. Poinsot (2000). A thickened flame model for large eddy simulations of turbulent premixed combustion. *Physics of Fluids 12*(7), 1843–1863. *(p. 25, 56, 57, 58, 134, 213)*

Colin, O. and M. Rudgyard (2000). Development of high-order taylor–galerkin schemes for LES. *Journal of Computational Physics 162*(2), 338 – 371. *(p. 85, 134, 213)*

Collin-Bastiani, F., J. M. Santiago, E. Riber, G. Cabot, B. Renou, and B. Cuenot (2018). A joint experimental and numerical study of ignition in a spray burner. *Proceedings of the Combustion Institute*. *(p. 10)*

Crowe, C., J. Chung, and T. Troutt (1988). Particle mixing in free shear flows. *Progress in Energy and Combustion Science 14*(3), 171 – 194. *(p. 4)*

Damkoehler, G. (1947). The effect of turbulence on the flame velocity in gas mixtures. *Zeitschrift fuer Elektrochemie und Angewandte Physikalische Chemiw 46*(11), 601–626. *(p. 4)*

Davis, S. and C. Law (1998). Laminar flame speeds and oxidation kinetics of iso-octane-air and n-heptane-air flames. *Symposium (International) on Combustion 27*(1), 521 – 527. Twenty-Seventh Sysposium (International) on Combustion Volume One. *(p. xv, 74)*

Esclapez, L., E. Riber, and B. Cuenot (2015). Ignition probability of a partially premixed burner using {LES}. *Proceedings of the Combustion Institute 35*(3), 3133 – 3141. *(p. 10, 128)*

Eyssartier, A., B. Cuenot, L. Y. Gicquel, and T. Poinsot (2013). Using {LES} to predict ignition sequences and ignition probability of turbulent two-phase flames. *Combustion and Flame 160*(7), 1191 – 1207. *(p. 10)*

Favre, A. (1965). The equations of compressible turbulent gases. Technical report, Institut de mecanique statistique de la turbulence. *(p. 30)*

Felden, A., L. Esclapez, E. Riber, B. Cuenot, and H. Wang (2018). Including real fuel chemistry in les of turbulent spray combustion. *Combustion and Flame 193*, 397 – 416. *(p. 3)*

Février, P., O. Simonin, and K. D. Squire (2005). Partitioning of particle velocities in gas–solid turbulent flows into a continuous field and a spatially uncorrelated random distribution: theoretical formalism and numerical study. *Journal of Fluid Mechanics 533*, 1–46. *(p. 35, 38)*

Fiorina, B., R. Baron, O. Gicquel, D. Thevenin, S. Carpentier, and N. Darabiha (2003). Modelling non-adiabatic partially premixed flames using flame-prolongation of ildm. *Combustion Theory and Modelling 7*(3), 449–470. *(p. 60)*

Fiorina, B., D. Veynante, and S. Candel (2015, Jan). Modeling combustion chemistry in large eddy simulation of turbulent flames. *Flow, Turbulence and Combustion 94*(1), 3–42. *(p. 54)*

Fiorina, B., R. Vicquelin, P. Auzillon, N. Darabiha, O. Gicquel, and D. Veynante (2010). A filtered tabulated chemistry model for {LES} of premixed combustion. *Combustion and Flame 157*(3), 465 – 475. *(p. 26, 59, 61, 62)*

Fox, R. O. (2012). Large-Eddy-Simulation Tools for Multiphase Flows. *Annual Review of Fluid Mechanics 44*, 47–76. *(p. 17, 34)*

Franzelli, B., E. Riber, M. Sanjosé, and T. Poinsot (2010). A two-step chemical scheme for kerosene–air premixed flames. *Combustion and Flame 157*(7), 1364 – 1373. *(p. 3, 134)*

Garcia, M. (2009). *Development and validation of the Euler-Lagrange formulation on a parallel and unstructured solver for large-eddy simulation*. Ph. D. thesis, Institut National Polytechnique de Toulouse. *(p. 18)*

Garcia, M., Y. Sommerer, T. Schönfeld, and T. Poinsot (2005, 01). Evaluation of euler-euler and euler-lagrange strategies for large-eddy simulations of turbulent reacting flows. *ECCOMAS Thematic Conference on Computational Combustion*. *(p. 35)*

Gicquel, O., N. Darabiha, and D. Thevenin (2000). Laminar premixed hydrogen/air counterflow flame simulations using flame prolongation of ILDM

with differential diffusion. *Proceeding of the combustion Institute 28*, 1901–1908. *(p. 60)*

Giusti, A. and E. Mastorakos (2017). Detailed chemistry les/cmc simulation of a swirling ethanol spray flame approaching blow-off. *Proceedings of the Combustion Institute 36*(2), 2625 – 2632. *(p. 34)*

Goey, P., J. van Oijen, H. Bongers, and G. R A Groot (2003). New flamelet based reduction methods: the bridge between chemical reduction techniques and flamelet methods. In *European Combustion Meeting*. *(p. 60)*

Granet, V., O. Vermorel, C. Lacour, B. Enaux, V. Dugué, and T. Poinsot (2012). Large-eddy simulation and experimental study of cycle-to-cycle variations of stable and unstable operating points in a spark ignition engine. *Combustion and Flame 159*(4), 1562 – 1575. *(p. 10)*

Greenberg, J., L. Kagan, and G. Sivashinsky (2013). A numerical study of polydisperse spray flame ignition and extinction fronts in a mixing layer. *Combustion Theory and Modelling 17*(6), 1053–1066. *(p. 10)*

Greenberg, J. B., L. S. Kagan, and G. I. Sivashinsky (2012). Effect of a fuel spray on edge flame propagation. *Atomization and Sprays 22*(4), 333–349. *(p. 10)*

H. H. Chiu, E. J. C. (1981). Group combustion of liquid fuel sprays. Technical report, Energy Technology Laboratory Report 81-2. *(p. 5)*

Ham, F., S. Apte, G. Iaccarino, X. Wu, and M. Herrmann (2003, 12). Unstructured les of reacting multiphase flows in realistic gas turbine combustors. In N. A. University (Ed.), *Annual Research Briefs - Center for Turbulence Research, NASA*, pp. 22. *(p. 18, 35)*

Hirschfelder, J., C. Curtiss, R. Bird, and U. of Wisconsin. Theoretical Chemistry Laboratory (1954). *Molecular theory of gases and liquids*. Structure of matter series. Wiley. *(p. 27, 49)*

Hubbard, G., V. Denny, and A. Mills (1975). Droplet evaporation: Effects of transients and variable properties. *International Journal of Heat and Mass Transfer 18*(9), 1003 – 1008. *(p. 48)*

Jones, W. and R. Lindstedt (1988). Global reaction schemes for hydrocarbon combustion. *Combustion and Flame 73*(3), 233 – 249. *(p. 3)*

Jones, W. P., S. Lyra, and S. Navarro-Martinez (2012). Numerical investigation of swirling kerosene spray flames using large eddy simulation. *Combustion and Flame 159*(4), 1539–1561. *(p. 18, 34)*

Jones, W. P. and A. Tyliszczak (2010, Dec). Large eddy simulation of spark ignition in a gas turbine combustor. *Flow, Turbulence and Combustion 85*(3), 711–734. *(p. 10, 128)*

Kader, B. (1981). Temperature and concentration profiles in fully turbulent boundary layers. *International Journal of Heat and Mass Transfer 24*(9), 1541 – 1544. *(p. 216)*

Kaufmann, A. (2004). *Towards Eulerian-Eulerian large eddy simulation of reactive two-phase flows*. Ph. D. thesis, Institut National Polytechnique de Toulouse. 2004INPT002H. *(p. 35, 36, 41)*

Kawai, S. and J. Larsson (2013). Dynamic non-equilibrium wall-modeling for large eddy simulation at high reynolds numbers. *Physics of Fluids 25*(1), 015105. *(p. 233)*

Kolmogorov, A. (1941). The local structure of turbulence in incompressible viscous fluid for very large reynolds numbers. *Akademiia Nauk SSSR Doklady 30*, 301–305. *(p. 28)*

Kuo, K. K. (1986). *Principles of combustion*. John Wiley and Sons. *(p. 42, 55)*

Lacaze, G., E. Richardson, and T. Poinsot (2009). Large eddy simulation of spark ignition in a turbulent methane jet. *Combustion and Flame 156*(10), 1993 – 2009. *(p. 10)*

Lancien, T., N. Dumont, K. Prieur, D. Durox, S. Candel, O. Gicquel, and R. Vicquelin (2016). Uncertainty quantification of injected droplet size in mono-dispersed eulerian simulations. In *International Conference on Multiphase Flow, Florence*. *(p. 87)*

Lancien, T., K. Prieur, D. Durox, S. Candel, and R. Vicquelin (2017). Large-eddy simulation of light-round in an annular combustor with liquid spray injection and comparison with experiments. *Journal of Engineering for Gas Turbines and Power 140*(2). *(p. 131, 141)*

Lefebvre, A. (1989). *Atomization and Sprays*. Taylor and Francis. *(p. 103)*

Lefebvre, A. and D. R. Ballal (2010). *Gas Turbine Combustion*. Taylor and Francis. *(p. xiii, 8, 9, 10, 81, 128, 129)*

Legier, J. P., T. Poinsot, and D. Veynante (2000). Dynamically thickened flame les model for premixed and non-premixed combustion. In *Proc. Summer Program, Center for Turbulence Research, NASA Ames/Stanford Univ.* *(p. 58, 134, 213)*

Letty, C., E. Mastorakos, A. R. Masri, M. Juddoo, and W. O'Loughlin (2012). Structure of igniting ethanol and n-heptane spray flames with and without swirl. *Experimental Thermal and Fluid Science 43*, 47 – 54. Seventh Mediterranean Combustion Symposium. *(p. 9)*

Lu, T. and C. K. Law (2008). A criterion based on computational singular perturbation for the identification of quasi steady state species: A reduced mechanism for methane oxidation with no chemistry. *Combustion and Flame 154*(4), 761 – 774. *(p. 3)*

Luo, K., H. Pitsch, M. G. Pai, and O. Desjardins (2011). Direct numerical simulations and analysis of three-dimensional n-heptane spray flames in a model swirl combustor. *Proceedings of the Combustion Institute 33*(2), 2143–2152. *(p. 18, 34)*

Ma, P. C., T. Ewan, C. Jainski, L. Lu, A. Dreizler, V. Sick, and M. Ihme (2017, Jan). Development and analysis of wall models for internal combustion engine simulations using high-speed micro-piv measurements. *Flow, Turbulence and Combustion 98*(1), 283–309. *(p. 233)*

Ma, P. C., M. Greene, V. Sick, and M. Ihme (2017). Non-equilibrium wall-modeling for internal combustion engine simulations with wall heat trans-

fer. *International Journal of Engine Research 18*(1-2), 15–25. *(p. 233)*

Maas, U. and S. Pope (1992a). Implementation of simplified chemical kinetics based on intrinsic low-dimensional manifolds. *Symposium (International) on Combustion 24*(1), 103 – 112. Twenty-Fourth Symposium on Combustion. *(p. 60)*

Maas, U. and S. Pope (1992b). Simplifying chemical kinetics: Intrinsic low-dimensional manifolds in composition space. *Combustion and Flame 88*(3), 239 – 264. *(p. 60)*

Machover, E. and E. Mastorakos (2016, 5). Spark ignition of annular non-premixed combustors. *Experimental Thermal and Fluid Science 73*, 64–70. *(p. 13, 129)*

Machover, E. and E. Mastorakos (2017). Experimental investigation on spark ignition of annular premixed combustors. *Combustion and Flame 178*(Supplement C), 148 – 157. *(p. xiii, 13, 14, 129)*

Marchione, T., S. Ahmed, and E. Mastorakos (2009). Ignition of turbulent swirling n-heptane spray flames using single and multiple sparks. *Combustion and Flame 156*(1), 166 – 180. *(p. 9, 128)*

Marrero Santiago, J., A. Verdier, C. Brunet, A. Vandel, G. Godard, G. Cabot, A. Boukhalfa, and B. Renou (2017, 10). Experimental study of aeronautical ignition in a swirled confined jet-spray burner. *Journal of Engineering for Gas Turbines and Power 140*. *(p. 15, 128, 129)*

Masri, A. R., A. AlHarbi, S. Meares, and S. S. Ibrahim (2012). A comparative study of turbulent premixed flames propagating past repeated obstacles. *Industrial & Engineering Chemistry Research 51*(22), 7690–7703. *(p. 180)*

Massot, M. (2007). *Multiphase Reacting Flows: Modelling and Simulation*, Chapter Eulerian Multi-Fluid Models for Polydisperse Evaporating Sprays, pp. 79–123. Vienna: Springer Vienna. *(p. 79)*

Mastorakos, E. (2009). Ignition of turbulent non-premixed flames. *Progress in Energy and Combustion Science 35*(1), 57 – 97. *(p. 8, 9)*

Maz'ja, V. G. (1985). *Sobolev Spaces*. Springer Series in Soviet Mathematics. *(p. 188)*

Mercier, R., P. Auzillon, V. Moureau, N. Darabiha, O. Gicquel, D. Veynante, and B. Fiorina (2014, Sep). Les modeling of the impact of heat losses and differential diffusion on turbulent stratified flame propagation: Application to the tu darmstadt stratified flame. *Flow, Turbulence and Combustion 93*(2), 349–381. *(p. 62)*

Moreau, M., O. Simonin, and B. Bédat (2010). Development of gas-particle euler-euler les approach: A priori analysis of particle sub-grid models in homogeneous isotropic turbulence. *Flow, Turbulence and Combustion 84*(2), 295–324. *(p. 51, 52)*

Mounaïm-Rousselle, C., L. Landry, F. Halter, and F. Foucher (2013). Experimental characteristics of turbulent premixed flame in a boosted spark-ignition engine. *Proceedings of the Combustion Institute 34*(2), 2941 –

2949. *(p. 10)*

Nakamura, M., F. Akamatsu, R. Kurose, and M. Katsuki (2005). Combustion mechanism of liquid fuel spray in a gaseous flame. *Physics of Fluids 17*(12), 123301. *(p. 7)*

Neophytou, A. and E. Mastorakos (2009). Simulations of laminar flame propagation in droplet mists. *Combustion and Flame 156*(8), 1627 – 1640. *(p. 103)*

Neophytou, A., E. Mastorakos, and R. Cant (2010). Dns of spark ignition and edge flame propagation in turbulent droplet-laden mixing layers. *Combustion and Flame 157*(6), 1071 – 1086. *(p. 10)*

Nicoud, F. and F. Ducros (1999). Subgrid-scale stress modelling based on the square of the velocity gradient tensor. *Flow, Turbulence and Combustion 62*(3), 183–200. *(p. 32, 85, 134, 213)*

Paulhiac, D. (2015). *Modélisation de la Combustion d'un spray dans un Bruleur Aéronautique*. Ph. D. thesis, INP Toulouse. *(p. xv, 67, 73, 74, 134)*

Pepiot-Desjardins, P. and H. Pitsch (2008). An efficient error-propagation-based reduction method for large chemical kinetic mechanisms. *Combustion and Flame 154*(1), 67 – 81. *(p. 3)*

Peters, J. and A. Mellor (1980). An ignition model for quiescent fuel sprays. *Combustion and Flame 38*, 65 – 74. *(p. 9)*

Peterson, B., D. L. Reuss, and V. Sick (2011). High-speed imaging analysis of misfires in a spray-guided direct injection engine. *Proceedings of the Combustion Institute 33*(2), 3089 – 3096. *(p. 10)*

Peterson, B., D. L. Reuss, and V. Sick (2014). On the ignition and flame development in a spray-guided direct-injection spark-ignition engine. *Combustion and Flame 161*(1), 240 – 255. *(p. 10)*

Philip, M. (2016). *Dynamique de l'allumage circulaire dans les foyers annulaires multi-injecteurs*. Ph. D. thesis. 2016SACLC034. *(p. xiv, 17, 181, 190, 191, 194)*

Philip, M., M. Boileau, R. Vicquelin, E. Riber, T. Schmitt, B. Cuenot, D. Durox, and S. Candel (2015). Large eddy simulations of the ignition sequence of an annular multiple-injector combustor. *Proceedings of the Combustion Institute 35*(3), 3159 – 3166. *(p. 2, 16, 17, 129, 131, 147, 149, 150, 154, 161, 191)*

Philip, M., M. Boileau, R. Vicquelin, T. Schmitt, D. Durox, J.-F. Bourgouin, and S. Candel (2015). Simulation of the Ignition Process in an Annular Multiple-Injector Combustor and Comparison With Experiments. *Journal of Engineering for Gas Turbines and Power 137*(3). *(p. 2, 16, 17, 129, 131, 147, 149, 161, 210)*

Poinsot, T. and S. Lele (1992). Boundary conditions for direct simulations of compressible viscous flows. *Journal of Computational Physics 101*(1), 104 – 129. *(p. 86, 213)*

Poinsot, T. and D. Veynante (2012). *Theoretical and Numerical Combustion,*

Third Edition. http://elearning.cerfacs.fr/combustion. *(p. xiv, 29, 30, 31, 54, 62)*

Pope, S. B. (2000). *Turbulent Flows*. Cambridge University Press. *(p. 3)*

Prieur, K. (2017). *Dynamique de la combustion dans un foyer annulaire multi-injecteurs diphasique*. Ph. D. thesis, Universite Paris-Saclay. *(p. 81, 192)*

Prieur, K., D. Durox, J. Beaunier, T. Schuller, and S. Candel (2017). Ignition dynamics in an annular combustor for liquid spray and premixed gaseous injection. *Proceedings of the Combustion Institute 36*(3), 3717 – 3724. *(p. xiii, 2, 12, 13, 15, 17, 129, 130, 131, 180, 185, 192, 197)*

Prieur, K., D. Durox, G. Vignat, T. Schuller, and S. Candel (2018). Flame and spray dynamics during the light-round process in an annular system equipped with multiple swirl spray injectors. *Proceedings of the ASME Turbo Expo*. *(p. xviii, xxiv, 122, 123, 129, 174, 192)*

Ranz, W. E. and W. R. Marshall (1952, March). Evaporation from drops, parts i and ii. *Chemical Engineering Progress 48*(3), 141–146. *(p. 43, 47)*

Reagana, M. T., H. N. Najm, R. G. Ghanem, and O. M. Knio (2003). Uncertainty quantification in reacting-flow simulations through non-intrusive spectral projection. *Combustion and Flame 132*(3), 545–555. *(p. 96)*

Reveillon, J. and F. Demoulin (2007). Evaporating droplets in turbulent reacting flows. *Proceedings of the Combustion Institute 31*(2), 2319 – 2326. *(p. 7)*

Reveillon, J. and L. Vervisch (2005). Analysis of weakly turbulent dilute-spray flames and spray combustion regimes. *Journal of Fluid Mechanics 537*, 317–347. *(p. 7, 118, 173)*

Reynolds, O. (1883). An experimental investigation of the cincumstances which determine whether the motion of water shall be direct or sinuous, and of the law of resistance in parellel channels. *Philosophical Transactions of the Royal Society of London 174*, 935–982. *(p. 3)*

Riber, E., V. Moureau, M. García, T. Poinsot, and O. Simonin (2009). Evaluation of numerical strategies for large eddy simulation of particulate two-phase recirculating flows. *Journal of Computational Physics 228*(2), 539 – 564. *(p. 81)*

Richardson, E. S. and E. Mastorakos (2007). Numerical investigation of forced ignition in laminar counterflow non-premixed methane-air flames. *Combustion Science and Technology 179*(1-2), 21–37. *(p. 10)*

Saghafian, A., V. E. Terrapon, and H. Pitsch (2015). An efficient flamelet-based combustion model for compressible flows. *Combustion and Flame 162*(3), 652 – 667. *(p. 67)*

Sanjosé, M. (2009). *Evaluation de la méthode Euler-Euler pour la simulation aux grandes échelles des chambres à carburant liquide*. Ph. D. thesis. 2009INPT066H. *(p. 49, 50)*

Sanjosé, M., J. M. Senoner, F. Jaegle, B. Cuenot, S. Moreau, and T. Poinsot (2011, 6). Fuel injection model for Euler–Euler and Euler–Lagrange large-

eddy simulations of an evaporating spray inside an aeronautical combustor. *Int. Journal of Multiphase Flow 37*(5), 514–529. *(p. 18, 81, 87)*

Schiller, L. and A. Naumann (1935). A drag coefficient correlation. *Zeitschrift des Vereins Deutscher Ingenieure 77*. *(p. 41)*

Schönfeld, T. and M. Rudgyard (1999). Steady and unsteady flow simulations using the hybrid flow solver avbp. *AIAA Journal 37*(11), 1378–1385. *(p. 2, 134)*

Senoner, J. M., M. Sanjosé, T. Lederlin, F. Jaegle, M. García, E. Riber, B. Cuenot, L. Gicquel, H. Pitsch, and T. Poinsot (2009). Eulerian and Lagrangian Large-Eddy Simulations of an evaporating two-phase flow. *Comptes Rendus Mécanique 337*(6–7), 458–468. *(p. 18)*

Shum-Kivan, F., J. M. Santiago, A. Verdier, E. Riber, B. Renou, G. Cabot, and B. Cuenot (2016). Experimental and numerical analysis of a turbulent spray flame structure. *Proceedings of the Combustion Institute 36*(2), 2567–2575. *(p. 34, 134)*

Shy, S., C. Liu, and W. Shih (2010). Ignition transition in turbulent premixed combustion. *Combustion and Flame 157*(2), 341 – 350. *(p. 9)*

Sierra, P. (2012). *Modeling the dispersion and evaporation of sprays in aeronautical combustion chambers*. Ph. D. thesis. 2012INPT0005. *(p. 39, 49, 50)*

Simmie, J. M. (2003). Detailed chemical kinetic models for the combustion of hydrocarbon fuels. *Progress in Energy and Combustion Science 29*(6), 599 – 634. *(p. 2)*

Sirignano, W. A. (1999). *Fluid Dynamics and Transport of Droplets and Sprays*. Cambridge University Press. *(p. 42)*

Smagorinsky, J. (1963). General circulation experiments with the primitive equations: 1. the basic experiment. *Monthly Weather Review 91*(3), 99–164. *(p. 51)*

Smallbone, A., W. Liu, C. Law, X. You, and H. Wang (2009). Experimental and modeling study of laminar flame speed and non-premixed counterflow ignition of n-heptane. *Proceedings of the Combustion Institute 32*(1), 1245 – 1252. *(p. xv, 73, 74)*

Smith, M., A. Birch, D. Brown, and M. Fairweather (1988). Studies of ignition and flame propagation in turbulent jets of natural gas, propane and a gas with a high hydrogen content. *Symposium (International) on Combustion 21*(1), 1403 – 1408. Twenty-First Symposuim (International on Combustion). *(p. 10)*

Spalding, D. (1953). The combustion of liquid fuels. *Symposium (International) on Combustion 4*(1), 847 – 864. Fourth Symposium (International) on Combustion. *(p. 44, 47)*

Squires, K. D. and J. K. Eaton (1991). Measurements of particle dispersion obtained from direct numerical simulations of isotropic turbulence. *Journal of Fluid Mechanics 226*, 1–35. *(p. 5)*

Stokes, G. G. (1851). On the effect of the internal friction of fluids on the

motion of pendulums. *Transactions of the Cambridge Philosophical Society 9*, 8. *(p. 41)*

Stull, D. R., H. Prophet, and U. States. (1971). *JANAF thermochemical tables [electronic resource] / D.R. Stull and H. Prophet, project directors* (2d ed. ed.). U.S. Dept. of Commerce, National Bureau of Standards Washington, D.C. *(p. 33)*

Subramanian, V., P. Domingo, and L. Vervisch (2010). Large eddy simulation of forced ignition of an annular bluff-body burner. *Combustion and Flame 157*(3), 579 – 601. *(p. 10, 128)*

Sung, C., C. Law, and J.-Y. Chen (2001). Augmented reduced mechanisms for no emission in methane oxidation. *Combustion and Flame 125*(1), 906 – 919. *(p. 3)*

Suzuki, T. and H. H. Chiu (1971). Multi droplet combustion on liquid propellants. In *Proceedings of the Ninth International Symposium on Space ane Technology and Science*, Volume 30, pp. 145–154. *(p. 5)*

Urzay, J. (2011). A revised spray-combustion diagram of diffusion-controlled burning regimes in fuel-spray clouds. *Annual Research Driefs of the Center for Turbulence Research*, 193–198. *(p. 7)*

van Oijen, J., F. Lammers, and L. de Goey (2001). Modeling of complex premixed burner systems by using flamelet-generated manifolds. *Combustion and Flame 127*(3), 2124 – 2134. *(p. 60)*

Vermorel, O., P. Quillatre, and T. Poinsot (2017). Les of explosions in venting chamber: A test case for premixed turbulent combustion models. *Combustion and Flame 183*, 207 – 223. *(p. 180)*

Veynante, D. and L. Vervisch (2002). Turbulent combustion modeling. *Progress in Energy and Combustion Science 28*(3), 193 – 266. *(p. 177)*

Vicquelin, R., B. Fiorina, N. Darabiha, O. Gicquel, and D. Veynante (2009). Coupling tabulated chemistry with large eddy simulation of turbulent reactive flows. *Comptes Rendus Mécanique 337*(6–7), 329 – 339. Combustion for aerospace propulsion. *(p. 61)*

Vicquelin, R., B. Fiorina, S. Payet, N. Darabiha, and O. Gicquel (2011). Coupling tabulated chemistry with compressible {CFD} solvers. *Proceedings of the Combustion Institute 33*(1), 1481 – 1488. *(p. 61)*

Vié, A., F. Laurent, and M. Massot (2013, 3). Size-velocity correlations in hybrid high order moment/multi-fluid methods for polydisperse evaporating sprays: Modeling and numerical issues. *Journal of Computational Physics 237*, 177–210. *(p. 79)*

Volpiani, P. S. (2017). *Dynamic wrinkling flame model for large eddy simulations of turbulent premixed combustion.* Ph. D. thesis. 2017SACLC005. *(p. 56)*

Wandel, A. P. (2014). Influence of scalar dissipation on flame success in turbulent sprays with spark ignition. *Combustion and Flame 161*(10), 2579 – 2600. *(p. 9)*

Wang, B., A. Kronenburg, G. L. Tufano, and O. T. Stein (2018). Fully

resolved dns of droplet array combustion in turbulent convective flows and modelling for mixing fields in inter-droplet space. *Combustion and Flame 189*, 347 – 366. *(p. 7)*

Westbrook, C. K. and F. L. Dryer (1981). Simplified reaction mechanisms for the oxidation of hydrocarbon fuels in flames. *Combustion Science and Technology 27*(1-2), 31–43. *(p. 3)*

Xiu, D. and G. E. Karniadakis (2002). The wiener–askey polynomial chaos for stochastic differential equations. *SIAM journal on scientific computing 24*(2), 619–644. *(p. 96)*

Yamashita, H., M. Shimada, and T. Takeno (1996). A numerical study on flame stability at the transition point of jet diffusion flames. *Symposium (International) on Combustion 26*(1), 27 – 34. *(p. 118, 173)*

Yoshizawa, A. (1986). Statistical theory for compressible turbulent shear flows, with the application to subgrid modeling. *The Physics of Fluids 29*(7), 2152–2164. *(p. 51)*

ÉCOLE DOCTORALE
Sciences mécaniques et énergétiques, matériaux et géosciences (SMEMAG)

Titre : Etude numérique de l'allumage diphasique de foyers annulaires multi-brûleurs

Mots clés : Combustion diphasique, Allumage circulaire, Propagation de flamme

Résumé : La phase d'allumage est une composante critique à prendre en compte lors de la conception et du dimensionnement d'une chambre de combustion aéronautique, en particulier lorsque de nouvelles technologies ou architectures sont envisagées dans l'objectif de réduire les émissions de polluants causées par la combustion de carburants d'origine fossile. Il est donc primordial d'atteindre une compréhension détaillée du processus complexe qu'est l'allumage dans des conditions réalistes afin d'être en mesure de choisir les meilleures géométries qui assurent un fonctionnement fiable, stable et sûr des moteurs tout au long de leur cycle de vie. Des simulations aux grandes échelles de l'allumage circulaire d'une chambre de combustion annulaire avec injection de carburant liquide sont réalisés pour trois points de fonctionnement et comparées avec les données expérimentales en termes de structure de flamme et de délai d'allumage. Une analyse détaillée des trois séquences d'allumage numériques permet d'identifier certains aspects clés de la propagation de la flamme dans le mélange froid diphasique. Enfin, les pertes thermiques aux parois sont prises en compte, dans l'objectif d'évaluer la capacité de la simulation à retrouver la forte chute de la vitesse de propagation observée expérimentalement lorsque les parois sont à température ambiante.

Title : Numerical study of two-phase ignition in annular multi-burner combustors

Keywords : Two-phase combustion, Light-round, Flame propagation

Abstract : Ignition is one of the critical issues that arise in the design and dimensioning of aeronautic combustors, in particular when new technologies are envisioned to reduce the amount of pollutants generated by the combustion of fossil fuels. It is therefore important to achieve a detailed understanding of this complex process in realistic conditions in order to enable informed design choices leading to reliable, stable and safe operation of the engines. Large eddy simulations of the light-round with two phase injection are carried out for three operating conditions and compared to experimental data in terms of flame structure and global duration. The liquid phase is described with a mono-disperse Eulerian approach. A detailed analysis of the three numerical light-round sequences allows to identify some key aspects of the flame propagation in the two-phase mixture. Interactions be- tween the flame, the flow field and the liquid sprays create heterogeneities in the liquid repartition and wakes on the down-stream side of the swirling jets formed by the injectors, with notable effects on the motion of the leading point and on the ab- solute flame velocity. Finally, heat losses at the walls are accounted for during the light-round in order to assess the simulation's ability to retrieve the marked slow- down of the flame propagation observed experimentally when the quartz walls are at ambient temperature.

Université Paris-Saclay
Espace Technologique / Immeuble Discovery
Route de l'Orme aux Merisiers RD 128 / 91190 Saint-Aubin, France